DEVELOPMENT OF NANOSTRUCTURED DIELECTRIC HYDROPHOBIC THIN FILMS FOR HIGH VOLTAGE INSULATOR

Ph.D. THESIS

by

VIKRAMADITYA DAVE

DEPARTMENT OF ELECTRICAL ENGINEERING
INDIAN INSTITUTE OF TECHNOLOGY ROORKEE
ROORKEE – 247667 (INDIA)
JANUARY, 2015

DEVELOPMENT OF NANOSTRUCTURED DIELECTRIC HYDROPHOBIC THIN FILMS FOR HIGH VOLTAGE INSULATOR

A THESIS

Submitted in partial fulfilment of the requirements for the award of the degree

of

DOCTOR OF PHILOSOPHY

in

ELECTRICAL ENGINEERING

by

VIKRAMADITYA DAVE

DEPARTMENT OF ELECTRICAL ENGINEERING
INDIAN INSTITUTE OF TECHNOLOGY ROORKEE
ROORKEE – 247667 (INDIA)
JANUARY, 2015

INDIAN INSTITUTE OF TECHNOLOGY ROORKEE
ROORKEE

CANDIDATE'S DECLARATION

I hereby certify that the work which is being presented in this thesis entitled **"DEVELOPMENT OF NANOSTRUCTURED DIELECTRIC HYDROPHOBIC THIN FILMS FOR HIGH VOLTAGE INSULATOR"** in partial fulfilment of the requirements for the award of the Degree of Doctor of Philosophy and submitted in the Department of Electrical Engineering of the Indian Institute of Technology Roorkee is an authentic record of my own work carried out during a period from December, 2010 to January, 2015 under the supervision of Professor H. O. GUPTA, Director, Jaypee Institute of Information Technology Noida and Dr. Ramesh Chandra, Professor, Institute Instrumentation Centre, Indian Institute of Technology Roorkee.

The matter presented in this thesis has not been submitted by me for the award of any other degree of this or any other Institute.

(**VIKRAMADITYA DAVE**)

This is to certify that the above statement made by the candidate is correct to the best of our knowledge.

(H.O. Gupta)
Supervisor

(Ramesh Chandra)
Supervisor

Date: _____

ABSTRACT

High voltage insulators are the backbone of any power system network. They can be defined as the devices which are used on transmission lines, transformers and distribution substations to support, separate or contain current carrying conductors at high voltage. All insulators have dual functions, mechanical and electrical, which commonly present conflicting demands to the designer.

A major problem of these insulators is the accumulation of air borne contamination on their surface. The major cause of pollutant accumulation on the insulator surface is the high surface energy due to their strong electrostatic bond among the various atoms in the material. The chief sources of contamination are coastal areas, salt industries, cement industries, volcanic activity areas, industrial burning and chemical industries. During a light rain or fog or mist, these contaminations get moistened and thus, form a conducting layer through which leakage current flows. Dry bands are formed as a consequence of the warming-up of the insulation surface layer. Partial arc appear throughout the dry bands which ultimately lead to surface flashover of the insulator. Thus, complete breakdown of the power system .

The main objective of present work was **to synthesize nanostructured dielectric hydrophobic thin films especially, Hafnium oxide (HfO_2), Hafnium oxynitride (HfO_xN_y), and Hafnium-titanium oxide (HfTiO) on glass and Quartz substrates by DC/RF magnetron sputtering technique and to investigate the effect of sputtering process parameters on structural, optical, hydrophobic and electrical properties of these materials in order to mitigate the problem of contamination.** A chapter-wise summary of the thesis is given below.

Chapter 1 gives an overview about the high voltage insulators used in electrical power system. It discusses the role of insulators and also the problem of contamination being by these insulators. The surface flashover phenomenon was described and its consequences were also highlighted. The economic loss incurred due to contamination was also highlighted in this chapter. Various mitigation techniques and their pros-cons has also been discussed in this chapter. Nanotechnology based coatings was put forward as a effective remedial measure and dielectric hydrophobic coating was suggested as a solution to this problem. Hafnium based oxide, oxynitride and composite was selected as a material to resolve this problem. Magnetron Sputtering was selected as a synthesis technique method

Chapter 2 presents the details of synthesis and characterization techniques, employed for the present research work. **Section 2.1-** A brief description as to the thin film growth modes, influenced by the interaction energies of substrate and film atoms is included in this section. **Section 2.2 –** The process

description and mechanistic details of DC/RF magnetron sputtering technique used for the deposition of thin films in the present work is discussed in this section. **Section 2.3-** The methodology for the characterization of deposited films by different techniques such as X-Ray Diffraction for the phase identification and grain size, surface morphology of the films by using techniques such as Atomic Force Microscopy (AFM) and elemental analysis using Electron Probe Microscopy (EPMA) and electron diffractin scattering (EDS) are discussed. The hydrophobic properties of deposited films were measured by water contact angle goniometer. The four probe measurement unit and impedance analyser was used to measure electrical properties of the sputter deposited thin films in the present work. UV-vis-NIR spectrophotometer used for optical property measurement was also highlighted in this chapter.

Chapter 3 describes the synthesis and characterization of **hafnium oxide** at different sputtering Parameters. **Section 3.1** give a brief introduction about the hafnium oxide and discusses the work of different research group contributed in synthesizing hafnium oxide by sputtering. **Section 3.2** discusses the effect of sputtering gas on structural, morphological, hydrophobic, optical and electrical properties of deposited nanostructured hafnium oxide thin film over glass insulators. All the deposited films were found to be hydrophobic as well as dielectric. The argon gas was found to be optimum sputtering gas at a O_2/Ar=0.5. **Section 3.3** discussed about the effect of sputtering pressure on different properties of HfO_2 films. The optimum pressure was obtained as 15m Torr where the film was monoclinic crystalline, hydrophobic, dielectric and possesses high resistivity of order 10^4 ohm-cm. **Section 3.4** discusses the different properties of HfO_2 as sputtering power is varied from 30 to 60 W.

Higher hydrophobicity was achieved at 50 and 60 W power with dielectric and insulating characteristics. However, due to economical reason 50 W was selected as a optimum power for HfO_2 coatings. **Section 3.5** deals with the effect of substrate temperature on the structural, hydrophobic, optical and electrical properties of HfO_2 films. The temperature was varied from room to 500 °C and higher hydrophobicity and crystallinity was obtained at 500 °C but the electrical resistivity was drastically reduced. Hence, 50 W, 15 mTorr, room temperature was selected as a optimum sputtering parameter for hydrophobic dielectric HfO_2 coating over glass insulators. **Section 3.6** deals with the electrical breakdown study on uncoated glass and optimized coated glass. An enhancement was obtained in the breakdown strength from 20 kV/mm to 23 kV/mm.

Chapter 4 presents in detail the synthesis and characterization details of **hafnium oxynitride** films. **Section 4.1** deals with the properties of hafnium oxynitride and also highlights the work done by the various research group. **Section 4.2** describes the effect of sputtering gas and oxygen partial pressure on the structural, morphological, hydrophobic and electrical property of HfO_xN_y. The optimum parameter were obtained for Ar gas at 10% oxygen partial pressure. **Section 4.2** deals with the substrate temperature effect on different properties of HfOxNy. The bi-phase characterization were obtained for all the deposited films with higher hydrophobicity at 400 °C. However, the dielectric constant and resistivity were less in comparison to the room temperature coated

film. Thus, from technical as well as economical point of view, room temperature was considered as optimum temperature. **In section, 4.3** variation of sputtering pressure was studied. The sputtering pressure was varied from 10 to 30 mTorr in steps of 5 mTorr. Higher hydrophobicity and resistivity was obtained for 20 mTorr sputtering pressure. **Section 4.4** describes the effect of power on various properties of HfO_xN_y coated at room temperature. The power was varied from 20 to 60 W. The optical, electrical and hydrophobic was same and higher for power 50 and 60 W. Hence, 50 W power was considered as the optimum economical power. Section **4.5** deals with electrical breakdown study of uncoated and optimized coated glass insulator. The breakdown strength was found to be 25 kV/mm which is slightly higher in comparison to the HfO_2.

Chapter 5 deals with the synthesis and characterization of HfTiO nanocomposite coating over glass substrate. **Section 5.1** gives introduction about nanocomposite coating. It also highlights the work of different research group over HfTiO coating. Only two parameter were studied for nanocomposite coating namely temperature and power. **Section 5.2** deals with the effect of temperature on hydrophobic, electrical and optical properties of HfTiO coating. Higher hydrophobicity, large dielectric constant and less resistivity were obtained at 500 °C temperature. **Section 5.3** deals the variation

of power of Ti target from 110 to 150 W in steps of 20 W keeping Hf target power constant equals to 50 W. The coating were hydrophobic for all power. The higher hydrophobicity and high dielectric properties were obtained at a Ti power of 150 W. The contact angle was **107.6°** and resistivity was also of order 10^4 at this power. **Section 5.4** describes the breakdown study of coated and HfTiO coated glass insulators. The breakdown strength was 37 kV/cm for optimized HfTiO coated glass.

Chapter 6 presents the summary and conclusion of the entire work presented in the thesis and also proposes the future directions in which these studies can be extended.

CONTENTS

LIST OF FIGURES

LIST OF TABLES

Journal Publications

1. **V. Dave**, P. Dubey, H.O. Gupta, R. Chandra, Effect of sputtering gas on structural, optical and hydrophobic properties of DC-sputtered hafnium oxide thin films, Surface & Coatings Technology 232 (2013) 425–431.
2. **V. Dave**, P. Dubey, H.O. Gupta, R. Chandra, Influence of sputtering pressure on the structural, optical and hydrophobic properties, Thin Solid Films 549 (2013) 2–7.
3. **V. Dave**, P. Dubey, H.O. Gupta, R. Chandra, Nanotechnology for outdoor High voltage insulator: An experimental Investigation, International Journal of ChemTech Research, 5 666-670 (2013).
4. **V. Dave**, R.K. Jain, Y. K. Gautama, A.K. Chawla, R. Chandra, A study on structural, optical and hydrophobic properties of oblique angle sputter deposited HfO_2 films, Applied Surface Science 283 (2013) 332–338.
5. **V. Dave**, H.O. Gupta, R. Chandra, Nanostructured Hydrophobic DC sputtered Inorganic Oxide coating for Outdoor Glass Insulators, Applied Surface Science, 295 231-239 (2014)
6. **V. Dave**, P.K. Mishra, H.O. Gupta, R. Chandra Potential impact of ambient gases and oxygen partial pressure on Structural, Hydrophobic, Optical and Electrical property of nanostructured HfO_xN_yfilm, Surface & Coatings Technology, Under review (2014)
7. **V. Dave**, A. Sanger, H.O. Gupta, R. Chandra, Potential impact of sputtering pressure on structural, hydrophobic, optical and electrical property of nanocrystalline HfO_xN_y thin film for decontamination application, Material Research Letter, Under review (2014)

Conference Publications

1. **V. Dave**, R.K. Jain, H.O. Gupta, R. Chandra , Structural and Hydrophobic properties of Reactive DC Magnetron sputtered Hafnium oxide thin film, International Conference on Nanoscience and Nanotechnology, January 2012, Hyderabad
2. **V. Dave**, H.O. Gupta, R. Chandra , Investigation of Hydrophobic and Optical properties of HfO_2 Coating on Ceramic Insulator, IEEE International Conference on Properties and Applications of Dielectric materials, July 2012, Bangalore
3. **V. Dave**, P.Dubey, H.O. Gupta, R. Chandra, Temperature dependent Structural, Optical and Hydrophobic Properties of Sputtered deposited HfO_2 films, International Conference on Optoelectronic Materials and Thin films for Advanced Technology, January 2013, Kochi
4. **V. Dave**, P. Dubey, H.O. Gupta, R. Chandra, Microstructural and Optical Properties of Sputter Deposited Hafnium oxy nitride films on glass substrate, IEEE International Conference on Energy effiecient Technologies for Sustainability, April 2013, Nagercoil.
5. **V. Dave**, H.O. Gupta,R. Chandra, Protective nanostructured metal oxynitride thin film coating for ceramic insulators: An experimental investigation, Intern ational conference on Nanotechnology, October 2013, Haldia
6. **V. Dave**, Arvind Kumar, P.K. Mishra, H.O. Gupta, R. Chandra, A comprehensive study on structural, optical, wettability and electrical properties of hard hafnium oxynitride thin film, , International conference on Structural and Physical properties of solids, December 2013, ISM Dhanbad
7. **V. Dave**, A. Sanger, H.O. Gupta, R. Chandra, Temperature dependent Non wettable Thin film Coating for Porcelain Insulators, International conference on Emerging Materials and processes 2014, Bhubaneswar
8. **V. Dave**, H. O. Gupta, R. Chandra, Temperature dependent obliquely deposited Anti-contamination coating of HfO_2 for glass insulators, International conference on metallurgical coatings and thin films 2014, San Diego-USA.
9. **V. Dave**, A. Sanger, H. O. Gupta, R. Chandra ,Anti Contamination Metal Oxynitride Thin Film Coating for Outdoor Insulators: An Experimental Investigation, International conference on Nanotechnology 2014, Pune

CHAPTER 1
INTRODUCTION AND LITERATURE REVIEWS

1.1 Introduction to Insulators

Modern society is strongly dependent on uninterrupted and reliable electric power supply.This requirement forces manufacturers to develop better and more reliable componentsand equipment for power generation, transmission and distribution.High voltage insulators belong to this group [**61,115**].

High voltage insulators are the backbone of any power system network. They can be defined as the devices which are used on transmission lines, transformers and distribution substations to support, separate or contain current carrying conductors at high voltage [**115**].All insulators have dual functions,mechanical and electrical, which commonly present conflicting demands to the designer.

The history of insulators began together with the development of electrical communications. Many materials classified as insulators among them wood,rubber,glass and numerous plastics have appeared in the production and transfer of electrical energy.Classical outdoor insulators are made of ceramics which includes glass and glazed porcelain, both of which are having high surface energy and brittle nature.Ceramic materials have been

used in insulators from 1800 onward.In 1850,the first porcelain insulators were introduced. A few years later,in 1858,glass type insulators appeared.

Ceramic insulators have over one century of service history.These insulators are being used from a low voltage up to the highest voltage existing today.This material has proven itself to resist environmental ageing and to be self supporting. The various advantages of these insulators are listed below[**87**].

(i) **High stability:**The strong ionic bond and close packing of the atoms provides high stability to the ceramic materials used as outdoor insulators.

(ii) **Greater mechanical strength:**The rigid nature of the ceramic material imparts significant mechanical strength to the insulators.These high strength insulators can be fabricated for both tension and cantilever loads.The porcelain housings employed for cable terminations,bushings and surge arrestors are self supporting and do not require other material**.**

(iii) **Low raw materials cost:**The principal raw materials of porcelain such as clays,feldspar and quartz are relatively inexpensive and readily available.

However, these materials have some limitations which are listed below.

(i) **Breakage:**Ceramics are very brittle.This means that they are easily broken in handling, transits or installation.

(ii) **Weight:**The very dense nature of ceramics makes them heavy. As the voltage rating increases, there is a compounding effect. This not only makes difficult handling,which can requires cranes, but it also means that expensive and large structural supports are necessary.

(iii) **Pollution performance:** The stable chemical bonds of ceramic material have high surface free energy.This property ensures that they have greater strength of adhesion towards contamination. Thus, porcelain and glass insulators are easily wetted.Water on the surface tends to form filament.Materials with such characteristics are known as hydrophilic. Hydrophilic surfaces do not perform well under polluted conditions.**Figure 1.1**show the picture of one such insulator which got polluted due to environmental contamination.

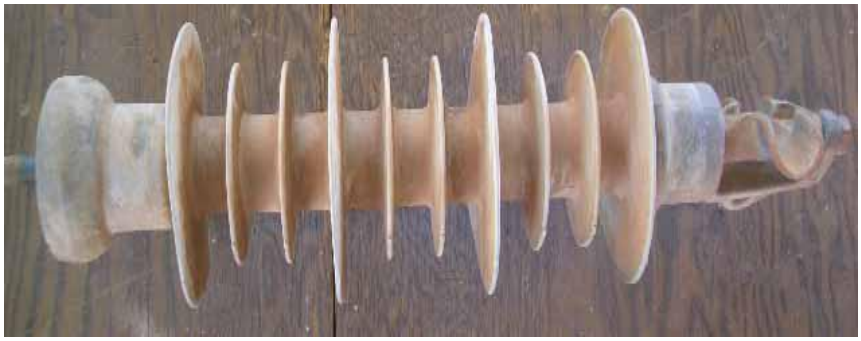

Figure 1.1 *Picture of a naturally contaminated insulator*

As already stated, a major problem of these insulators is the accumulation of air borne contamination on their surface. The major cause of pollutant accumulation on the insulator surface is the high surface energy due to their strong electrostatic bond among the various atoms in the material [**115**]. The chief sources of contamination are coastal areas, salt industries, cement industries, volcanic activity areas, industrial burning and chemical industries [57-58]. During a light rain or fog or mist, these contaminations get moistened and thus, form a conducting layer through which leakage current flows. Dry bands are formed as a consequence of the warming-up of the insulation surface layer. Partial arc appear throughout the dry bands which ultimately lead to surface flashover of the insulator. Thus, complete breakdown of the power system [**87**].

1.2 Types of Contamination

The level and the type of contamination of a region are associated with the sources of pollution as well as with weather factors of the place. **Table 1.1**shows the pollutants and the sources that produce them[**102,76**].These contaminants along with moisture can result in uncontrolled leakage current leading to flashover.

Table 1.1*Contaminants and their sources*

Contaminant	Sources of Contaminant
Salt	• Coastal areas • Salt Industries • High ways with deposit of snow where salt is used to melt the snow
Cement	• Cement Plant • Construction sites • Rock quarries
Earth	• Ploughed fields • Earth moving on construction projects

Fertilizers	• Fertilizer Plants • Frequent use of fertilizers in cultivated fields
Metallic	• Mining handling processes • Mineral handling processes
Coal	• Coal mining • Coal handling plants/thermal plants • Coal burning/bricks kilns areas
Volcanic ash	• Volcanic activity areas
Defecation	• Roosts of birds areas
Chemical	• Wide variety of chemical/process industries ,oil refineries
Smog	• Automobile emissions at highways crossing • Diesel engine emissions at railway crossing
Smoke	• Wild fire • Industrial • Agriculture burning

1.3 Flashover mechanism

The apparent paradox in pollution flashover is that catastrophic electrical discharges are produced, spanning up to meters of air,by electrical

potential.The underlying causeis the localised evaporation of a film of electrolyte gives rise to breaks in the conductive film-so called dry bands,across which electric stresses sufficient to ionise the air generatedand thus arc generated.Arcs in a gas,once established,can readily be extended without extinction by relatively slow separation of the electrodes between which they burn.

For much of its life an insulator will run with dry bands on its surface which is intermittently spanned by discharges. The combination of conductivity and electrical stress will further generate a self sustaining arc which causes the flashover of the insulators.

1.3.1 Stages of the flashover process

Contamination flashover requires the occurrence of following stages[**58**]:

(i) A sufficient degree of the contaminant composed of some ionic soluble salt, delivered to the insulator and deposited on its surface

(ii) A light rain or mist or fog that moistens the surface but does not createa washing effect.

(iii) The mixture of contamination and moisture produces a conducting film such that a current flows through the contamination layer.

(iv) Due to flow of current,some portion of insulator surface dries up and thus, dry bands are produced.

(v) The total line to ground voltage now appears across these small dry bands and flashover of the dry band occurs.

(vi) These arcs gradually grow outward and flashover of the insulator occurs when the arcs extend and meet.

Figure 1.2*Flashover of a high voltage insulator*.

1.3.2 Consequences

As discussed above, surface flashover damages the whole insulator and ultimately results into a complete breakdown of the power system network. This in turn results into a great economic loss to the consumers as well to the owner of the power company.A 250 ms outage can shut down a paper machine, resulting in hours of down time, possible equipment damage and loss of millions of dollars [**57**]. It is worth mentioning that the failure at any single point ofthe transmission network can bring down the entire system.Recent reports on grid disturbance in India indicatethe loss of 5000

million rupees and 97% of interconnectedgeneration on January 2, 2001. Similar disturbances of lessermagnitudes were also observed during the period of December2002 and 2005, February and December 2006, January andFebruary 2007, and March 2008. One of the major causesidentified was the contamination-induced flashovers.These events have amply portrayed that the performance ofoverhead transmission insulators and that used inoutdoor substations is a critical factor which governs thereliability of power delivery systems.

1.4Mitigation

It was understood that in order to prevent flashover,leakage current must be minimized. The practices used by utilities can be classified into the following groups[**57**].

(i) Remove accumulation of contamination on insulators by periodic cleaning

(ii) Minimize accumulation of contamination on the insulator surface with the use of aerodynamic profiles

(iii) Increase the leakage distance by using additional bells or extra long leakage distance units on string insulation.

(iv) Keep large area of the insulator dry for a longer time during natural wetting either by the use of a resistive glaze or by use of fog bowl design which has a difficult to wet underskirt area.

(v) Prevent water filming on the insulator surface by coating insulators withwater repellent materials(Hydrophobic).

The **first method** which is common and quite effective,is to maintain a regular insulator washing or cleaning schedule.This method is labor intensive and therefore, expensive and is restricted to few areas where contamination problem is very severe.

The **second method** which employs aerodynamic insulator profiles whose surfaces are more successfully cleaned by wind and rain can help in reducing contamination flashovers.But this method eliminates the undersheds in the insulator which help in increasing the creepage distance without adding to the overall string height.Therefore,this practise is restricted to special areas such as deserts.

The **third method** of increasing the leakage distane is costly to adopt universally and in addition, it is restricted by tower dimensions and clearances.This method requires periodic cleaning but at reduced frequency.

The **fourth method**of using a resistive glaze in an attempt to maintain a dry insulator surface has been used with some success.The glaze allows a small current to flow which results in a constant resistive heating.This tends to maintain large area of the insulator surface dry,thereby minimizing leakage current.The main concern with resistaive glaze is maintaining the transistion

between the conductive glaze and metal end caps.Also the electrical performance of glazed insulator decreases within short span of time.

The last method of minimizing contamination flashover is to use a hydrophobic coating to prevent water filming on the insulator surface,This method is quite popular and present reserch work focuses on this method

1.5Concept ofHydrophobicity

The concept of hydrophobic surfaces is originally drawn from the inspiration oflotus leaves in nature. The very high water repellency and the self-cleaning properties exhibited by the lotus leaf have been referred to as “lotus effect”, which has been attributed to a combined effect of the hydrophobicity induced by the epicuticular wax and the surface roughness resulted from the hierarchical structures on the leaf (**Figure 1.3**).

Figure 1.3*Lotus Leaf effect*

1.6Wetting on Surfaces

1.6.1 Wetting on flat surfaces

When a liquid droplet is deposited on a chemically homogenous and physically flat (or smooth)solid surface (**Figure1.2**), the surface wettability is mainly determined by the surface chemicalcomposition[**180**]. The liquid contact angle on the flat surface (or the intrinsic water contactangleθ_{flat}), can be correlated to three interfacial free energies, *i.e.* free energies at the solid-air(γ_{SV}) solid-liquid (γ_{SL}) and liquid-air (γ_{LV}) interfaces, by the Young's equation[**201**]:

$$cos\theta_{flat} = \frac{\gamma_{SV} - \gamma_{SL}}{\gamma_{LV}} \qquad (1)$$

where γsl can be estimated using[6]

$$\gamma_{SL} = \gamma_{SV} + \gamma_{LV} - \sqrt{\gamma_{SV}\gamma_{LV}} \qquad (2)$$

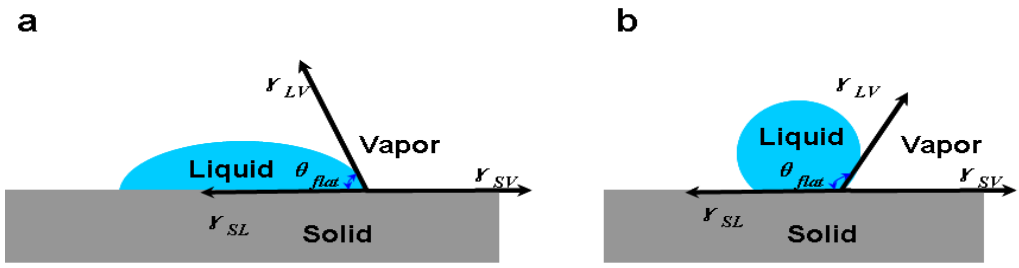

Figure 1.4. *Contact angle of a liquid on an ideally flat surface (Young's model). For water, if* θ_{flat}*<90°, it is an intrinsically hydrophilic surface (a); if* θ_{flat}*>90°, it is an intrinsically hydrophobic surface (b).*

According to Eqns. (1) and (2), the surface hydrophobicity increases with decreasing the surface free energy of the solid-air interface (SVγ*)*. When $\theta_{flat}$is smaller than 90°, the solid surface is considered intrinsically hydrophilic; when $\theta_{flat}$is greater than 90°, the solid surface is considered intrinsically hydrophobic.

Further increase of the hydrophobicity requires manipulation of the surfacetopography.

1.6.2 Wetting on rough surfaces

The effect of surface roughness on wettability was first discussed by Wenzel in 1936 [**188**] and then by Cassie and Baxter in 1944 [**16**]. Wenzel suggested that the effective surface area increases as the surface becomes rough, and hence water will tend to spread more on a rough hydrophilic substrate to develop more solid-liquid contact, while spread less on a rough hydrophobic

substrate to decrease the contact area to solid, both of which are thermodynamically more favourable. A key assumption of this conclusion is that water is in complete contact withthe solid surface, which is called Wenzel state (**Figure1.4a**). The relationship between the apparent contact angle on a rough surface (θ_{rough}) and its intrinsic contact angle (θ_{flat}) has been described by the Wenzel equation:

$$cos\theta_{roug\,h} = rcos\theta_{flat} \quad (3)$$

Where*r* is the roughness factor, defined as the ratio of the actual surface area to its horizontal projection. Since r is always greater than 1 for a rough surface, this equation predicts that if $\theta_{flat} \geq$, $\theta_{rough} \geq \theta_{flat}$, and if$\theta_{flat} \leq 90$,$\theta_{rough} < \theta_{flat}$. Therefore, in the Wenzel state, surfaceroughness will make intrinsically hydrophobic surfaces more hydrophobic and intrinsicallyhydrophilic surfaces more hydrophilic

1.7Literature review

Literature review is related to development of material technology to mitigate contamination problem in high voltage insulators

1.7.1Conventional coating

The fundamental reason that ceramic insulator wets is because they have high surface energy which means that moisture tend to spread forming a low resistance surface rather than bead up into small isolated droplets which results in a high surface resistance. If the tendency of spreading or wetting

can be overcome by aprotective coatingthen contaminated insulator surface would present a higher resistancethus, minimizing leakage current to levels obtained during dry conditions. An effective protective coating for water filming prevention needs to be of low surface energy which makes the surface water repellent.Oil is inherentlywater repellent due to its low interfacial surface tensionwith water.In fact some of the earliest ceramic insulators (1920) in contaminated areas were designed with an oil reservoir that constantly bled oil making the whole insulator water repellent. But this proved to be impractical due to complicated geometry,possibility of rain and wind depleting the oil reservoir and necessity for constant refilling of the oil [**63**].There are other compounds such as waxes,paints,lacquers and varnishes that have been tried as coatings on ceramic insulators.But the use of these is rather limited due to concerns on their long term performance.They are apparently easily weathered and subject to loss in electrically high stress area by corona.

1.7.2Grease Coating

Grease coating is also a method to mitigate contamination problem.Two types of greases namely petroleum jellies and silicone grease were being used in Europe and North America.Grease coating was an effective practical countmeasure for preventing contamination flashover on a large scale.However, the short intervals between regreasing in highly

contaminated areas and the associated high cost of regreasing, necessitated the development of longer term solutions to the insulator contamination problem[**102**].

1.7.3Room Temperature Vulcanized Coating (RTV)

The need for a longer lasting coating that has an increased resistance to UV and dry band arcing motivated the development of polymer hydrophobic coatings.Room temperature vulcanized (RTV) coating came out as a solution to this problem. The RTV coating can be applied to ceramic insulator by dipping, painting or spraying. The RTV coating is one component liquid polymer which when exposed to moisture in air,vulcanizes into a flexible rubber**[40]**.Commercially available RTV insulator coating consist of

(i) Polydimethylsiloxane(PDMS)polymer

(ii) Alumina trihydrate filler

(iii) Catalyst

(iv) Cross linking agent

A combination of silicone polymer and alumina trihydrate filler provides an arc resistant elastomer with long term stability to limit leakage current and therefore prevent flashover.The silicone polymer gives hydrophobic property, thereby limiting leakage current.

RTV coated insulators are subjected to ageing. The degree of ageing of the RTV coated insulators depends upon the pollution level of the environment

and on the service voltage. In addition, RTV coated insulators are exposed to environmental stresses and electrical stresses. Environmental stresses are ultra violet (UV) radiation, moisture, temperature extremes and air–borne pollutants including acids, bases and hydro carbon compounds [**93**]. Pollution is a part of the environmental stress and plays a vital role in the performance of the outdoor insulation system. The pollution deposit on the surface of the RTV coated insulator leads to surface erosion and the chemical composition of the surface changes and thus, the surface of the coating loses its electrical properties like surface resistance and hydrophobicity [**34,60**]. The main reason for the surface erosion is dry band arcing over the surface of the insulator, which occurs due to the conduction of electricity over the wet surface of the insulator. The wetting of the insulator surface takes place because of sea breeze, fog, early morning dew etc.

1.7.4Polymer insulator

Another way of remediating pollution performance of insulators is to use polymeric insulators. Polymeric insulators offer numerous advantages over porcelain[**33, 38, 62**].These are

1. Light Weight
2. Better pollution performance.

3. Polymer insulators are having safe flashover because of hollow core housing
4. Processing time is shorter in comparison to ceramic Insulators

However, polymer insulators are also suffering from some drawbacks [**44**].

1. Weathering degradation: Polymer materials have weaker bonds than porcelain which means they can be aged and changed by the multiple stresses encountered in service.
2. High raw material costs
3. Low mechanical strength: Polymer insulation is typically not rigid nor self supporting.

From the foregoing discussion, it is clear that each technique has some drawbacks.Hence, new effective method is required to mitigate the problem of contamination.A ray of hope arises with the advent of nanotechnology.

1.8Nanotechnology

Nanotechnology describe "creation,analysis and application of structure, molecular materials, inner interfaces and surfaces with at least one critical dimension or with manufacturing tolerances below 100 nanometers". The decisive factors is that new functionalities and properties resulting from the nanoscalability of system components are used for the improvement of existing products or the development of new products and application

options. Such new effects and possibilities are predominantly based on the ratio of surface to volume atoms and on the quantum mechanical behaviour of the elements of the material[**17,22]**.

In contrast to coarser-structured materials, nanomaterials dispose of drastically modified properties concerning physical, chemical and biological features. Physical material properties of a solid such as electric conductivity, magnetism, fluorescence,hardness or strength change fundamentally in accordance to the number and arrangement of the interacting atoms, ions and molecules [**156**].

Christofsumereder et al.[**200**]have reported that the nanotechnology can be successfully applied to electrical engineering applications.These include

1. Improvement in the conductivity of metals used as conductors.
2. Improvement in the properties of insulators
3. Miniaturizing of design and thus, reduction of used material.

In this respect, the concept of Nanodielectric was first of all given by Lewis.According to this,nanofillers like SiO_2,Al_2O_3etc. can be used for polymer insulators to improve its mechanical, electrical and thermal properties. Many research group has reported promising results in this respect [**106**].However a less work has been done on the ceramic

insulators.Yuzhen et.al [**203**] has reported the synthesis of titanium oxide (TiO_2) coating over ceramic insulator using sol-gel method.

1.9Material selection for coating(Target material)

The protection of insulation byhydrophobic coating is one of the most important and versatile means of improving ceramic insulator performance. We have the following choice in this respect

(i) Metal

(ii) Semiconductor

(iii) Dielectric

The metal choice is rejected as it will aid in the process of flashover.The second choice of semiconductor is also rejected as due to thermal effect semiconductor will also become conductor and thus aid in flashover.The last choice of dielectric is the most suitable for coating material

1.10Dielectric materials

The dielectric material chosen should possess following properties.

(1)The Dielectric constant of the material should be high

(2)The Dielectric material should be thermodynamically stable in contact with ceramic materials.

(3)The band gap should be large

(4)The refractive index should be fairly good

Presently, many researchers are searching for inorganic dielectric materialsto replaceRTV. Since a higher dielectric constant means we can grow thickerfilms to reduce leakage current, why not use dielectrics with the highest dielectricconstants? Many metal oxides and ferroelectric materials have been investigated ascandidate materials, but most of them are not stable in contact with ceramic. Furthermore, the dielectric constant of materials generally tends to increase as the band gap decreases,making it difficult to select a material with a large band gap and dielectric constant **[26]**.

For example, $SrTiO_3$ thin films have a dielectric constant of approximately 300 at room temperature but a band offset of nearly zero. Therefore, this material cannot insulate against leakage current [**26**].

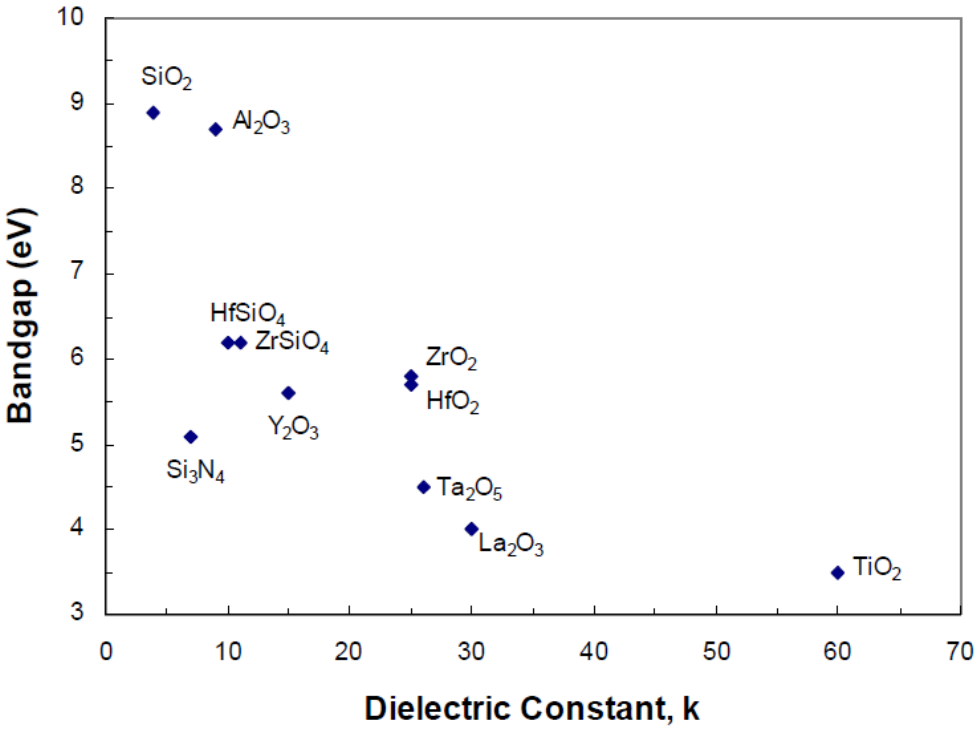

Figure 1.5*Graph between Dielectric constant and bandgap of inorganic oxides*

Zirconium oxide (ZrO_2) and hafnium oxide (HfO_2) promises to be useful as dielectrics material. ZrO_2 and HfO_2 have a dielectric constant of about 25 and a large band gap. Theband gap of HfO_2 and ZrO_2 is about 6 eV. Both ZrO_2 and HfO_2 are theoretically more thermodynamically stable with ceramic material.

Both materials have been shownto have good properties. In fact, successful transistors with ZrO_2 and HfO_2 have been fabricated with the present polysilicon gate material **[116,164**].Inaddition to this,hafnium oxy nitride (HfO_xN_y) and zirconium oxy nitride has also been successfully applied as gate dielectrics for electronic applications.Also, TiO_2 has been successfully applied for ceramic insulator.Hence,TiO_2 can also be used as a composite material with HfO_2.Thus, the potential candidate for dielectric coating will be

1. **Hafnium oxide (HfO_2)**
2. **Hafnium oxy nitride (HfO_xN_y)**
3. **Composite of HfO_2 and TiO_2 (HfTiO)**

1.11Synthesis Technique

The above mentioned material have been successfully synthesised as gate dielectric for electronic applications. These have been synthesized by various physical vapour deposition methods like sputtering, thermal evaporation,ebeam evaporation and pulse laser deposition[**3,5**]. **Table**

1.2shows a comparison between different physical vapour deposition methods.From table it is clear that sputtering is the best method among physical vapour deposition methods.Hence, we will develop dielectric hydrophobic coating using DC/RF magnetron sputtering [**101,176**] method.

Table 1.2 *Comparative evaluation of thin film processes*

Process	Material	Uniformity	Impurity	Grain Size	Film Density	Deposition Rate	Substrate temperature	Directional	Cost
Thermal Evaporation	Metal or low melting pint material	Poor	High	10-100nm	Poor	1-20 Å/s	50-100°C	Yes	Very low
E-beam Evaporation	Both metals and dielectrics	Poor	Low	10-100nm	Poor	10-100Å/s	50-100°C	Yes	High
Sputtering	Metals, Semiconductors, Insulators and dielectrics	Very Good	Low	1-100nm	Good	Metal: 100Å/s Dielectric: 10Å/s	RT-850°C	Some Degree	High
PECVD	Mainly Dielectric	Good	Very low	10-100nm	Good	10-100Å/s	300-400°C	Some degree	Very high
LPCVD	Mainly Dielectric	Very Good	Very Low	1-10nm	Good	10-100Å/s	600-1200°C	isotropic	Very high

1.12 Scope and objectives

The insulators are the main component of a HV line as well of equipments like transformer etc.However they are suffering from problem of contamination due to which insulator flashover occurs.This in turn interrupts the power supply.This causes a great economic losses to the concern unit. Hence to reduce these losses,attempt has been to develop hydrophobic coatings for the high voltage insulators.These coating will increase the overall reliability of the system.

A critical review of the literature reveals that the service and research experience about the hydrophobic coating application on the ceramic insulators is limited. Not much literature is available on the performance of RTV coated ceramic insulators under pollution conditions.

Very limited studies are conducted on development of new hydrophobic coatings for ceramic insulators. In this context the present work assumes significance. However with introduction of nanotechnology. It is possible to develop new effective hydrophobic coatings for the ceramic insulators.

Transition metal oxides, their oxynitrides and their composites are attractive materials for industrial and engineering applications due to their remarkable physical,dielectric and mechanical properties including high hardness, high melting point, chemical inertness and good thermodynamic stability**[46].** Deposition conditions like deposition temperature, sputtering power,

sputtering pressure, gas flow rate, deposition time etc. significantly affect the microstructure and other properties of the hydrophobic coatings. Although a literature is available on theproperties of these materials but the application area was different. Therefore, present research work is envisaged to develop the dielectric hydrophobic coatings by magnetron sputtering upon identifying the optimum process parameters. The micro-structural features of the coatings formed under different processing conditions need to be thoroughly characterized by FE-SEM, AFM and XRD.The optical properties will be investigated through UV spectrophotometer.The dielectric property will be investigated using impedance analyser and four probe electrical unit.The hydrophobicity will be measured through contact angle goniometer.

1.12.1 Objectives ofResearch Work:

The main objectives of my research work are asfollows:

- ✓ Development of optimum dielectric hydrophobic coatings of HfO_2,HfO_xN^y and HfTiOon substrates like glass and quartz by magnetron sputtering technique.
- ✓ To study the effect of deposition parameters on the micro-structural features of the coatings.

- ✓ To characterize the micro structural features of coatings by instruments like X-ray Diffractometer (XRD),Atomic force microscopy (AFM)and scanning electron microscope (SEM).
- ✓ To characterize the optical property of coating using UV spectrophotometer to determine thickness,refractive index and band gap of the deposited films.
- ✓ To measure the dielectric property of the deposited films using impedance analyser
- ✓ To measure electrical property of the coating using nanovoltmeter and source meter
- ✓ To measure hydrophobicity using water contact angle goniometer.

1.13 Proposed Research Plan

The proposed research work is envisaged to investigate the influence of process parameters on the micro structural,hydrophobic, dielectric and optical properties of HfO_2, HfON and HfTiO dielectric coatings on glass and quartz substrate.These coatings will be developed using DC/RF Magnetron sputtering. The research work consist of following aspects

1.13.1 Synthesis

The preparation of these hydrophobic dielectric coatings will be carried out by physical vapor deposition (PVD) techniques such as DC and RF magnetron sputtering. Various parameters such as deposition temperature,

power, sputtering pressure, deposition time, gas flow rate, etc., will be optimized for fabricating the good quality coatings. The coatings will be deposited on various substrates such as glass and quartz to study its influence on the structural evolution of coatings.

1.13.2Characterization

The physical, electrical, optical etc.properties of the coating/film will be investigated using different equipment like X-ray Diffractometer,atomic force microscopy etc. The information which is revealed by these equipment is listed below

- X-ray Diffraction(XRD) for the phase identification, crystallite size and texture analysis.
- Surface morphology and roughness measurement using Atomic force microscopy(AFM)
- Elemental analysis of the coating using EDAX attached with FE-SEM
- Optical property using UV-Vis NIR spectrophotometer.Through optical data, we can calculate thickness,band gap,refractive index of the film
- Thickness measurement using surface profilometer.
- Hydrophobicity was measured using contact angle goniometer

- Electrical property of the deposited films will be investigated using Keithley source meter and nanovoltmeter
- Dielectric property of the films using impedance analyser

CHAPTER 2

PROCESSING AND CHARACTERIZATION TECHNIQUES

2.1 Processing of Thin Films

Thin films are now absorbed into the broad subject area of Surface Engineering. Surface engineering encompasses the modification of a surface by application of a thin film through plasma enhancement, ion bombardment, self-assembly, nanomachining, chemical treatment, or other processes. It is now being used in virtually every area of technology including automotive, aerospace, missile, power, electronic, biomedical, textile, petroleum, petrochemical, machine tools and construction industries. A wide range of advanced functional properties including physical, chemical, electrical, optical, electronic, magnetic, mechanical, hydrophilic/hydrophobic, wear-resistant and corrosion-resistant properties are imparted at the required substrate surfaces by these surface engineering techniques. Almost all types of materials, including metals, ceramics, polymers, and composites can be deposited onto similar or dissimilar materials. It is also possible to form coatings of advanced materials such as metallic glass, polymers, superlattices, photocatalysts, graded deposits, metamaterials, multicomponent deposits, etc.

Thin film coatings are used to modify the physical and chemical properties and morphology of a surface or substrate, which makes them a broad subset of surface engineering. A thin film can consist of one homogeneous composition, crystalline phase composition and microstructure, or have an inhomogeneous multilayer or composite structure. Substrate preparation is critical and the surface morphology and composition of a substrate can also be modified by diffusion, plasma treatment, self-assembly, chemical etching and reactive heat treatment. The resulting surface will influence the properties, structure, adhesion and surface texture of a thin film. For example, ion or gas nitriding hardens the surface of stainless steel and significantly improves the performance of tribological coatings deposited onto the surface (Martin P. M. 2010).

The property of a film of a specific material formed by any atomistic deposition process depends on four factors, namely:

- *Substrate surface condition before and after cleaning and surface modification* - e.g. surface morphology (roughness, inclusions, particulate contamination), surface chemistry (surface composition, contaminants), mechanical properties, surface flaws, outgassing, preferential nucleation sites and the stability of the surface.
- *Details of the deposition process and system geometry* - e.g. deposition process used, angle-of-incidence distribution of the depositing adatom flux, substrate temperature, deposition rate, gaseous

contamination, concurrent energetic particle bombardment (flux, particle mass, energy).

- *Details of film growth on the substrate surface* - e.g. condensation and nucleation of the arriving atoms (adatoms), interface formation, interfacial flaw generation, energy input to the growing film, surface mobility of the depositing adatoms, growth morphology of the film, gas entrapment, reaction with deposition ambient (including reactive deposition processes), changes in the film properties during deposition.
- *Post deposition processing and reactions* - e.g. chemical reaction of the film surface with the ambient, subsequent processing, thermal or mechanical cycling, corrosion, interfacial degradation; surface treatments such as burnishing of soft surfaces, shot peening, overcoating ("topcoat"), or chemical modification such as chromate conversion (Mattox D. M. 1998).

There are four general categories of thin film deposition that have emerged over the past few decades: atomistic growth, particulate deposition, bulk coating and surface modification. In atomistic processes, atoms form a film by condensing onto a substrate and migrating to nucleation and growth sites. Adatoms often do not occupy their lowest possible energy configurations and the resulting structure contains high concentrations of structural imperfections (dangling bonds, voids, lattice mismatch, etc.). The

depositing atoms can also react with the substrate material to form a complex interfacial region. The energy of the adatoms is a critical factor in determining the microstructure/morphology and depends on the deposition process and source of atoms. Sources of atoms can be thermal evaporation, sputter deposition, vaporized chemical species (CVD), plasma species (ion plating, cathodic arc), or ionic species in an electrolyte (electrodeposition). Low-energy atomistic deposition is characterized by depositing species incident on a surface where they condense, are relatively immobile, and grow into a continuous coating. Mobility of adatoms to their lowest energy state increases with increased energy. Nucleation and growth mechanisms of the condensing species also determine the crystallography and microstructure of the thin film coating. These particles can react with or implant into the substrate in high-energy processes. Particulate deposition processes involve molten or solid particles and the resulting microstructure of the deposit depends on the solidification or sintering of the particles. Bulk coating processes such as painting involve the application of large amounts of coating material onto the surface at one time. Surface modification involves ion, thermal, mechanical, or chemical treatments which alter the surface composition or properties. **Table 2.1** shows a number of overlay and surface modification processes that can be used for deposition of thin films.

Table 2.1 *Classification of Surface Engineering processes [180].*

Atomistic/Molecular deposition	**Particulate Deposition**	**Bulk coatings**	**Surface modification**
Electrolytic Environment	*Thermal Spray*	*Wetting*	*Chemical Conversion*
Electroplating	Flame Spray	*Processes*	Wet chemical solution
Electroless plating	Arc-wire spray	Dip coating	(dispersion & layered)
Displacement plating	Plasma spraying	Spin coating	Gaseous (thermal)
Electrophoretic deposition	D-gun	Painting	Plasma (thermal)
	High-vel-oxygen-		
Vacuum Environment	fuel (HVOF)	*Fusion Coatings*	*Electrolytic Environment*
Vacuum evaporation		Thick films	Anodizing
Ion beam sputter deposition	*Impact Plating*	Enameling	Ion substitution
Ion beam assisted deposition		Sol-gel coatings	
(IBAD)		Weld overlay	*Mechanical*
Laser vaporization			Shot peening
Hot-wire & low pressure		*Solid Coating*	Work hardening
CVD		Cladding	
Jet vapor deposition		Gilding	*Thermal Treatment*
Ionized cluster beam			Thermal stressing
deposition			
			Ion Implantation
Plasma Environment			Ion beam
Sputter deposition			Plasma immersion ion
Arc vaporization			implantation
Ion Plating			
Plasma enhanced (PE)CVD			*Roughening and*
Plasma polymerization			*Smoothing*
			Chemical

Chemical Vapor Environment	Mechanical
Chemical vapor deposition (CVD)	Chemical-mechanical polishing
Pack cementation	Sputter texturing
Chemical Solution	*Enrichment & Depletion*
Spray pyrolysis	Thermal
Chemical reduction	Chemical

The choice of a deposition technique for thin films usually depends on the specific characteristics of films required for a study or application of interest. The basic requirement of good quality thin films are i) good uniformity of the films throughout exposed area, ii) the films with good physical and chemical properties such as low stress, good adhesion to the substrates, high density, low films defects (pinhole density), controlled grain size and its distribution, boundary property & orientation and iii) equipment initial cost and running cost. The comparative of some most commonly used deposition techniques for thin films are given in **Table 2.2**.

Table 2.2 *Comparative evaluation of thin film deposition techniques.*

Process	**Material**	**Uniformity**	**Impurity**	**Grain Size**	**Film Density**	**Deposition Rate**	**Substrate temperature**	**Directional**	**Cost**
Thermal Evaporation	Metal or low melting pint material	Poor	High	10-100nm	Poor	1-20 Å/s	50-100^{o}C	Yes	Very low
E-beam Evaporation	Both metals and dielectrics	Poor	Low	10-100nm	Poor	10-100Å/s	50-100^{o}C	Yes	High
Sputtering	Metals, Semiconductors,	Very Good	Low	1-100nm	Good	Metal: 100Å/s	RT-850^{o}C	Some Degree	High

	Insulators and dielectrics					Dielectric: 10Å/s			
PECVD	Mainly Dielectric	Good	Very low	10-100nm	Good	10-100Å/s	300-400°C	Some degree	Very high
LPCVD	Mainly Dielectric	Very Good	Very Low	1-10nm	Good	10-100Å/s	600-1200°C	isotropic	Very high

2.2 Sputtering

In Physical vapor deposition (PVD) technique, the synthesis of thin films is usually carried out from the same material whose nanoparticles are to be synthesized; its purity is decided by purity of the starting materials, base vacuum and purity of the ambient gas atmosphere (Gohil *et al.* 2008). The sputtering process which is a PVD process involves the physical vaporization of atoms from a surface by momentum transfer from bombarding energetic atomic sized particles. The energetic particles are usually ions of a gaseous material accelerated in an electric field. This technique is part of physical vapor deposition techniques which includes thermal evaporation and pulsed laser deposition (PLD). The most common approach for growing thin films by sputter deposition is the use of a magnetron source in which positive ions present in the plasma of a magnetically enhanced glow discharge bombard the target. The target can be powered in different ways, ranging from direct current (DC) for conductive targets to radio frequency (RF) for non-conductive targets, to a variety of

different ways of applying current and/or voltage pulses to the target. For the different physical vapor deposition (PVD) techniques, magnetron sputtering is used extensively in the scientific community and competes with pulsed laser deposition as the most important deposition technique.

The schematic diagram of a simple DC sputtering system is shown in **figure 2.1** which consists of a vacuum chamber, target and a substrate holder. The target is a 2 inch dia disc of material to be deposited which is connected to the negative terminal of a DC power supply. Target and substrate serve as electrodes and face each other in a typical sputtering chamber. The first step in the sputtering process is the pumping of the vacuum chamber to a typical base pressure of 10^{-6} torr or more. An inert gas, typically argon with a pressure usually ranging from a few to 100mtorr, is introduced into the system as the medium to initiate and maintain a discharge. When an electric field of several kilovolts per centimeter is introduced or a DC voltage is applied to the electrodes, a glow discharge is initiated and maintained between the electrodes. A very little current flows at first due to the small number of charge carriers in the system after the initial application of the voltage. Once sufficient number of charge carriers builds up, the free electrons will strike the Ar neutrals to create Ar^+ ions and more free electrons. The newly created free electrons can now ionize additional Ar neutrals thus multiplying the number of Ar^+ ions. In this visible glow maintained between the electrodes, the Ar^+ ions in the plasma gets

accelerated towards direction of the cathode and strike the target. Free electrons will be accelerated by the electric field and gain sufficient energy to ionize argon atoms. So the positive ions (Ar^+) in the discharge strike the cathode (the source target) and this bombardment creates a cascade of collisions in the target material's surface. These multiple collisions results in the ejection of neutral target (or sputter) atoms through momentum transfer from the surface into the gas phase. These atoms are then directed towards the substrate to form a thin film.

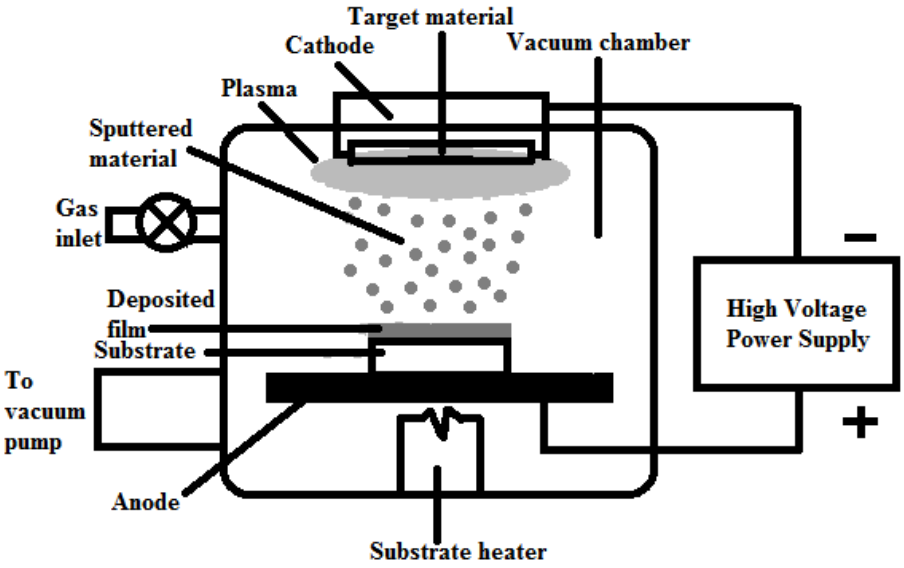

Figure 2.1 *A schematic diagram of a simple DC sputtering system.*

So when the right voltage is applied across the electrodes with a suitable gas pressure, the gas breakdowns into plasma. Plasma is a gaseous environment that contains enough ions and electrons to be a good electrical conductor. Plasmas are maintained by the continuous introduction of energy

which accelerates electrons to energies which are capable of ionizing atoms by electron-atom collisions. The inelastic collisions between electrons and atoms/molecules in the plasma produce a large number and variety of excited species, radicals, and ions without leading to a high thermal gas temperature, as is necessary in thermal (flame) ionization.

The sputtering yield is the ratio of the number of atoms ejected to the number of incident bombarding particles and depends on the chemical bonding of the target atoms and the energy transferred by collision. The sputtering yields of various materials bombarded by a variety of ion masses and energies have been determined experimentally (Laegried and Wehner. 1961, Wehner and Rosenberg 1961, Rosenberg and Wehner 1962) and have been calculated from first principles using Monte Carlo techniques (Yamamura *et al.* 1983). **Table 2.3** shows some masses of gaseous ions and target materials and the approximate sputtering yield by bombardment at the energies indicated (Vossen and cuomo 1978). It may be mentioned that the sputtering yields are generally less than one at bombarding energies of several hundred electron volts, indicating the large amount of energy input is necessary to eject one atom.

Table 2.3 *Sputtering Yields by 500eV Ions.*

	Be (9)	Al (27)	Si (28)	Cu (64)	Ag (106)	W (184)	Au (197)
He^+ (4 amu)	0.24	0.16	0.13	0.24	0.2	0.01	0.07
Ne^+ (20 amu)	0.42	0.73	0.48	1.8	1.7	0.28	1.08
Ar^+ (40 amu)	0.51	1.05	0.50	2.35	2.4-3.1	0.57	2.4
Kr^+ (84 amu)	0.48	0.96	0.50	2.35	3.1	0.9	3.06
Xe^+ (131 amu)	0.35	0.82	0.42	2.05	3.3	1.0	3.01

Magnetic fields (magnetron) can also be applied to the plasma region in order to improve the sputtering performance. The most common magnetron source is the planar magnetron where the sputter-erosion path is a closed circle or elongated circle ("racetrack") on a flat surface as shown in **figure 2.2 (**Waits R. K. 1978, Mattox *et al.* 1987). A closed circulating path can easily be generated on any surface of revolution such as a post or spool, inside of a hollow cylinder, a conical section, or a hemispherical section (Mattox D. M. 1998). A static magnetic field at surface of the sputtering target can be produced by a permanent magnet. The magnetic field generated is parallel to the cathode (the target) surface as shown in **figure 2.2**. This magnetic field forces the secondary electrons to move perpendicular to both the electric field (normal to the surface) and the magnetic field (parallel to the surface). The ions will experience dual field environment of Lorentz force which is the force on a point charge due to electromagnetic fields and is given by the following equation

$$F = q[E + (v \times B)] \tag{2.1}$$

where '*F*' is the force (in Newton), '*E*' is the electric field (in Volt/m), '*B*' is the magnetic field (in Tesla), '*q*' is the electric charge of the particle (in coulombs), '*v*' is the instantaneous velocity of the particle (in m/s) and 'x' is the vector cross product.

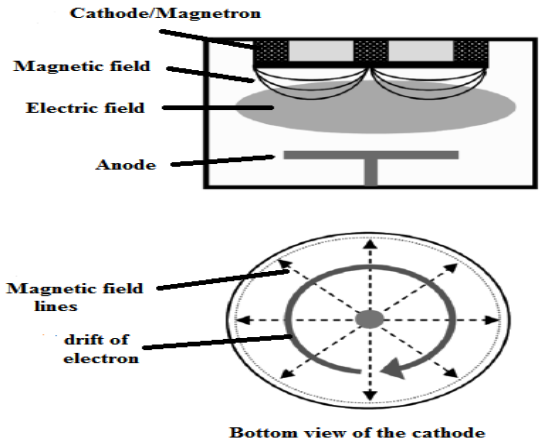

Figure 2.2 *The magnetic field configuration for a circular planar magnetron cathode.*

This force causes electrons to move parallel to the cathode surface, where they form a current loop of drifting secondary electrons (**figure 2.2**). As a result, these secondary electrons are trapped in a region close to the target. These electrons eventually lose their kinetic energy through collisions with gas atoms causing ionization, or with other electrons, which generates heat. This results in dense plasma near the target, which increases the deposition rate as it enhances the ionization of sputtering gas. However, this plasma does not affect the ejected atoms, as they have no charge and remain

unaffected by the magnetic field. The magnetron requires cooling because of the heat generated by the energetic collisions around the target.

So the sputtering target generally is actively cooled as the cold surface minimizes the amount of radiant heat in a sputtering system and is an advantage over thermal evaporation in vacuum where the radiant heat load can be appreciable. The low level of radiant heat is one factor that allows thermally-sensitive surfaces to be placed near the sputtering target. Cooling also prevents diffusion in the target which could lead to changes in the elemental composition in the surface region when alloy targets are used.

The simplest and least expensive way to operate the magnetron is using a DC power supply that was discussed earlier. Nowadays, a special power supply for sputter deposition is used, which include an arc suppression unit. Arcs often occur during reactive sputter deposition if oxygen/nitrogen as reactive gases is used that may build-up oxide/nitirde on the edges of the erosion groove where the sputter rate is low. Arcs can be characterized as a low voltage and high current discharge. When the electric circuit ‘detects’ a strong decrease in the discharge voltage and/or a strong increase in the discharge current, it switches the power off for a small period (typically a few microseconds) to draw electrons, decrease charging, and prevent the arc from fully developing. Arcing can seriously damage a target by local melting, but it also degrades quality of the deposited film owing to

the presence of particulates and/or pinholes while eventually destroying the power supply.

An effective way to prevent arcing during reactive magnetron sputtering (discussed in **section 2.1.1**) is pulsing the applied voltage. In contrast to RF magnetron sputtering, the frequency is much lower and is typically 50-250 kHz depending on the application (Sproul *et al.* 2005). The discharge voltage generally cycles between a high negative voltage and a low positive voltage. The negative voltage part of the cycle is used to perform the sputtering, as the ions bombard the cathode. The low positive voltage part of the cycle is used to attract electrons to prevent charge build-up. Because of the higher mobility of the electrons, this part of the cycle can be relatively short compared to the total cycle time.

At frequencies above 50 kHz, the ions do not have enough mobility to allow establishing a DC diode-like discharge and the applied potential is felt throughout the space between the electrodes. The electrons acquire sufficient energy to cause ionizing collisions in the space between the electrodes and thus the plasma generation takes place throughout the space between the electrodes. When an RF potential, with a large peak to peak voltage, is capacitively coupled to an electrode, an alternating positive/negative potential appears on the surface. During part of each half cycle, the potential is such that ions are accelerated to the surface with enough energy to cause sputtering while on alternate half-cycles, electrons reach the surface to

prevent any charge buildup. Typical RF frequencies employed range from 5 to 30 MHz however; 13.56 MHz has been reserved for plasma processing by the Federal Communications Commission and is widely used (Cao G. 2004). So when a high-frequency (typically 13.56 MHz) power source is applied between two electrodes, the light (low-mass) electrons respond instantaneously to the rapidly varying field, while the heavier ions are inertially confined.

The key element in RF sputtering is that the target self-biases to a negative potential and behaves like a DC target. Such a self-negative target bias is a consequence of the fact that electrons are considerably more mobile than ions and have little difficulty in following the periodic change in the electric field. It is also important to note that since RF power supplies are designed to look into circuits with a purely resistive 50Ω load, a tunable matching network is required to damp out the complex reactance (both capacitance and inductance) of the discharge. RF sputtering can be performed at low gas pressures (<1mtorr) and can be used to sputter electrically insulating and semiconductor materials. The primary disadvantage in the use of RF power supplies for magnetron sputtering in addition of being expensive is the inherently low deposition rate.

2.2.1 Reactive Magnetron Sputtering

Reactive sputtering is the sputtering of an elemental target in the presence of a gas that will react with the target material to form a compound. In one sense, all sputtering is reactive because there are always residual gases in the chamber that will react with the sputtered species. However in reality, reactive sputtering occurs when a gas is purposely added to the sputtering chamber to react with the sputtered material. Examples are when oxygen is injected into the chamber with the sputtering of aluminum to form aluminum oxide or when nitrogen is added with the sputtering of titanium to form titanium nitride. Reactive sputtering was developed in the 1950s to deposit the doped Ta-N films for hybrid circuits (Sproul *et al.* 2005).

Reactive sputter deposition (Westwood, W. D. 1989, 1990) relies on: (a) the reaction of the depositing species with a gaseous species, such as oxygen or nitrogen, (b) reaction with an adsorbed species, or (c) reaction with a co-depositing species such as carbon to form a compound. The reactive gas may be in the molecular state (e.g., N_2, O_2) or may be "activated" to form a more chemically reactive or more easily adsorbed species. Typically, the reactive gases have a low atomic masses (N=14, O=16) and are thus not effective in sputtering. It is therefore desirable to have a heavier inert gas such as argon to aid in sputtering. Mixing argon with the reactive gas also aids in activating the reactive gas by the excitation

processes. The nature of the sputtering gas influences the rate of sputtering from the target. The use of inert and reactive gas mixtures probably results in a metallic mode of sputtering, while the use of only reactive gas for example (N_2) is likely to result in a nitride mode of sputtering with a significantly lower sputtering rate (Chandra *et al.* 2005).

The basic issue faced during reactive puttering is that the reactive gas combines with target material to form a compound. Ideally this reaction takes place on the surface of the substrate, but in reality it occurs not only at the substrate but also on the fixturing and chamber walls and on the target. It is the reaction on the target surface that leads to the classic reactive sputtering problem known as "poisoning" of the sputtering target. The sputtering rate for the compound material that forms on the target is usually significantly less than the rate for the elemental target material thus reducing the deposition rate and sputtering efficiency. This problem is controlled by having a high sputtering rate (magnetron sputtering) and controlling the availability of the reactive gas by mass flow controller such that there will be enough reactive species to react with the film surface to deposit the desired compound but not so much that it will unduly poison the target surface.

In some reactive deposition configurations, the inert gas is injected around the sputtering target and the reactive gas is injected near the substrate surface. This inert "gas blanket" over the target surface is helpful in reducing target poisoning in some cases. In reactive deposition, the depositing

material must react rapidly or it will be buried by subsequent depositing material. Therefore, the reaction rate is an important consideration. The reaction rate is determined by the reactivity of the reactive species, their availability, and the temperature of the surface. The reactive species can be activated by a number of processes including:

- Dissociation of molecular species to more chemically reactive radicals
    - (e.g., $N_2 + e^- \rightarrow 2N^o$ and $NH_3 + e^- \rightarrow N^o + 3H^o$)
- Production of new molecular species that are more chemically reactive and/or more easily absorbed on surfaces
    - (e.g., $O_2 + e^- \rightarrow 2O^o$ then $O^o + O_2 \rightarrow O_3$)
- Production of ions-recombination at surfaces releases energy
- Adding internal energy to atoms and molecules by creating metastable excited states-deexcitation at surfaces releases energy
- Increasing the temperature of the gas
- Generating short wavelength photons (UV) that can stimulate chemical reactions
- Generating energetic electrons that stimulate chemical reactions.
- Ions accelerated from the plasma to the surface promote chemical reactions on the surface (bombardment enhanced chemical reactions).

The use of reactive sputtering has proliferated, particularly over the past decade. It is used to produce colored wear resistant decorative coatings

such as TiN (gold), TiC_xN_y (bronze, rose, violet or black as x and y are varied) and ZrN (brass). Coatings such as TiN and $(Ti,Al)C_xN_y$ are used as wear resistant coatings on tools, molds and other surfaces. It is also used to produce oxide films such as ZrO_2 and TiO_2 which are used to form anti-reflection and band-pass coatings on optical components. Indium-tin-oxide (ITO) is a transparent electrical conductor and silicon oxide is a material of interest as transparent, moisture permeation-barrier materials for packaging applications. Reactive sputtering is also used extensively by manufacturers of coated architectural glass, roll or web coatings, coated cutting tools, optical coatings, decorative and functional coatings for plumbing and hardware items, microelectronic devices (barrier layers, high k dielectrics, and resistive films), automotive windshields and mirrors, micro-electro-mechanical systems (MEMS) devices, surface acoustic wave devices and transparent conductive oxides.

2.2.2 Description of Sputter Deposition Technique

The actual magnetron sputtering system that was custom designed by Excel Instruments, India and installed in Nano Science laboratory is shown in **figure 2.5**. The system has two different arrangements as shown in **figure 2.5,** one in which three sputter gun slots are located in vertical position 120° apart. The substrate heater is having rotational arrangement so it can be used to sputter single target material or for preparing bilayers/multilayers from

maximum three target materials at same time. The elemental targets of Mg, Pd, Cr, Co, Nb and Ni were used for the preparation of Mg, Pd/Mg, Pd/Mg/Cr and Pd/Nb/Co thin films/multilayers respectively. In the other configuration, three sputter guns slots are inclined and confocally arranged at the centre of the substrate heater. This is used for co-sputtering of two or maximum three different/same target materials at the same time. This arrangement for preparing their respective co-sputtered Pd/MgNi films has been used.

The corning glass substrates are fixed on a heater with the help of clips and/or silver paste. The temperature of the substrate is controlled via the temperature controller of heater. After mounting the substrates, the chamber is evacuated using a turbo molecular pump (Pfeiffer, Germany) backed by rotary pump. A base pressure of 4 x 10^{-6}torr or more could be achieved by pumping the chamber. After evacuation, one of the inert gas such as argon/helium (99.999% purity) along with reactive gases such as nitrogen and oxygen (99.999%) required for preparation of metal oxynitride films is supplied into the chamber via gas inlet valve. The CESAR RF power supply (600W at 13.56 MHz) was used for sputtering with an impedance matching network procured from Advanced Energy, USA. The major reason behind using RF sputtering for conductive element targets (Cr, Ti, Zr) is the likelihood for the formation of insulating metal oxide/nitride layer on the targets during deposition due to target poisoning. The RF magnetron

sputtering will maintain the sputtering rate as the availability of the reactive gases is carefully monitored by mass flow controllers (MKS Instruments USA). Simultaneously, the gate valve is brought into almost closed state (throttling) so as to match the gas influx and pumping-out rate. With proper throttling, the inert gas pressure and flow rate inside the chamber can be made very stable. The sputtering pressure measurement inside the chamber was done by Baratron capacitance manometers (MKS Instruments USA). The manometers have standard Inconel all-welded sensors to maximize resistance to corrosive process gases and ensure safe operating environments and precise measurements.

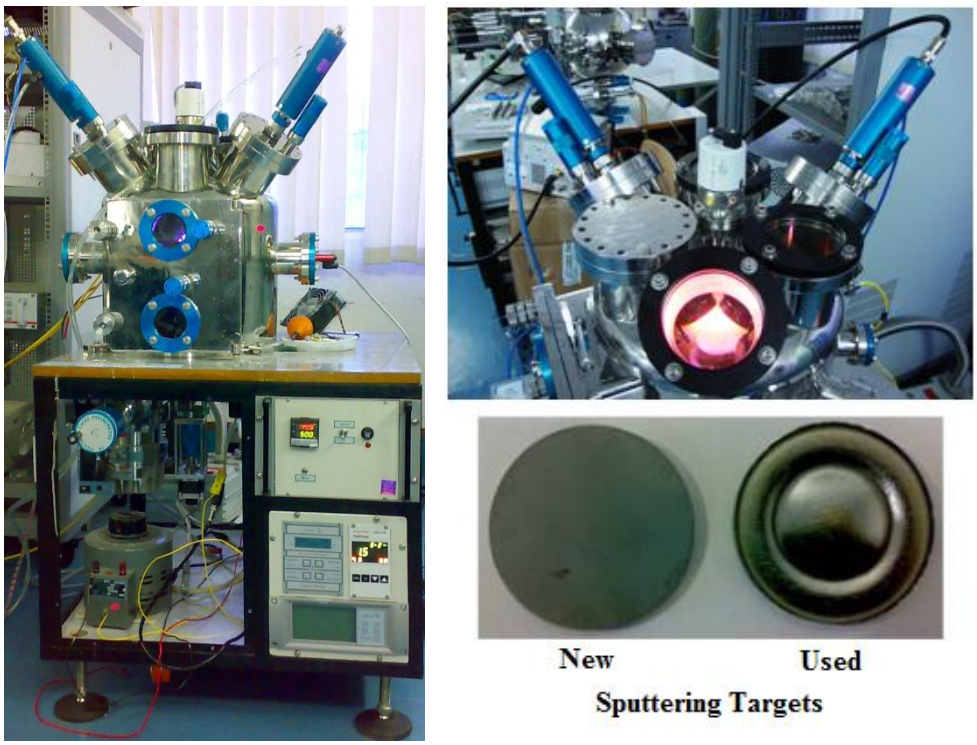

Figure 2.3 *Custom designed magnetron sputtering chamber.*

2.3 Characterization Techniques

After deposition of thin films using reactive magnetron sputtering technique by altering different process conditions, the structural, wettability and optical properties were investigated by XRD, EDS, AFM, surface profiler, contact angle measuring system, UV-Vis-NIR spectrophotometer, etc. The brief descriptions of all the characterization techniques used for deposited metal oxynitride thin films are discussed in this section.

2.3.1 X-ray Diffraction

X-ray diffraction (XRD) is one of the most powerful non-destructive technique for analyzing a wide range of materials from research and development to production and engineering environments. Because of the advancements in instrument engineering, technology and computational aspects, XRD methods are being applied for a wide range of materials, enabling answers to many different types of diffraction challenges. Applications include phase analysis, determination of crystalline structure and orientation, measurement of thickness and interfacial roughness by X-Ray Reflectivity (XRR) measurements, determination of texture, residual stress and strain in films, studies of nanomaterial development and measurements of their reactivity and polymorph screening (Martin P. M. 2010). XRD is the most widely used technique for general crystalline

material characterization. Owing to the huge data bank available covering practically every phase of every known material (powder diffraction patterns), it is routinely possible to identify phases in polycrystalline bulk material and to determine their relative amounts from diffraction peak intensities. Phase identification for polycrystalline thin films, using standard equipment and diffraction geometries, is also possible down to thicknesses of 100Å. For completely random polycrystalline thin films, relative amounts are also easily determined. The phenomenon of the X-ray diffraction by crystals results from a scattering process in which X-rays are scattered by the electrons of the atoms without change in wavelength. As the wavelength of X-rays is close to atomic size (~1.5Å), they get diffracted by atoms and ions. If, as in the case of crystals, the atoms or ions are arranged in a particular fashion, then the diffracted X-rays interfere constructively or destructively with each other depending on the path difference.

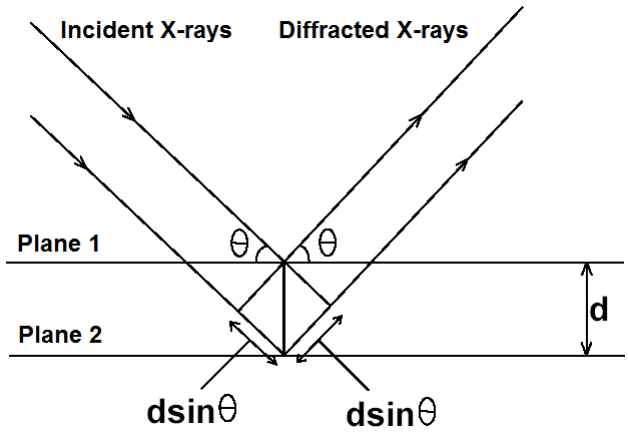

Figure 2.4 *Crystal planes and Bragg's Law.*

The interaction of X-ray radiation with crystalline sample is governed by Bragg's law as shown in **figure 2.4** who formulated the condition for constructive interference as,

$$2d\sin\theta = n\lambda \tag{2.2}$$

where, '*d*' is the inter-planer spacing for a given set of *hkl* plane, 'θ' is the Bragg's angle between the atomic plane and the X-rays, '*n*' is an integer (1,2,3,….,), and 'λ' is the wavelength of the X-rays. If the total path difference is equal to $n\lambda$ (as *n* being an integer and λ being the wavelength), the constructive interference will occur and a group of diffraction peaks can be observed which gives rise to X-ray patterns.

The three-dimensional symmetry of the unit cell was not taken account into consideration in the derivation of Bragg's law. Due to particular positions of the atoms in the unit cell, Bragg's law is necessary but not sufficient condition for diffraction. The total diffraction intensity from a unit cell can be determined by summing up the waves from each atom. If the scattering amplitude from the i_{th} atom, with fractional dimensionless coordinates u_i, v_i, w_i is f_i, the relative intensity scattered by the unit cell for a given reflection *hkl* is proportional to

$$F_{hkl} = \sum_{i=1}^{N} f_i e^{2\pi i(hu_i + kv_i + lw_i)} \tag{2.3}$$

The term F_{hkl} is called structure factor and describes the effect of crystal structure on the intensity of the diffracted beam (Cullity B. D. 1978). Using equation 2.3, structure factors of some simple Bravais lattice types are shown in **table 2.4.**

Table 2.4 *Structure factors and reflection conditions.*

Bravais	**Structure factor**	**Reflections**	**Reflections**
Simple	$F = f$	All	None
Body-centered	$F = f(1+e^{\pi i(h+k+l)})$	(h+k+l) even	(h+k+l) odd
Face-centered	$F = f(1+e^{\pi i(h+k)}+e^{\pi i(h+l)}+e^{\pi i(l+k)})$	h, k, l unmixed	h, k, l mixed

The schematic diagram of X-ray diffractometer and its experimental set up (Bruker D8 Advance) are shown in **figure 2.5a** and **figure 2.5b, respectively.** The Cu-Kα (λ =1.54Å) radiation at applied voltage of 40kV and filament current of 40mA in Bragg-Brentano (θ-2θ) scan mode was employed. Whenever the Bragg condition ($2d\sin\theta = n\lambda$) is satisfied, the incident X-ray beam is diffracted at the specimen and reaches the detector. The detector converts the X-ray quanta into electron pulses, which are recorded by recorder. Bruker D8 Advance diffractometer uses NaI scintillation counter as a detector which can detect the diffracted radiations in the wavelength ranging from 0.5 to 3Å. Monochromators are used to suppress the undesired portions of radiation. To restrict the irradiated

specimen area, aperture diaphragm is arranged between the tube and the specimen. The second aperture diaphragm shields the strong scattered radiation of the first aperture diaphragm. The resolution depends upon the detector diaphragm. The scattered radiation diaphragm is used to suppress undesired scattered radiation. The phase identification for all samples reported here was performed by matching the peak positions and intensities in the experimental diffraction patterns to those in the JCPDS (Joint Committee on Powder Diffraction Standards) database.

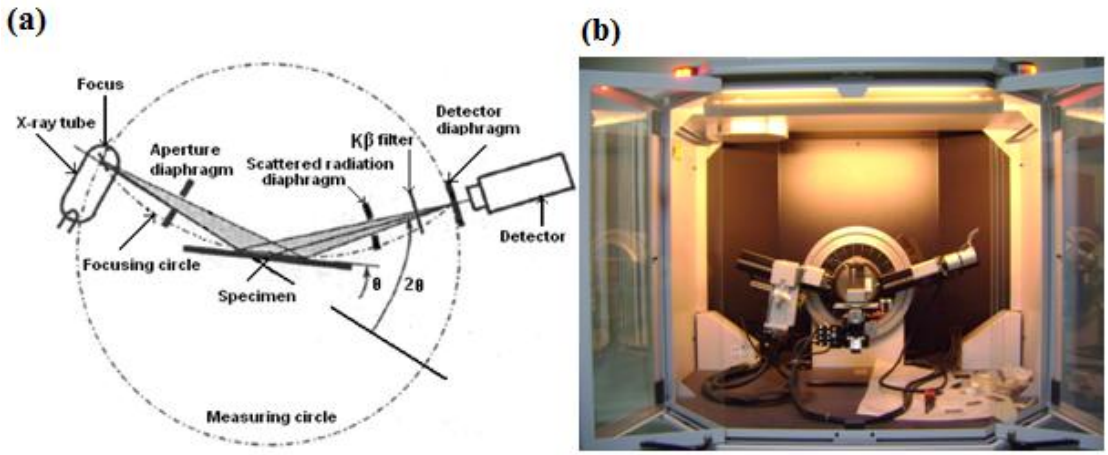

Figure 2.5 (a) *A schematic diagram of X-ray diffractometer and* ***(b)*** *the experimental set up of X-ray diffractometer (Bruker D8 Advance).*

The crystallographic information is obtained by evaluating‘*d*’ values and indexing of reflections. The characteristics diffraction pattern of a given substance can always be obtained whether the substance is present in pure state or as one constituent in a mixture of several substances. This fact is the basis of the diffraction method of chemical analysis. X-ray diffraction

pattern is characterized by a set of line positions (2θ) and a set of relative intensities (I). The angular position of lines depends on the wavelength of the incident ray and spacing (*d*) of the lattice planes.

One of the frequent applications of XRD analysis is to determine the average crystallite size and lattice strain in nanocrystalline thin film materials. The peak broadening in XRD patterns for nanomaterials is the result of the finite size effect. For a finite size nanocrystal, the number of X-ray radiation reflected from successive lattice planes that add up to produce constructive or destructive interference becomes finite and therefore they cannot reinforce or cancel out completely. So, for nanocrystalline materials, the average crystallite size which is an important parameter can be determined from the width of the Bragg reflection and is given by the Scherrer formula

$$D_{avg} = \frac{0.9\lambda}{B\cos\theta_b}$$

(2.4)

where D_{avg} is the average crystallite dimension perpendicular to the reflecting planes, λ is the X-ray wavelength, B is the finite size broadening i.e. full width at half maximum (FWHM) of the Bragg reflection in the radians on the 2θ scale and θ_b is the Bragg reflection angle. The average crystallite size for all deposited thin films was calculated by using the formula (2.4)

2.3.2 Energy-Dispersive X-Ray Spectroscopy (EDS)

Interaction of an electron beam with a sample target produces a variety of emissions, including X-rays. An Energy-Dispersive X-Ray Spectroscopy (EDS) detector is used to separate the characteristic X-rays of different elements into an energy spectrum. EDS system software is used to analyze the energy spectrum in order to determine the abundance of specific elements. EDS can be used to find the chemical composition of materials down to a spot size of a few microns, and to create elemental composition maps over a much broader raster area. These capabilities provide fundamental compositional information for a wide variety of materials. EDS systems are typically integrated into either a SEM or EPMA instrument. It include a sensitive X-ray detector, a liquid nitrogen dewar for cooling, and software to collect and analyze energy spectra. The detector is mounted in the sample chamber of the main instrument at the end of a long arm, which is itself cooled by liquid nitrogen.

With modern detectors and electronics, most Energy-Dispersive X-Ray Spectroscopy (EDS) systems can detect X rays from all the elements in the periodic table above beryllium (Z = 4) if present in sufficient quantity. Most applications of EDS are in electron column instruments like the scanning electron microscope (SEM), the electron probe microanalyzer

(EPMA), and transmission electron microscopes (TEM). X-ray spectrometers with X-ray tube generators as sources and Si(Li) detectors have been used for both X-Ray Fluorescence Spectroscopy (XRF) and X-ray diffraction (XRD). With a radioactive source, an EDS system is easily portable and can be used in the field more easily than most other spectroscopy techniques. With a minimum detection limit (MDL) of 100-200 ppm for most elements, an EDS system is capable of detecting less than a monolayer of metal film on a substrate using Kα lines at moderate accelerating voltages of 5-15keV.

The EDS detector normally consists of a small piece of semiconducting silicon or germanium which is held in such a position that as many as possible of the X-rays emitted from the specimen fall upon it. Since X-rays cannot be deflected, the detector must be in line of sight of the specimen. This means that in a scanning electron microscope (SEM), it normally occupies a similar position to the secondary electron detector. In order to collect as many X-rays as possible, the silicon should be as near to the specimen as is practicable. In SEM, it may be possible to place the detector 20mm or less from the specimen, but the problems are greater with a transmission electron microscope (TEM) because the specimen is within the objective lens.

If a voltage is applied across the semiconductor, a current will flow as each X-ray is absorbed in the detector and the magnitude of the current will

be exactly proportional to the energy of the X-ray. In practice, if pure silicon is used, the current generated is minute compared with the current which flows normally when a voltage is applied; in other words the resistivity is too low. This is overcome by three stratagems which combine to make the final detector seem rather more complicated than it really is.

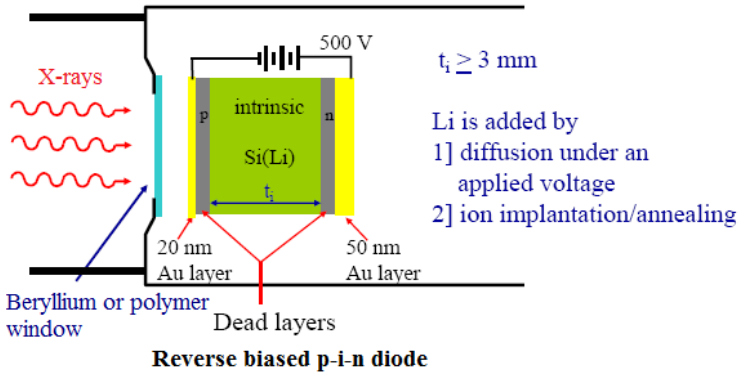

Figure 2.6 *A schematic diagram of energy dispersive Si(Li) detector.*

The resistivity of the silicon is increased by (i) making the whole detector a semiconductor p-i-n junction which is reverse biased, (ii) doping the silicon with a small concentration of lithium and (iii) cooling the whole detector to liquid nitrogen temperature (77K) (Goodhew *et al.* 2001). **Figure 2.6** shows the Si(Li) detector which is the most commonly used energy-dispersive detector. The lithium atoms are used to compensate the relatively low concentration of grown-in impurity atoms by neutralizing them. In the diffusion process, the central core of the silicon will become intrinsic, but the

end away from the lithium will remain p-type and the lithium end will be n-type, this results in a p-i-n diode.

A reverse bias electrical field in a range of 100-1000 volts is applied to thin layers of gold evaporated onto the front and back surface of the diode. The detector shown schematically in **figure 2.6** consists of Si(Li) semiconductor junction in which the ‘i' region occupies most of the 3mm thickness. Thin layers of gold are necessary on both surfaces of the detector so that the bias potential can be applied. The film of gold on the outer face of the detector must be as thin as possible so that very few X-rays are absorbed in it; a layer only 20nm thick provides adequate conductivity. When an X-ray enters the intrinsic region of the detector through the p-type end, each incoming X-ray excites a number of electrons into the conduction band of the silicon leaving an identical number of positively charged holes in the outer electron shells which in turn produces a number of electron-hole pairs in the detector. It required 3.8eV of energy for one such pair, so for example a 6.4KeV X-ray absorbed by the silicon atoms will produce about 1684 electron-hole pairs or a charge of about 2.7×10^{-13} Coulombs. The current which normally passes between the gold electrodes is very small indeed until an X-ray enters the detector, then the resultant current can be amplified and measured fairly easily.

Both charge carriers move freely through the lattice and are drawn to the detector contacts under the action of the applied bias field to produce a

signal at the gate of a specially designed field effect transistor (FET) mounted directly behind the detector crystal. The transistor forms the input stage of a low-noise charge-sensitive preamplifier located on the detector housing. The output from the preamplifier is fed to the main amplifier, where the signal is finally amplified to a level that can be processed by the analog-to-digital converter (ADC) of the multichannel analyzer (MCA). The schematic diagram of the EDX system is shown in **figure 2.7a** and the experimental set up of EDX attached to FE-SEM (Model: FEI Quanta 200F) procured from FEI Company Netherland is shown in **figure 2.7b**.

The height of the amplifier output pulse is proportional to the input preamplifier pulse, and hence is proportional to the X-ray energy. For the amplifier pulse to be recognized in the ADC, it must exceed the lower level set by a discriminator, which is used to prevent noise pulses from jamming the converter. Once the pulse is accepted, it is used to charge a capacitor that is discharged through a constant current source attached to an address clock typically operating at 50 MHz. The time to discharge the capacitor to 0V is proportional to the pulse amplitude and hence to the X-ray energy. The 50-MHz clock produces a binary number in one of the 1024 channels typically used by the MCA in accordance with the time of the discharge and increments the previously collected number in that channel by 1. By an energy calibration of the channels in the MCA, the collection of X-ray pulses may be displayed on a CRT as an energy histogram.

Detectors are maintained under vacuum at liquid nitrogen temperature to reduce electronic noise and to inhibit diffusion of the lithium when the bias voltage is applied. The gold-coated outer surface is usually further protected by a thin window of beryllium or a polymer. This window is necessary to prevent contaminants from the specimen chamber of the microscope from condensing on the very cold surface of the detector and forming a further barrier to the entry of X-rays. Windowless detectors or detectors with ultra-thin windows of formvar or some other polymer film are now available and these extend the analytical range down to boron. However such detectors need to be used in microscopes which have extremely good vacuum systems and need very careful protection from accidental air leaks such as those that occur during specimen changes.

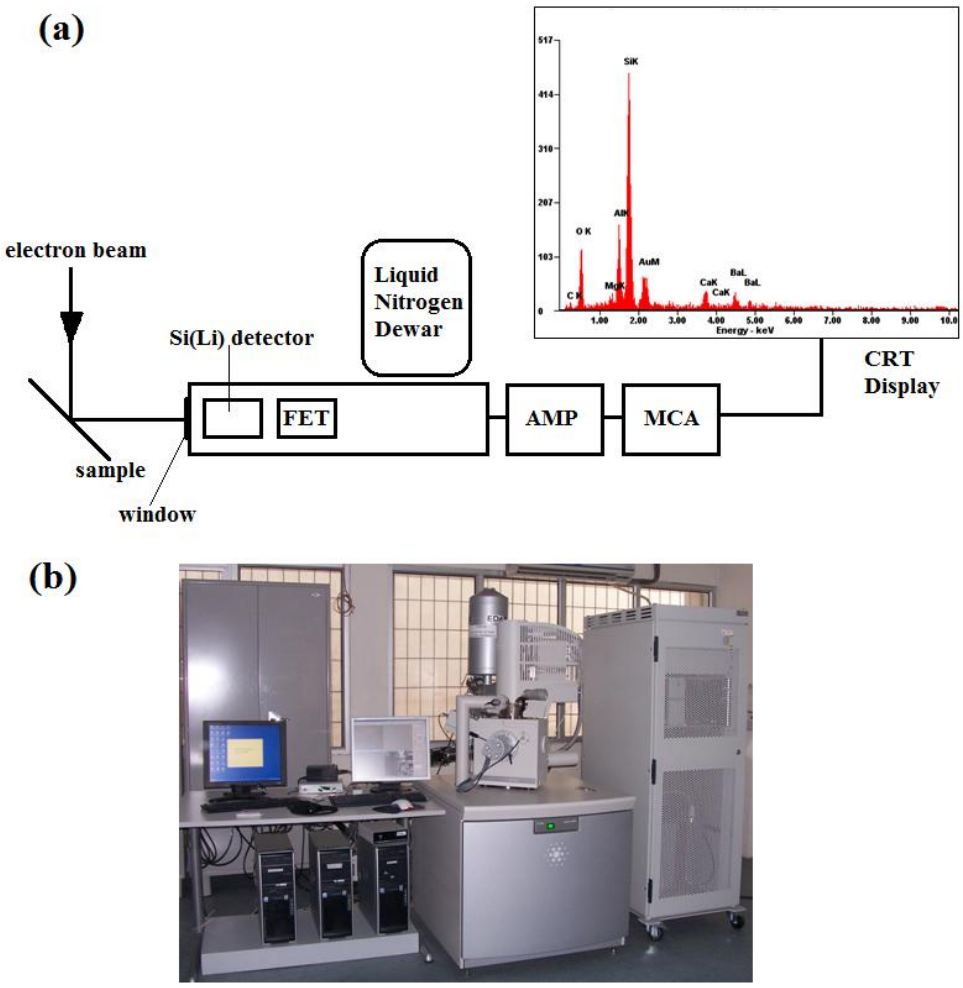

Figure 2.7 (a) *A schematic diagram for EDS system and*

(b) *the experimental setup of FEI Quanta 200F system.*

EDS has been used for quality control and test analysis in many industries including computers, thin films, semiconductors, metals, cement, paper and polymers. It has been used in medicine in the analysis of blood, tissues, bones, and organs; in pollution control, for asbestos identification; in field studies including ore prospecting, archeology, and oceanography; for

identification and forgery detection in the fine arts; and for forensic analysis in law enforcement.

2.3.3 Atomic Force Microscopy (AFM)

Atomic force Microscopy (AFM) provides a number of advantages over different microscopy techniques as observed from the comparisons of various microscopes given in **table 2.5** (Kaufmann E. N. 2003). AFMs probe the sample and make measurements in three dimensions, *x*, *y,* and *z* (normal to the sample surface), thus enabling the presentation of three-dimensional images of a sample surface. This provides a great advantage over any microscope available previously. With good samples (clean, with no excessively large surface features), resolution in the *x*-*y* plane ranges from 0.1 to 1.0 nm and in the *z* direction is 0.01 nm (atomic resolution). AFMs require neither a vacuum environment nor any special sample preparation, and they can be used in either an ambient or liquid environment. With these advantages, AFM has significantly impacted the fields of materials science, chemistry, biology, physics, and the specialized field of semiconductors.

Table 2.5 *Comparison of various microscopes.*

Technique	Probe/ Principle	Environment	Sample Requirements	Resolution (nm) XY	Z
Scanning Tunneling Microscopy (STM)	Electron tunneling	Air, vacuum, liquid	Flat, conductor	0.1-0.2	10^{-3}
Atomic Force Microscopy (AFM)	Forces: attractive, Repulsive, contact, noncontact	Air, vacuum, liquid	Flat, insulator, conductor	0.1-1.0	0.01
Transmission Electron Microscopy (TEM)	Electron transmission	High vacuum	Solid, 10nm thin	0.2	-
Scanning Electron Microscopy (SEM)	Secondary electrons	High vacuum	Solid, conductive	2	-
Scanning Auger Microscopy (SAM)	Auger emission	Ultrahigh vacuum	Conductive	10	-
Scanning Secondary Ion Mass Spectroscopy (SIMS)	Ion sputtering	Ultrahigh vacuum	Most samples	100	-

AFM monitors the force between a sharp tip and the sample and utilizes this force to produce images. There is a piezoelectric actuator to precisely control the sensor above the surface and to raster the tip across the sample, there is a control system to provide feedback to the piezoelectric

actuators and display the images, and there is an isolation system to dampen ambient vibrations. A schematic diagram of an atomic force microscope is shown in **figure 2.8a** and the laboratory set up of the AFM system used in the present studies is shown in **figure 2.8b** which is the NTEGRA model from NT-MDT , Russia. In this case, the probe is a microfabricated, cantilevered, force sensor that deflects as a result of the sample-induced forces placed on the sharp tip that is positioned on or above the sample surface. The cantilever deflects upward in the case of a net repulsive force or downward in the case of a net attractive force. In the case of an AFM, this deflection, usually associated with topography, is utilized to generate an image of the sample surface. The deflection can be measured using an optical lever, in which a laser diode is focused on the end of the cantilever, which is typically angled downward from horizontal at around 10°. A laser is focused onto the end of the cantilever, the reflective coating on the back side of the cantilever permits reflection of the laser light to a position-sensitive photodiode detector located some distance away from the cantilever. Any forces acting on the tip result in a bending (vertical forces) or twisting (lateral forces) of the cantilever and therefore result in a different reflection angle. The difference of the output of the photodiodes is used as output signal, which is proportional to the deflection of the cantilever. Depending on the mode of operation, the photodiode signal is used directly or as a feedback signal. A feedback loop continuously checks the feedback signal,

compares it to some user defined set point value and adjusts the height of the tip over the sample such that the difference is minimized. Stable operation is possible if the feedback signal is monotonous in the tip-surface distance. The tip is then kept at a height corresponding to a constant interaction over the sample surface. Either the cantilever or the sample is mounted to a piezoelectric element, which provides the necessary means to position the tip relative to the sample in 3D space.

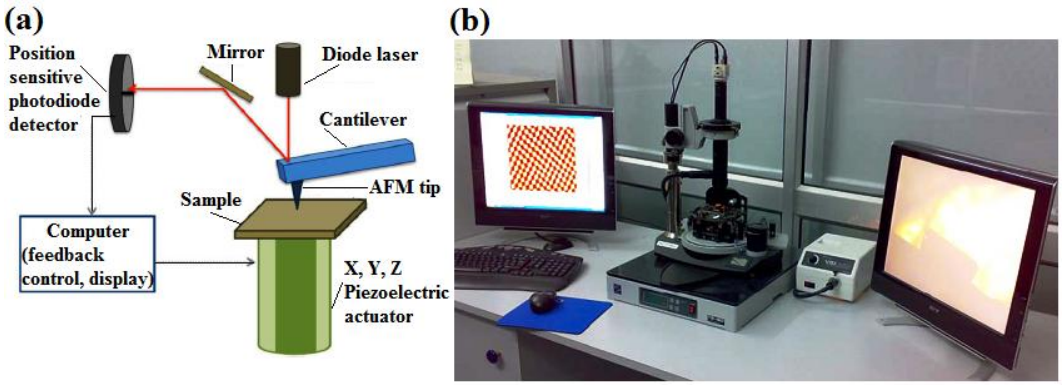

Figure 2.8 (a) *A schematic diagram of an atomic force microscope (AFM) and* ***(b)*** *the laboratory set up of AFM (NT-MDT: NTEGRA).*

Similarly to the scanning tunneling microscope, the AFM can be operated under a wide array of controlled operating environments such as ambient, condensed phase (aqueous) and vacuum conditions, at elevated temperatures and pressures, and at cryogenic temperatures. This permits this instrument to be utilized in a large number of scientific disciplines, including biology, materials synthesis and characterization, geochemistry, and

nanomechanics. Because of its unique ability to measure forces and image non-conducting materials, the AFM has become particularly important in the biological field for imaging of proteins, biological structures, and cells as well as for directly measuring interaction forces between complementary structures (e.g. DNA strands, antigen-antibody, actin-myosin). The ability to image surfaces under controlled environments in real time allows the researcher to observe the time-dependent changes in dynamic systems and obtain kinetic data for a wide variety of systems.

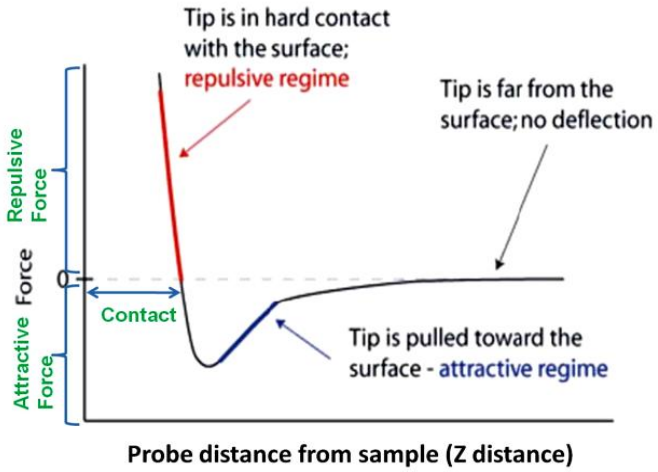

Figure 2.9 *Interaction force between tip and the sample surface as function of distance.*

The interaction force between the scanning tip and sample surface is the essential parameter to determine the AFM scanning mode. In the force-distance diagram illustrated in **figure 2.9** the contact and non-contact regime are clearly indicated as the function of the distance between tip and sample surface. By decreasing the gap between the scanning tip and sample surface,

the interaction forces can change from attractive to repulsive. As the atoms are gradually coming closer to each other, they first attract each other. This attraction increases until the atoms are so close together that they begin to repel each other. With further reducing the gap, the repulsive force can dramatically increase due to the Pauli exclusion principle and become the dominant interaction with progressive weakening of the attractive force. Further reduction in distance than this distance (zero force), the total Van der Waals force becomes positive (repulsive). This distance will not change, therefore any more attempt to force the sample and tip closer will result in deformation or damage to the sample or the tip. With varying interaction force, the cantilever deflects in different ways. It can be bent upward, downward or twisted. There are two other forces that arise during the scan:

(i) a capillary force that is caused by a build-up of water. In real conditions (in ambient air), practically always some humidity is present in air and a water layer is adsorbed on the sample and tip surfaces.

(ii) on the tip; the force is caused by the cantilever itself, which is like a force caused by a compressed spring.

The AFM can operate in a number of imaging modes including contact mode, non-contact mode and tapping mode (also called semi-contact or intermittent mode). In the contact regime, the cantilever is held less than a few nanometers from the sample surface, and the interatomic force between

the cantilever and the sample is repulsive. In the non-contact regime, the cantilever is held on the order of tens to hundreds of angstroms from the sample surface, and the interatomic force between the cantilever and sample is attractive (largely a result of the long-range Van der Waals interactions).

Contact mode is the most common method of operation of the AFM and is useful for obtaining 3D topographical information on nanostructures and surfaces. As the name suggests, the tip and sample remain in close contact as the scanning proceeds. In contact mode, a relatively soft silicon nitride cantilever is typically used to probe the surface. Most cantilevers have spring constants < 1 Nm, which is less than effective spring constant holding atoms together. The force on the tip is repulsive with a mean value of 10^{-9}N and around 0.5nm probe-surface separation distance. This force is set by pushing the cantilever against the sample surface with a piezoelectric positioning element. In contact mode AFM, the deflection of the cantilever is sensed and compared in a DC feedback amplifier to some desired value of deflection. If the measured deflection is different from the desired value the feedback amplifier applies a voltage to the piezo to raise or lower the sample relative to the cantilever to restore the desired value of deflection. The voltage that the feedback amplifier applies to the piezo is a measure of the height of features on the sample surface.

Advantages:

- High scan speeds

- Atomic resolution is possible
- Easier scanning of rough samples
- Lateral forces, can be used to provide information on the friction
(drag resistance)

Disadvantages:

- Lateral forces can distort the image
- Capillary forces from a fluid layer can cause large forces normal to the tip-sample interaction
- Combination of these forces reduces spatial resolution
- Tip may scratch the surface, change its intrinsic features and can cause damage to soft samples (however imaging in liquids often resolves this issue)

Non-contact mode is a method where the cantilever is oscillated above the surface of the sample at distance such that it is no longer in the repulsive regime but in the attractive regime of the inter-molecular force curve. In non-contact imaging, the tip is oscillated at its resonant frequency at around 0.1-10nm probe-surface separation distance above the surface. Changes in the long-range attractive Van der Waals forces exerted on the tip due to topography cause the resonant frequency of the cantilever to shift. The signal applied to the piezoelectric actuators needed to keep the resonant

frequency constant is then used to generate a topographic image. So attractive Van der Waals forces acting between the tip and the sample are detected, and topographic images are constructed by scanning the tip above the surface. Since the attractive forces from the sample are substantially weaker than the forces used by contact mode, therefore the tip is given a small oscillation so that AC detection methods can be used to detect the small forces between the tip and the sample by measuring the change in amplitude, phase, or frequency of the oscillating cantilever in response to force gradients from the sample. Non-contact imaging is mostly used in vacuum systems, where instabilities due to surface adsorbents (i.e. water, contamination) are minimal.

Advantages:

- Very low force is exerted on the sample (10^{-12}N) surface
- No damage is caused to soft samples
- Extended probe lifetime

Disadvantages:

- Lower lateral resolution limited by tip-sample separation
- Contaminant layer on surface can interfere with oscillation
- Slower scan speed
- Usually only applicable in extremely hydrophobic samples with a minimal fluid layer

- Need ultra high vacuum to have best imaging

Tapping mode is another mode of operation for AFM. Unlike the operation of contact mode, where the tip is in constant contact with the surface, in tapping mode, the tip makes intermittent contact having around 0.5-2nm probe-surface separation distance. In this mode, the cantilever is made to oscillate at its natural frequency by using a piezo-electric crystal. The oscillating tip is moved close to the sample surface till it begins to just tap it and is then immediately lifted off again, while the sample is continuously scanned below the tip. Because the contact time is a small fraction of its oscillation period, the lateral forces are reduced dramatically. The change in oscillation amplitude during the tapping period is used as a feedback to maintain constant height or force between the tip and the sample. In constant height mode, the tip is kept at a fixed height at or above the surface and the cantilever deflection, is used to generate an image. In constant current mode, a constant force mode fixes the deflection of the cantilever and the position of the cantilever above the surface, as controlled by the piezoelectric actuators, is used to generate a topographic image. The feedback voltage serves as a measure of the surface features. As the tip is not dragged over the sample, there is no damage caused to the sample and also the tip is prevented from sticking to the sample surface due to adhesion. This method usually gives higher resolution than the previous two methods. Tapping mode is usually preferred to image samples with structures that are

weakly bound to the surface or samples that are soft (polymers, thin films). There are two other types of image contrast mechanisms in tapping mode:

Amplitude imaging The feedback loop adjusts the *z*- axis movement so that the amplitude of the cantilever oscillation remains (nearly) constant. The voltages needed to keep the amplitude constant can be compiled into an (error signal) image, and this imaging can often provide high contrast between features on the surface.

Phase imaging The phase difference between the driven oscillations of the cantilever and the measured oscillations can be attributed to different material properties. For example, the relative amount of phase lag between the freely oscillating cantilever and the detected signal can provide qualitative information about the differences in chemical composition, adhesion, and friction properties.

Advantages:

- Higher lateral resolution (1nm to 5nm)
- Lower forces and less damage to soft samples in air
- Almost no lateral forces
- Also good for biological samples

Disadvantages:

- Slower scan speed than in contact mode
- More challenging to image in liquids

The choice of AFM mode depends on the surface characteristics of interest and on the hardness/stickiness of the sample. Contact mode is most useful for hard surfaces; a tip in contact with a surface, however, is subject to contamination from removable material on the surface. Excessive force in contact mode can also damage the surface or blunt the probe tip. Tapping mode is well-suited for imaging soft biological specimen and not for hard surface (DNA, carbon nanotubes, thin films). Non-contact mode is another useful mode for imaging soft surfaces, but its sensitivity to external vibrations and the inherent water layer on samples in ambient conditions often causes problems in the engagement and retraction of the tip. In the studies described in this thesis, intermittent contact mode (also named tapping mode) AFM is used to explore the surface morphology of deposited thin films.

2.3.4 Thickness Measurement using Stylus Profilometer

One of the most important parameters of a coating is its thickness, due to which a coating geometry reduces to two dimensions as compared to the bulk samples which are three dimensional. Most technological applications of coating require films of definite thickness as it affects properties of the coatings.

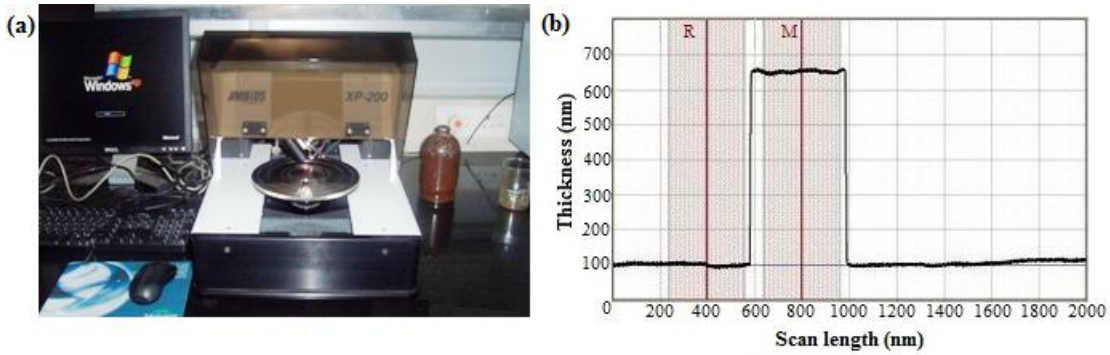

Figure 2.10 (a) *Stylus profilometer (XP-200) used for present work and* ***(b)*** *step contour trace of deposited titanium oxynitride thin films.*

The stylus profilometer was used to measure the film thickness which is shown in **figure 2.10a**. This method consists of measuring the mechanical movement of a stylus as it is made to trace the topography of a film-substrate step. A metallic needle stylus with tip radius of ~10 micron fastened to a lever arm serves as the electromagnetic pick up. The arm is delicately balanced so that the load on the stylus is very small. The stylus force is adjustable from 1 to 10 mg. A platinum stylus is moved vertically in contact with a film for specified distance and specified contact force. The vertical movement of the stylus is detected with a transducer, amplified 105 to 106 times, and then fed into a recorder. Then the film thickness is directly readout as the height of the resulting step contour trace by placing the reference cursor (R) on the substrate and the measurement cursor (M) on the vertical movement as shown in **figure 2.10b** which is the thickness profile of deposited titanium oxynitride thin film at 4.0% oxygen partial pressure in

argon atmosphere. The vertical axis (y-axis) shows the thickness of the film and horizontal axis (x-axis) shows the horizontal displacement of the tip. Stylus instruments required a “step” in the film to measure thickness which is more often the preferred method when measuring thickness of the films. The required step in the films was obtained by masking some part of the substrates during deposition by clip. We have measured thickness of the deposited films using a thickness profilometer (Model: XP-200, Ambios Technology Inc. USA). This XP-200 stylus profiler is a computerized, high sensitivity surface profiler, used to measure step height in a variety of applications. It features the ability to measure precision step heights from 10 Å to 100 microns.

2.3.5 Contact Angle Measuring System

Wetting is the spreading and contact of a liquid over a solid surface (substrate). If sufficiently intimate contact is achieved between the two phases, a physical attraction due to inter-molecular forces develops causing the liquid to conform to the surface on a macro and micro scale, displacing air and thus minimizing interfacial flaws (Duncan *et al.* 2005). Contact angles are closely related to wettability, the lower the contact angle the greater the wettability and is used as a relative measure of the surface energy. There are two different ways of measuring contact angle from the drop

- A contact angle can be measured on *static drop*. The drop produced has

a constant volume during the measurement.

- A contact angle can be measured on *dynamic drop*. The contact angle is measured while the drop is being enlarged or reduced; the boundary surface is being constantly newly formed during the measurement. Contact angles measured on increasing drops are known as advancing angles; those measured on reducing drops as receding angles.

The advantage of static contact angle measurement is that the needle does not remain in the drop during the measurement which is the case during measurement of dynamic contact angle. This presents the drop from being distorted (particularly important for small drops). In addition, when determining the contact angle from the image of the drop, it is possible to use methods which evaluate the whole drop shape and not just the contact area.

The static sessile drop was used for the determination of the contact angle on the deposited films by Drop Shape Analysis (DSA) software. The basis for the determination of the contact angle is the image of the drop on the surface. In the DSA software, the actual drop shape and the contact line (baseline) with the solid are first determined by the analysis of the grey level values of the image pixels. To describe this more accurate, the software calculates the root of the secondary derivative of the brightness levels to receive the point of greatest changes of brightness. A mathematical model which is used to calculate the contact angle is adapted to fit the drop shape. The drop shape analysis is done by Young-Laplace (sessile drop fitting) method which is theoretically the most

exact method for calculating the contact angle. In this method, the complete drop contour is evaluated; the contour fitting includes a correction which takes into account the fact that it is not just interfacial effects which produce the drop shape, but that the drop is also distorted by the weight of the liquid it contains. After the successful fitting of the Young-Laplace equation, the contact angle is determined as the slope of the contour line at the 3-phase contact point. Moreover, this model assumes a symmetric drop shape; therefore it cannot be used for dynamic contact angles where the needle remains in the drop. The physical-mathematical principles of the Young-Laplace method are described below which is concerned with the calculation of the surface tension/energy of the drop.

The force per unit length of the perimeter acting perpendicular to the perimeter is defined as the *surface tension 'γ'.* Molecules in the interfacial region have a higher potential energy than molecules in the bulk phases because of an imbalance of intermolecular attractive forces. This result in an excess free energy per unit area associated with the surface that is numerically equivalent to the surface tension, as shown below. Consider a flat rectangular patch of fluid interface of width W and length L. In order to expand the length to $L+\Delta L$, an amount of work $\gamma W \Delta L$ must be done at the boundary. The product $W\Delta L$ is just the change in area ΔA of the surface. The work done to increase the area is thus $\Delta A\gamma$, which corresponds to the increase in surface free energy. Thus, the surface tension γ is seen to be equivalent to

the surface free energy per unit area. So surface energy is defined as the work necessary to separate two surfaces beyond the range of the forces holding them together and is given in energy per unit area. So surface energy is often referred to as surface tension and is often expressed in dynes/cm (a surface tension of 1 dyne/cm or 1 mN/m is equivalent to a surface free energy of 1 mJ/m^2). The surface energy concept is useful for understanding the shapes adopted by liquid surfaces (Webster J. G. 1999).

The interface between a solid and a liquid has a surface free energy associated with it. When a liquid droplet rest on a solid surface surrounded by air than this system contains three different types of interfaces: solid-gas, solid-liquid and liquid-gas, each with a characteristic surface free energy per unit area. The state of minimum free energy for the system then involves trade-offs in the surface area for the various interfaces. The region of contact between the gas, liquid and solid is termed the contact line (base line). The liquid-gas surface meets the solid surface with an angle θ measured through the liquid which is known as the contact angle. The contact angle attains a value that minimizes the free energy of the system and is thus a characteristic of a particular solid-liquid-gas system. When the system is in static mechanical equilibrium, the contact line is motionless, meaning that the net force on the line is zero. Forces acting on the contact line arise from the surface tensions of the converging solid-gas, solid-liquid and liquid-gas interfaces, denoted by γ_{SG}, γ_{SL} and γ_{LG} respectively. The condition of zero net

force along the direction tangent to the solid surface gives the following relationship between the surface tensions and contact angle θ by Young equation.

The contact angle is thus seen to be dependent on the surface tensions between the various phases present in the system and is therefore an intrinsic property of the system. Surface tension is always positive for interfaces between immiscible phases and it always tends to decrease the area of interface. This tendency gives rise to a pressure difference between fluids on either side of a curved interface, with the higher pressure on the concave side of the interface. This pressure difference results in phenomena such as a capillary rise, bubble and drop formation, etc. A formula describing the pressure difference ΔP across the curved interface is given by the Young-Laplace equation which reflects the balance between surface tension and external forces such as gravity. It relates the pressure difference across a curved interface to the surface tension and the mean curvature of a two-dimensional surface specified in terms of the two principal radii of curvature R_1 and R_2, which are measured in perpendicular directions of the interface. A detailed mechanical analysis of curved surfaces shows that the pressure change across the surface is directly proportional to the surface tension and to the mean curvature of the surface:

$$\Delta P = \gamma\left(\frac{1}{R_1} + \frac{1}{R_2}\right) \tag{2.5}$$

where γ is the surface tension and the quantity in brackets is twice the mean curvature. Equation (2.5) is known as the Young-Laplace equation and the pressure change across the interface is termed the Laplace pressure. Measurement of the Laplace pressure for a surface of known curvature then allows a determination of the surface tension. Thus for a given value of γ, the shape of a drop may be determined from known physical parameters such as density and gravity, and known geometrical quantities, such as the radius of curvature at the apex. The inverse i.e., determination of the surface tension, 'γ' from the shape is also possible.

Several methods of surface tension measurement are based on the measurement of the static shape of an axisymmetric drop or bubble or on the point of mechanical instability of such drops or bubbles. In a gravitational field, a drop or bubble that is attached to a solid support assumes a non-spherical shape. **Figure 2.11a** shows the shape of a hanging droplet, also known as a pendant drop and **figure 2.11b** shows a so-called sessile drop. Axisymmetric air bubbles in water attain the same shapes as water drops in air, except that they are inverted. A bubble supported from below is thus called a hanging or pendant bubble, and a bubble supported from above is called a captive or sessile bubble. The reason for the deviation of the shape from that of a sphere can be understood from eq. (2.5). The hydrostatic pressure changes with depth more rapidly in a liquid than in a gas. The pressure difference across the surface of a pendant drop in air therefore

increases from top to bottom, requiring an increase in the mean curvature of the surface according to eq. (2.5). The drop in **figure 2.11a** has a neck at the top, which means that the two principal radii of curvature have opposite signs and cancel to some extent. At the bottom of the drop, the radii of curvature have the same sign, thus making the mean curvature larger. The Young-Laplace equation can be written as coupled first-order differential equations in terms of the coordinates of the interface for an axisymmetric surface in a gravitational field as:

$$\frac{dx}{ds} = \cos\phi$$

$$\frac{dz}{ds} = \sin\phi \qquad (2.6)$$

$$\frac{d\phi}{ds} = \frac{2}{b} + \left(\frac{\Delta\rho g}{\gamma}\right) z - \frac{\sin\phi}{x}$$

$$x(0) = z(0) = \phi(0) = 0$$

where x and z are the horizontal and vertical coordinates, respectively, with the origin at the drop apex; s is the arc-length along the drop surface measured from the drop apex; and ϕ is the angle between the surface tangent and the horizontal **(figure 2.11a).**

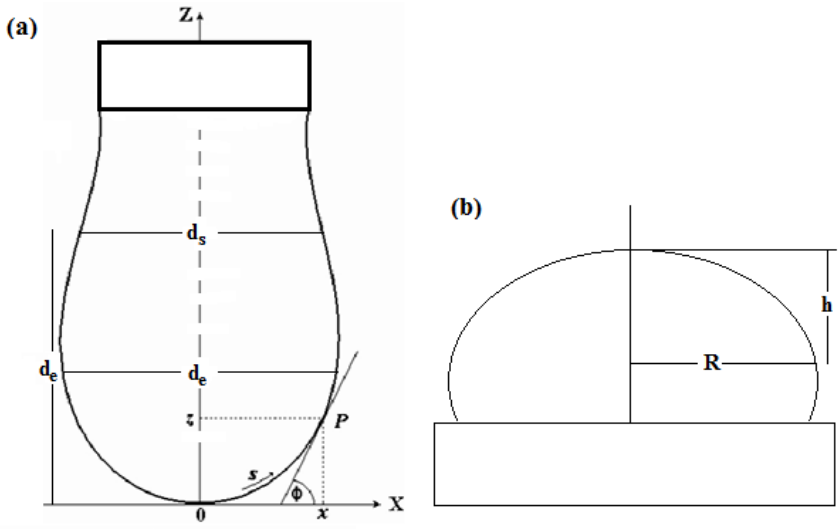

Figure 2.11 (a) *A pendant drop showing the characteristic dimensions* d_e and d_s *and the coordinates used in the Young–Laplace equation and*

(b) *A sessile drop showing the characteristic dimensions R and h .*

The parameter *b* is the radius of curvature at the apex of the drop or bubble, $\Delta\rho$ is the density difference between the two phases, and *g* is the acceleration of gravity. Numerical integration of eq. (2.6) allows one to compute the shape of an axisymmetric fluid interface. Comparison of computed shapes with experimentally measured shapes of drops or bubbles is a useful method of measuring surface tension. If all lengths in eq. (2.6) are made dimensionless by dividing them by *b*, the resulting equation contains only one parameter, $\beta = \Delta\rho g b^2 / \gamma$, which is called the Bond number (or shape factor). The shape of an axisymmetric drop bubble or meniscus depends only on this one dimensionless parameter. The Bond number can also be written

as $\beta = 2b^2 / a^2$ where $a = \sqrt{2\gamma / \Delta\rho g}$ is known as the capillary constant and has units of length.

The shape of an axisymmetric sessile drop (**figure 2.11b**) depends on only a single parameter the Bond number, as discussed above. The Bond number is a measure of the relative importance of gravity to surface tension in determining the shape of the drop. For Bond numbers near zero, surface tension dominates and the drop is nearly spherical. For larger Bond numbers, the drop becomes significantly deformed by gravity. In principle, the method involves obtaining an image of the drop and comparing its shape and size to theoretical profiles obtained by integrating eq. (2.6) for various values of β and b. Once β and b have been determined from shape and size comparison, the surface tension is calculated from:

$$\gamma = \frac{\Delta\rho g b^2}{\beta} \tag{2.7}$$

For pendant drops, the ratio d_s / d_e is correlated to a shape factor H from which surface tension is calculated according to:

$$\gamma = \frac{\Delta\rho g d_e^2}{H} \tag{2.8}$$

From the sessile drop, the contact angle and surface energy for the deposited films are determined by DSA software**.** A digital image of a sessile drop can be analyzed on a desktop computer in 1 or 2 seconds. Typically, several hundred coordinates on the edge of the drop are located with subpixel

resolution by computer analysis of the digital image. The size, shape, horizontal and vertical offsets of the theoretical profile given by eq. (2.6) are varied by varying four parameters: β, b and the pixel coordinates of the drop apex, x_0 and z_0. A best fit of the theoretical profile to the measured edge coordinates is obtained by minimizing an objective function. The algorithms can simultaneously track the surface area and volume of the drop or bubble.

The most widely used method is to measure the angle of a sessile drop resting on a flat solid surface using a goniometer-microscope equipped with an angle-measuring eyepiece or, more recently, a video camera (CCD) equipped with a suitable magnifying lens, interfaced to a computer with image-analysis software to determine the tangent value precisely on the captured image. A schematic diagram for contact angle measuring system is shown in **figure 2.12a** and the experimental setup of the system (DSA 100 Easy Drop) procured from Kruss, Germany is shown in **figure 2.12b**.

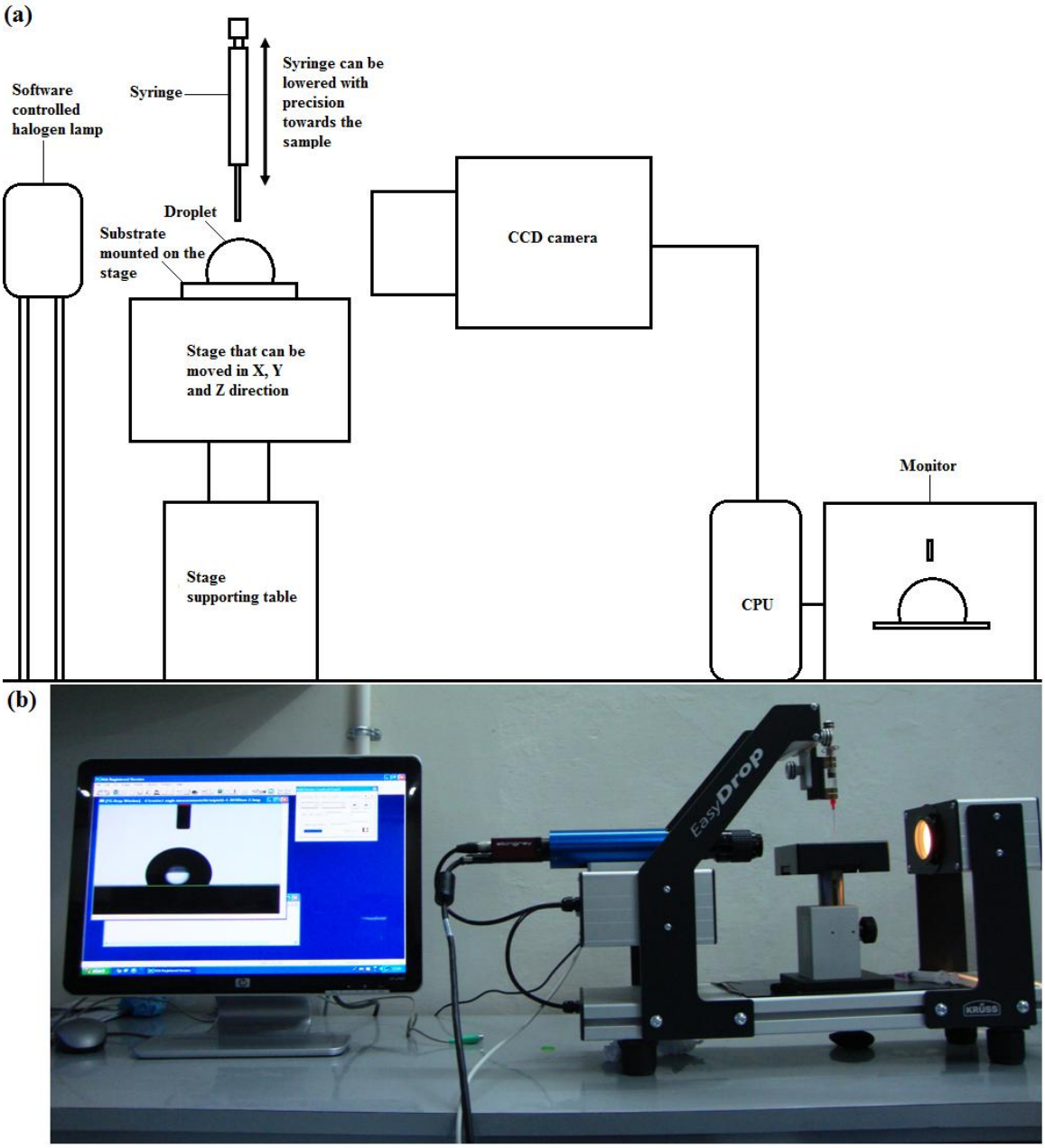

Figure 2.12 (a) *A schematic diagram for contact angle measuring system and* ***(b)*** *the experimental setup of the system (DSA 100 Easy Drop).*

Before any measurements are taken, the measurement stage is leveled by adjusting the stage supporting table. A substrate or sample whose contact angle is to be determined is then placed on the stage. The instrument uses a

micro-syringe mounted in an arm that can be moved in vertical and horizontal direction to dispense a liquid drop over the measurement location on the sample. The syringe will handle drop volumes from 3 to 10 µl with 0.1 µl resolution. Once the position of the syringe is adjusted according to the sample, the drop formed at the tip of the needle is lowered slowly and forms the contact angle when it strikes the surface of the sample. Drop images are acquired using a CCD camera and in line incident illuminator software controlled optical halogen lamp. The action appears live on the computer screen and the salient images are captured to the computer's memory for later image analysis. The CCD camera can capture images at very fast rate of around 25-60 frames per second. The measurement location on the platform can be shifted to facilitate formation of another drop on the same surface. So the drop profile is photographed, the evaluation of the drop image takes place in the window of the software: the baseline is determined automatically for measuring the contact angle and the tangent of the sessile drop profile at the three-phase contact point drawn onto the image is used to determine the value of the contact angle and surface energy by the DSA software as discussed earlier.

2.3.6 UV-Vis-NIR Spectrophotometer

Ultraviolet and visible absorption spectroscopy is the measurement of the attenuation of a beam of light after it passes through a sample or after reflection from a sample surface. UV-Vis-NIR Spectrophotometer includes a variety of absorption, transmittance and reflectance measurements in the ultraviolet (UV), visible (Vis) and near-infrared (NIR) spectral regions. The UV-Vis spectral range is approximately 190 to 900nm. This definition originates from the working range of a typical commercial UV-Vis spectrometer. The short wavelength limit for simple UV-Vis spectrometers is the absorption of UV wavelengths <180 nm by atmospheric gases. Purging a spectrometer with nitrogen gas extends this limit to 175 nm. Working beyond 175nm requires a vacuum spectrometer and a suitable UV light source. The long-wavelength limit is usually determined by the wavelength response of the detector in the spectrometer. Higher end commercial UV-Vis-NIR spectrometers extend the measurable spectral range into the NIR region as far as 3300 nm. This unit includes the use of UV-Vis-NIR instruments because of the importance of characterizing the NIR properties of materials for lasers, amplifiers and low-loss optical fibers for fiber-optic communications and other applications (Kaufmann E. N. 2003).

UV-Vis-NIR spectroscopy is one of the more ubiquitous analytical and characterization techniques in science. There is a linear relationship between absorbance and absorber concentration, which makes UV-Vis-NIR spectroscopy especially attractive for making quantitative measurements.

Spectral lines observed in the UV-visible region correspond to the energy difference between two well-defined electronic energy levels of the absorbing atom or molecule. When an atom or molecule absorbs energy in that region, its electrons are promoted from a state of lowest energy, i.e. the ground state, to states, or orbitals, of higher energy. UV-visible spectroscopy thus provides direct evidence about electron energy jumps between distinct energy levels. Therefore, UV-Vis-NIR spectroscopy is useful to the exploration of the electronic properties of materials and materials precursors in basic research and in the development of applied materials. Materials that can be characterized by UV-Vis-NIR spectroscopy include semiconductors for electronics, lasers, & detectors, transparent or partially transparent optical components, solid-state laser hosts, optical fibers, waveguides & amplifiers for communication and material for solar energy conversion. It is useful in characterizing optical properties such as the absorption, transmission and reflectivity of a variety of technologically important materials such as pigments, coatings, thin films, windows and filters. The use of UV-Vis spectroscopy in materials research can be divided into two main categories: (i) quantitative measurements of an analyte in the gas, liquid, or solid phase and (ii) characterization of the optical and electronic properties of a material.

A typical UV-Vis-NIR spectrophotometer has a deuterium discharge lamp for the UV-range and a tungsten-halogen lamp for visible-NIR range. A schematic diagram of the components of a typical UV-Vis-NIR

spectrophotometer is shown in the **figure 2.13a** and the experimental setup of Varian Cary 5000 UV-Vis-NIR spectrophotometer procured from Varian Inc. USA is shown in **figure 2.13b** which has wavelength range from 175-3300nm. The functioning of this instrument is relatively straightforward. A beam of light from a UV and/or visible-NIR light source is separated into its component wavelengths by a prism or diffraction grating. Each monochromatic (single wavelength) beam in turn is split into two equal intensity beams by a half-mirrored device. One beam, the sample beam, passes through the compound being studied while the other beam passes through the reference. The intensities of these light beams are then measured by electronic detectors and compared. The intensity of the reference beam, which should have suffered little or no light absorption, is defined as I_0. The intensity of the sample beam is defined as I. Over a short period of time, the spectrometer automatically scans all the component wavelengths in the manner described. The ultraviolet (UV) region scanned is normally from 175 to 400 nm, the visible portion is from 400 to 800 nm and the NIR range from 800-3300nm.

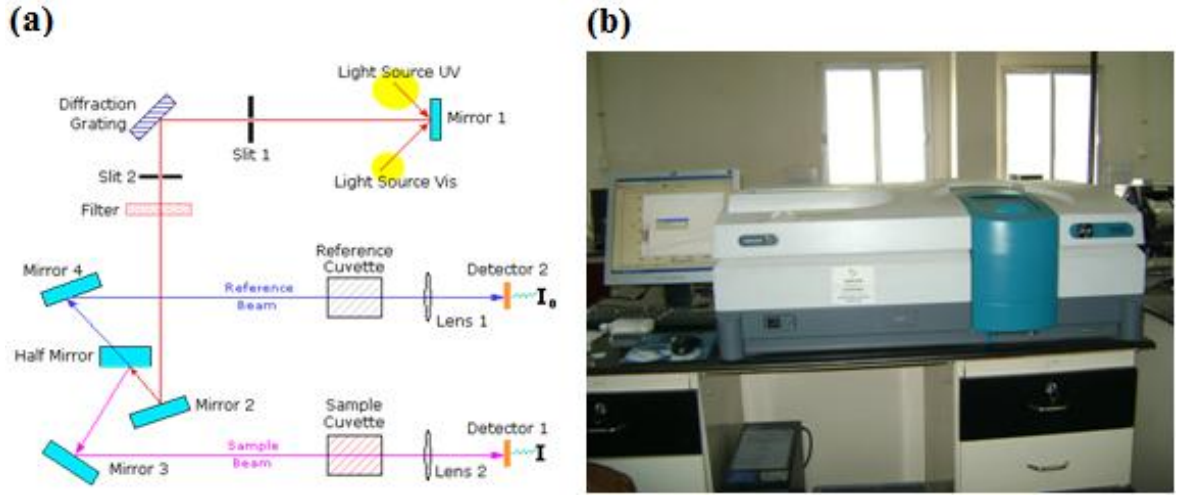

Figure 2.13 (a) *A schematic diagram of a UV-Vis-NIR spectrophotometer and*

(b) *the experimental set-up of UV-Vis-NIR spectrophotometer (Varian Cary 5000).*

If the sample compound does not absorb light of a given wavelength, then $I = I_0$. However, if the sample compound absorbs light then I is less than I_0, and this difference may be plotted on a graph versus wavelength. Absorption may be presented as transmittance $(T = I/I_0)$ or absorbance $(A = \log I_0/I)$. If no absorption has occurred then T = 1.0 and A = 0. Most spectrometers display absorbance on the vertical axis, and the commonly observed range is from 0 (100% transmittance) to 2 (1% transmittance). The wavelength of maximum absorbance is a characteristic value. Different compounds may have very different absorption maxima.

2.3.6.1 Determination of Refractive Index, Packing Density, Thickness and

Band Gap

For a partially transparent thin film, it is possible to determine the refractive index as well as thickness by measuring the transmission of light through it. The refractive index and thickness of the deposited films were determined from their transmission spectra by the formula suggested by Manifacier *et al.* 1976. **Figure 2.14a** represents a thin film with refractive index *n*, deposited on glass substrate with refractive indices n_1 , and n_0 is the refractive index of the medium i.e. air.

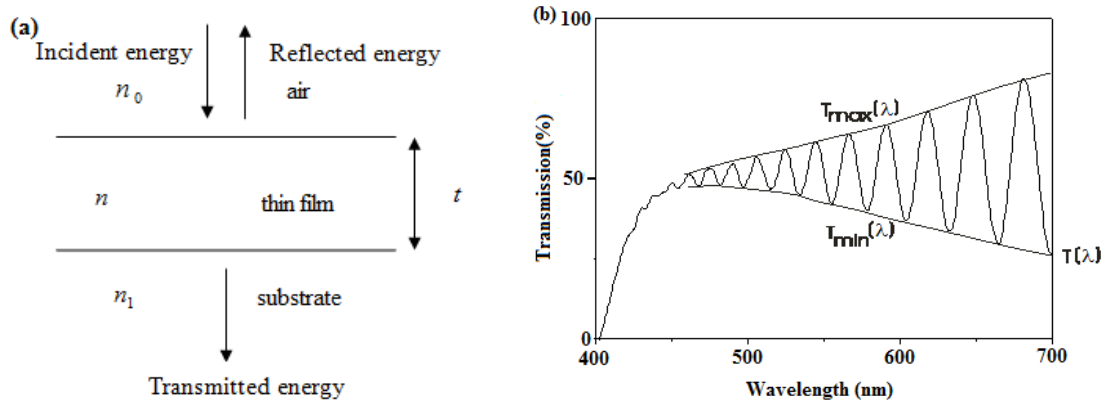

Figure 2.14 (a) *Reflection and transmission of light by a thin film deposited on substrate and* ***(b)*** *transmission spectra for a thin film.*

In the case of partially transparent thin films, the modulations in intensity can be observed in the reflectance and transmittance spectra due to interference between the light reflected from the front and back surface of the film. **Figure 2.14b** shows the transmission spectra of a thin film

deposited on glass substrate. Here we consider $T_{\min}$ and $T_{\max}$ as continuous function of λ through $n(\lambda)$. These functions which are the envelopes of the maxima $T_{\max}(\lambda)$ and the minima $T_{\min}(\lambda)$ in the transmission spectrum and are shown in **figure 2.14b**. For a thin film on a transparent substrate, the extreme values of the transmission are given by the formulae

$$T_{\max} = \frac{16 n_0 n_1 n^2 \alpha}{(C_1 + C_2 \alpha)^2} \tag{2.9}$$

$$T_{\min} = \frac{16 n_0 n_1 n^2 \alpha}{(C_1 - C_2 \alpha)^2} \tag{2.10}$$

where $C_1 = (n + n_0)(n_1 + n), C_2 = (n - n_0)(n_1 - n)$ and

$\alpha = \exp(-4\pi kt/\lambda) = \exp(-Kt)$. Here K is the absorption coefficient of the thin film. The ratio of equation (2.9) and (2. 10) gives

$$\alpha = \frac{C_1[1-(T_{\max}/T_{\min})^{1/2}]}{C_2[1+(T_{\max}/T_{\min})^{1/2}]} \tag{2.11}$$

Then, from equation (2.9),

$$n = [N + N^2 - n_0^2 n_1^2)^{1/2}]^{1/2} \tag{2.12}$$

where $$N = \frac{n_0^2 + n_1^2}{2} + 2 n_0 n_1 \frac{T_{\max} - T_{\min}}{T_{\max} T_{\min}} \tag{2.13}$$

Equation (2.12) shows that refractive index n of thin films is explicitly determined from $T_{\max}, T_{\min}$, n_1 and n_0 at the same wavelength. The thickness *t* of the thin film can be calculated from two maxima or minima and is given by

$$t = \frac{M\lambda_1\lambda_2}{2(n(\lambda_1)\lambda_2 - n(\lambda_2)\lambda_1)} \tag{2.14}$$

where M is the number of oscillations between the two extrema (M=1 between two consecutive maxima or minima); $\lambda_1, n(\lambda_1) and \lambda_2, n(\lambda_2)$ are the corresponding wavelengths and index of refraction.

The packing density of films can be determined using the Bragg & Pippard model as discussed by Xiao *et al.* 2009 which is given by

$$p = \frac{n^2 - 1}{n^2 + 2}\frac{n_b^2 + 2}{n_b^2 - 1} \tag{2.15}$$

where n is the refractive index of the thin films at a particular wavelength and n_b is the bulk refractive index value of the material. So the refractive index, thickness and packing density of all the deposited films were determined from eq. (2.12), (2.14) and (2.15) respectively.

We have used the Tauc relation for the determination of the optical band gap of deposited thin films which is given by

$$\alpha h\upsilon = A(h\upsilon - E_g)^n \tag{2.16}$$

where α is the absorption coefficient, A depends on the transition probability and can be assumed to be constant within the optical frequency range, h is Planck's constant, υ is the photon frequency, so $h\upsilon$ is the energy of the incident photons, E_g is the band gap corresponding to transitions indicated by the value n which is characteristic of the type of the optical transition process. The power parameter n has the value of 1/2 for a direct

allowed optical transition and the value of 2 for an indirect allowed optical transition process. The deposited thin films of chromium oxynitride, titanium oxynitride and zirconium oxynitride are having indirect optical transition, so the value of parameter *n* is taken 2 for the determination of the band gap for all thin films. An extrapolation of the linear region of a plot of $(\alpha h\upsilon)^{1/2}$ on the y-axis versus photon energy $h\upsilon$ on the x-axis gives the value of the band gap for deposited transition metal oxynitride thin films.

2.3.7 I*mpedance analyzer*

Dielectric constant is an important parameter of any insulating material. It describes the interaction of a material with an electric field. It is a measure of how much energy from an external field is stored in a material. It is measured by an instrument called as impedance analyser. When using an impedance-measuring instrument to measure permittivity, the parallel plate method is usually employed. An overview of the parallel plate method is shown in Figure 2. The parallel plate method, also called the three terminal method in ASTM D150, involves sandwiching a thin sheet of material or liquid between two electrodes to form a capacitor. The measured capacitance is then used to calculate permittivity. In an actual test setup, two electrodes

are configured with a test fixture sandwiching dielectric material. The impedance-measuring instrument would measure capacitance and a software program would calculate dielectric constant.

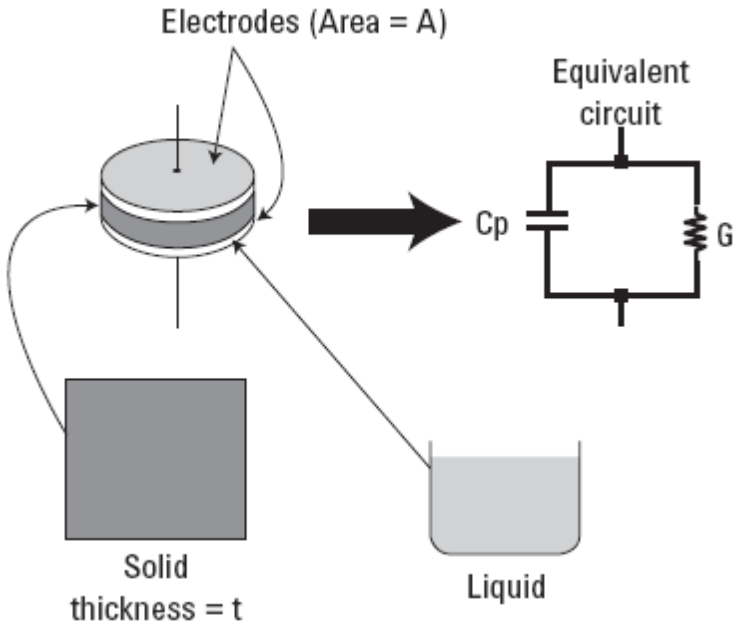

Figure 2.15 *Parallel plate capacitor method*

The Agilent 4294A (Fig is a powerful tool for design, qualification, quality control and production testing of electrical and electronic components. Circuit designers and developers can also benefit from the performance/functionality offered. Moreover, the 4294A's high measurement performance and capable functionality delivers a powerful tool to circuit design and development as well as materials research and development (both electronic and non electronic materials) environments. The following are application examples:

Electronic devices

Passive component

• Impedance measurement of two terminal components such as capacitors, inductors, ferrite beads, resistors, transformers, crystal/ ceramic resonators, multi-chip modules or array/network components.

Semiconductor components

• C-V characteristic analysis of varactor diodes.

• Parasitic analysis of a diode, transistor, or IC package terminal/leads.

• Amplifier input/output impedance measurement.

Other components

• Impedance evaluation of printed circuit boards, relays, switches, cables, batteries, etc.

Materials

Dielectric material

• Permittivity and loss tangent evaluation of plastics, ceramics, printed circuit boards, and other dielectric materials.

Magnetic material

• Permeability and loss tangent evaluation of ferrite, amorphous, and other magnetic materials.

Semiconductor material

Permittivity, conductivity, and C-V characterization of semiconductor.

Figure 2.16 Impedance analyzer used for measurement of capacitance of thin film

2.3.8 Four probe electrical measurement unit

Four probe method

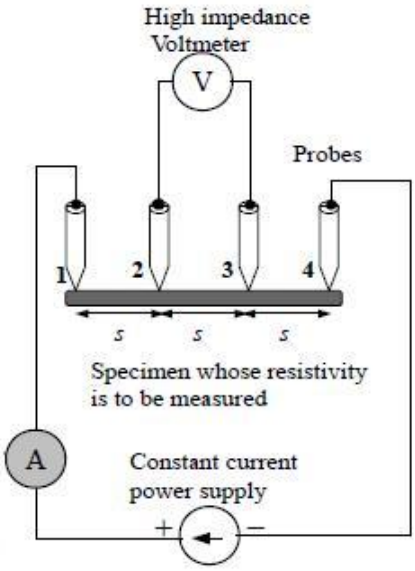

Figure 2.17 Schematic diagram of four probe arrangement

Four probe method allows the measurement of resistivity of sample having wide variety of shapes, including resistivity of small volumes within bigger

pieces of semiconductor. Thus resistivity can be determined with good accuracy. The schematic diagram is shown in Fig.3.18. Four sharp probes are placed on a flat surface of material, current is passed through two outer electrodes and the floating potential is measured across the inner pair. If the flat surface on which probes set is adequately large and crystal is big the crystal may be considered to be a semi finite volume. The surface on which probes rest, may be mechanically lapped to prevent the minority carrier injection and make good contact. For resistivity measurement by four probes method certain assumptions are considered-

- ✓ In a given area of measurement resistivity is uniform.
- ✓ The surface of sample is flat so that there is no surface leakage current.
- ✓ The four probes contact the surface at points that lie in a straight line.
- ✓ The diameter of contact should be small compared to the distance between probes.

Four probes in practice

Four probes attached with Kithley electrical measurement unit is used for measurement of sheet resistivity of material. The current and voltage measurement is carried out by 6221 current source and 2182A nanovoltmeter.

2.3.9 Breakdown strength Test Meter

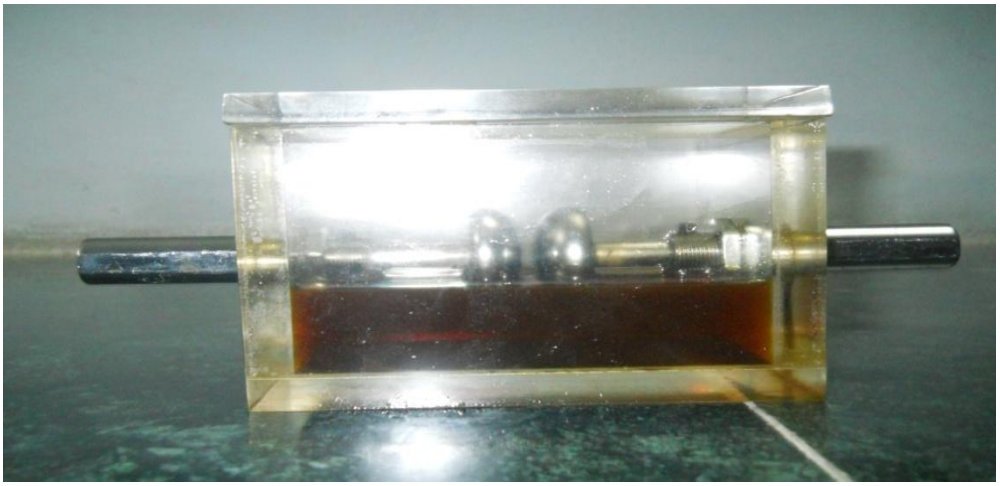

Figure 2.18 *Breakdown Test Meter*

The breakdown strength is defined as the maximum electric field that a pure material can withstand under ideal conditions without breaking down (i.e., without experiencing failure of its insulating properties). The theoretical dielectric strength of a material is an intrinsic property of the bulk material and is dependent on the configuration of the material or the electrodes with which the field is applied. The "intrinsic dielectric strength" is measured using pure materials under ideal laboratory conditions. At breakdown, the electric field frees bound electrons. If the applied electric field is sufficiently

high, free electrons from background radiation may become accelerated to velocities that can liberate additional electrons during collisions with neutral atoms or molecules in a process called avalanche breakdown. Breakdown occurs quite abruptly (typically in nanoseconds), resulting in the formation of an electrically conductive path and a disruptive discharge through the material. For solid materials, a breakdown event severely degrades, or even destroys, its insulating capability.

Factors affecting apparent dielectric strength are

- ✓ it increases slightly with increased sample thickness.
- ✓ it decreases with increased operating temperature.
- ✓ it decreases with increased frequency.
- ✓ for gases (e.g. nitrogen, sulfur hexafluoride) it normally decreases with increased humidity.
- ✓ for air, dielectric strength increases slightly as humidity increases

The unit of dielectric strength is volts per meter (V/m). It is also common to see related units such as volts per centimeter (V/cm), megavolts per meter (MV/m).

The breakdown strength of the coated and uncoated glass insulator is measured using custom designed apparatus as shown in figure 2.18. The apparatus has been designed as perm ASTM 149D.

CHAPTER 3
SYNTHESIS AND CHARACTERIZATION OF HAFNIUM OXIDE

3.1 Introduction

Hafnium (IV) oxide is an inorganic compound with the chemical formula HfO_2. It is also known as **hafnia**. This colourless solid is one of the most common and stable compounds of hafnium. It is an electrical insulator with a band gap of approximately 6 eV. HfO_2 is quite inert. It reacts with strong acids such as concentrated sulfuric acid and with strong bases. It dissolves slowly in hydrofluoric acid to give fluorohafnate anions. At elevated temperatures, it reacts with chlorine in the presence of graphite or carbon tetrachloride to give hafnium tetrachloride. HfO_2 is reported to exhibit attractive properties like high dielectric constant (ε=25) , wide band gap (E_g=5.7eV), high melting point and thermodynamically stable [**27**].**Table 3.1** lists some other properties of hafnium oxide. Among the materials with medium dielectric constant, ZrO_2 and HfO_2 are attracting much attention. Hf forms the most stable oxide with the highest heat of formation (ΦHf=271Kcal/mol) among the elements in group IVA of the periodic table (Ti,Zr,Hf).

HfO_2 thin film in the form of coating finds its applications in various electronic devices [**8,14,190**] and optical systems [**117, 205**]. However, HfO_2 has not been utilized as a protective coating for outdoor high voltage insulators. Also less work has been done in exploring hydrophobic property of HfO_2 thin film. Research group of A. feng [**43**] has reported the maximum water contact angle of 74^0 for HfO_2 thin film.

Hafnium oxide in the form of thin layer has been synthesized by various techniques like chemical vapour deposition [**6,114**], electrochemical deposition [**42**], atomic layer deposition [**41**], pulse laser deposition [**94**], rf and DC sputtering [**204,168,3**] and electron beam evaporation [**37**]. Each method has its own merits and demerits. The reactive sputtering method provides many advantages like uniform coating, good adhesion, reproducibility and high deposition rate [**105**]. Looking to these advantages, we are depositing HfO_2 coating for glass insulator through DC reactive sputtering.

Table 3.1 *Properties of hafnium oxide*

Properties	Compound Formula	Molecular Weight	Melting point	Boiling point	Density g/cm^3	Exact mass g/mol	Charge
	HfO_2	210.49	2758 °	5400 °	9.68	251.989	0

Various research groups have examined the different properties of HfO_2 like structural, optical, electrical and dielectric. Aygun et al. have deposited HfO_2 thin film using DC sputtering by varying O_2/Ar ratio **[4]**. They concluded that the HfO_2 film remains amorphous at low substrate temperature but get crystallize at higher temperature. The optical parameter i.e. refractive index was reported to be temperature as well as sputtering power dependent. Bharathi et al. have reported the grain size and strain effects on the optical and electrical properties of nanocrystalline hafnium oxide film. Their experimental investigations indicated that the monoclinic HfO_2 nanocrystals are highly oriented along the (-111) direction. The band gap of the film varied in the range 5.42-5.60 eV which was near to the bulk value. They have also reported an increment in the conductivity of the film with the increase in grain size [**11**]. Martinez et al. have synthesized HfO_2 films by high pressure reactive sputtering and reported that the structure of the film (amorphous or polycrystalline) have no significant effect on the band gap. However, amorphous films were found to have a higher refractive index and a lower transparency than polycrystalline films [124]. A detailed thin film growth structure of oxygen engineered monoclinic HfO_2 was studied by Hildebrandt et al. They reported that the oxidation conditions induces a switching between (-111) and (002) texture of

hafnium oxide. They also correlated the bandgap with the oxygen vacancies. For high oxygen vacancy concentrations, defect bands were form inside the bandgap. The resistivity also changes by several orders of magnitude as a function of oxidation conditions. The influence of O_2/Ar flow ratio on the deposition rate, structure and optical properties of HfO_2 thin films was studied by Liu et al. [**110**]. The thin film prepared after oxygen introduction have random orientation, weakened crystallinity and smaller crystallite size. The refractive index was showing an increasing trend with the increment of O_2/Ar ratio. The research group of Ming et al. have observed a great variation in the bandgap of the hafnium oxide thin film of different thickness[**128**]. Huang et al. through their experiments came to conclusion that HfO_2 thin film grown by RF sputtering and treated under NH_3 plasma shows an enhanced electrical properties by reducing the leakage current drastically and increasing the dielectric constant [73].

The above study clearly reveals that the different properties of HfO_2 film were dependent on the sputtering parameters. Owing to this view, HfO_2 film were synthesized over glass insulators by varying sputtering parameters namely sputtering or reactive gas, working pressure, substrate temperature and deposition time. In addition to this, HfO_2 thin films were also deposited

obliquely. The films were characterized in order to investigate the structural, morphological, hydrophobic, electrical and dielectric properties.

3.2 Effect of Sputtering gas on Structural, Optical, Hydrophobic and electrical properties of DC sputtered Hafnium Oxide thin films

3.2.1 Experimental Detail

Hafnium oxide nanocrystalline thin films were deposited on glass and quartz substrates by DC magnetron sputtering in a custom designed 12 inch diameter chamber (Excel Instruments, India) using a 99.99% pure hafnium target (2" dia and 5 mm thickness). The substrates were cleaned by rinsing in ultrasonic baths of acetone and dried under nitrogen gas. The chamber was evacuated by a turbomolecular pump. It is backed up by a rotary pump. The base pressure was below 2x10-6 Torr. Thereafter high purity (99.9%) oxygen along with inert gases (He and Ar) was bled into the chamber. The flow of oxygen was kept constant (10 sccm) while the inert gases flow was varied from 10 to 50 sccm. The ratio of the gas mixture was controlled and measured using mass flow controller and capacitance manometers (MKS), respectively. The gas pressure was kept at 15 mTorr for all depositions. During each sputtering experiment,

the gas pressure was carefully monitored and kept constant since the sputtering current is extremely sensitive to the pressure of the sputtering gas. The sputtering was carried for a period of one hour at room temperature. The sputtering was done at 50W power. The target to substrate distance was kept constant at 41mm. Other than the sputtering gas, all parameters were constant during the set of experiments.

3.2.2 Results and Discussions

3.2.2.1 Structural Property

Hafnium oxide films were deposited using O_2+ Ar and O_2+He gases with different O_2/ (Ar or He) ratio at room temperature (27^0C) and 50 W sputtering power**. Figure 3.1 and 3.2** show the XRD pattern of the nanocrystalline thin films of hafnium oxide deposited with varying O_2/Inert gas (Ar or He) ratio. It is noticed that in XRD pattern of HfO_2 grown in argon atmosphere, the dominant peak is observed around 28^0 of 2θ attributed to (-111) monoclinic phase of HfO_2 [**4**]. However in XRD pattern of HfO_2 grown in helium atmosphere, the dominant peak is observed around 34^0 of 2θ attributed to (002) monoclinic phase. The possible reason may be that peak at (-111) in argon atmosphere is due to surface energy minimization while dominant peak at (002) in helium atmosphere is due to strain energy minimization. Argon atoms are

heavier in comparison to helium atom so the energy transferred by the recoil argon atoms to the films is more in comparison to helium. Hence mobility of the adatom is higher which lead to orientation corresponding to lower surface energy.

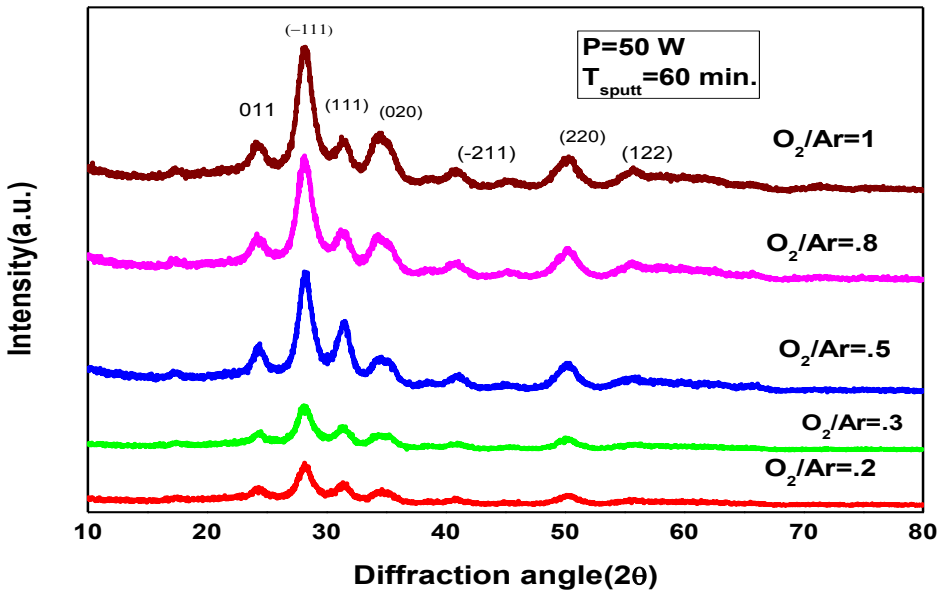

Figure 3. 1 *XRD patterns of deposited hafnium oxide at different O_2/Ar gas ratio.*

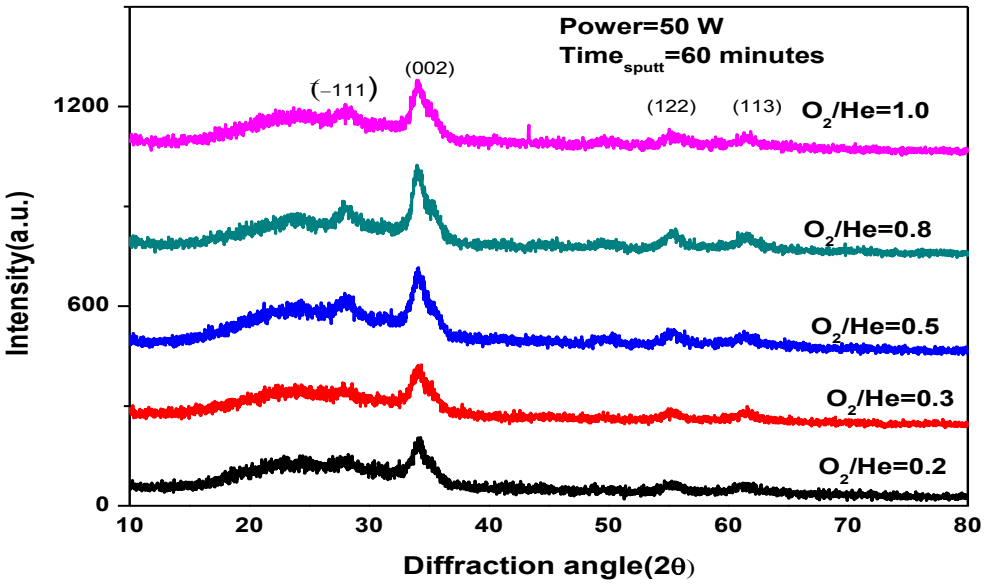

Figure 3. 2 *XRD patterns of deposited hafnium oxide at different O_2/He gas ratio.*

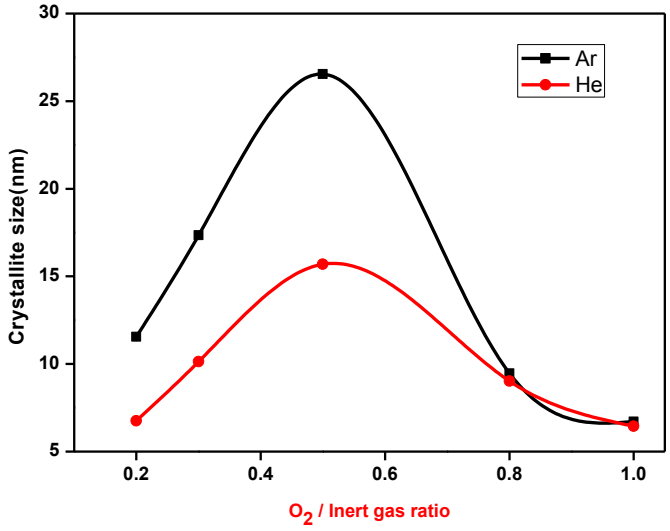

Figure 3. 3 *Particle size as a function of O_2/inert gas ratio.*

The average crystallite size, *t* of the samples was calculated using well known Scherrer formula [**30**]. **Figure 3.3** shows the variation of particle size as oxygen to inert gas (Ar or He) is varied. In both cases, the particle size increases as the ratio is increased from 0.2 to 0.5 and then it starts decreasing as we move from 0.5 to 1. This phenomenon can be explained on the basis of oxygen partial pressure. The increment in crystallite size up to O_2/inert gas ratio=0.5 may be due to transfer of energy by the oxygen atom to the films which in turn increases the mobility rather than resputtering. Whenever oxygen is present in the sputtering phenomenon, resputtering of the growing film material occurs by high energy O^{2-} ions. However as oxygen to inert gas ratio is increased beyond 0.5, partial pressure of oxygen increases which results in resputtering due to heavy oxygen ions [**59**]. Thus crystallite size reduces. Also it was observed that average crystallite size in helium case is smaller as compare to argon case. This observation can be justified through mean free path. The mean free path (λ) of the atoms and pressure (*P*) has following relation [120]

$$\lambda = (2.33*10^{-20}\ T_s)/\ (P\delta^2_m\ ) \qquad (3.1)$$

where *P* is the pressure, T_s is the temperature and δ_m is the atomic diameter of the sputtering gas. Thus, the mean free path of the gas atoms decreases as the size of the gas atoms increases. This in turn increases the collision frequency which leads to agglomeration and growth of particle before arriving at the

substrate. Hence we can expect an increase in the crystallite size with increase in atomic mass of sputtering gas [149].

The at.% of hafnium and oxygen obtained through EDS for the coated samples are shown in **Table 3.2**. The best match with the theoretical result (Hf=66.66%, O=33.33%) is obtained for O_2/(Ar or He)=0.5.

Table 3.2 *Elemental analysis of HfO_2 in different inert gas atmosphere*

O_2/Inert gas ratio	Argon case		Helium Case	
	at.% Hf	at.% O	at.% Hf	at.% O
0.2	60.23	39.77	60.13	39.21
0.3	62.25	37.75	62.14	37.86
0.5	66.66	33.34	64.12	35.88
0.8	64.16	35.84	64.56	35.44
1.0	63.10	36.9	63.12	36.88

3.2.2.2 Morphological Property

The AFM micrographs of the coating deposited in Ar and He atmosphere are shown in **figure 3.4** and **3.5** respectively. The AFM micrographs clearly reflect that the crystallite size is large in case of sample deposited in argon as compared to that deposited in helium atmosphere. The rms value of surface roughness was calculated using software attached with AFM. Figure **3.6** shows

the variation of surface roughness with O_2/inert gas ratios. The graph supported the fact that as particle size increases, surface roughness increases and vice versa.

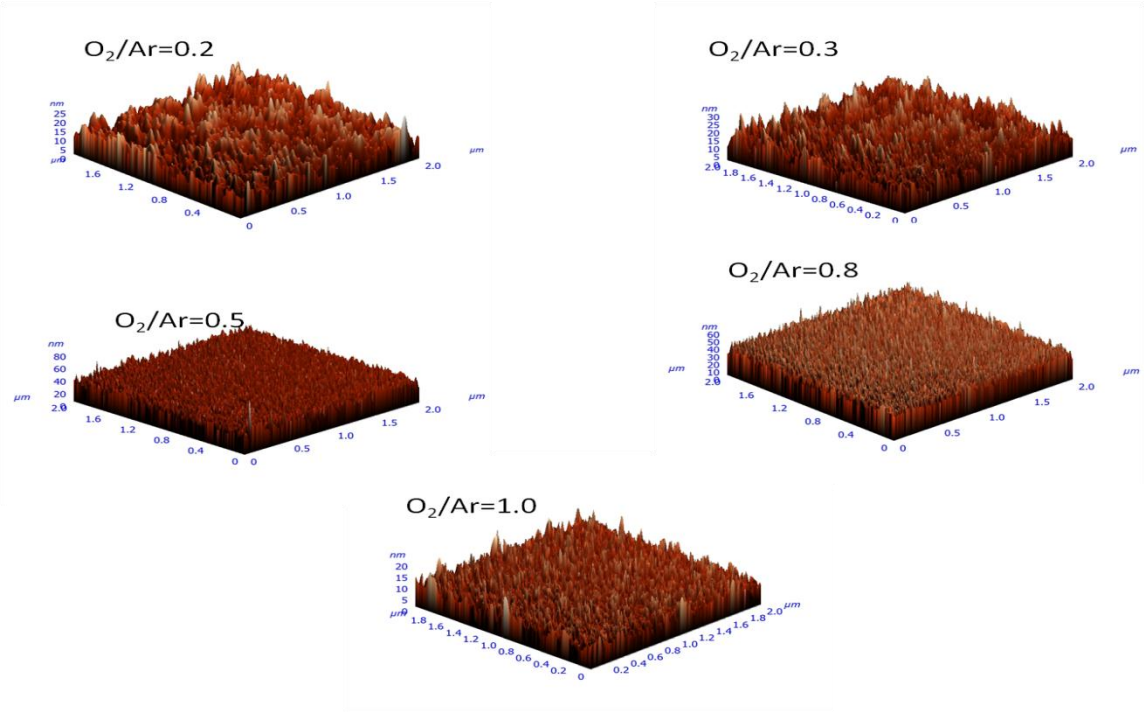

Figure 3.4 *AFM micrographs of hafnium oxide films deposited at varying O_2/Ar ratio.*

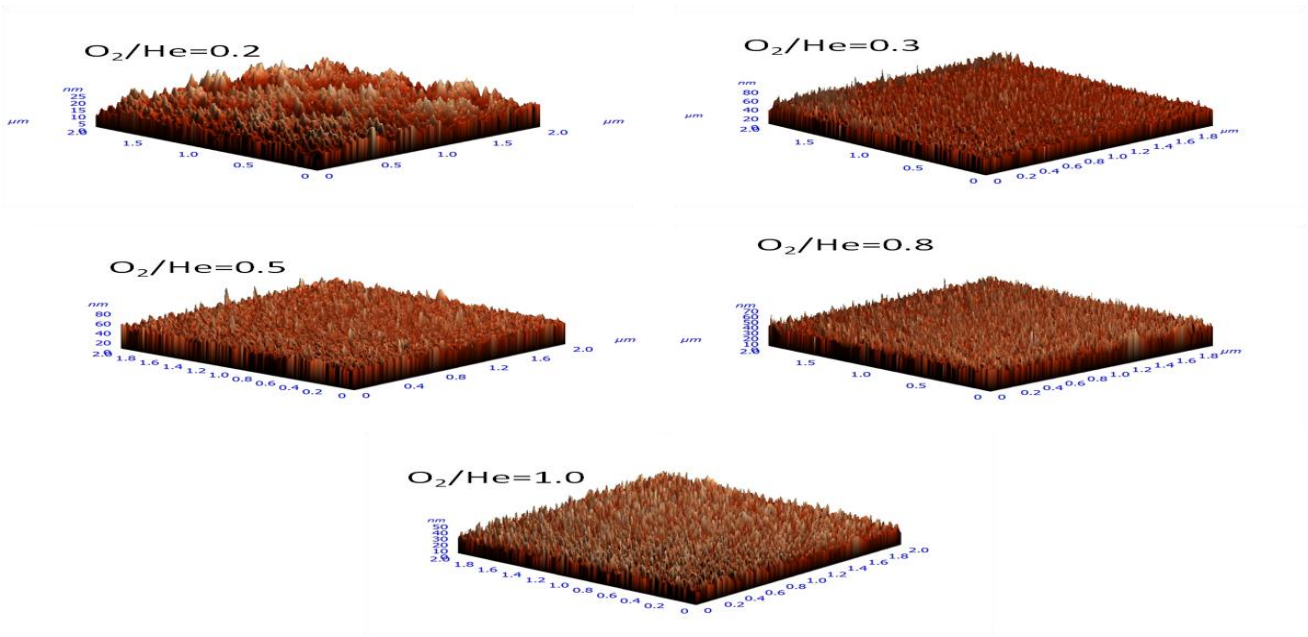

Figure 3.5 *AFM micrographs of hafnium oxide films deposited at varying O_2/He ratio.*

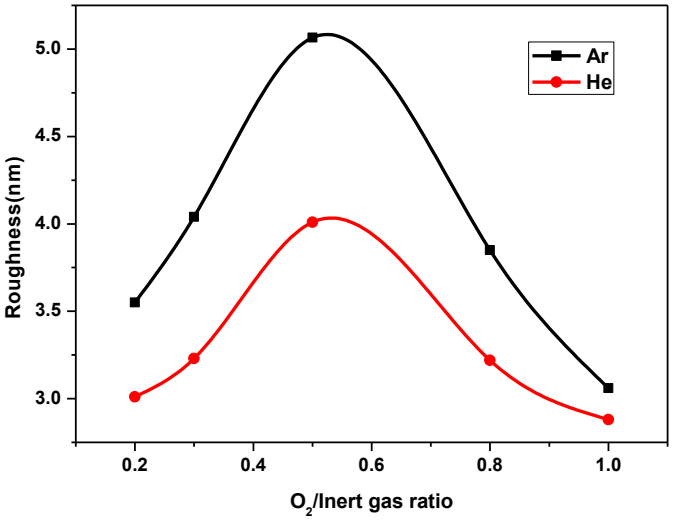

Figure 3.6 *Variation of roughness with O_2/inert gas ratio.*

3.2.2.3 Hydrophobicity

The surface roughness plays an important role in determining the hydrophobicity of coatings. Literature has revealed that surfaces with nanotextures used to form hydrophobic surfaces [**142**]. The relation between surface roughness and contact angle is best described by Wenzel [**188**]

Wenzel clearly depicts that for a hydrophobic case ($\theta_b > 90^0$), as roughness increases, wettability decreases and vice versa. Similarly for a hydrophilic case, with the increase of roughness, wettability increases and vice versa. The role of surface roughness on hydrophobicity was also studied. To determine the hydrophobicity, static angle measurements were made by dropping 3 µl distilled water on the sample surface and using sessile drop measurement method. The values of the static contact angle are the averages of ten measured values. Water contact angle was being measured for each sample. **Figure 3.7** shows the variation of water contact with O_2/Ar and O_2/He ratios. From graph it is clear that as O_2/Ar ratio is increased from 0.2 to 0.5, contact angle and roughness both increases and hence hydrophobicity. Further increment in the ratio (0.5 to 1) reduces the contact angle as well as roughness and thereby hydrophobicity. The same trend is observed in O_2/He case. The maximum

contact angle obtained is 102.25^0 and 99.14^0 for argon and helium case respectively. It is observed that in both case Wenzel model is satisfied.

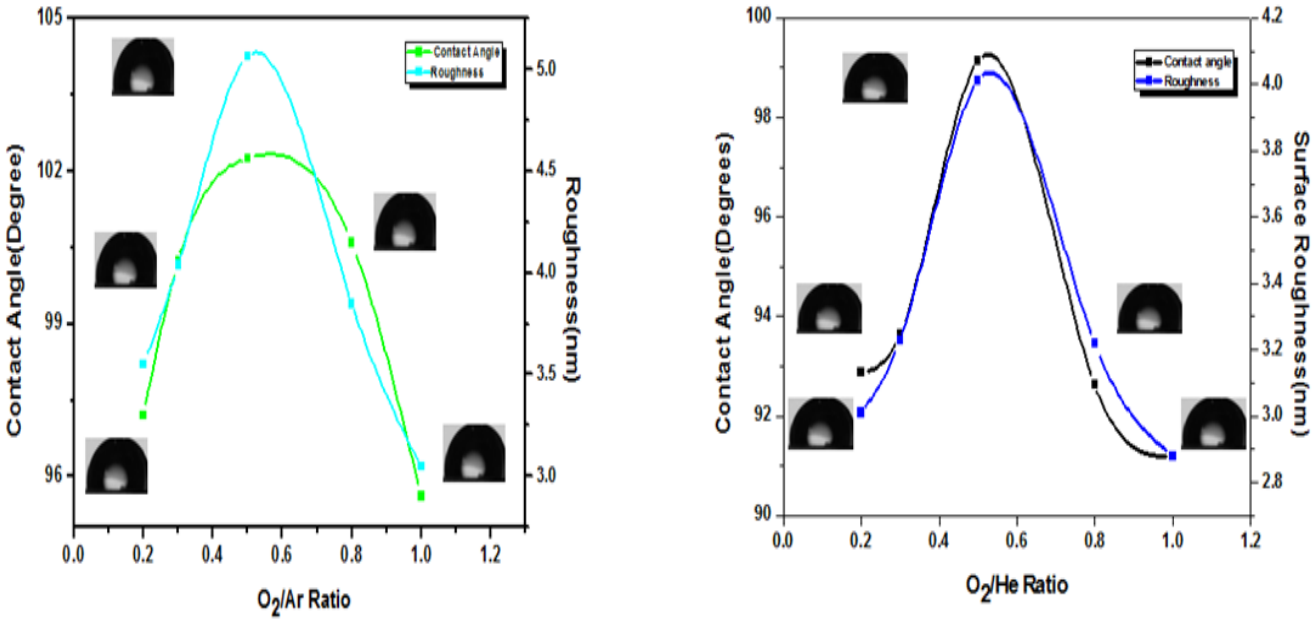

Figure 3.7 *Variation of contact angle and roughness as O_2/inert gas (Ar or He) ratio is varied*

3.2.2.4 Optical Property

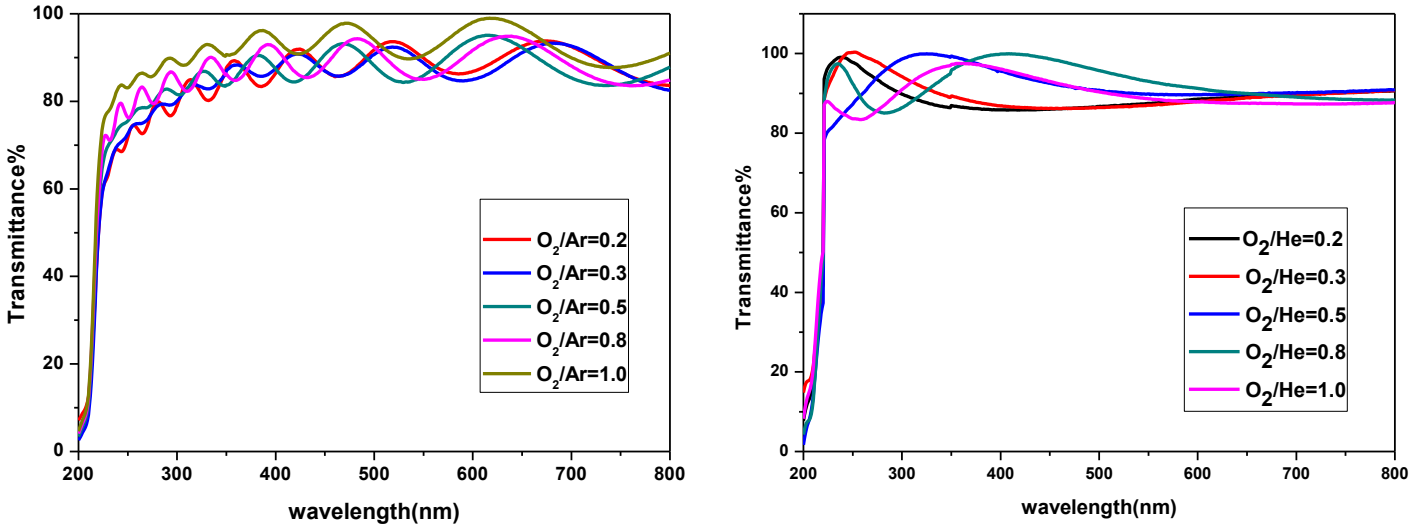

Figure 3.8 *(a) Transmittance spectra of HfO_2 as a function of O_2/Ar gas ratio.*

(b) Transmittance spectra of HfO_2 as a function of O_2/He gas ratio.

Transmittance spectra of the samples deposited in Ar and He atmosphere for different oxygen partial pressure is shown in **figure. 3.8(a)** and **(b)** respectively. Interference effect has developed oscillations in the spectrum of transmittance. The average transmission is more than 80% in the visible region for all the samples deposited in argon and helium atmosphere. The refractive index of the film was calculated using Manificier et al. model [**121**].

The refractive index calculated at λ=550 nm is shown in **Table 3.3**. It is observed that as oxygen partial pressure is increased, the refractive index

decreases. Thus, refractive index depends inversely on oxygen partial pressure. The oxygen to inert gas (Ar and He) ratio of 0.2 gives the highest refractive index for the deposited films. The probable reason may be that as the oxygen partial pressure is increased,

Table 3.3 *Optical parameters of hafnium oxide*

O_2/Inert gas Ratio	**Refractive Index (Argon case)**	**Refractive Index (Helium case)**	**Band gap (Argon case)**	**Band Gap (Helium case)**
			(eV)	**(eV)**
0.2	1.95	1.98	5.23	5.30
0.3	1.93	1.95	5.27	5.33
0.5	1.90	1.92	5.32	5.50
0.8	1.85	1.90	5.35	5.42
1.0	1.84	1.88	5.43	5.36

the diffusion rate of oxygen into the interfacial region increases which results into the formation of undesired interfacial layer between film and substrate. This prevents the growth rate of HfO_2 [**34**].The refractive index lies between 1.84-1.96 [**114**] for argon case and for helium case it lies between 1.88-1.98 [**82**].

Optical absorption coefficient (α) was calculated as a function of the wavelength in the range of 200-800nm. The optical band gap (E_g) of the samples was determined using the Tauc relation [**171**]. The reported value of m

is 2 for indirect bandgap and ½ for direct band gap [68].The literature has stated that HfO_2 has indirect band gap [**124**] as well as direct band gap [**11**]. However, in case of HfO_2 thin films, indirect band gap is widely used having m=2 [**11**]. The method for the determination of optical bandgap (E_g) involves plotting a graph of $(\alpha hv)^{1/2}$ against hv. Extrapolating the linear part of the graph to the abscissa yields the corresponding band gap**. Figure 3.9 and 3.10** show the plot of $(\alpha hv)^{1/2}$ on y-axis versus photon energy hv on the x-axis for the samples deposited in O_2+Ar and O_2+He atmosphere, respectively. From **figures 3.9 and 3.10**, E_g is found to be 5.37-5.43 eV for O_2+Ar and 5.38-5.58 eV for O_2+He case for nanocrystalline hafnium oxide films. It is observed that with increase in oxygen partial pressure, the oxygen concentration increases which lead to rise in band gap of the deposited films irrespective of the inert gas used. It is also observed that the band gap in helium case is higher in comparison to the argon case. This can be explained with the help of XRD pattern. The XRD pattern shows that the particle size is smaller in helium than that in argon and calculated bandgap values indicate the same [**204**].The absorption coefficient in O_2/He samples was found to be saturated. This may be probable due to absorption band [**11**].

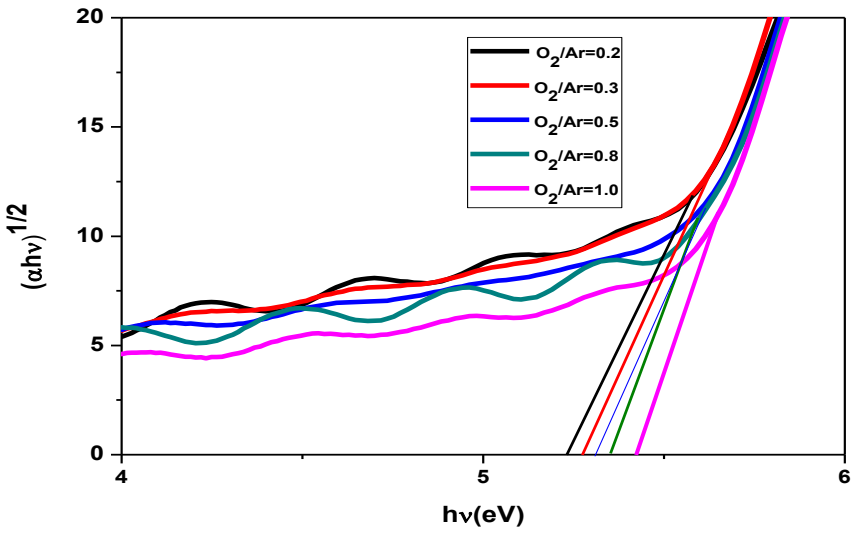

Figure 3.9 *Band gap of hafnium oxide films for different O_2/Ar gas ratio.*

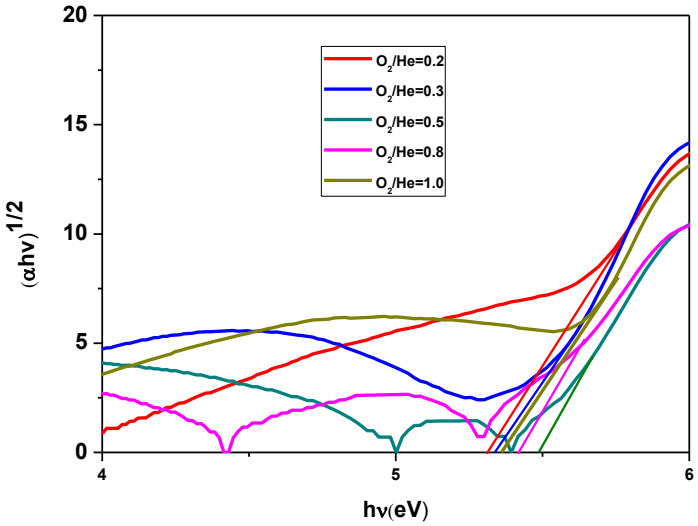

Figure 3.10 *Band gap of hafnium oxide films for different O_2/He gas ratio.*

The thickness of the deposited film was measured through surface profilometer. The same was calculated using the relation given below from the transmission data [**191**].

The thickness was also verified through SEM. **Figure 3.11** shows one such representative cross section image of hafnium oxide film. **Table 3.4** lists the thickness calculated/measured from the above mention methods. The thickness of the deposited samples calculated from above three methods is in close agreement with each other. It is also observed that the deposition rate is less in helium case in comparison to argon case. This can be explained on the basis of collisions theory [**143**]. The number of collisions during sputtering depends upon M_g/M_s ratio where M_g and M_s are mass of inert gas and sputter atom respectively. The sputtering rate increases with decrease in M_g/M_s ratio and vice versa. The mass of argon gas is approximately 10 times more than helium atom, so M_g/M_s ratio is

lower for helium as compared to argon. This leads to more efficient momentum transfer of sputtered atoms in argon atmosphere in comparison to the helium.

Table 3.4 *Thickness of the deposited films*

O_2/Inert Gas Ratio	Thickness (nm)					
	Argon case			Helium case		
	Surface profilometer	Optical Data	SEM cross section	Surface profilometer	Optical Data	SEM cross section
0.2	825	813	810	517	526	528
0.3	801	808	805	488	493	496
0.5	775	784	785	364	377	369
0.8	685	691	685	338	348	344
1.0	613	622	623	293	297	301

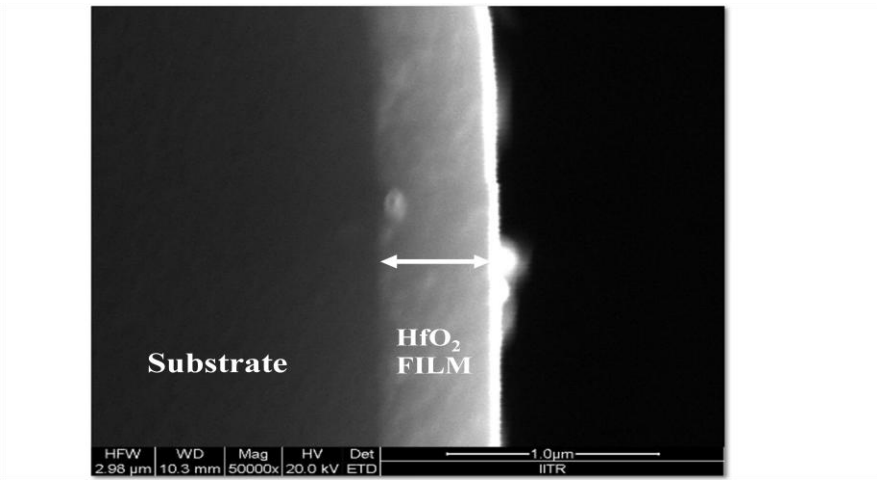

Figure 3.11 *Cross section SEM image of HfO_2 film*

3.2.2.5 Electrical property

Figure 3.12 shows the variation of electrical resistivity of the films deposited in Ar as well as He atmosphere. The resistivity of the films is of the order 10^4 Ω-cm and is higher in argon case in comparison to He. The resistivity was decreasing upto O_2/inert gas =0.5 and then starts increasing. This can be correlated with the particle size as small particle size provides more grain boundaries which in turn provides more impedance to the flow of electrons and thus, increases the resistivity of the film.

Figure 3. 13 shows the variation of the dielectric constant for films deposited in Ar and He atmosphere. The dielectric constant of the deposited HfO_2 was maximum (24.2) for film deposited at O_2/Ar=0.2 ratio while minimum (19.4) for the film deposited at O_2/He =1.0 ratio. The dereasing trend of the dielectric constant can be attributed to the thickness of the film. Natori et al reported the direct dependence of dielectric constant on the thickness of the film.

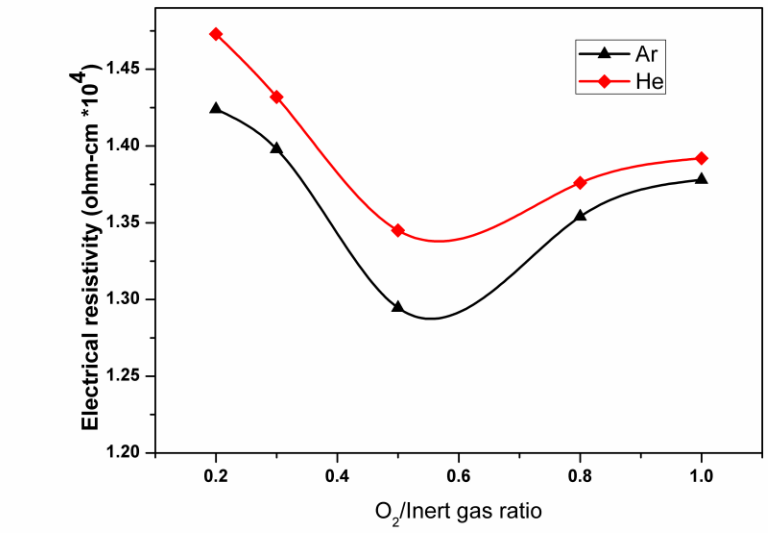

Figure 3.12 *Variation of resistivity for different O_2/inert gas ratio.*

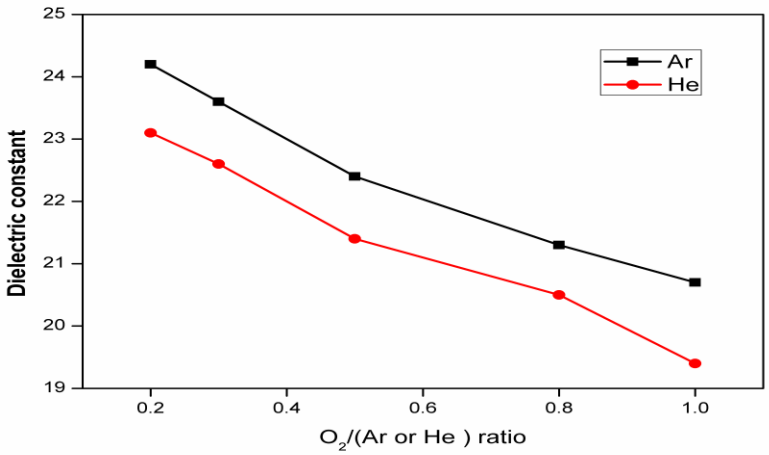

Figure 3.13 *Variation of dielectric constant for different O_2/inert gas ratio.*

3.2.3 Conclusions

In summary, we have successfully deposited HfO_2 film on glass insulator by DC sputtering in the presence of two inert gases namely; argon and helium. HfO_2 films are found to be hydrophobic in both the cases and the hydrophobicity is better in films deposited in argon atmosphere. In addition higher deposition rate, bigger particle size and better transparency are good features obtained in films deposited in argon atmosphere. Also, the best contact angle is obtained at O_2/Ar=0.5 ratio. The bandgap is also high at this ratio (5.32 eV) ensuring dielectric property of the films. The electrical resistivity was of the order 10^4 Ω-cm for all the deposited films ensuring the insulating nature of the film and was highest for film deposited at O_2/Ar=0.5. The dielectric constant was also high (22.9) at this ratio.

3.3 Effect of Sputtering pressure on Structural, Optical, Hydrophobic and electrical properties of DC sputtered Hafnium Oxide thin films

3.3.1 Experimental Detail

HfO_2 films were prepared by the DC reactive magnetron sputtering method in a custom designed chamber (Excel Instruments India). The purity of the Hf metal target is 99.9% with a diameter of 2 inch and 5-mm thick. Glass and quartz were used as substrates. The substrates were cleaned by rinsing in ultrasonic bath of acetone and dried with pure nitrogen gas. The substrates were mounted onto the substrate holder. The distance between the target and the substrate was 41 mm. Before deposition, the vacuum chamber was evacuated using a turbomolecular pump to 2 x10-6 mTorr. The turbomolecular pump is backed by a rotary pump. The sputtering gas Ar with a purity of 99.99% and the reactive gas O2 with a purity of 99.99% were introduced to the chamber separately .The flow of the gases was controlled and measured by the standard mass flow controllers (MKS) and capacitance manometers (MKS) respectively. The target was pre-sputtered for 10 min with Ar gas to remove the surface contamination of target. The deposition conditions are listed in **Table 3.5**.

Table 3.5 *Sputtering parameters for HfO_2 Films*

Deposition Conditions	
Base Pressure	$2*10^{-6}$ Torr
Working Pressure Range	5 mTorr - 25 mTorr
Ar gas flow	20 sccm
0_2 gas flow	10 sccm
Sputtering Power	50 W
Substrate Temperature	Room temperature
Substrate-target distance	41 mm

3.3.2 Results and Discussions

3.3.2.1 Structural Property

The XRD patterns of nanocrystalline HfO2 films at different sputtering pressures are shown in **figure 3.14**. The dominant peak was obtained at about 28°. It is attributed to diffraction from It(-111) planes of monoclinic phase of HfO_2 [**3**]. The other less dominant peaks are attributed to the orientation (011), (111), (020) and (220) of monoclinic phase of HfO_2. No diffraction peaks from tetragonal or cubic phase were obtained. The XRD patterns reveals that as the sputtering pressure increases from 5 mTorr to 25 mTorr, intensity of dominant peak (-111) increases which is a indicative of increase in the average crystallite

size and hence crystallity of the films. However as the pressure was increased from 15 mTorr to 25 mTorr, the intensity of (-111) peak decreases. The average crystallite size‘t’ was estimated from the well known Scherrer’s formula [29].

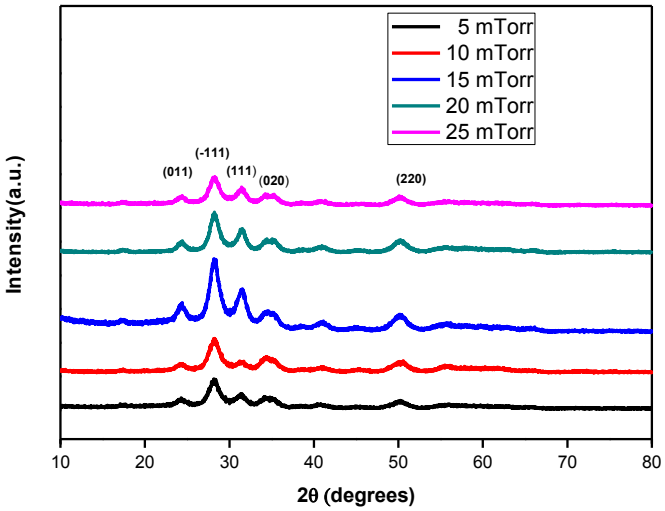

Figure 3.14 *XRD patterns of deposited Hafnium oxide at different Sputtering pressure.*

Figure 3.15 shows the variation of average crystallite size as the pressure is increased. The increment in the crystallite size with the increment of pressure upto 15 mTorr can be explained by the relationship of the mean free path with the molecular diameter of the sputtering gas as given by

$$d_m = 2.330 \times 10^{-20} T/(P\gamma 2) \qquad (3.2)$$

where dm is the mean free path, T is the temperature, P is the sputtering pressure and γ is the molecular diameter. According to the above equation, as the pressure is increased, the mean free path decreases so that the sputtered

atoms undergo a large number of collisions. As a consequence, the sputtered atoms have a higher probability of agglomeration which in turn increases the crystallite size before arriving at the substrate surface [30]. The average crystallite size decreases as the pressure is increased from 15 mTorr to 25 mTorr. This can be explained by the mobility of the crystallites. The mobility of the crystallites decreases with the increase of sputtering pressure. As the sputtering pressure is increased beyond 15 mTorr, the mean free path decreases and the energy of the sputtered particles arriving at the substrate surface reduces because of collisions with Ar ions. Thus, less energy is left for surface diffusion. This will result in the decrease of the surface mobility of the sputtered particles [**17**].

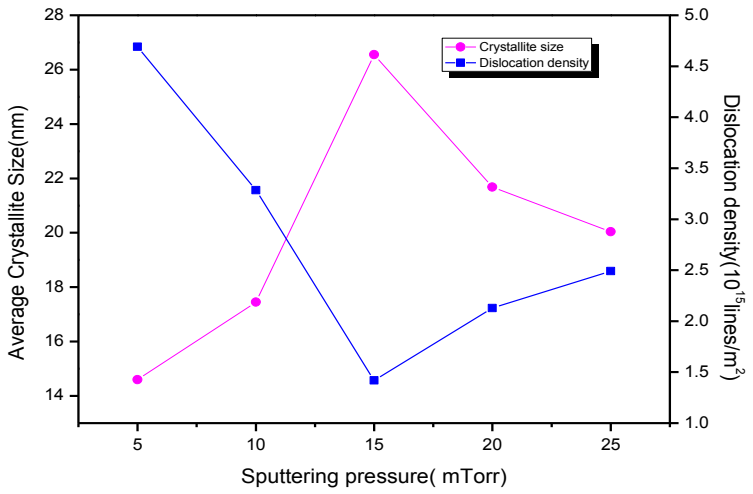

Figure 3.15 *Variation of average crystallite size and dislocation density as a function of sputtering pressure.*

The stoichiometry of crystalline films was measured by EDX. **Table 3.6** lists the at.% of hafnium and oxygen at different sputtering pressure. The O/Hf ratio is 2:1 for all the deposited samples.

Table 3.6 *Parameters of HfO_2 films at different presuure*

Sputtering Pressure (mTorr)	O (at.%)	Hf (at.%)	Avg. %Transmittance	Extinction Coefficient	Band Gap(eV)
5	67.34	32.66	95	0.28	5.24
10	67.76	32.24	93	0.33	5.27
15	66.66	33.37	90	0.41	5.32
20	67.01	32.99	93	0.37	5.31
25	67.15	32.85	94	0.35	5.28

3.3.2.2 Morphological Property

The AFM micrographs of the films deposited at different sputtering pressure is shown in **figure 3.16**. The scan area of each micrograph was 2μm x 2μm. It can be seen from the AFM micrographs that the HfO_2 films have similar morphologies. They are all constituted with round particles approximately coalesced. However, the size of these particles was not same when the sputtering pressure was varied. The surface roughness was determined for the thin films from the AFM images by the instrument's data analysis software.

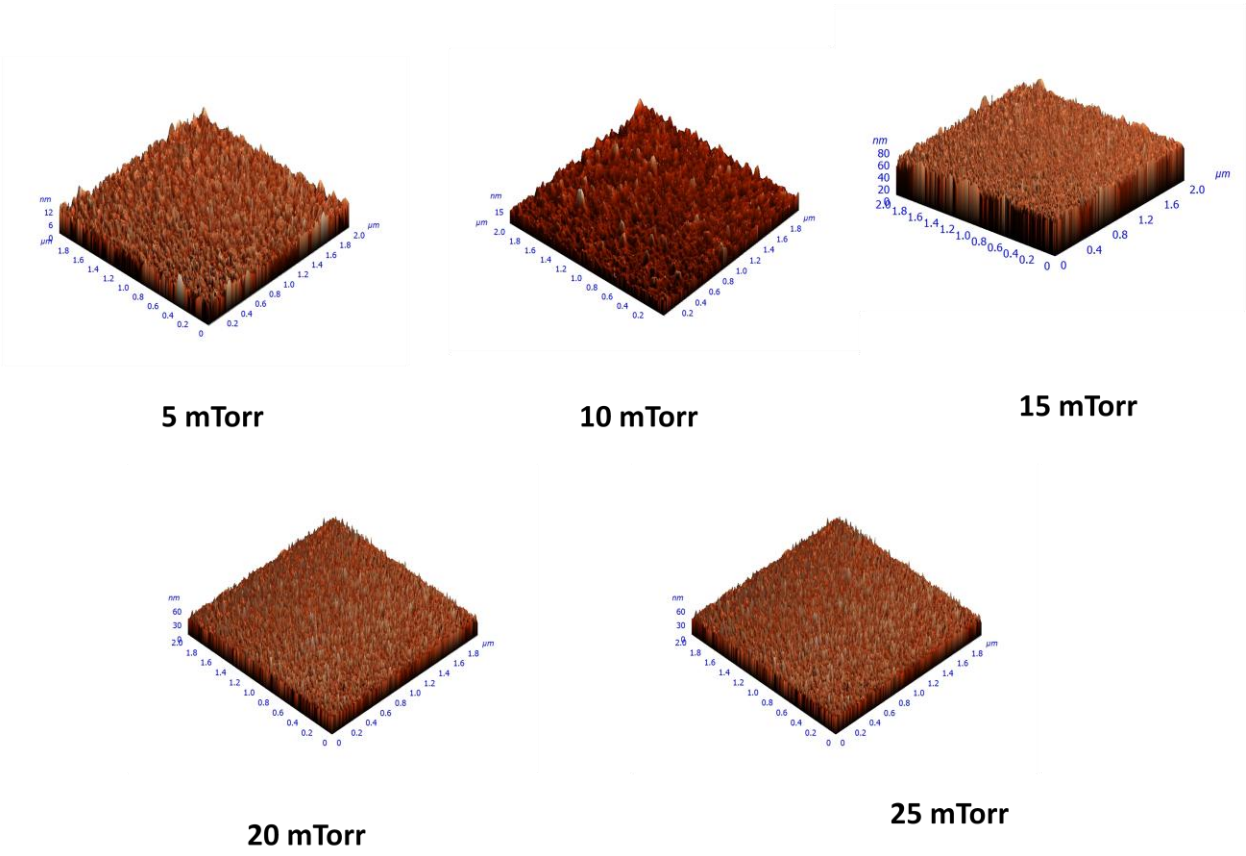

Figure 3.16 *3-D AFM micrographs of HfO_2 films at different pressure.*

Table 3.7 *Optical Parameters of HfO_2 films*

Sputtering Pressure (mTorr)	O (at.%)	Hf (at.%)	Avg. %Transmittance	Extinction Coefficient	Band Gap(eV)
5	67.34	32.66	95	0.28	5.24
10	67.76	32.24	93	0.33	5.27
15	66.66	33.37	90	0.41	5.32
20	67.01	32.99	93	0.37	5.31
25	67.15	32.85	94	0.35	5.28

The rms surface roughness was measured at five different locations of each HfO_2 film. **Figure 3.17** shows the variation of rms surface roughness with sputtering pressure. The roughness increases as the pressure is increased from 5 mTorr to 15 mTorr and then its starts decreasing upto 25 mTorr. The maximum value of surface roughness is obtained at 15 mTorr of sputtering pressure. This can be explained by the crystallite size. As pressure was increased from 5 mTorr to 15 mTorr, crystallite size increases, hence roughness increases. A further increase in pressure upto 25 mTorr decreases the crystallite size which in turn reduces the roughness of the films [**140**].

3.3.2.3 Hydrophobicity

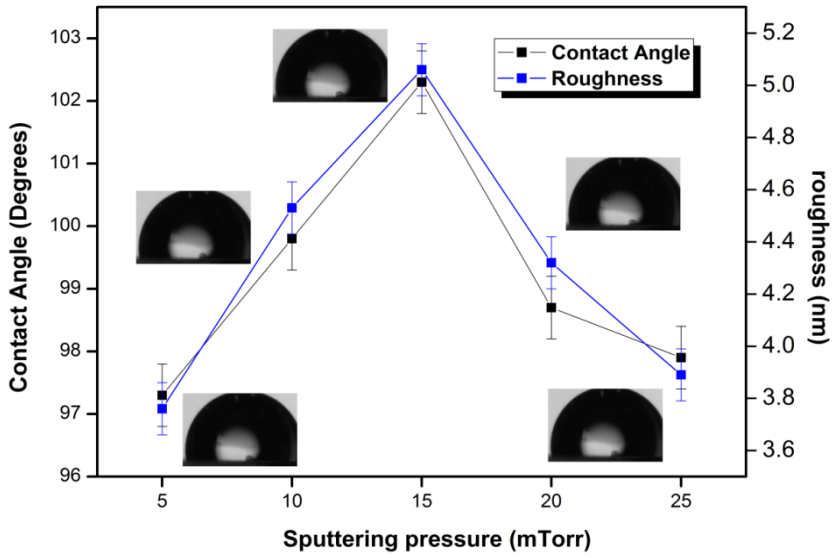

Figure 3.17 *Variation of contact angle and roughness as a function of sputtering pressure.*

Hydrophobicity of the films was determined by water contact angle measurement on freshly prepared thin films. Sessile drop method was used to measure contact angle. The contact angles reported in this work were the average values of ten readings taken on each sample obtained with drop of 3µl size. **Figure 3.17** also shows the variation of contact angle with sputtering pressure. All the samples of HfO_2 are found to be hydrophobic. The contact angle (hydrophobicity) increases as sputtering pressure was increased from 5mTorr and reached a maximum value of 102.3° at 15 mTorr. A further increment in pressure from 15 mTorr has resulted in decrement in the contact

angle and hence hydrophobicity. The hydrophobicity follows the same trend as roughness. The influence of roughness on contact angle (hydrophobicity) has been explained by Cassie and Baxter [**16**]. Their assumption was that the liquid may not fill the surface cavities creating air pockets, which results in solid–air–liquid interfaces. Consequently, the increase in roughness in those cases enhances the hydrophobicity of the surface. Wenzel has also related the surface roughness with contact angle. According to Wenzel's equation, after enhancing the roughness of a solid surface, a hydrophilic surface ($\theta < 90°$) becomes more hydrophilic ($\theta w < 90°$) and a hydrophobic surface ($\theta > 90°$) becomes more hydrophobic ($\theta w > 90°$).

3.3.2.4 Optical Property

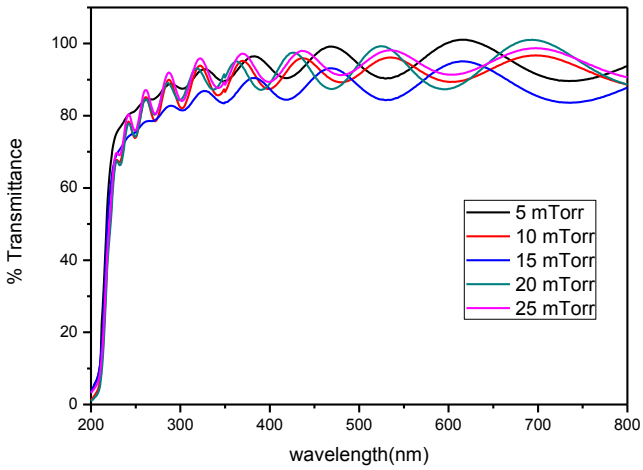

Figure 3.18 *Optical transmission curve of hafnium oxide films deposited at different sputtering pressure.*

The transmittance spectrum for all the samples deposited on glass substrates were recorded as a function of wavelength and were shown in **figure 3.18**. The

oscillations in the spectrum with wavelength are due to interference effect. The average transmission of each sample is shown in **table 3.7**. It is observed that the average transmission was decreasing as the sputtering pressure was increased from 5 mTorr to 15 mTorr while the level of average transmission increases beyond 15 mTorr pressure. Hydrophobicity and transparency have inverse relationship. Enhancement in the surface roughness will increase the hydrophobicity but on other end it will introduce the sources of light scattering. Consequently, transparency of the deposited films will decrease. However, the change in roughness in the deposited films is very small (~ 1nm) that roughness cannot be an alone factor for the large change (5%) in the transparency. There may be other factor like extinction coefficient for this change. The average transmission in each sample was above 90%. Thus, the deposited films are not only hydrophobic but transparent also.

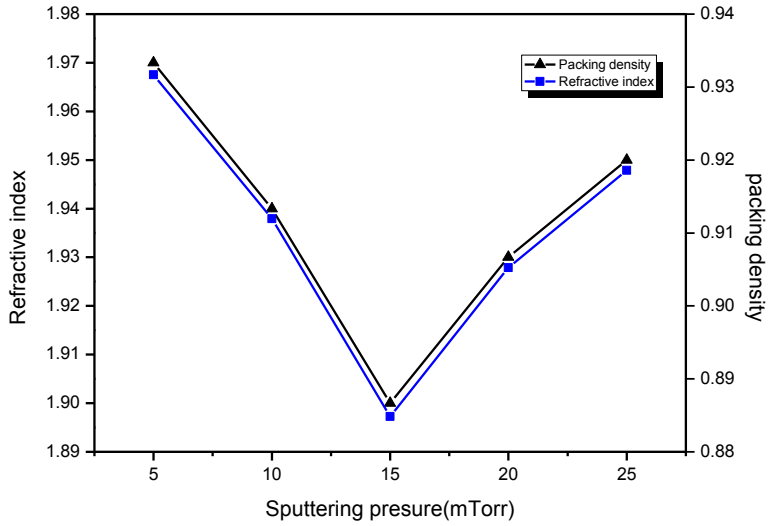

Figure 3.19 *Refractive index and packing density of HfO_2 films deposited at different sputtering pressure.*

The refractive index of the deposited films was evaluated by transmission data using envelope method [191].

Figure 3.19 shows the variation of refractive index of films deposited at different sputtering pressure at a wavelength of 550 nm. The refractive index of the films lies in the range 1.90-1.97 [**117**] which is close to the bulk value [**124**].The refractive index decreases as pressure is increased from 5 mTorr to 15 mTorr and then its starts increasing beyond 15 mTorr of sputtering pressure. The change in refractive index of HfO2 coating with sputtering pressure may be attributed due to change in transparency of the deposited film which was dependent on roughness of the films as already discussed above [**39**].

Assuming the bulk value of refractive index of HfO2 as 2.1 [**4**] at 550 nm and using the calculated refractive index of the HfO2 films, the variation of packing density with sputtering pressure is shown in **figure 3.19**. The packing density of the HfO_2 films was maximum when sputtering pressure was 5 mTorr. This shows the formation of a closely packed structure.

The thickness of the film was measured by surface profilometer. The transmission data was also used to calculate thickness (d) of the deposited films.

The thickness was also verified through SEM cross section image. **Table 3.8** lists the thickness of the deposited films by above mentioned methods. The thickness of the each film measured /calculated by different method are in close agreement with each other, irrespective of the method used. The thickness of HfO_2 films increases as sputtering pressure was varied from 5 mTorr to 15 mTorr and then starts decreasing beyond 15 mTorr. The reason may be attributed to the packing density. Less packing density may lead to loose packing structure which in turn increases the thickness of the film with the same amount particles condensing on the substrate. The packing density at 15 mTorr sputtering was 0.88 which was minimum. Consequently maximum thickness of 865 nm was obtained for HfO_2 coating at 15 mTorr pressure.

Table 3.8 *Thickness of HfO_2 by different methods*

Sputtering pressure (mTorr)	Thickness of HfO_2 films(nm)		
	Surface profilometer	SEM Cross Section	Optical data
5	722	727	725
10	748	755	752
15	775	785	784
20	750	757	754
25	746	741	742

Optical absorption coefficient (α) was calculated as a function of the wavelength in the range of 200-800nm. Extinction coefficient (k) of the HfO_2 films deposited at different pressure was calculated . The calculated value of extinction coefficient at λ=550 nm was shown in **table 3.7**. The value of k was initially increasing upto 15 mTorr and then declines beyond this pressure. It is the extinction coefficient which is largely responsible for increase or decrease in the transparency of the films. The scattering of grains is the main contributory factor in determining the extinction coefficient of the deposited films. Large grain size leads to enhancement of scattering effect which in turn decreases the transparency of films [**39**]. As the pressure varies from 5 mTorr to 15 mTorr, the value of k increases from 0.28 to 0.41 due to increase in grain size which in turn decreases average transparency from 95% to 90%. Beyond 15 mTorr of sputtering pressure, the value of k decreases due to reduction in grain size which results into increment of transparency from 90% to 94%.

The optical band gap (Eg) of nanocrystalline hafnium oxide film was determined from the absorption coefficient (α) using the Tauc relation [**77**].

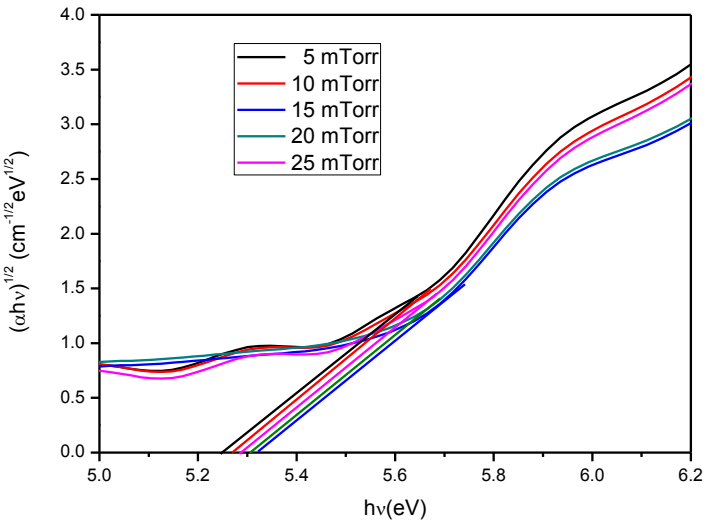

Figure 3.20 *Optical band gap of HfO_2 film at various sputtering pressure.*

The parameter n has a value 2 for an indirect band gap and ½ for direct band gap. The literature has widely stated that HfO_2 is an indirect bad gap dielectric material having n=2. The factor B is the probability parameter for transition and can be assumed to be constant within optical frequency range. **Figure 3.20** shows the plot of (αhν)1/2 on the y axis versus photon energy hν on the x-axis for the samples deposited by varying sputtering pressure. The band gap was evaluated by extrapolating the straight line part of the curves $(\alpha h\nu)^{1/2}$. The calculated values of the band gap at different sputtering pressure are shown in table 3.7. The band gap of HfO_2 film lies in the range of 5.24-5.32 eV which is

near to its bulk value [**11**]. Thus, maintaining the insulating property in the deposited films. The maximum value of band gap was 5.32 eV obtained at a sputtering pressure of 15 mTorr. The band gap of HfO2 films slightly increases as sputtering pressure was increased from 5 mTorr to 15 mTorr and decreases to small amount as pressure is further increased beyond 15 mTorr. The reason may be attributed to crystallite size. The bandgap follows the same trend as the crystallite size. This small variation in band gap may be due to the effect of lattice expansion [**9**]. The quantum effect is absent in this case [**13**].

3.3.2.5 Electrical Property

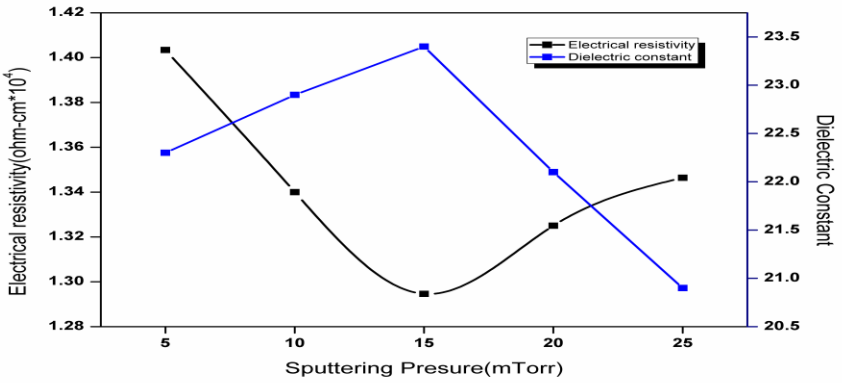

Figure 3.21 *Variation of electrical resistivity and dielectric constant with sputtering pressure.*

The electrical resistivity of deposited HfO_2 samples was measured at room temperature. **Figure 3.21** shows variation of resistivity with sputtering pressure. The resistivity decreases with increasing size and vice versa. Resistivity is

reported to increase with grain size reduction due to increasing grain boundary volume and associated impedance to the flow of charge carriers. The electrical resistivity is also dependent on the parameters like vacancies, dislocations and strain present in nanocrystalline materials [**199**]. Crystallite size reduction increases the effect of above mentioned parameters which in turn increases the resistivity of the films. The high value of electrical resistivity also ensures the insulating property of the HfO_2 films. **Figure 3.21** also shows the variation of dielectric constant as a function of sputtering pressure. The dielectric constant of the deposited films exhibits a increasing trend upto 15 mTorr and then follows a decreasing trend. The maximum value of dielectric constant was 23.2 at 15 mTorr and minimum (19.2) at 25 mTorr.

3.3.3 Conclusions

Nanocrystalline HfO_2 films were fabricated on glass insulator at different sputtering pressure and their geometrical, optical, hydrophobic and electrical properties were investigated. Highly oriented monoclinic structure along the (-111) direction was found at a sputtering pressure of 15 mTorr. Crystal defects were also found to be minimum in this film. The contact angle(102.3^o), band gap (5.32 eV) and film thickness was also found to be maximum at 15 mTorr of sputtering pressure However, there is slight decrease in transparency and refractive index at this sputtering pressure which can be neglected in respect of

higher hydrophobicity. The resistivity and the dielectric constant of the hydrophobic film was also high at 15 mTorr pressure. Thus, 15 mTorr of sputtering pressure can be treated as an optimum pressure for synthesizing dielectric hydrophobic coating for outdoor insulators. The results also provide a functional relationship between geometrical, electrical and hydrophobic properties of hafnium oxide films with respect to sputtering pressure.

3.4 Effect of Power on Structural, Optical, Hydrophobic and Electrical properties of DC sputtered Hafnium Oxide thin films

3.4.1 Experimental Detail

The HfO_2 films were deposited by DC-magnetron sputtering on glass, quartz and ITO glass substrates in a custom designed 12-in. diameter chamber (Excel Instruments, India) at room temperature. The HfO_2 coated quartz substrates were used for calculating the bandgap of the films as their transparency range extends down to 200 nm and covers the absorption edge of HfO_2. A 2-in. diameter and 5-mm thick hafnium target of 99.99% purity was used for the sputtering. The substrates were thoroughly cleaned by rinsing in an ultrasonic baths of acetone and methanol and dried under nitrogen gas. The chamber was initially evacuated by a turbo molecular pump backed by a rotary pump. During each deposition, the base pressure was better than 2×10^{-6} Torr and the distance between the substrate and the target was kept 41 mm. The

sputtering was carried out in an argon (99.999 % pure) atmosphere while oxygen was used as a reactive gas. The flow rate of oxygen and argon in the chamber was 10 sccm and 20 sccm respectively. The gas pressure was kept 15 mTorr for all depositions. The HfO_2 coating was fabricated by sputtering parameter namely power. The sputtering power was varied from 30 to 60 W keeping deposition time 1hr. Before starting the actual experiment, the target was pre-sputtered for 15 min with a shutter located in between the target and the substrate. This shutter was used to control the deposition time.

3.4.2 Results and Discussion

3.4.2.1 Structural Analysis

X-ray diffraction analysis was carried out to determine the preferred orientations and structural transformation of HfO_2 films on glass substrate at different sputtering power. **Figure 3.22** shows the XRD pattern of the nanocrystalline films of hafnium oxide deposited at varying DC power. The XRD curve clearly reveals that all deposited films are polycrystalline in nature and the dominant peak occurs at $2\theta \approx 28^0$ which corresponds to (-111) orientation of monoclinic phase of HfO_2 [**4**]. The other less dominant peak belongs to (011), (111), (020), (-211), (220) and (122) orientation. Moreover, the diffraction peaks in the XRD patterns become more intense and sharper as

the DC power was increased from 30 W to 50W, indicating an enhanced crystallinity for the films deposited at high DC power. However, if the power is further increased to 60 W, the crystallinity of the film decreases.

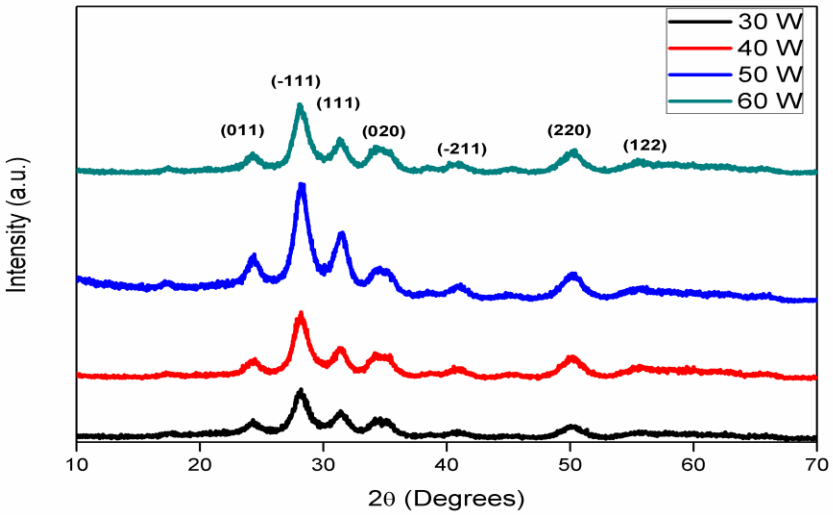

Figure 3.22 *XRD patterns of HfO_2 films deposited at different sputtering power.*

The average crystallite size of the thin film was calculated using the Debye-Scherrer formula [**30**]. **Figure 3.23** shows the variation of crystallite size with sputtering power. The crystallite size lies in the range of 15 - 27 nm. The crystallite size increases with increase in power upto 50 W and then diminishes for 60 W power. The enhancement in the crystallinity and crystal size of hafnium oxide films can be associated with the change of the kinetic energy of the sputtered particles with the DC power. As the sputtering power increases,

the kinetic energy of the sputtered particles also increases. Thus, the sputtered particles have sufficient energy to migrate on the substrate and hence results in the higher growth of the crystallite size. Therefore, the crystallinity is improved. However, the excessive supply of DC power over than 50 W may cause a degradation of the preferred orientation and limits the growth of crystallity of deposited film. This results into less intense dominant peak and also reduction in crystallite size [**101-199**].

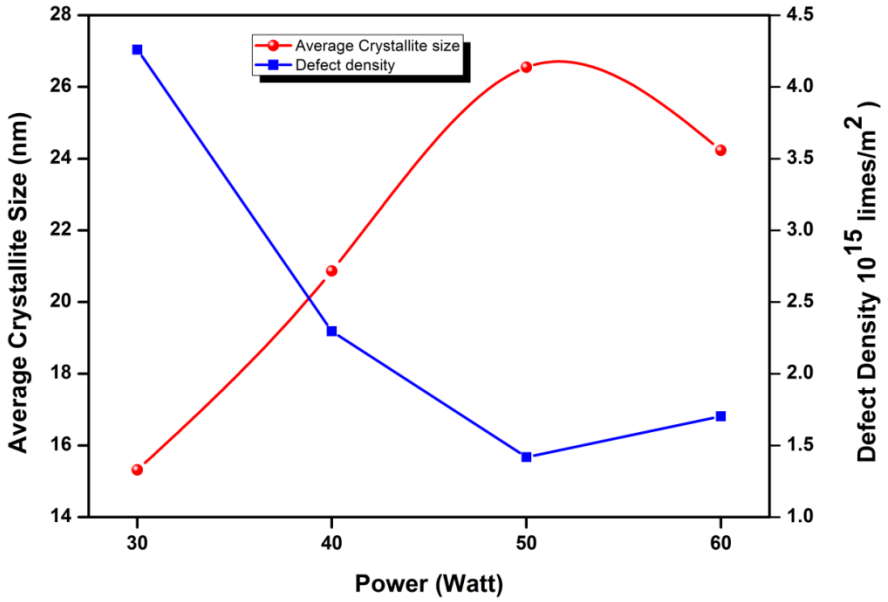

Figure 3.23 *Average crystallite size and defect density of HfO_2 films as a function of sputtering power.*

The dislocation density (δ) which is an indicative of number of crystal defects in a thin film was calculated using the following relation [**127**]

$$\delta = \frac{1}{t^2} \ lines/m^2 \qquad (3.3)$$

Dislocation density as a function of sputtering power is shown in **figure 3.23**. It is clear from the figure that minimum amount of defects (1.41 x 10^{15} lines/m^2) are present in the HfO_2 film deposited at 50 W sputtering power. The residual strain (σ) in the deposited samples is calculated using equation [**137**]

$$\sigma = \frac{E_y\,(d - d_0)}{\tau\, d_0} \qquad (3.4)$$

where E_y is the young modulus of the film, d is the crystallite plane spacing of the films, d_o is the standard plane space from X-Ray diffraction files and τ is the poison ratio. E_y=220 GPa and τ=0.3 [**170**] for HfO_2 films. The residual stress was calculated for the dominant peak having orientation (-1, 1, 1) plane of the monoclinic phase. All the values obtained are negative which indicates a compressive stress in the films. **Figure 3.24** shows the variation of residual stress of the films with sputtering power. A decrement in the residual stress of the films is observed up to 50 W sputtering power and then a slight increment at 60 W power. This behaviour can be attributed to the dislocation and grain boundaries which are dependent on crystallite size. Films with large crystallite size have low residual stress. This is because films with large crystallite size have less dislocation and grain boundaries which ultimately results into low residual stress [**48**].

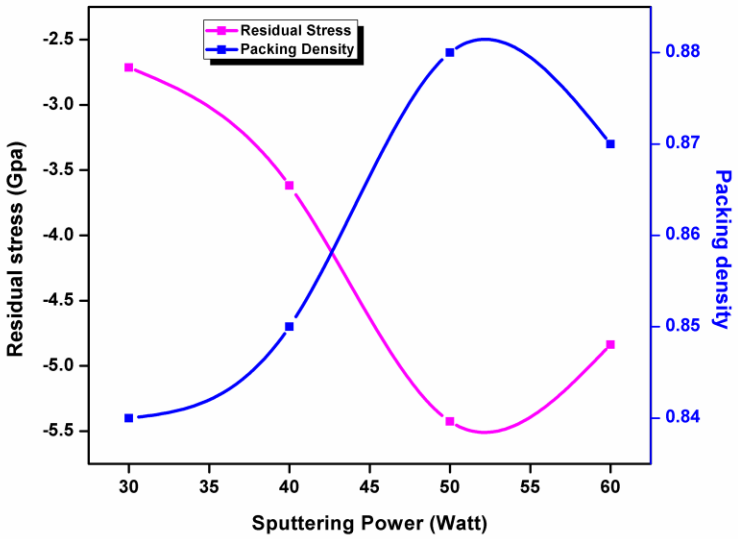

Figure 3.24 *Variation of residual stress of deposited hafnium oxide films with DC sputtering power.*

3.4.2.2 Surface morphology and chemical composition

The surface morphology of the HfO_2 films was studied using AFM. The three dimensional AFM images obtained for HfO_2 films deposited at various DC power at 15mTorr pressure are shown in **figure 3.25**. The AFM micrographs corresponds to a scan area of 2μm x 2μm.It can be seen that the hafnium oxide films have same morphologies. They all are constituted with a large number of nanoscale asperities. Each asperity consists of surface nanograins that are used to form a surface peak. However the size and

roughness of these varies with sputtering power. Table I lists rms roughness of HfO_2 samples at different sputtering power. It is clear that as sputtering power is increased from 30 to 50 W, roughness value also increases from 3.52 nm to 5.06 nm and then it decline to 4.80 nm with further increment of power. This behaviour of roughness may be correlated to the particle size which was earlier calculated through XRD. The increment in power upto 50 W increases the particle size which in turn enhances the roughness while decrement in particle size beyond 50 W power reduces the roughness.

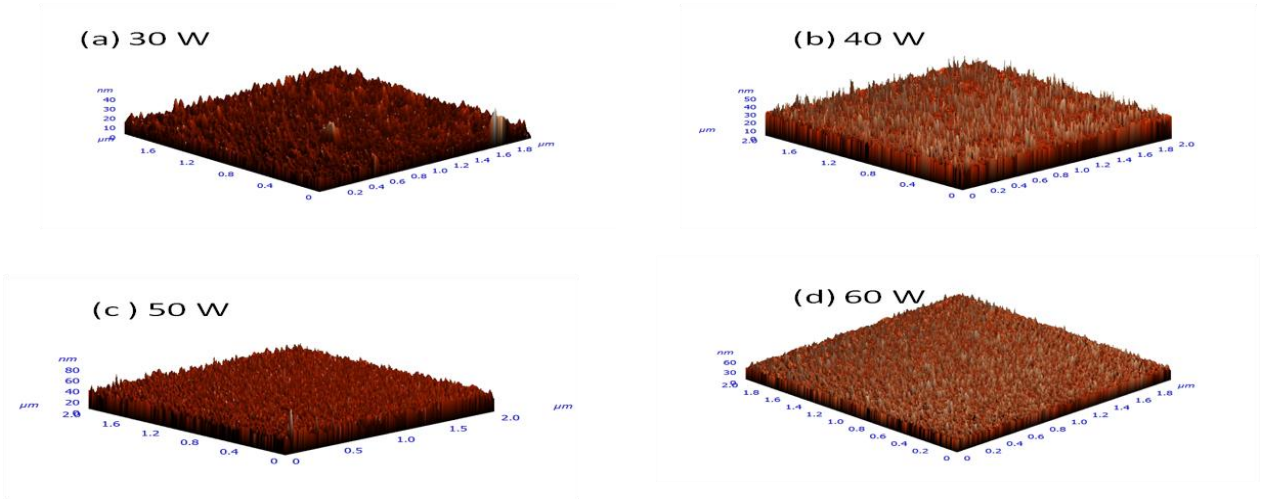

Figure 3.25 *AFM micrographs of film deposited at different sputtering power.*

Table 3.9 *Roughness and EDS data of deposited HfO_2 samples at different sputtering power.*

Sputtering power (Watt)	Roughness (nm)	at% Hf	at% O
30	**3.52**	**37.45**	**62.55**
40	**4.52**	**35.37**	**64.63**
50	**5.08**	**33.23**	**66.77**
60	**4.80**	**32.88**	**67.12**

The chemical composition analysis was done through EDS. **Table 3.9** shows the at% of hafnium and oxygen as sputtering power is varied from 30 to 60 W. The O/Hf ratio is approximately two for film deposited at 50 and 60 W power while for all other deposited samples, it is less than two. The O/Hf ratio less than two is clearly indicative that hafnium was not fully oxidized for the samples deposited at sputtering power other than 50 and 60 W. This can be associated with the fact that the increased kinetic energy due to increment in DC power enhanced the activity of the sputtered particles and thus, facilitated the formation of the Hf-O bond. Therefore, the oxidation of Hf atoms is increased and the oxygen vacancy in the thin films is decreased with increasing DC power.

3.4.2.3 Optical properties

The sputtering power also influences the optical properties of the deposited films. The optical property was investigated to examine the transmission coefficient of the glass after post deposition. High transmission

coefficient reveal less absorption of light and hence, less degradation of material as these insulators are installed in open atmosphere. The refractive index of the film was calculated to ascertain the packing density of the film which will play an important role in achieving hydrophobic property. To investigate the degree of transparency of the DC sputtered HfO_2 coatings, measurements of optical transmission was carried out using UV-Nis-NIR spectrophotometer. **Figure 3.26** shows the optical spectra of HfO_2 films deposited at different sputtering power in the wavelength range 200-800 nm.

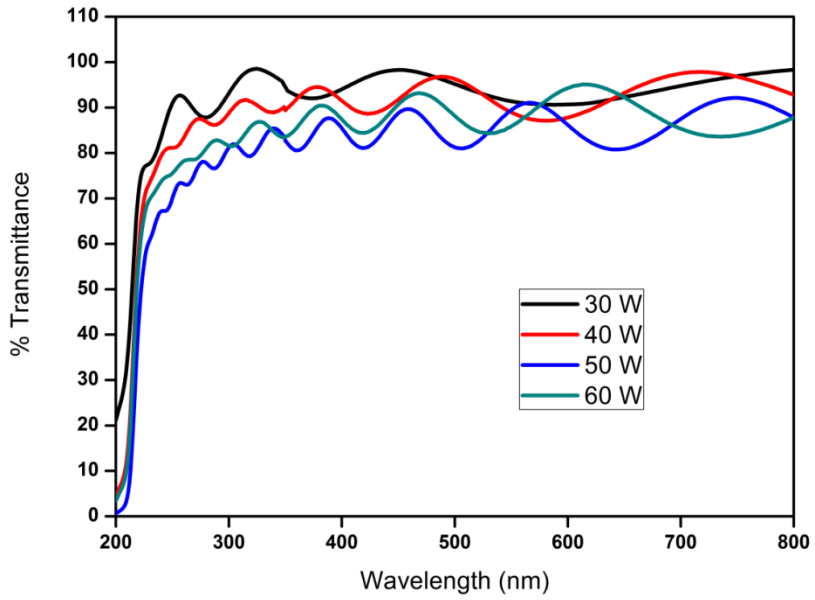

Figure 3.26 Transmission spectrum of HfO_2 samples deposited at different DC power.

Two important features are evident. Firstly, the transparency decreases as the power increases and secondly, the average transmission for all the samples was found out to be greater than 80% in the visible region. Maximum transparency was observed for film developed at 30 W power. The decrease in the transmission as the power is increased was due to enhancement of the surface roughness. Surface roughness and transparency have inverse relationship. Providing surface roughness to the coatings means introducing sources of light scattering which in turn decreases the transparency of the films. The transmission data was used to obtain the refractive index of the film using relation provided by Manifacier [**121**]. The refractive index of the deposited samples calculated at λ=550 nm is shown in **table 3.10.**

Table 3.10 *Optical parameters of HfO_2 films.*

DC power (Watt)	Refractive index (at 550 nm wavelength)	Extinction coefficient	Bandgap (eV)
30	**1.85**	**0.014**	**5.34**
40	**1.87**	**0.035**	**5.43**
50	**1.92**	**0.048**	**5.53**
60	**1.90**	**0.032**	**5.46**

The refractive index obtained is consistent with that reported for sputtered HfO_2 films [**37**]. Also the refractive index values of hafnium oxide films grown under the sputter powers of 30 and 40W are too much lower than that of bulk value of HfO_2 .However the refractive index for 50 W is very close

to that of bulk hafnium oxide [**81**]. Beyond 50-W power, refractive index decreases. This can be ascribed to the fact that the sputtered particles at 50 W power have higher kinetic energy which results into high packing density and hence higher refractive index

Assuming the bulk value of refractive index of HfO_2 as 2.1 [81] at 550 nm and using the calculated refractive index of the HfO_2 films, the variation of packing density with sputtering power is shown in **figure 3.24**. The packing density of the HfO_2 films is maximum (0.88) when sputtering power was 50 W. This shows the formation of a closely packed structure of HfO_2 film on glass substrate. Also, the packing density shows a linear relationship with the residual stress. Higher residual stress leads to more compact structure which in turn enhances the packing density of the film. Higher packing density also provides a favourable platform for the deposited film in achieving hydrophobicity. A loose structured film (low packing density) will increase the wettability of the film.

The thickness of the deposited film was calculated using the transmission data [**167**]. The same was measured through surface profilometer. The thickness was also verified through SEM cross section image. **Figure 3.27** show one such representative cross section image of hafnium oxide film deposited at 50 W. **Table 3.11** lists the thickness calculated/measured from the above mention

methods. The thickness of the deposited samples calculated from above three methods is in close agreement with each other. The deposition rate (thickness/time of deposition) of the films was calculated and was found in the range of 8.76 nm/min to 13.06 nm/min. The maximum deposition rate was reported for 50 W DC power.

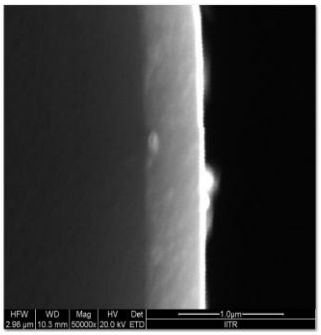

Figure 3.27 *Typical cross section SEM image of HfO_2 film over glass substrate to calculate thickness.*

Table 3.11 Thickness of film by different methods

Sputtering DC Power (Watt)	**Thickness (nm)**		
	Surface profilometer	**Optical Transmission Data**	**SEM cross section**
30	**425**	**415**	**422**
40	**530**	**525**	**528**
50	**600**	**591**	**585**
60	**558**	**565**	**562**

Based on the transmission spectra, the measured transmittance T is converted into absorption coefficient (α) using the following relationship [**97**]

$$\boldsymbol{\alpha = -\frac{1}{c}\, ln \frac{(n-1)(n-n_1)\left\{\frac{T_{max}}{T_{min}}+1\right\}^{0.5}}{(n+1)(n+n_1)\left\{\frac{T_{max}}{T_{min}}-1\right\}^{0.5}}} \qquad (\mathbf{3.5})$$

where *c* is the thickness of the film. The extinction coefficient (*k*) of the film was calculated at a wavelength of 550 nm using equation (3.6) and listed in **table 3.10**.

$$\boldsymbol{k = \frac{\alpha\lambda}{4\pi}} \qquad (\mathbf{3.6})$$

The extinction coefficient is increasing upto 50 W power and then declines for 60W power. The extinction coefficient verifies the decreasing or increasing trend of transparency of HfO_2 coated glass with power.

The bandgap of the film was also calculated in order to ascertain whether HfO_2 film in nanostructured form retains its dielectric property or not. The band gap of the nanocrystalline HfO_2 films was estimated from the absorption coefficient (α) using Tauc relation.

Here the indirect band gap [**155**] of the HfO_2 coatings was evaluated by extrapolating the linear part of the curves $(\alpha h\nu)^{1/2}$ and $h\nu=0$ as shown in **figure**

3.28. The calculated value of band gap at different sputtering power is shown in **table 3.10**. The

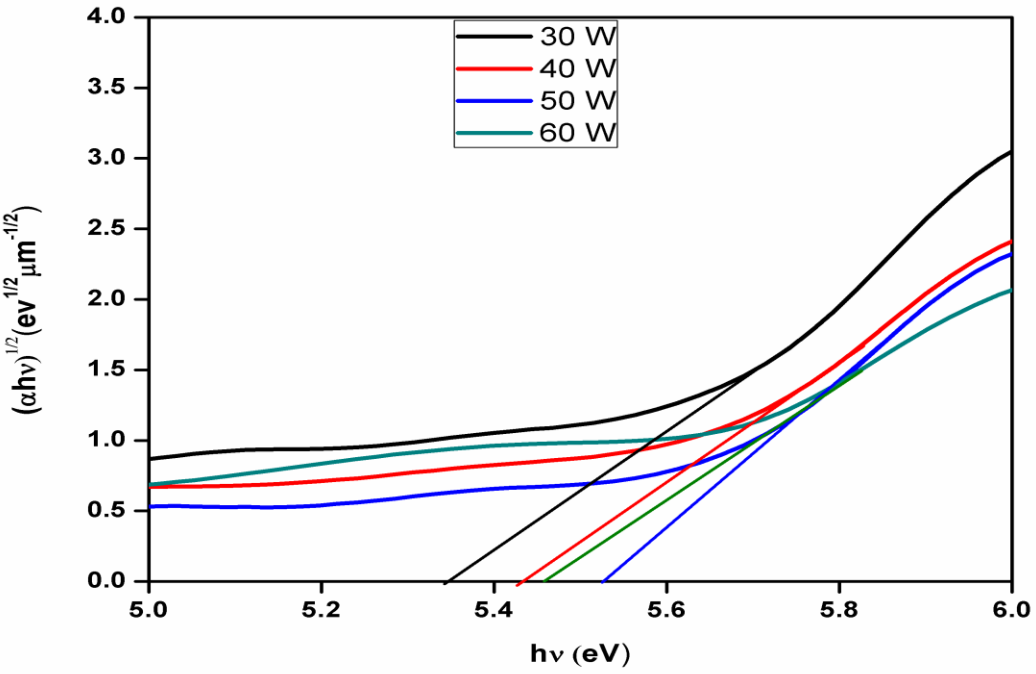

Figure 3.28 *Bandgap determination of hafnium oxide films at different sputtering power.*

band gap energy is in the range of 5.34-5.53 eV. The band gap value of all the films is close to the bulk value [**6**] as well as to the theoretically calculated value [**196**] for the poly crystalline HfO_2 films. The variation of E_g as a function of sputtering power is shown in **table 3.10** and is found to be linear. It is observed that the changes in E_g are insignificant and were linearly increasing with the crystallite size. This reveals that quantum confinement effects are absent and small changes in bandgap may be due to lattice expansion [**187**].

3.4.2.4 Hydrophobic property

The wettability of HfO_2 coatings were evaluated by measuring the water contact angle using sessile drop method at ambient temperature. The distilled deionised water droplets (about 3 µl) were dropped on the deposited coating surfaces using a microsyringe. The average value of the water contact angle was determined by experimental drop profiles at five different positions for the same sample. The variation of water contact angle and rms roughness of HfO_2 films as a function of sputtering power is shown in **figure 3.29**. All the deposited samples were found to be hydrophobic and the contact angle lies in the range 98.23°-102.3°. The contact angle and surface roughness bears a linear relationship, thus satisfying the Wenzel model. The maximum contact angle (102.3°) occurs at a sputtering power of 50 W where roughness is also high (5.08 nm).

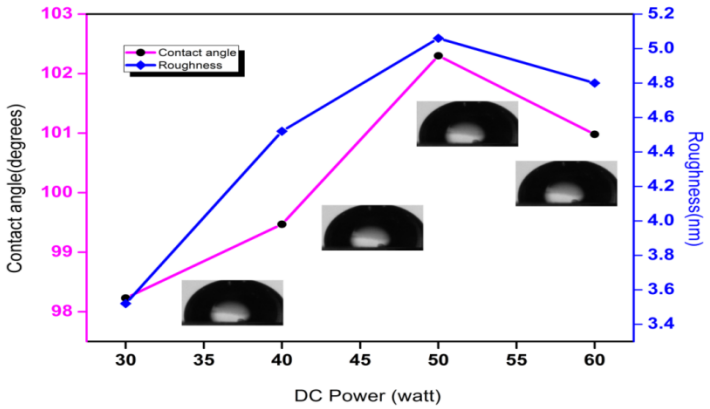

Figure 3.29 *Contact angle and roughness of deposited HfO_2 films as a function of power.*

3.4.2.5. Electrical properties

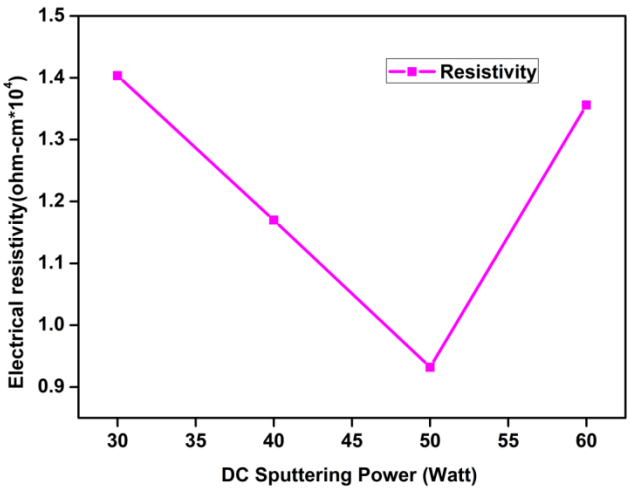

Figure 3.30 *DC power effect on electrical resistivity of hafnium oxide films.*

Figure 3.30 shows the variation of resistivity of deposited HfO_2 films with sputtering power .The resistivity is of order of 10^4 and in the range of 0.93-1.40 x 10^4 Ω-cm. The resistivity was following a decreasing trend as DC power is increased from 30 W to 50 W and then again it increases beyond 50 W power. The resistivity of a material is dependent on factors like vacancies, dislocations, lattice strain and distortions which are common in nanocrystalline materials. These imperfections act as hurdle to the motion of charge carries and hence, increases the resistivity. Resistivity is also dependent on crystallite size. It is reported to increase with grain size reduction due to the increasing grain boundary volume [**82**]. The observed resistivity is showing an indifferent trend towards EDS data. The at.% of oxygen reveals that the resistivity of the film

should increase with power due to decrease in oxygen vacancy. Hence, it can be concluded that the observed trend of resistivity may be due to dominant effect of dislocation density and lattice strain. Moreover, the resistivity behaviour with sputtering power was also favoured by extinction coefficient data and crystallite size calculated from XRD data.

The dielectric constant of the film was calculated by forming a stack of ITO/HfO_2/Ag. The top electrode of Ag was fabricated using shadow mask through sputtering. **Figure 3.31** shows the plot of dielectric constant of HfO_2 film as a function of frequency in the range of 48.5-52.5 Hz. This low frequency range is selected because an outdoor insulator operates in this zone only. It is clear from the figure that the dielectric constant of deposited sample at a particular sputtering power practically remains constant within the prescribed frequency range. However, dielectric constant shows an increasing trend upto 50 W power. It attains a maximum value of ~23 at 50 W power which is very close to the bulk value [14]. Further increment in power i.e. at 60 W power, a slight reduction in dielectric constant was observed. This behaviour of dielectric constant with increasing power for HfO_2 can be readily correlated to the thickness of the films. Natori et al. theoretically concluded that as thickness decreases, dielectric constant also decreases [**132**]. Hwang et al. also showed through experiments that the dielectric properties of high dielectric thin

films are critically dependent upon the film thickness [**74**]. The inset picture in **figure 3.31**shows the variation of thickness with DC power.

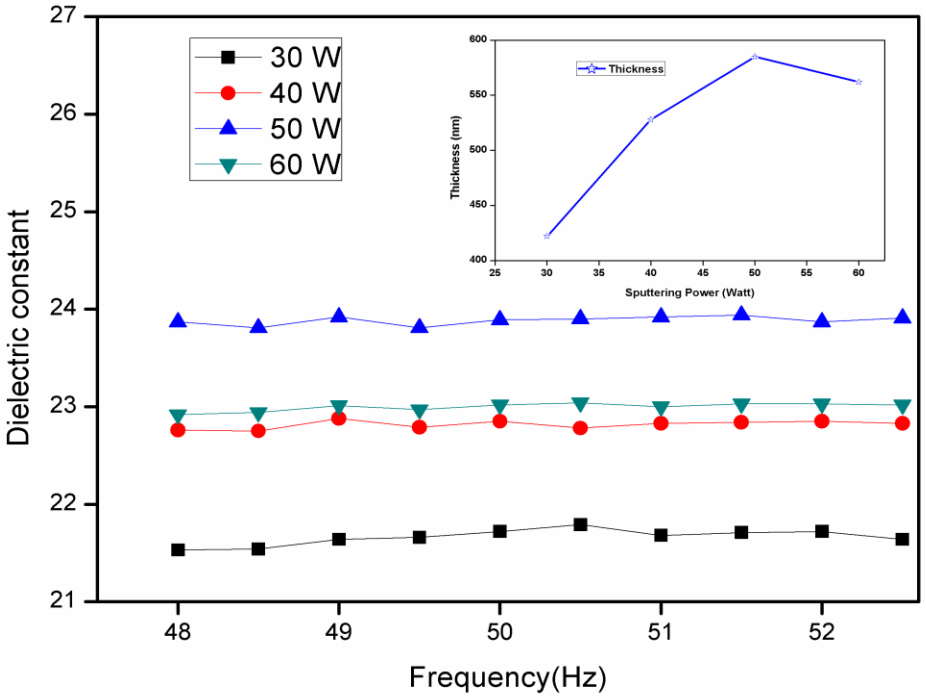

Figure 3.31 *Sputter power effect on dielectric constant of HfO_2*

The dielectric constant is maximum (ε_{max} =23.12) for 585 nm thick film which is also highest thickness among deposited samples.

3.4.3 Conclusions

The nanostructured hafnium oxide films were developed on glass insulator at different DC sputtering power. The microstructural characterization shows

that all the samples were polycrystalline in nature with adequate surface roughness to have hydrophobicity and good transparency (> 80%).The deposited hydrophobic films also have high texture coefficient for (-111) orientation of monoclinic phase of HfO_2. The contact angle (102.3^o), refractive index (1.92), bandgap (5.53 eV), dielectric constant (~23) and deposition rate (9.75 nm/min) are maximum for the film deposited at 50 W power. However, the electrical resistivity was found to be less for 50 W power but change in resistivity is very less that it can be neglected for all practical purpose. The high bandgap values ensures that HfO_2 in film form still retain the dielectric property. High dielectric constant of the deposited film gives an indication that film can bear high electric field applied to outdoor insulators. Thus, parameters of hydrophobic HfO_2 film deposited at 50 W power found to be optimum for the glass insulator.

3.5 Effect of substrate temperature on Structural, Optical, Hydrophobic and electrical properties of DC sputtered Hafnium Oxide thin films

3.5.1 EXPERIMENT

Hafnium oxide thin films were deposited on glass and quartz substrates by DC magnetron sputtering in a 12 inch diameter chamber(Excel Instruments, India) using a 99.99% pure hafnium target (2 in. diameter and 5-mm thick).The substrates were initially cleaned thoroughly in an ultrasonic bath with the

mixture of trichloroethylene and distilled water. They are dried under nitrogen gas. The chamber was evacuated by a turbo pump which is backed up by a rotary pump. The base pressure was kept $2x10^{-6}$ Torr. Thereafter, high purity (99.9%) oxygen along with inert gas (Ar) was passed into the chamber. The flow of oxygen and argon was kept 10 sccm and 20 sccm respectively. The ratio of the gas mixture was controlled using mass flow controller while pressure was measured using capacitance manometer. The gas pressure was kept at 15 mTorr for all depositions. The gas pressure was kept constant for every deposition since sputtering current is highly sensitive to sputtering gas pressure. The sputtering was carried for a period of one hour at different substrate temperature. The substrate temperatures were room temperature, 100 ^{o}C, 200 ^{o}C, 300 ^{o}C and 400 ^{o}C. The power was kept 50W. The target to substrate distance was 41mm. All the parameters were kept constant during each deposition process except deposition temperature.

3.5.2 Results and Conclusions

3.5.2.1 Structural Property

The XRD patterns of HfO_2 deposited at various deposition temperatures are shown in **figure 3.32**. In all deposited samples, the emergence of broad hump at $2\theta = 28^0$ indicates the existence of (-111) plane of the monoclinic HfO_2 structure

which is the most common HfO_2 phase [**4**]. However as the substrate temperature is increased from room to 400^{o}C, the intensity of the dominant peak increases. Thus, crystallinity of the film increases as the deposition temperature is increased. The average crystallite size, d of the samples was calculated using the Scherrer formula. **Figure 3.33** shows the variation of crystallite size with temperature. The crystallite size increases as the deposition temperature increases.

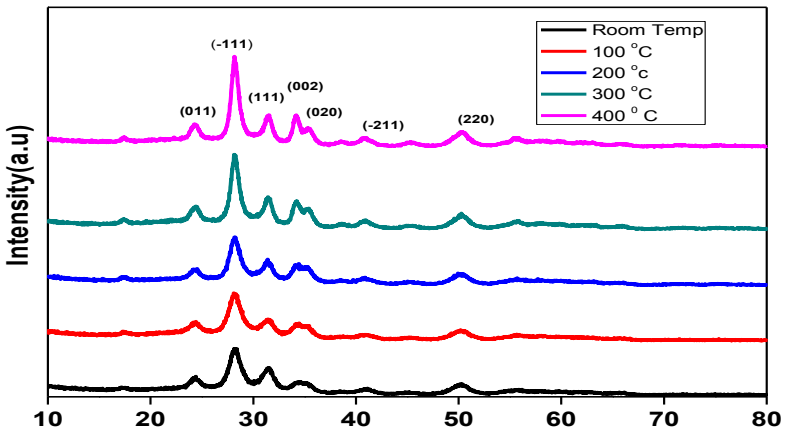

Figure 3.32 *XRD patterns of hafnium oxide at different temperature*

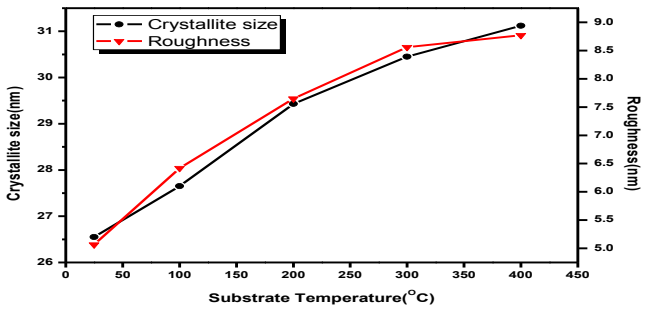

Figure 3.33 *Crystallite size and roughness of HfO_2 films as a function of temperature*

3.5.2.2 Morphological Property

The surface topography of the films was studied by AFM. The AFM micrographs obtained for HfO_2 film with scan area of 2μm x 2μm are shown in **figure 3.34**. It can be seen on the AFM micrographs that the HfO_2 films have similar morphologies. They are all constituted with nodules approximately coalesced. However, the size of these nodules is not same when the deposition temperature varies. The surface roughness was measured using the software attached with the AFM. **Figure 3.33** also shows the variation of roughness with the substrate temperature. The roughness lies in the range of 5-9 nm. It is observed that as deposition temperature increase, the surface roughness increases. This may be due to the fact that as the substrate temperature increases, films get more crystallized and thus, grains grew larger which in turn enhances the roughness [**118-119**].

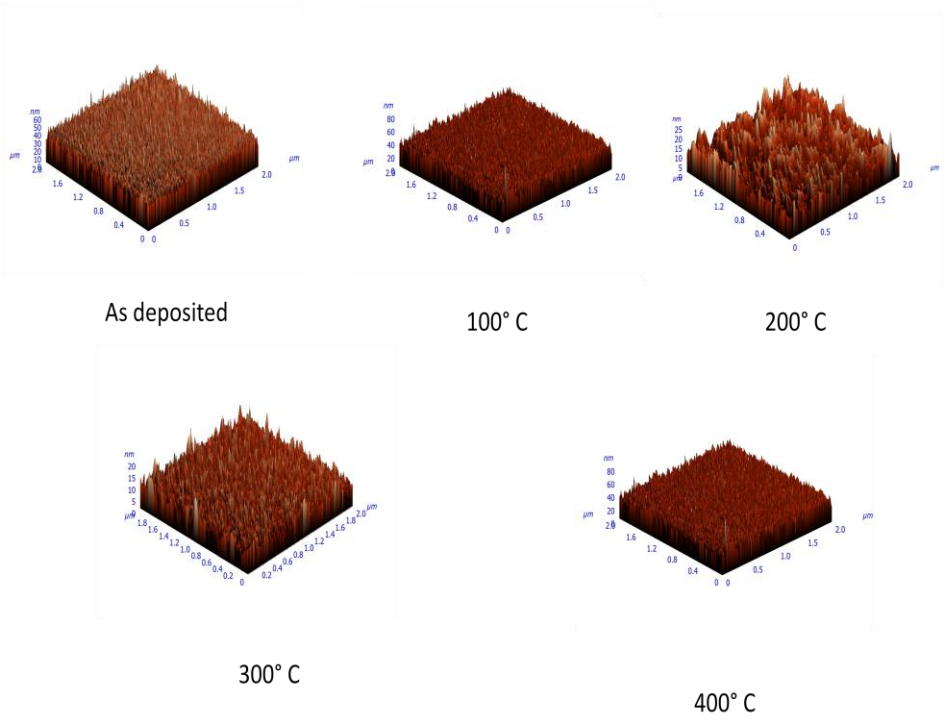

Figure 3.34 *AFM images of HfO_2 films at different substrate temperature*

3.5.2.3 Optical Property

The spectral variations of transmission for the HfO_2 films deposited onto glass substrate at various deposition temperatures were measured over the wavelength range 300-800 nm and are shown in **figure 3.35.** The films deposited at room temperature, 100ºC, 200ºC, 300ºC, 400ºC have an average transmittance value upto 96%, 94%, 91%, 88% and 85% respectively, in the visible range. It is clear from the graph that as deposition temperature increases, transmission decreases. As described above, the films become rougher as the deposition temperature increases. This result in more scattered light and hence

less transmittance. The refractive index of the film was estimated from the transmission spectrum by following formula [**122**].

The calculated refractive index at different deposition temperature at 600 nm wavelength is shown in **table 3.12**. It is clear that as deposition temperature increases, refractive index increases.

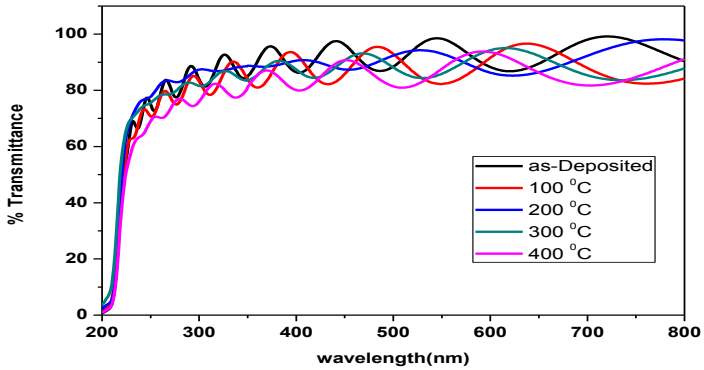

Figure 3.35 *Transmission spectra of HfO_2 as a function of temperature*

The calculated thickness and the measured thickness (through surface profilometer) of the HfO_2 films are shown in **table 3.12**. Both results are in close agreement with each other. It is also observed from the table that thickness was not much influenced by the substrate temperature. This suggests that the deposition depends solely on the number of sputtered atoms which subsequently reach the substrate. The other effects such as local pressure reduction in the sputtering plasma, variation in the sticking coefficients of

hafnium or oxygen and re-sputtering from the substrate are negligible. The bandgap was also calculated using Tauc relation and shown in **table 3.12**. It is evident that the band gap is decreasing which may be probably due to increase in the crystallite size [**150**].

TABLE 3.12 *Calculated parameters for HfO_2 films*

Sample No.	Temperature (^{O}C)	Refractive index	Thickness by %T data (nm)	Thickness By surface profiler (nm)	Bandgap (eV)
1	As Deposited	1.92	784	775	5.53
2	100	1.96	778	772	5.44
3	200	1.98	774	768	5.32
4	300	2.01	771	767	5.20
5	400	2.02	769	765	5.07

3.5.2.4 Hydrophobicity

Figure 3.36 shows the variation of water contact with deposition temperature. The contact angle increases as the deposition temperature increases. As temperature increase, surface roughness increases and hence hydrophobicity increases.

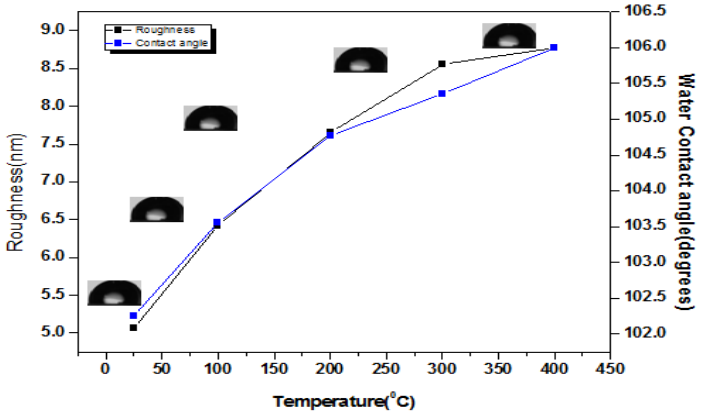

Figure 3.36 *Variation of contact angle and roughness with substrate temperature*

3.5.2.5 Electrical property

Figure 3.37 shows the variation of resistivity and dielectric constant as a function of substrate temperature. The resistivity as well as dielectric constant both were decreasing as the temperature was increased [**92, 159**]. The decrement in the resistivity may be due to higher packing density with temperature while decrement in dielectric constant was due to decrement in the thickness of the film.

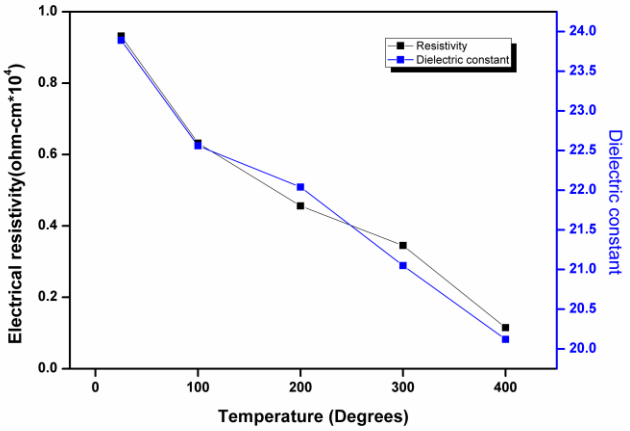

Figure 3.37 *Variation of resistivity and dielectric constant with temperature*

3.5.3 CONCLUSIONS

Hydrophobic thin film of HfO_2 was successfully deposited on glass insulator. It is observed that with the increase in the substrate temperature, the hydrophobicity increases. The increase in the hydrophobicity with temperature was attributed to the increment in surface roughness. However there is decrease in transmittance, resistivity, band gap and dielectric constant as deposition temperature was enhanced. Results of the XRD reveal that crystallinity increases with increase in temperature. Hence, higher temperature cannot be considered as a optimum temperature as it will lead to more leakage current which is undesirable for insulators. Hence, as deposited films are considered as the optimum films from temperature point of view.

3.6 Breakdown Test

Breakdown test was carried out on both uncoated and optimally coated glass insulators at power frequency i.e. 50Hz. The breakdown strength of coated glass was found out to be 23 kV/mm which was higher in comparison to that of uncoated glass i.e. 20 kV/mm.

4.1 Introduction

In the previous chapters, we have already discussed about the hydrophobic behavior of hafnium oxide. However, HfO_2 is a poor barrier to oxygen diffusion at higher temperature. This results in higher leakage current and thus, poses a question on the reliability issue. Incorporation techniques have been widely used to resolve this problem by doping elements like Al, N, Er and Ti [**64, 67**]. Venkataraj et al. reported the improvement in the electrical properties of HfO_2 by incorporating nitrogen in it [**179**]. He et al. [**65**] obtained enhancement in the dielectric constant of HfO_2 by doping nitrogen in it. The foregoing study clearly reveals that hafnium oxynitride can be competitive candidate against HfO_2 for protecting the outdoor insulators from contamination.

The metal oxynitride like zirconium oxynitride (ZrO_xN_y) and chromium oxynitride (CrO_xN_y) has been explored for wettability and found to be hydrophobic [**153**]. However, literature is not available on water repellent property of hafnium oxynitride. Hence, it we are investigating the wettability property of hafnium oxynitride film.

A large number of studies reported various deposition methods to fabricate hafnium oxynitride (HfO_xN_y) thin films, such as ion beam-assisted deposition [**185**], plasma assisted chemical vapour deposition [**103**], metal organic chemical vapour deposition [**24**] and reactive magnetron sputtering (DC, RF) [**179, 174**]. Each deposition technique is unique and has its own advantages and disadvantages. In this study, HfO_xN_y thin films were deposited by DC magnetron sputtering on glass substrates without a post-annealing treatment. DC magnetron sputtering has same outstanding characteristics like contamination free deposition, high deposition rate, reproducibility and high density of the deposited layer [**108**]. The structural, hydrophobic, optical and electrical properties of HfO_xN_y films were investigated with respect to deposition temperature to combat the contamination problem of outdoor insulators.

Various research group has studied the different properties of HfO_xN_y by varying different sputtering parameters. Liu et al. has synthesized HfO_xN_y by directly using HfO_2 as a target material in the presence of N_2/Ar atmosphere [**110**]. The thermal and micro structural characteristics for the HfO_xN_y were investigated by annealing in the temperature range 800-1000 °C. It was reported that the HfO_xN_y remain in the amorphous state upto 800 °C annealing temperature. However, after annealing, HfO_xN_y can effectively suppress oxygen

diffusion. A slight increase in the surface roughness was also obtained after annealing. Optical properties like refractive index was also reported by the same group which was lying in the range 2.4-2.6. Park et al. have reported significant reduction in leakage current density and superior thermal and electrical stability for hafnium oxynitride films [**145**]. It is clear from the above discussion that the structural, optical and other properties of hafnium oxynitride are influenced by the sputtering parameters like pressure, temperature, power etc. Hence, a study was carried out to find out the optimum parameters for the synthesis of hafnium oxynitride using different sputtering parameters.

4.2 Effect of Sputtering gas on Structural, Optical, Hydrophobic and electrical properties of DC sputtered Hafnium Oxynitride thin films

4.2.1 Experimental Detail

Hafnium oxynitride nanocrystalline thin films were deposited on glass and quartz substrates by DC magnetron sputtering in a custom designed 12 inch diameter chamber (Excel Instruments, India) using a 99.99% pure hafnium target (2" dia and 5 mm thickness). The substrates were cleaned by rinsing in ultrasonic baths of acetone and dried under nitrogen gas. The chamber was evacuated by a turbo molecular pump. It was backed up by a rotary pump. The base pressure was below 2.66×10^{-4} Pa. Thereafter, high purity (99.9%) oxygen

and nitrogen along with inert gas (He and Ar) were bled into the chamber. The flow of nitrogen and inert gas was kept constant 20 sccm and 20 sccm, respectively while the flow of oxygen was varied in such a way to obtain 2.5%, 5%, 7.5%, 10% and 15% partial pressure. The ratio of the gas mixture was controlled and measured using mass flow controller and capacitance manometers (MKS), respectively. The gas pressure was kept at 2 Pa for all depositions. During each sputtering experiment, the gas pressure was carefully monitored and kept constant since the sputtering current is extremely sensitive to the pressure of the sputtering gas. The sputtering was carried for a period of one hour at room temperature. The sputtering was done at 50W power. The target to substrate distance was kept constant at 41mm. Other than the sputtering gas, all parameters were constant during the set of experiments.

4.2.2 Results and Discussion

4.2.2.1 Structural Property

X-ray diffraction (XRD) analysis was carried out to determine the preferred orientations and structural transformations with varying oxygen partial pressure in argon as well as in helium atmosphere. **Figure 4.1** shows the XRD pattern of

nanocrystalline hafnium oxynitride thin films deposited in Ar atmosphere at different oxygen partial pressure. The XRD pattern reveals the (104) and (1013) orientations that correspond to rhombohedral HfN [JCPDS-00-023-1096] and the (011), (-111), (111) and (-211) orientations of monoclinic HfO_2, simultaneously [**109**]. The dominant peak corresponds to (-111) phase of HfO_2. The intensity of the dominant peak increases as the oxygen partial pressure is increased from 2.5% to 10%. Further, the intensity remained constant.

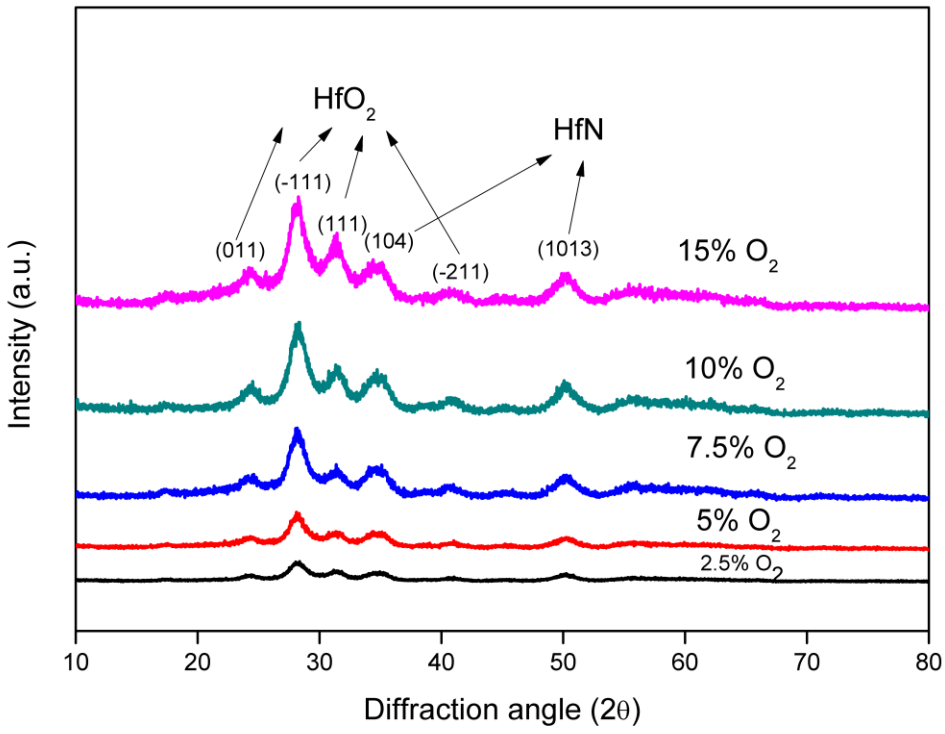

Figure 4.1 *XRD pattern of Hafnium oxynitride films deposited in Ar atmosphere.*

Table 4.1 lists the average crystallite size. The crystallite size of the deposited samples lie in the range 10.34-15.66 nm and increases up to 10% oxygen partial pressure and then remain constant, thus justifying the intensity behaviour of XRD pattern. **Figure 4.2** shows the XRD pattern of HfO_xN_y thin film deposited in helium atmosphere. The pattern reveals only (-111) orientation of HfO_2. No peak of Hf-N

Table 4.1 *Crystallite and particle variation with O_2 partial pressure*

O_2 Partial Pressure (%)	**Crystallite Size (XRD) (nm)**		**Particle size (AFM) (nm)**	
	Ar	**He**	**Ar**	**He**
2.5	10.34	7.56	13.35	8.33
5	12.34	8.34	14.98	9.95
7.5	14.69	9.44	17.26	11.23
10	15.65	11.32	20.23	13.95
15	15.66	11.44	20.56	13.89

was seen indicating that the volume fraction of HfN is too low to provide a visible peak in the XRD pattern of the deposited films [**103**]. Also, the peak intensity of dominating phase increases with oxygen partial pressure upto 10.0% and then practically remains constant. **Table 4.1** also lists the average crystallite size of the thin film deposited in the He atmosphere. The size of the crystallites lie in the range 7.56- 11.44 nm and were smaller than that deposited in Ar atmosphere.

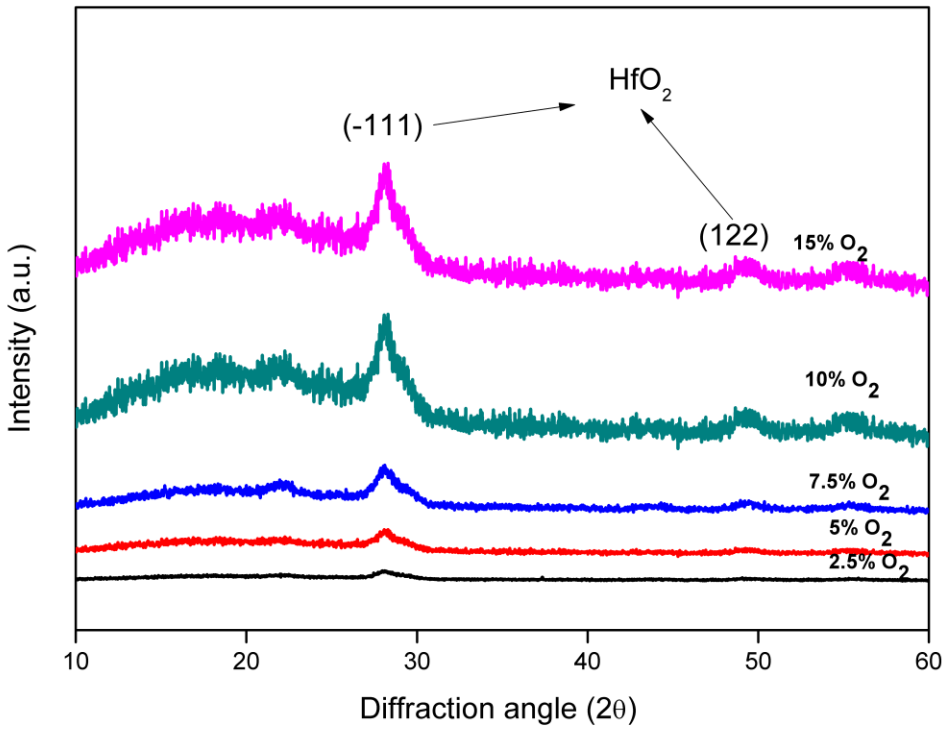

Figure 4.2 *XRD pattern of Hafnium oxynitride films deposited in He atmosphere.*

It is clear that the nature of the sputtering gas strongly influences the film structural properties. This can be explained through mean free path theory as well as Penning ionization principle. The mean free path of the gas atoms decreases as the size of the gas atoms increases. This in turn increases the collision frequency which leads to agglomeration and growth of particle before arriving at the substrate. Hence, we can expect an increase in the crystallite size with increase in atomic mass of sputtering gas [**174**]. The process of Penning ionization that occurs in plasma, in which some particles in the ground state, such as O_2 are ionized by transfer of the energy from the rare gas atoms in neutral excited metastable states. The first ionization potential of He gas (24.58

eV) is much higher than the first ionization potential of O_2 (13.6 eV), hence, it could easily ionize the oxygen atoms [**108**]. However, Ar (15.75 eV) could not ionize oxygen easily through penning ionization process because difference between their ionization potential is very small. Hence, the formation of hafnium oxide in helium atmosphere occurs easily due to enhancement of the reaction metals atoms with oxygen through the Penning ionization process.

Table 4.2 *Thickness and elemental analysis of hafnium oxynitride films.*

O_2 Partial Pressure (%)	Thickness (nm)				Elemental Analysis (at.%)					
	Surface profilometer (± 10 nm)		Optical data		Ar			He		
	Ar	He	Ar	He	Hf	O	N	Hf	O	N
2.5	785	515	776	501	34.01	53.65	12.34	34.77	61.67	3.56
5	678	487	665	474	34.67	54.88	10.45	34.89	61.9	3.21
7.5	603	422	594	410	34.78	56.88	8.34	34.55	62.58	2.87
10	589	397	545	387	34.81	59.63	5.56	34.63	63.03	2.34
15	589	397	545	387	34.82	59.64	5.54	34.62	63.06	2.32

The thickness of the deposited films was measured by surface profilometer and shown in **Table 4.2**. The deposition rate (thickness/time) was evaluated and was higher for argon case (~13 nm/min) in comparison to He (~ 9 nm/min). However, the growth rate is decreasing in both cases. This variation can be explained by taking into consideration the target poisoning effect by both reactive gases. With the increasing oxygen fraction, the oxide layer formation gains importance which in turn poison the target making it more difficult for material ejection to occur [**145**]. An increase in the deposition rate was observed by Venkataraj et al. [**179**] with the increase in the nitrogen flow for zirconium oxynitride films but we have increased the oxygen content which in turn has reduced nitrogen content, ultimately leads to decreased deposition rate.

4.2.2.2 Composition Analysis

The elemental analysis of the deposited HfO_xN_y film was done through EPMA. **Table 4.2** lists the at.% of the hafnium oxynitride films deposited in Ar and He atmosphere. It is evident from the table that the nitrogen content was continuously decreasing in both cases as the oxygen partial pressure was increased. The probable reason may be the higher reactivity of oxygen in comparison to the nitrogen [**103**]. It is also observed that the nitrogen content was very less in helium deposited film, thus confirming the previous assumption of presence of nitrogen in low volume fraction.

4.2.2.3 Morphological property

The effect of O_2 partial pressure on the morphology of the HfO_xN_y was studied by AFM images. **Figure 4.3 and 4.4** shows the 3-D AFM micrographs of hafnium oxynitride films deposited at different O_2 partial pressure in Ar and He atmosphere, respectively. It can be observed that the microstructure of all deposited films was characterized by high density columnar structure. The surface consists of many asperities and valleys [**114**]. The average particle size of each sample was estimated using the software attached to the AFM and compared with the XRD results as

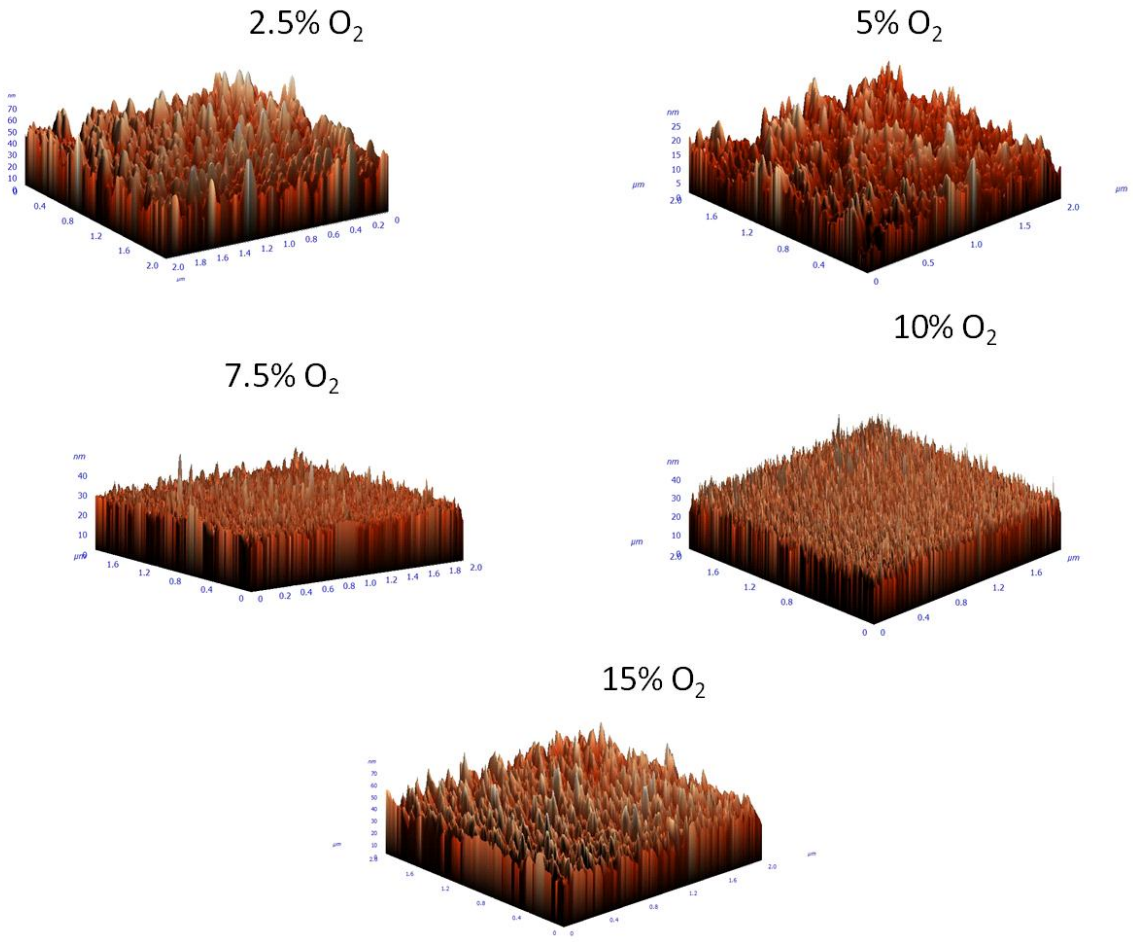

Figure 4.3 *AFM micrographs of HfO_xN_y films grown in Ar environment.*

shown in **Table 4.1**. It is seen that the average particle size measured by AFM is larger than that calculated by XRD. This ambiguity can be ascribed to the fact that AFM measurements result from agglomeration of the particles whereas XRD gives an average crystallite size [**30**]. Roughness of a thin film plays an important role in describing some of its properties like optical, mechanical and wettability. The root mean square (rms) roughness of the HfO_xN_y film was evaluated and its variation with oxygen partial pressure for both cases was portrayed in **figure 4.5**. The rms roughness bear a linear trend with O_2 partial pressure and lie in the range 6.89 - 4.86 nm for Ar deposited films while 4.97-3.01 nm for He deposited films. The rising trend of surface roughness in both cases can be explained through the growth of crystallite size. The crystallize size of the film gradually increases with the oxygen partial pressure which in turn increases the roughness. Also, the roughness was found to be less in He case because of smaller crystallite size.

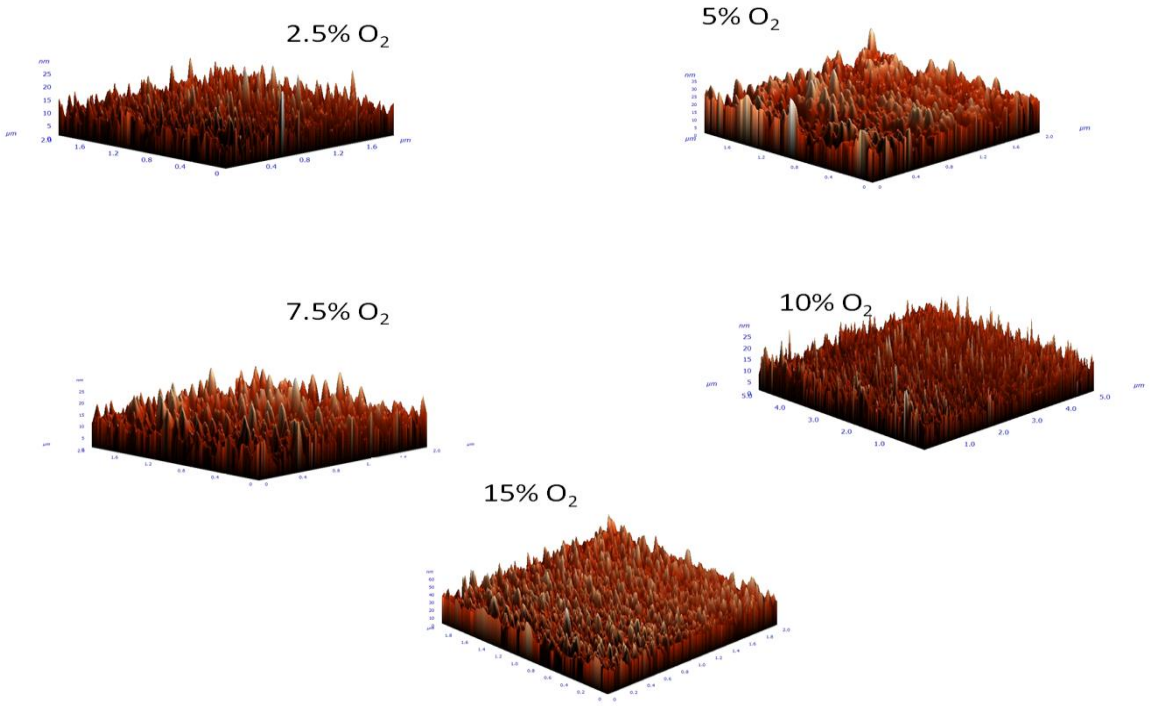

Figure 4 .4 *AFM micrographs of HfO_xN_y films grown in He environment.*

4.2.2.4 Hydrophobicity

The wetting behaviour of HfO_xN_y is characterized by the value of the water contact angle (WCA). Static contact angles of deionised water were measured with water contact goniometry at room temperature by dropping water droplets of 3µl on the respective surfaces using sessile drop method. A minimum of ten measurements on different spots was recorded for each sample. **Figure 4.5** shows the variation of water contact angle with oxygen partial pressure for both sputtering gases and its correlation with roughness. All

samples were found out to be hydrophobic. Also, the hydrophobicity i.e. WCA bears a linear relationship with surface roughness. The minimum WCA was 91.23 ° for the sample deposited in He atmosphere and the maximum contact angle was 97.23° for the sample deposited in Ar atmosphere at 10% and 15% oxygen partial pressure. The maximum (6.89 nm) and the minimum (3.09 nm) surface roughness occurs at the highest and the smallest contact angle respectively. Thus, all samples were following the trend of Wenzel's surface roughness model.

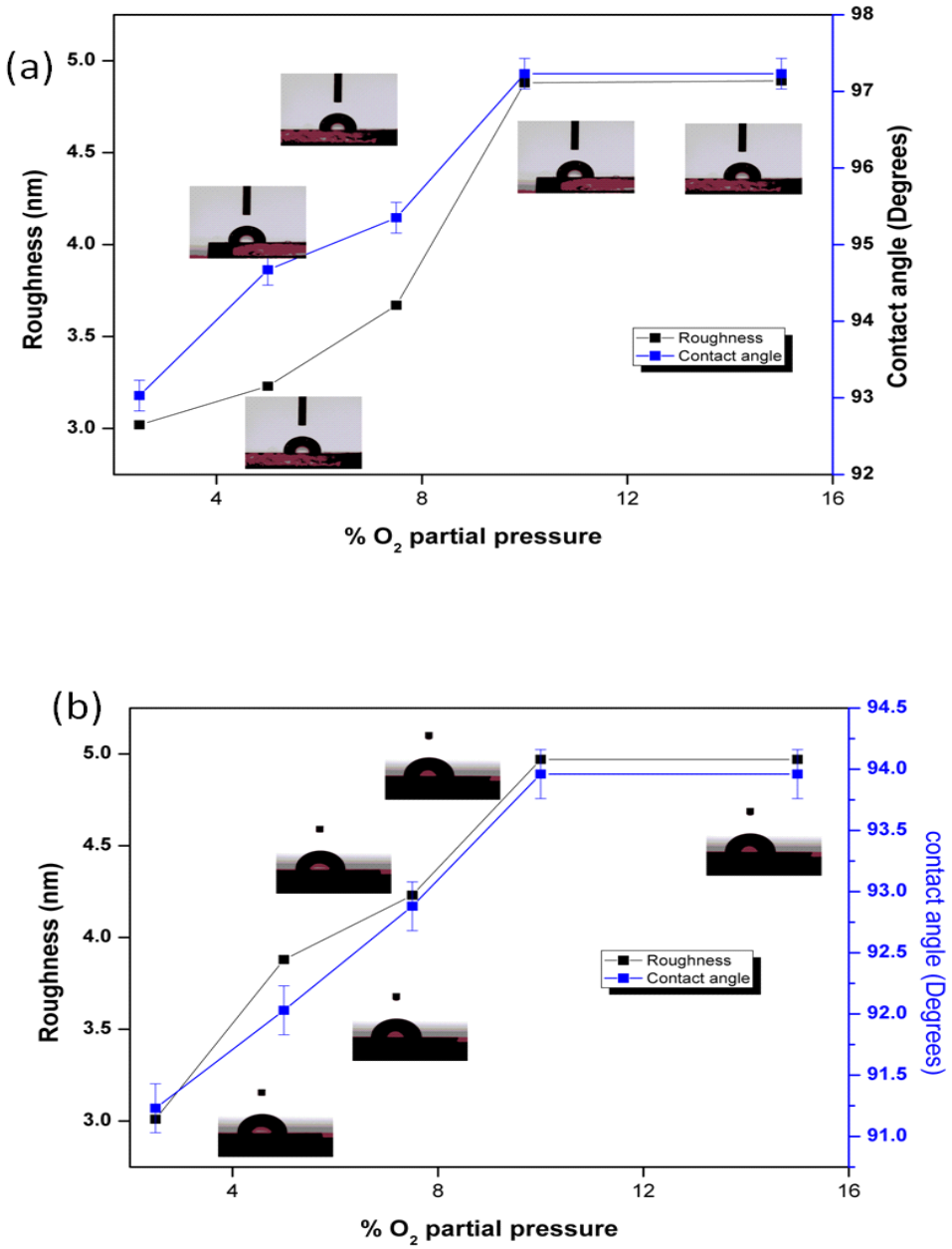

Figure 4.5 *Variation of water contact angle and surface roughness with O_2 partial pressure for HfO_xN_y film deposited in (a) Ar (b) He environment.*

4.2.2.5 Optical properties

To investigate the effect of ambient gas and oxygen partial pressure on the optical properties of hafnium oxynitride films, the transmittance spectra of all the samples was measured in the spectral range of 200-800 nm wavelengths. The representative optical transmission spectrum of HfO_xN_y films grown in Ar and He atmosphere is shown in **figure 4.6 and 4.7**, respectively. The oscillations in the spectra were due to the interference effect. The experimental results show that the transparency of the films increases with increase in the oxygen partial pressure. **Table 4.3** lists the average transmission in the visible region for all the samples. The average transmission was largest (92%) for film deposited at 15% O_2 partial pressure in He atmosphere while it was least (83%) for the film deposited at 2.5% partial pressure in Ar atmosphere. The increment in the transmission coefficient with O_2 partial pressure can be attributed to the extinction coefficient of the films as well as to the thickness of the films. The decrement of the thickness of HfO_xN_y film with oxygen partial pressure in both cases leads to higher transmission of light. The refractive index of the deposited films was calculated using transmission data using Manifacier model [**122**].

The refractive index of films deposited at different O_2 partial pressure was calculated at a wavelength of 550 nm and is shown in **Table 4.3**. The refractive index

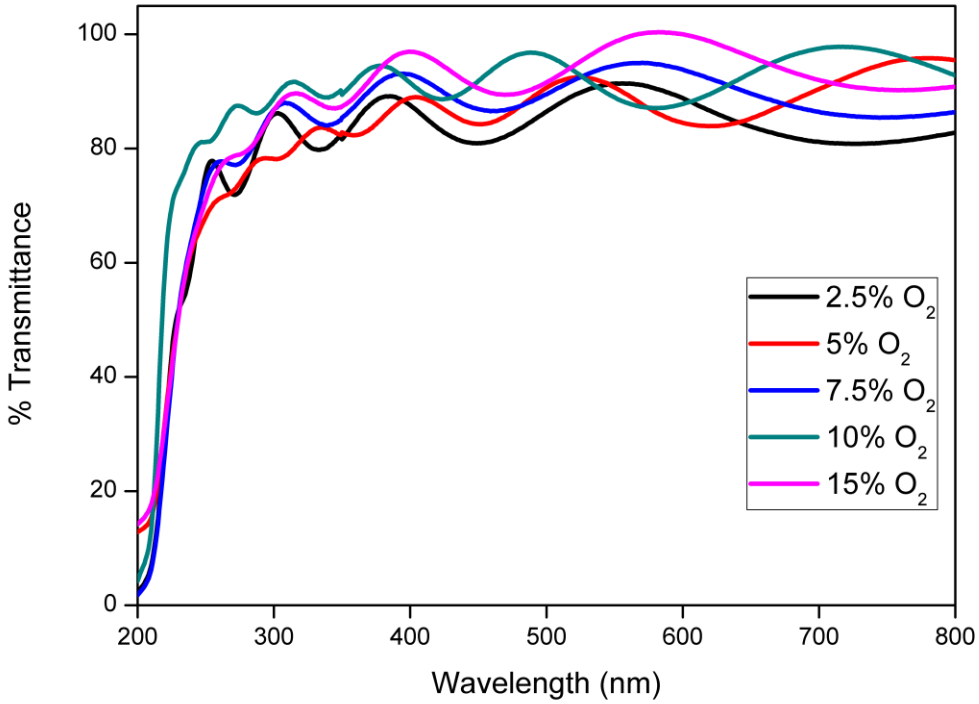

Figure 4.6 *Transmittance curve of hafnium oxynitride films deposited at different oxygen partial pressure in Argon atmosphere.*

lie in the range 1.95-2.1 for Ar case while it lie in the range 2.05-2.13 for He case. The represented data were consistent with the results reported in the literature [**111**]. The refractive index was highly affected by the composition of the film. It can be seen that the refractive index was significantly affected by the

O_2 partial pressure. There is a gradual increase in refractive index with the increment in O_2 partial pressure. This may be probably due to increased packing density and the improved

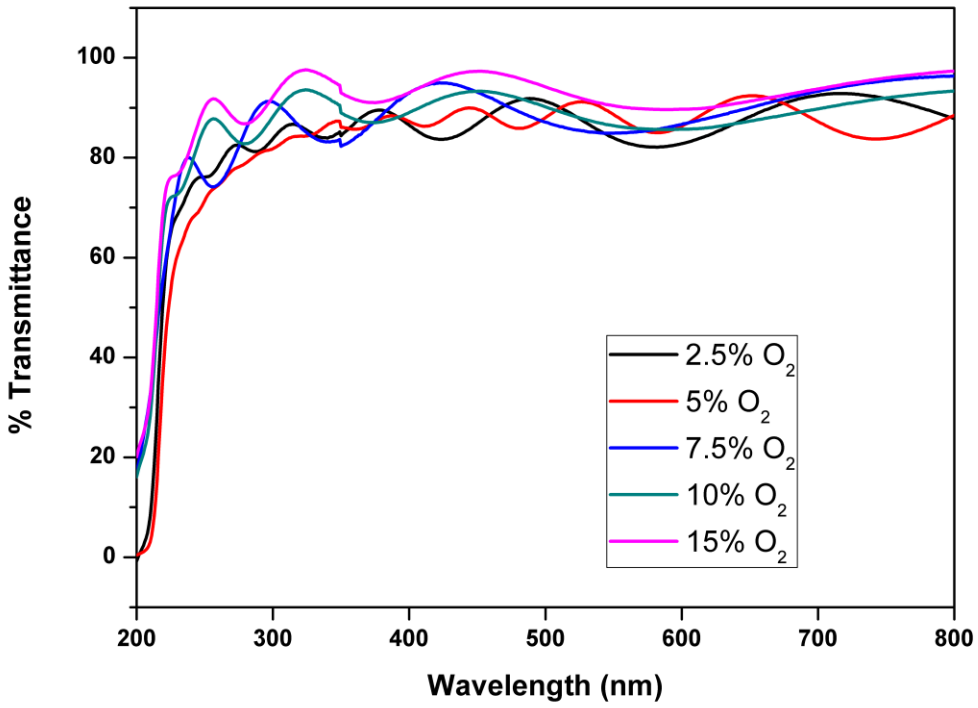

Figure 4.7 *Transmittance curve of hafnium oxynitride films deposited at different partial oxygen pressure in Argon atmosphere.*

crystallinity of the films [**25**]. The packing density (P) was calculated by

assuming the bulk value of refractive index of HfO_xN_y as 2.2 [**91**] at 550 nm and using the calculated refractive index of the HfO_xN_yfilms, the variation of packing density with O_2 partial pressure is shown in Table 3. The packing density of the hafnium oxynitride film was maximum (0.81) at 15% and 10% O_2 partial pressure and minimum at 2.5% O_2 partial pressure (0.71) for films deposited in Ar atmosphere. The packing density in He case is high but the difference is very small. The packing density data clearly shows the formation of a closely packed structure of the film at higher O_2 partial pressure and verifies the above mentioned justification for refractive index.

Table 4.3 *Optical parameters of HfOxNy films*

%O_2 Partial Pressure	**Average Transmission (%)**		**Refractive index (λ=550 nm)**		**Band gap (eV)**		**Packing Density**		**Extinction Coefficient (λ=550 nm)**	
	Ar	**He**	**Ar**	**He**	**Ar**	**He**	**Ar**	**He**	**Ar**	**He**
2.5	**83%**	**85%**	**1.95**	**2.05**	**5.08**	**5.40**	**0.73**	**0.79**	**0.038**	**0.033**
5	**85%**	**86%**	**1.97**	**2.10**	**5.18**	**5.44**	**0.75**	**0.81**	**0.032**	**0.031**
7.5	**89%**	**90%**	**2.03**	**2.12**	**5.25**	**5.46**	**0.77**	**0.82**	**0.026**	**0.023**
10	**90%**	**91%**	**2.1**	**2.14**	**5.29**	**5.48**	**0.81**	**0.83**	**0.023**	**0.021**
15	**90%**	**92%**	**2.1**	**2.14**	**5.35**	**5.51**	**0.81**	**0.83**	**0.023**	**0.020**

The data of transmission spectra was also used to calculate the thickness (d) of the film using the relation [**121**]. **Table 4. 2** also lists the value of thickness

calculated by the above mentioned method. The results were in close agreement with surface profiler data. Based on the transmission spectra, the measured transmittance T is converted into absorption coefficient (α) using the following relationship [**121**]. The extinction coefficient (*k*) of the film was calculated at a wavelength of 550 nm using the equation (13) and listed in **table 4.2.** The extinction coefficient is decreasing with increasing O_2 partial pressure in both Ar and He cases, thus verifies the increasing trend of transparency of HfO_xN_y films.

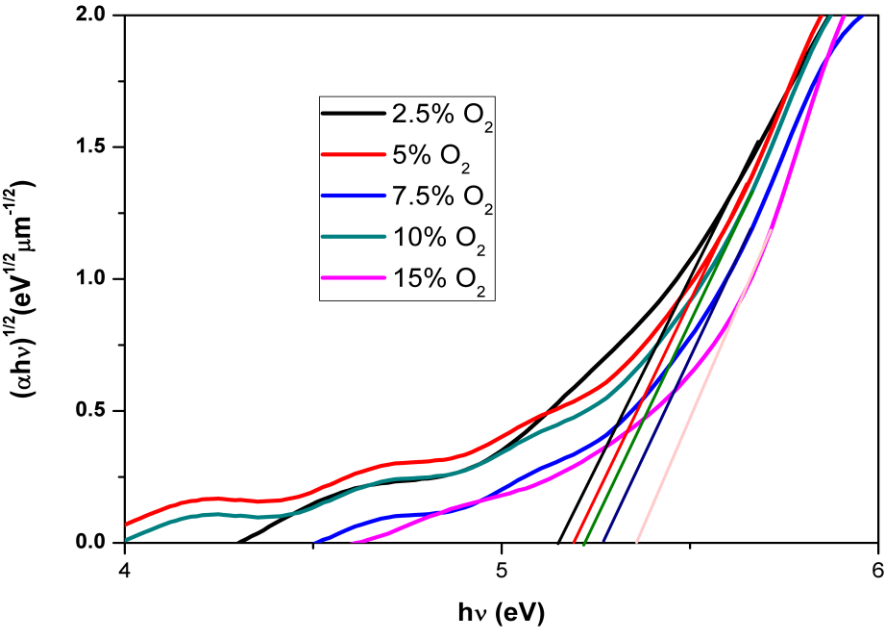

Figure 4. 8 *Bandgap calculation for HfO_xN_y films developed in Ar environment.*

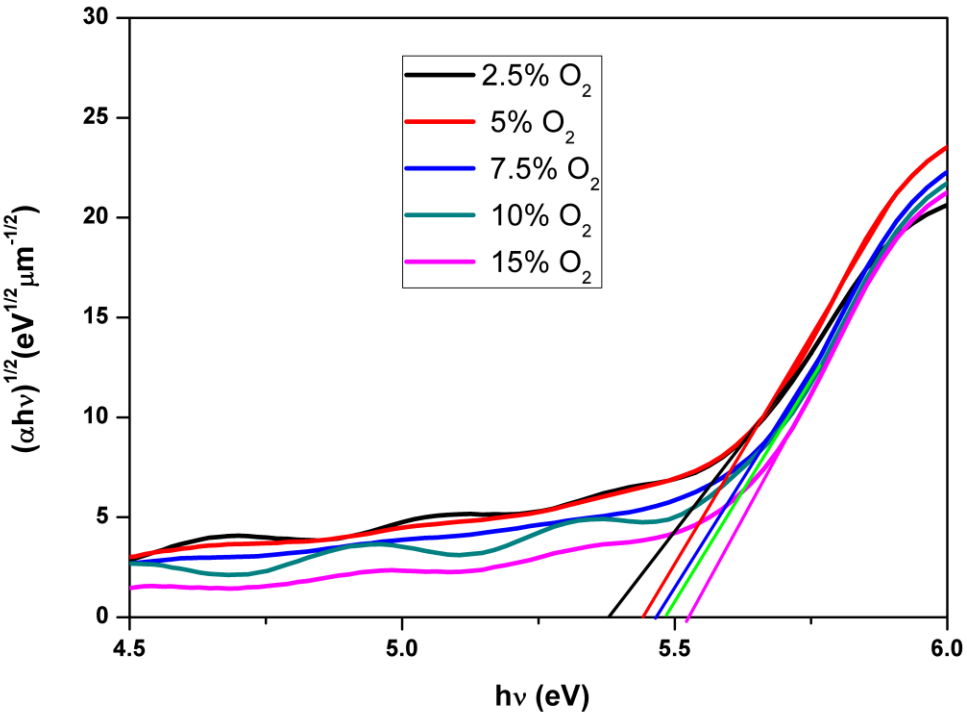

Figure 4. 9 *Bandgap calculation for HfO_xN_y films developed in He atmosphere.*

The optical band gap (E_g) of nanocrystalline hafnium oxynitride film was determined from the absorption coefficient (α) using the Tauc relation.

The literature has widely stated that HfO_xN_y is an indirect bad gap dielectric material having n=2 [**113**]. **Figure 4.8 and 4.9** shows the plot of $(\alpha h\nu)^{1/2}$ on the y axis versus photon energy hν on the x-axis for the samples deposited by varying O_2 partial pressure in Ar and He atmosphere, respectively. The band gap was evaluated by extrapolating the straight line part of the curves $(\alpha h\nu)^{1/2}$. The calculated values of the band gap at different oxygen partial pressure are

shown in **Table 4.3**. The band gap of HfO_xN_y film developed in Ar atmosphere lies in the range of 5.08-5.35 eV [**111**] and for the films grown in He atmosphere, it lies in the range 5.51-5.40 eV. The value of bandgap for HfO_xN_y films is very near to the bulk value of HfO_2 [**112**]. Thus, high band gap values ensure that the deposited films retain the insulating property even in the nanostructured form. The maximum value of band gap was 5.51 eV obtained for the film deposited at 15% of O_2 partial pressure in He atmosphere. The band gap was increasing with the rise in the partial pressure. This can be explained through EPMA data. The EPMA data clearly reveals that as the partial pressure was raised, a decrement in the concentration of nitrogen was found. Asahi et al. have shown that substitutional doping of N into TiO_2 leads to the increment in N 2p states which in turn decrease the band gap [**2**]. However, in HfO_xN_y thin films, reduction in nitrogen concentration leads to decrement in N 2p states which in succession increases the band gap of the films. The small variation in the band gap may be due to the effect of lattice expansion [**13**]. The quantum size effect is absent in this case.

4.2.2.6 *Electrical properties*

The resistivity of hafnium oxynitride films was measured using four probe Van der Pauw technique at room temperature. **Figure 4.10** shows the resistivity

variation with oxygen partial pressure for both sputtering gas. The resistivity was showing a diminishing trend as the oxygen content is increasing. The maximum value of resistivity was reported for the film deposited at 2.5% O_2 partial pressure while minimum value was measured for the film deposited at 15% and 10% oxygen partial pressure for both gases. This behaviour of the resistivity can be correlated to packing density and lattice defects. The resistivity decreases with increasing packing density. Low packing density implies a loose structure which has more lattice defects like voids and impurities. These lattice defects are the sources of electron scattering [**26**] which in turn increases the material resistivity. The packing density (**Table 4.3**) of HfO_xN_y was increasing with increase in pressure and hence, resistivity of deposited samples shows a declining trend.

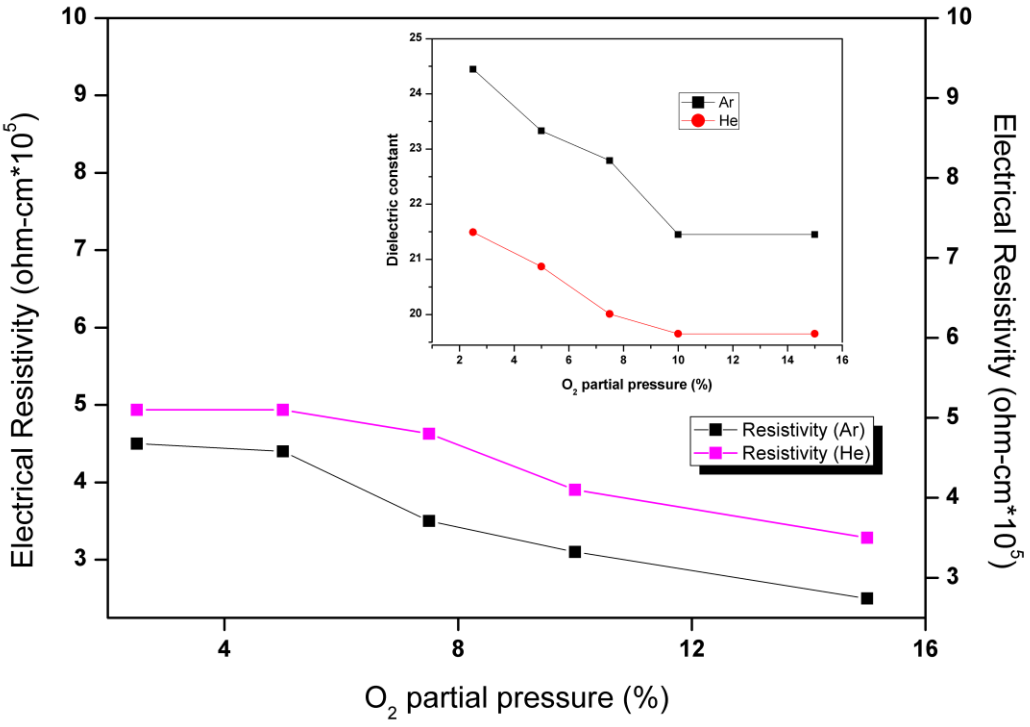

Figure 4.10 *Variation of resistivity and dielectric constant of hafnium oxynitride films as a function of O_2 partial pressure in two different inert atmospheres.*

The dielectric constant (ε) was measured to examine the high electric field bearing capacity of the deposited films. The measurements were carried out at 50 Hz frequency because outdoor insulators operate at this frequency only. A metal/insulator/metal stack was formed by depositing HfO_xN_y on indium-tin-oxide (ITO) glass under same experimental conditions and then Au was deposited on the film as a top electrode. **Figure 4.10** also shows the dielectric constant variation with the O_2 partial pressure. The ε was high (~24) for the film

deposited film in $Ar+N_2+O_2$ atmosphere at low O_2 partial pressure (2.5%) and shows a decreasing movement as the partial pressure was raised. This may be probably due to the decrease in the electronic polarizabilty of Hf-N bond as nitrogen concentration reduces with the rise of the O_2 partial pressure [**183**]. Moreover, theoretical calculations as well as experiments have reported that dielectric constant is also dependent on the thickness of the film [**74,132**]. The same trend was observed in HfO_xN_y film case. Thus, dielectric constant of the HfO_xN_y film was thickness as well nitrogen content dependent.

4.3 Conclusions

Nanostructured hydrophobic thin film of hafnium oxynitride was developed for glass insulator. Both ambient gases and the reactive gas oxygen have significant influence on the different properties of HfO_xN_y films. Maximum contact angle was obtained for the film deposited in Ar atmosphere at 10 and 15% O_2 partial pressure. The optical band gap, refractive index and packing density was also high for these deposited films. However, the resistivity and dielectric constant are less for these films in comparison to the other deposited films but the difference is very small that it can be neglected for practical purpose. To be more economical, the film deposited at 10% O_2 partial pressure in Ar

atmosphere can be considered as the optimal coating for glass insulators to mitigate contamination problem.

4.3 Effect of temperature on structural, electrical, optical and hydrophobic properties of nanocrystalline transition metal oxynitride thin film coated on glass insulators

4.3.1 Experiment

Hafnium oxynitride films were deposited on glass and quartz substrates by DC magnetron sputtering in a custom designed 12 in. diameter chamber (Excel Instruments). The substrates were initially cleaned thoroughly in an ultrasonic bath with a mixture of distilled water and trichloroethylene and were then washed with boiled acetone. Further, the substrates were dried under nitrogen gas and then mounted on the substrate holder of the chamber. A pure (99.99%) hafnium target of 50 mm diameter and 3 mm thick wa s mounted on the magnetron cathode of the chamber. The substrate to target distance was fixed to 41mm. High-purity argon (99.99%) was used as a sputtering gas while pure (99.9%) oxygen and nitrogen were used as reactive gases. The flow of the gases was controlled and measured by using mass flow controller (MKS). A turbo based pumping system was used to a chieve a base pressure below $2x10^{-6}$ Torr. The working pressure in the vacuum chamber was kept 20 mTorr and was measured by a compact gauge (Pfeiffer

Vacuum). The gas pressure was carefully monitored to keep it constant as the sputtering current is highly sensitive to the sputtering pressure. The deposition was carried out at different substrate temperature varying from room temperature (as-deposited) to 400^{o}C at a fixed DC power of 50 W. During each deposition, the target was presputtered for 10 minutes in order to ascertain the same state of the targets in every run. The deposition time was 1 hour for each sample.

4.3.2 Results and Discussion

4.3.2.1 Structural analysis

The typical X-ray diffraction (XRD) patterns of HfO_xN_y films deposited at different substrate temperature are shown in **Fig. 4.11**. All the deposited films were polycrystalline in nature with the pattern of monoclinic HfO_2 [JCPDS 34-104] and preferred orientation at (-111) phase. The monoclinic phase of HfO_2 is the most stable state in comparison to its cubic, orthorhombic and tetragonal structure [**4]**. In addition to the dominant peak (-111) existing at diffraction angle of approx. 28^{o}, weak peaks of orientation (110), (111), (002) and (-112) and (220) were also visible in the XRD pattern. Weak peaks of HfN was also observed. This can be attributed to the higher reactivity of oxygen which in turn favours the formation of metal-oxygen (Hf-O) bonds rather than metal- nitrogen (Hf-N) bonds.The intensity of the dominant peak increased with rise in

deposition temperature and was maximum at 400°C. The reactivity of oxygen atoms arriving at the substrate enhanced with the increase of substrate temperature which led to more crystallization of the films. The average crystallite size (*t*) was estimated from the integral width of the diffraction lines using the Scherrer equation [**30**] after background subtraction and correction for instrumental broadening.

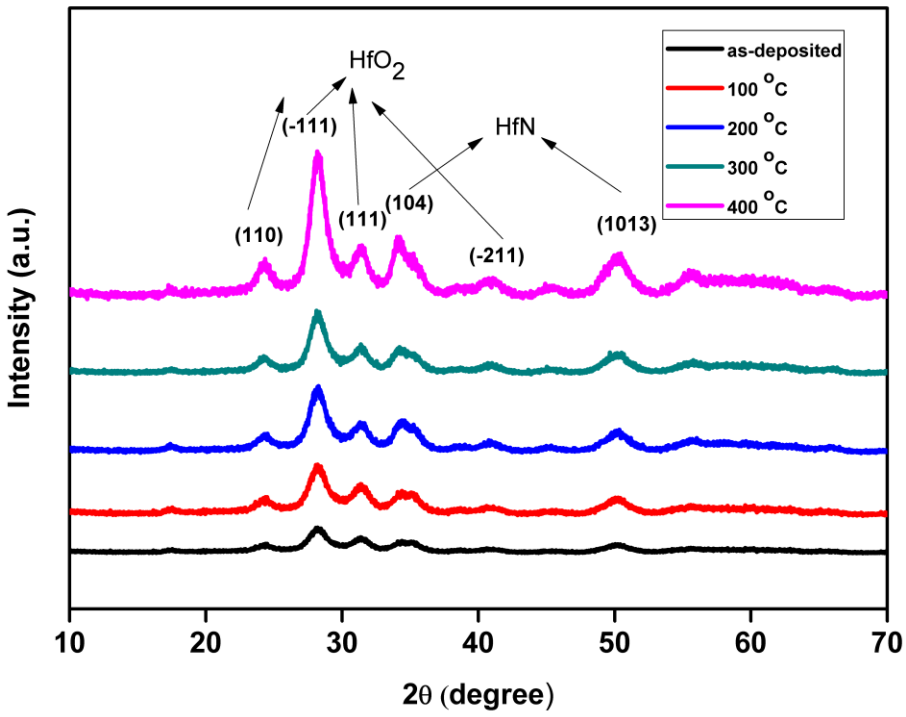

Figure 4.11 X-ray diffraction pattern of HfO_xN_y films at different substrate temperature.

Figure 4.12 shows the variation of crystallite size with substrate temperature. The mean crystallite size was in the range of 10.34-20.43 nm. The average crystallite size increased with increasing deposition temperature due to greater thermal activation and diffusion [**161**]. Narrowing of XRD peak width with increasing temperature agreed well with the crystallite coarsening at higher deposition temperature. The dislocation density, indicative of the number of defects in the films, was also calculated.

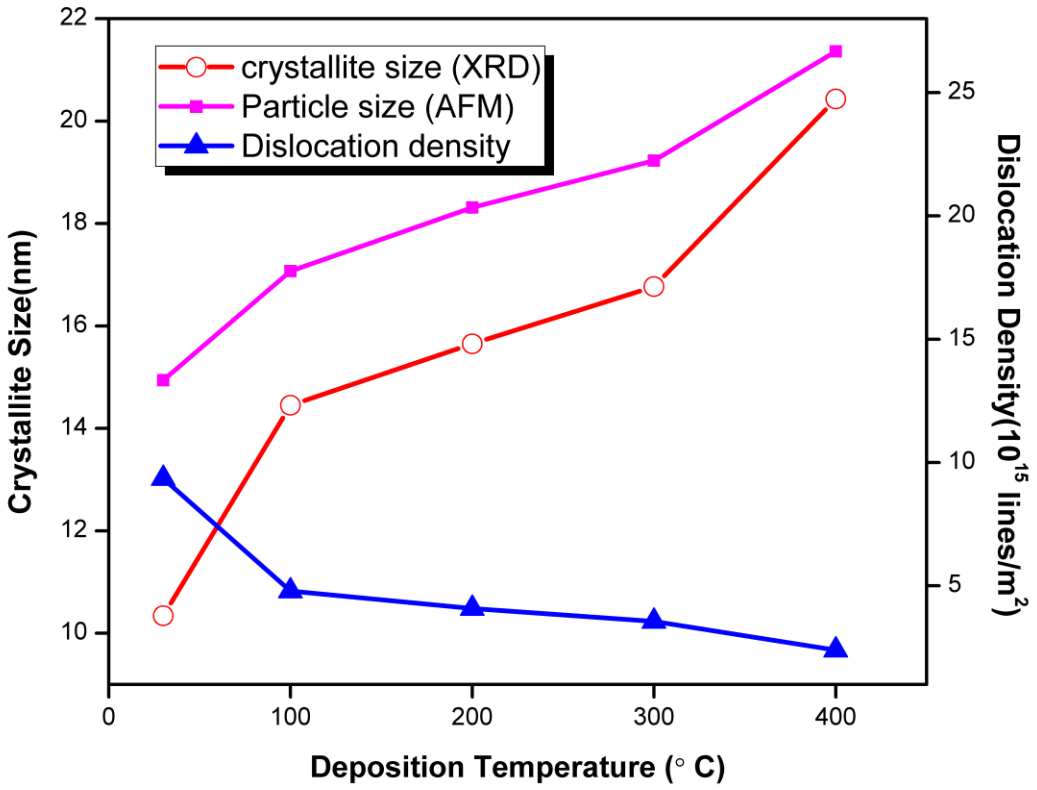

Figure 4.12 *Variation of Crystallite size and dislocation density with substrate temperature*

Figure 4.12 also shows the variation of dislocation density with substrate temperature. The dislocation density is showing decreasing trend with the deposition temperature. Minimum dislocation density ($2.39x10^{15}$ lines/m^2) was obtained at 400^oC which clearly reflects that the higher compactness of the grains and least crystal defects in the film were obtained at the higher deposition temperature. The thermal energy produced by enhancing the deposition temperature leads to the enrichment of mobility of active atoms which in turn fills the voids and thus, reduces the crystal defects.

4.3.2.2 Composition analysis

The elemental analysis of HfO_xN_y thin film was done through EDS both on the surface as well as on cross section. The variation of the measured composition on the sample is within±0.5 (within EDS error limits). **Table 4.4** lists the at.% of hafnium, oxygen and nitrogen in the deposited sample at different substrate temperature in both modes. The results mutually agree with each other. It is clear from the table that hafnium at. % remains almost constant while the N_2 at. % decreases and O_2 at. % increases as the temperature was raised. The probable reason for the decrement in the nitrogen content was the enhanced reactivity of oxygen at elevated temperature which in turn causes more surface oxidation. Thus, oxygen atoms replace the nitrogen atoms leading to formation of HfO_2 film. Liu et al. have reported that reduction in nitrogen

content with an increase in temperature leads to greater mobility of Hf and O atoms [**110**]. Chio et al. concluded that the crystallilty of hafnium oxynitride films deposited at high temperature increases with the decrease in nitrogen content, thus establishing the correctness of XRD results [**24**].

Table 4.4 *Elemental analysis of HfO_xN_y films*

Substrate Temperature (°C)	EPMA on Surface			EPMA on cross section		
	Hf at.%	O at. %	N at. %	Hf at.%	O at. %	N at. %
As-Deposited	64.36	26.43	9.21	64.56	26.41	9.03
100	64.12	27.85	8.03	64.45	27.23	8.32
200	64.25	28.30	7.45	64.57	28.22	7.21
300	64.34	29.62	6.04	64.32	29.55	6.13
400	64.45	30.22	5.33	64.48	30.25	5.27

4.3.2.3 Morphological study

The effect of deposition temperature on the microstructure and morphology of the HfO_xN_y was studied by AFM images. **Figure 4.13(a)-(e)** shows the 3-D AFM micrographs of hafnium oxynitride films deposited at different substrate temperature. It can be observed that the microstructure of all deposited films was characterized by high density columnar structure. The average particle size of each sample was estimated using the software attached to the AFM and compared with the XRD results as shown in **figure 4.12**. It was seen that the average grain size measured by AFM was larger than that calculated by XRD. This ambiguity can be ascribed to the fact that AFM measurements result from

agglomeration of the particles whereas XRD gives an average crystallite size [**20**]. Roughness of a thin film plays an important role in describing some of its

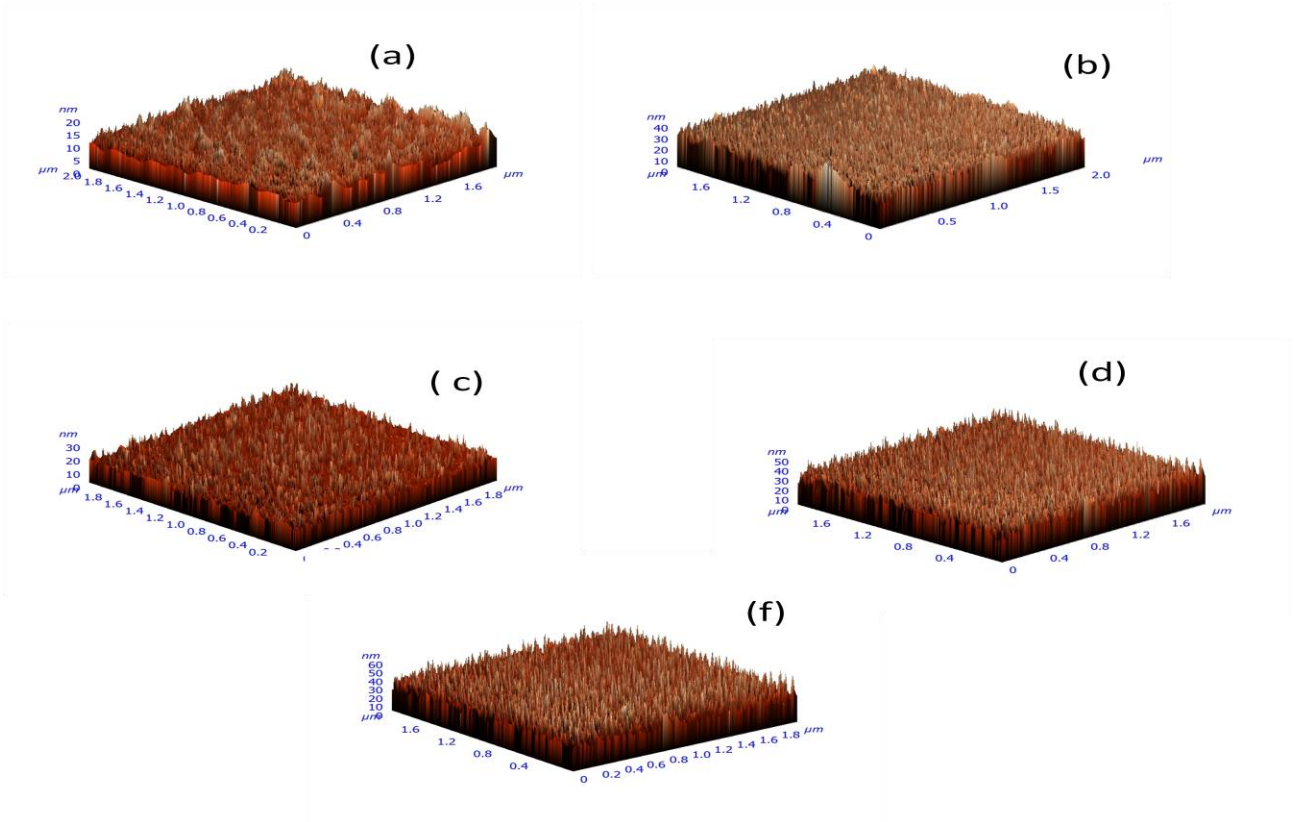

Figure 4.13 3-D AFM micrographs of hafnium oxynitride films (a)as-deposited (b)100°C (c) 200°C (d) 300°C (e) 400°C

properties like optical, mechanical and wettability. The root mean square (rms) roughness of the HfO_xN_y film was evaluated and its variation with deposition temperature was portrayed in **Figure 4.14**. The rms roughness bears a linear trend with temperature and lies in the range 3.02- 4.9 nm. The rising trend of surface roughness can be explained through the growth of crystallite size. The crystallize size of the film gradually increased from 10.43 nm to 20.43 nm with the substrate temperature which in turn increased the roughness. Initially, as the deposition temperature was increased from room to 300 °C, the change in the roughness was very small (~0.83 nm). However, as the temperature was increased from 300 °C to 400 °C, the change in the roughness was found to be very large (~1nm). This reflects that at 400 °C both large crystallite size as well as the decrement in the nitrogen content plays a simultaneous role in providing large change to the surface roughness of the film. Yuan et al. [**202**] have correlated an inverse relationship of surface roughness with nitrogen content in HfO_xN_y thin film.

4.3.2.4 Hydrophobicity

The wetting behaviour of HfO_xN_y was characterized by the value of the water contact angle. The water contact angle of a solid is an important parameter in surface science and its measurement provides a simple and reliable technique to interpret the hydrophobic behaviour of surface and its energies. The static water contact angles of HfO_xN_y thin films were measured with water contact goniometry at room temperature by dropping water droplets of 3µl on the respective surfaces using the sessile drop method. A minimum of ten measurements on different spots were recorded for each sample. **Figure 4.14** shows the variation of water contact angle (WCA) with temperature and its correlation with roughness. All samples were found hydrophobic. Also, the hydrophobicity i.e. WCA bears a linear relationship with surface roughness. The minimum WCA was 94.03 ° for the as-deposited sample and the maximum contact angle was 97.2° for the sample deposited at 400°C. The maximum (4.9 nm) and the minimum (3.02 nm) surface roughness occurs at the highest and the smallest contact angle. Thus, all samples are satisfying the surface roughness model of the Wenzel.

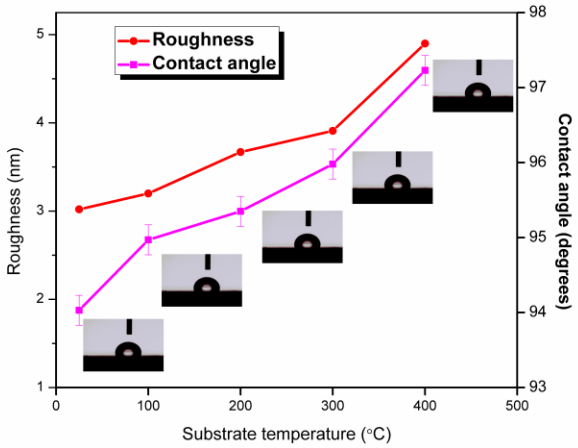

Figure 4.14. Roughness and water contact angle of deposited film as a function of substrate temperature.

4.3.2.5 Optical Properties

To investigate the effect of substrate temperature on the optical properties of hafnium oxynitride films, the transmittance spectra of all the samples was measured in the spectral range of 200-800 nm wavelengths. The representative optical transmission spectrum of HfO_xN_y films is shown in **figure 4.15**. The oscillations in the spectra were due to the interference effect. The experimental results show that the transparency of the films decreased as the deposition temperature increased. **Table 4.5** lists the average transmission in the visible region for all the samples. The average transmission was the largest (88.5%) for as-deposited film while it was the least (84.2%) for the film deposited at 400°C temperature. The transmission coefficient reduction with temperature can be

attributed to changes in the crystallite size and surface roughness of the films. Large crystallite size leads to higher roughness which in turn increases the sources of light scattering and thus, reduces the transmission level.

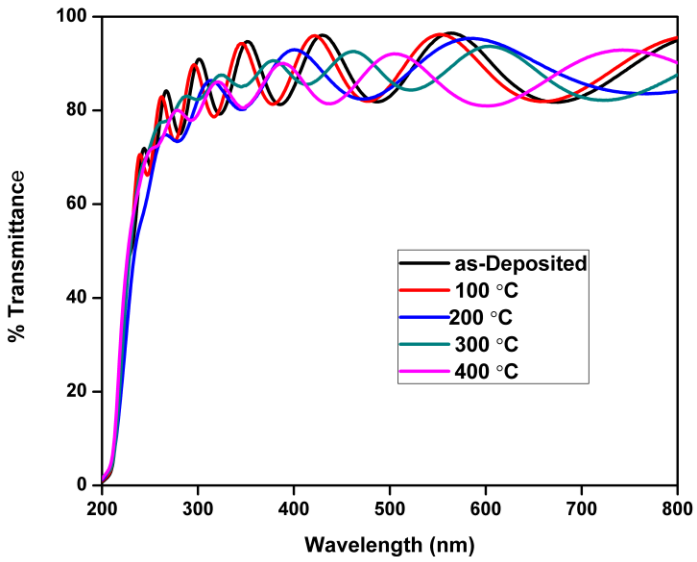

Figure 4.15 *Transmittance spectra of HfO_xN_y film at different deposition temperature.*

The refractive index of the deposited films was calculated using transmission data using Manifacier model [**121**]. The refractive index of the films deposited at different temperature was calculated at a wavelength of 550 nm and is shown in **Table 4.5**. The refractive index lies in the range of 1.91-2.12 and is consistent with the results reported in the literature [**114**]. It can be also seen that the refractive index was significantly affected by the substrate temperature. There is a gradual increase in refractive index with the substrate

temperatures. This may be probably due to increased packing density and the improved crystallinity of the films. It is a known fact that the as-deposited films have a lower packing density with some voids because of the loose arrangement of the atoms. The high deposition temperature results in the release of such voids and increases the mobility of atoms in the films. This results in the formation of more closely packed structure which leads to high refractive index of the deposited films. The packing density (P) was also calculated.

Table 4.5 Optical data of HfO_xN_y films

Substrate Temperature	Average Transmission (%)	Refractive Index	Band Gap	Extinction Coefficient (λ=350 nm)
As-deposited	**88.5**	**1.91**	**5.08**	**0.026**
100	**87.9**	**1.95**	**5.18**	**0.031**
200	**86.5**	**2.01**	**5.25**	**0.039**
300	**85.8**	**2.03**	**5.29**	**0.043**
400	**84.2**	**2.12**	**5.35**	**0.052**

Assuming the bulk value of refractive index of HfO_xN_y as 2.2 at 550 nm and using the calculated refractive index of the HfO_xN_y films, packing density of the deposited films was calculated. The packing density of the hafnium oxynitride film was maximum (0.82) when temperature was 400°C and minimum for as-deposited film (0.71). This shows the formation of a closely packed structure of the film at higher temperature and verifies the above mentioned justification for refractive index.

The thickness of the films was measured through surface profilometer. The data of transmission spectra was also used to calculate the thickness (d) of the film using the relation [**167**]. SEM cross section was also utilized for the cross verification of the thickness data. **Figure 4.16** shows a representative cross-section SEM image of HfO_xN_y film. **Table 4.6** lists the value of thickness calculated/measured by the above mentioned three methods. The results were in close agreement to each other. The deposition rate (thickness/time) decreased from 12.53 nm/min to 10.75nm/min as the substrate temperature was enhanced. The declining trend of thickness is also an indicative of increased packing density.

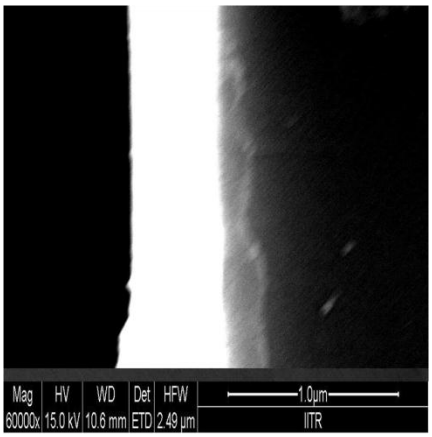

Figure 4.16 *Typical cross section image of hafnium oxynitride film deposited at 400 °C.*

Optical absorption coefficient (α) was calculated as a function of the wavelength in the range of 200-800 nm. The extinction coefficient (k) of the HfO_xN_y films deposited at different temperature using absorption coefficient

$$k = \alpha \lambda / 4\pi$$

Table 4.6 *Thickness of the deposited films*

Substrate Temperature(°C)	Thickness (nm)		
	Optical Transmission Data	Surface profilometer	SEM cross section
As-Deposited	752	743±5	749±2
100 °C	731	724±4	728±2
200 °C	698	688±5	695±4
300 °C	675	667±6	671±2
400 °C	645	641±4	644±3

The calculated value of extinction coefficient at λ=350 nm is shown in **Table 4.5**. The value of *k* linearly varied with the substrate temperature. The extinction coefficient plays an important in determining the change in the transparency of the films. The scattering of grains is the main contributory factor in determining the extinction coefficient of the deposited films. Large grain size leads to enhancement of scattering effect which in turn decreases the transparency of films [50]. As the deposition temperature was increased from room temperature to 400°C, the value of *k* increased from 0.026 to 0.052 due to enlargement of grain size. This in succession reduced the average transparency of the deposited films from 88.5% to 84.8%.

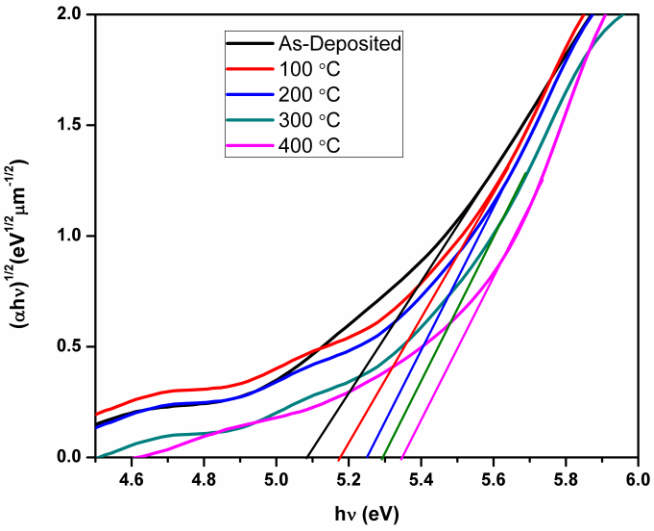

Figure 4.17 *Band gap determination of HfO_xN_y films.*

The optical band gap (E_g) of nanocrystalline hafnium oxynitride film was determined from the absorption coefficient (α) using the Tauc relation [51]

The parameter n has a value 2 for an indirect band gap and ½ for the direct band gap. The literature has widely stated that HfO_xN_y is an indirect bad gap dielectric material having n=2. **Figure 4.17** shows the plot of $(\alpha h\nu)^{1/2}$ on the y axis versus photon energy hν on the x-axis for the samples deposited by varying deposition temperature. The band gap was evaluated by extrapolating the straight line part of the curves $(\alpha h\nu)^{1/2}$. The calculated values of the band gap at different substrate temperature are shown in **Table 4.5**. The band gap of

HfO_xN_y film lies in the range of 5.08-5.35 eV [**183**] which is near to the bulk value of HfO_2 [**179**]. Thus, high band gap values ensure that the deposited films retain the insulating property even in the nanostructured form. The maximum value of band gap was 5.35 eV obtained at a substrate temperature of 400 °C. The band gap was increasing with a rise in the deposition temperature. This can be explained through EPMA data. The EPMA data clearly reveals that as the temperature was raised, a decrement in the concentration of nitrogen was found. Asahi et al. have shown that substitutional doping of N into TiO_2 leads to the increment in N 2p states which in turn decreases the band gap [**2**]. However, in HfO_xN_y thin films reduction in nitrogen concentration leads to decrement in N 2p states which in succession increases the band gap of the films. The small variation in the band gap may be due to the effect of lattice expansion [**183**]. The quantum size effect is absent in this case.

4.3.2.6 Electrical properties

The resistivity of hafnium oxynitride films was measured using four probe Van der Pauw technique at room temperature. **Figure 4.18** shows the resistivity variation with substrate temperature. The resistivity was showing a diminishing trend as the deposition temperature was enhanced. The maximum value of resistivity was reported for as-deposited film while minimum value was measured for the film deposited at 400 °C. This behaviour of the resistivity can

be correlated with the packing density and lattice defects. The resistivity decreases with increasing packing density. Low packing density implies a loose structure which has more lattice defects like voids and impurities. These lattice defects are sources of electron scattering [**13**] which in turn increases the material resistivity. The packing density of HfO_xN_y was increasing with increase in temperature and hence, resistivity of deposited samples showed a declining trend.

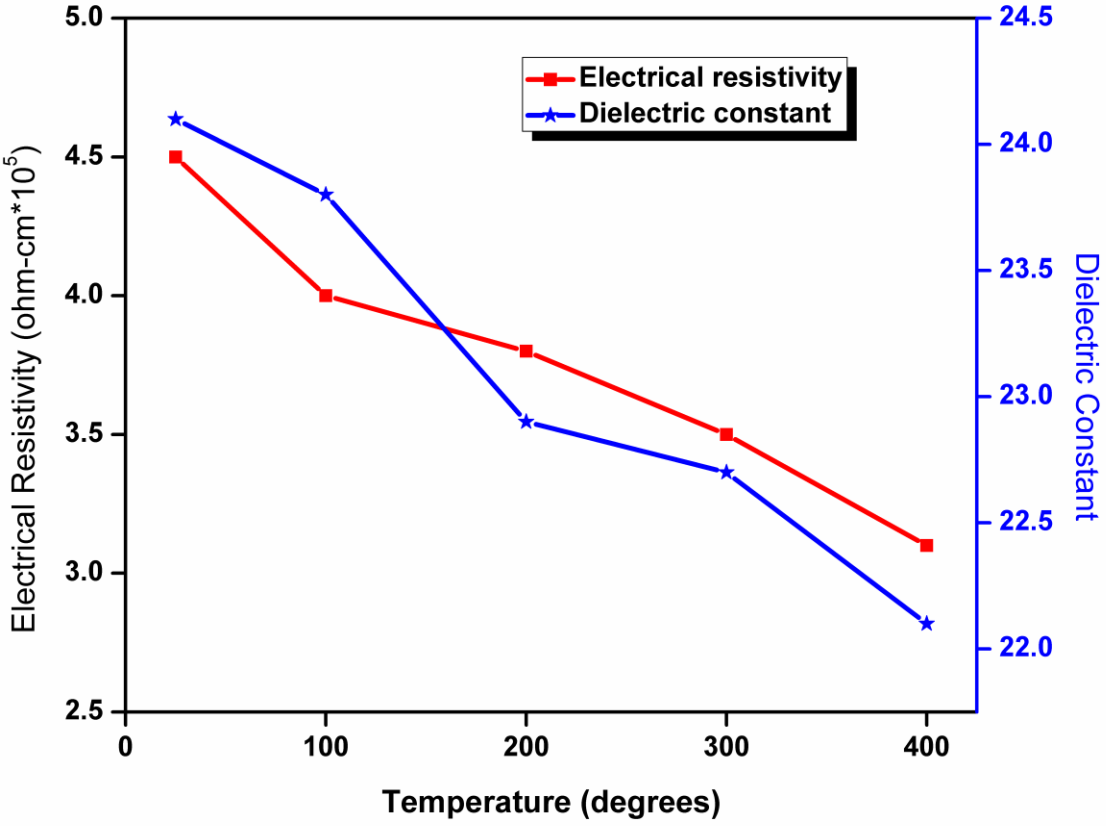

Figure 4.18 *Electrical resistivity and dielectric constant of deposited films at different substrate temperature.*

The dielectric constant (ε) was measured to examine the high electric field bearing capacity of the deposited films. The measurements were carried out at 50 Hz frequency because outdoor insulators operate at this frequency. A metal/insulator/metal stack was formed by depositing HfO_xN_y on indium-tin-oxide (ITO) glass under same experimental conditions and then Au was deposited on the film as a top electrode. **Figure 4.18** also shows the dielectric

constant variation with the deposition temperature. The ε is high (~24) for the as-deposited film and shows a decreasing movement as the temperature is raised. This may be probably due to the decrease in the electronic polarizabilty of Hf-N bond as nitrogen concentration reduces with the rise of the deposition temperature [**26**]. Moreover, theoretical calculations as well as experiments have reported that dielectric constant is also dependent on the thickness of the film [**74,132**]. The same trend was observed in HfO_xN_y film case. Thus, dielectric constant of the HfO_xN_y film has been found to be dependent on thickness as well nitrogen content.

4.3.3 Conclusions

Nanocrystalline hydrophobic hafnium oxynitride films were deposited on the glass insulators by DC magnetron sputtering at various substrate temperatures. The influence of the substrate temperature on the structural, hydrophobic, optical and electrical properties of the HfO_xN_y films was experimentally investigated. An increase in the substrate temperature led to an improvement in crystallinity and roughness, which in turn increased the hydrophobicity of the HfO_xN_y films. However, a degradation of the electrical property was observed at higher substrate temperatures. The highest WCA (97.2°) was obtained at the deposition temperature of 400 °C which was

justified through roughness kinetics. The refractive index (2.12) as well as the band gap (5.35) was high at 400 °C indicating the compactness and insulating nature of the deposited film. However, the value of electrical resistivity and the dielectric constant of the film at 400 °C was less in comparison to the as-deposited film. In this research work, higher hydrophobicity of the dielectric film was achieved at higher deposition temperature but at reduced electrical resistivity and dielectric constant. This in turn may increase the surface leakage current which is undesirable. Hence, room temperature deposited film can be considered as an optimum temperature for the deposited oxynitride film.

4.4 Effect of sputtering pressure on structural, hydrophobic, optical and electrical property of nanocrystalline HfO_xN_y thin film.

4.4.1 Experiment

Hafnium oxynitride thin films were deposited on glass and quartz substrate by DC magnetron sputtering in a custom designed 12 in. diameter chamber (Excel Instruments, India). A 2 in. diameter hafnium target of 99.97% purity was used for the sputtering. The chamber was initially evacuated to about 2×10^{-6} Torr by a turbomolecular pump backed by a rotary pump for rough vacuum. Thereafter, pure (99.9%) nitrogen, oxygen and argon gas was bled into the chamber. The flow rate of nitrogen, argon and helium was kept 20, 20, 2 sccm respectively. The ratio of the gas mixtures was measured using mass flow meter (MKS). The gas pressure was varied from 10 mTorr to 30 mTorr in steps of 5. During each sputter deposition, the gas pressure was carefully monitored and kept constant since the sputtering current is extremely sensitive to the pressure of the sputtering gas. Sputtering was carried out for a period of 1 h at a fixed DC power of 50 W at room temperature. The target to substrate distance was 41 mm. Other than the sputtering gas pressure, all other parameters were kept constant during each deposition.

4.4.2 Results and Discussion

4.4.2.1 Structural Analysis

X-ray diffraction analysis was carried out to determine the phase and the preferred orientations of the HfoxNy film at different sputtering pressure. **Figure 4.18** shows the XRD patterns of the deposited films as a function of pressure. All the deposited films were polycrystalline in nature. The dominant and the weak peaks belongs to the monoclinic phase of HfO_2. Weak Hf-N peak of orientation (104) and (1014) were present in all the deposited film which may be due to high reactivity of oxygen in comparison to nitrogen. The intensity of the dominant orientation (-111) existing at $2\theta=28°$ increases as the sputtering pressure was raised from 10 mTorr to 20 mTorr which clearly indicates the improvement in the crystallilty of the film. However, the intensity of the dominant peak reduces beyond 20 mTorr signifying decrement in the crystallilty of the deposited films. In order to attain the detailed structure information, the average crystallite size was calculated from the dominant peak using well known Debye –Scherer formula and the results were shown in the **Figure 4.19**. The crystallite size of the films was between 10-20 nm. The crystallite size initially follows an increasing trend upto 20 mTorr and then further increment of pressure reduces the size. The increment in the crystallize

size can be explained through mean free path which is inversely proportional to the pressure. Thus, as pressure increases upto 20 mTorr, mean free path of the sputtered atoms decreases which in turn increases the collision frequency and reduces the energy level of sputtered hafnium atoms. The reduction in the energy level leads to agglomeration of the sputtered particle before reaching the substrate and hence, enhanced crystallite size. However, at higher pressure (> 20 mTorr) the reduction in crystallite size can be attributed to the reduced mobility of the crystallites. The declination in the mobility was due to the lower energy content of the grains.

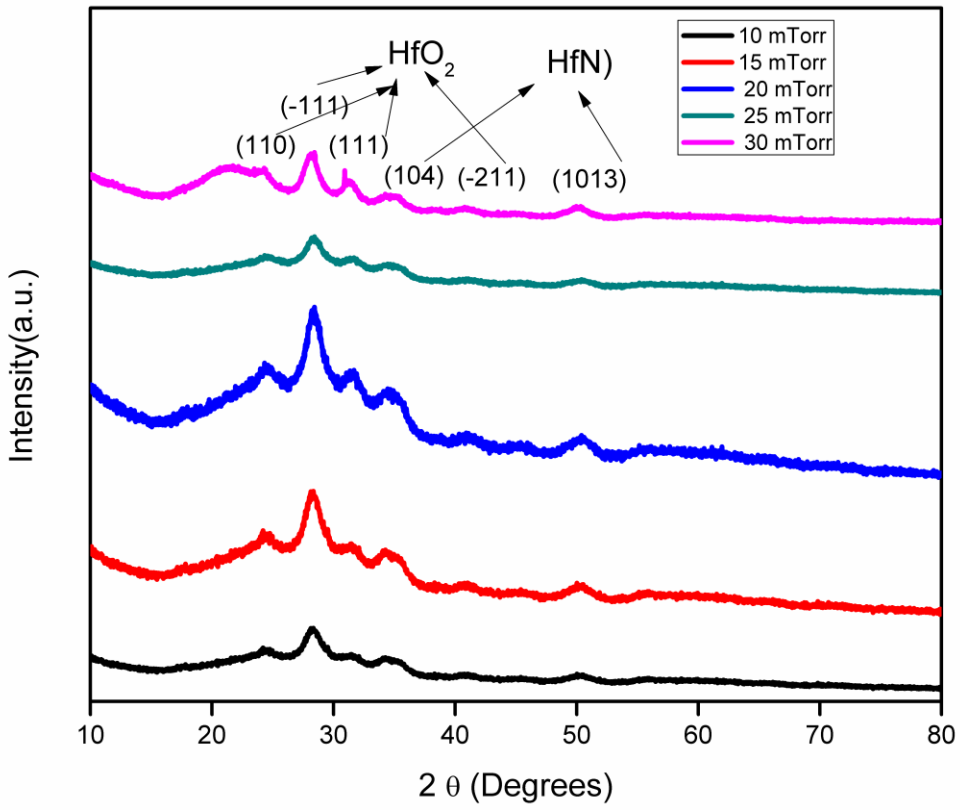

Figure 4.19 *X-ray diffraction pattern of HfO_xN_y films at different sputtering pressure.*

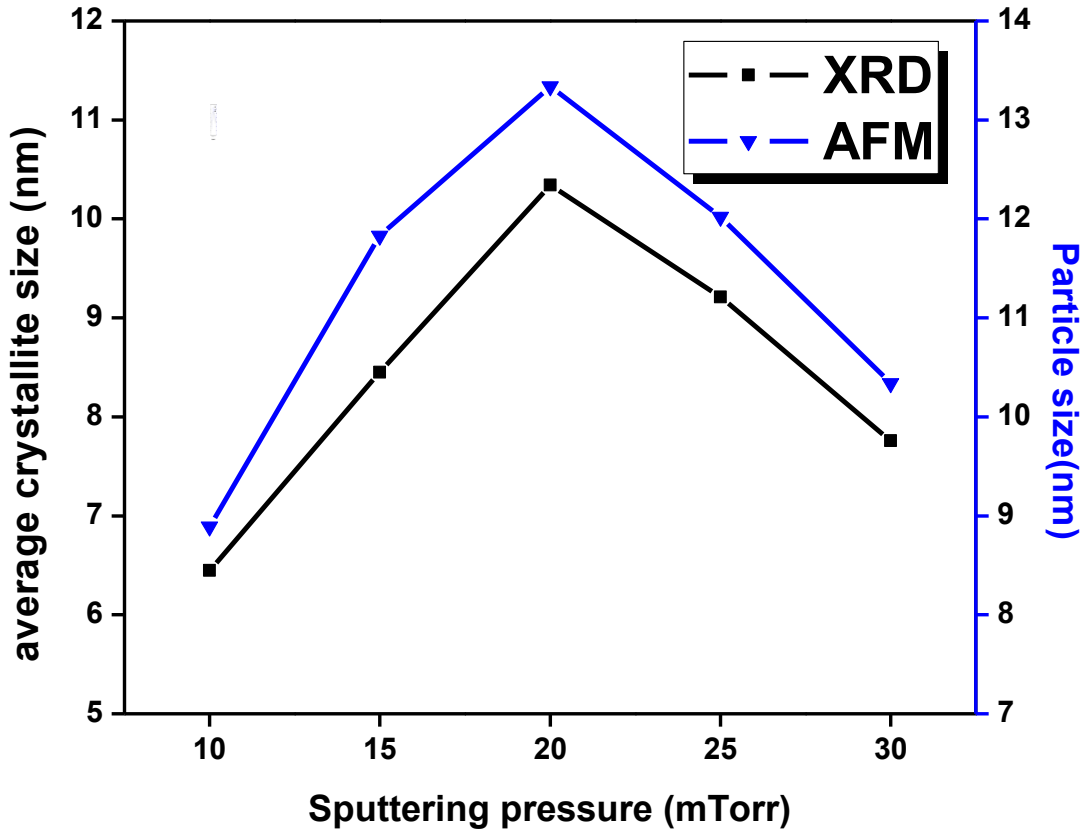

Figure 4.20 *Variation of crystallite size and particle size with pressure*

The thickness of the film measured through surface profilometer was used in evaluating the deposition rate. The thickness was also cross verified through SEM cross section image and both results were mutually agreeing with each other as shown in **table 4.7**. The deposition rate (thickness/time) clearly reveals that the film deposited at 20 mTorr has maximum value. Optimum sputtered Hf

particles reach the substrate for pressure <20 mTorr but beyond this, some of the Hf atoms are scattered away from the substrate due to low mean free path, resulting in lower deposition rate. The well known poisoning effect of the target by the reactive gases may be another factor for the reduction of deposition rate.

Table 4.7 *Thickness of the film by different method*

Sputtering Pressure (mTorr)	**Thickness (nm)**		
	Optical Transmission Data	**Surface profilometer**	**SEM cross section**
10	**650**	**643±5**	**649±2**
15	**711**	**717±4**	**718±2**
20	**752**	**743±5**	**749±2**
25	**670**	**665±6**	**673±2**
30	**655**	**645±4**	**648±3**

4.4.2.2 Elemental Analysis

The elemental analysis is shown in **table 4.8**. It is clear that at.% of N_2 is decreasing while that oxygen is increasing with pressure. The higher reactivity of the oxygen favours the formation of metal-oxygen bond rather than metal-nitrogen bond [**65**].

Table 4.8 *Elemental analysis of hafnium oxynitride film*

Sputtering Pressure (mTorr)	**EPMA on Surface**		
	Hf at.%	O at. %	N at. %
10	62.34	25.57	12.09
15	63.12	26.38	10.5
20	64.36	26.43	9.21
25	64.34	28.62	7.04
30	64.45	29.34	6.21

4.4.2.3 Morphological property

The surface topography of the deposited films was examined through 3-D AFM micrographs shown in **figure 4.20**. The rough surface of glass substrate provides the driving force for the growth of a rough and columnar structure of HfO_xN_y film. The images clearly reveals that the morphology is relatively uniform and dense for all films. Particle analysis was performed to obtain more information about the morphology i.e. rms roughness and grain size. The grain size measured by AFM follows the same trend as the average crystallite size as shown in inset of **figure 4.19** but it is much larger than that calculated by XRD. This ambiguity can be ascribed to the fact that AFM measurements result from agglomeration of the particles whereas XRD gives an average crystallite size

[**30**].The variation of rms roughness with pressure is shown in fig. 3 and is found out to be pressure sensitive.

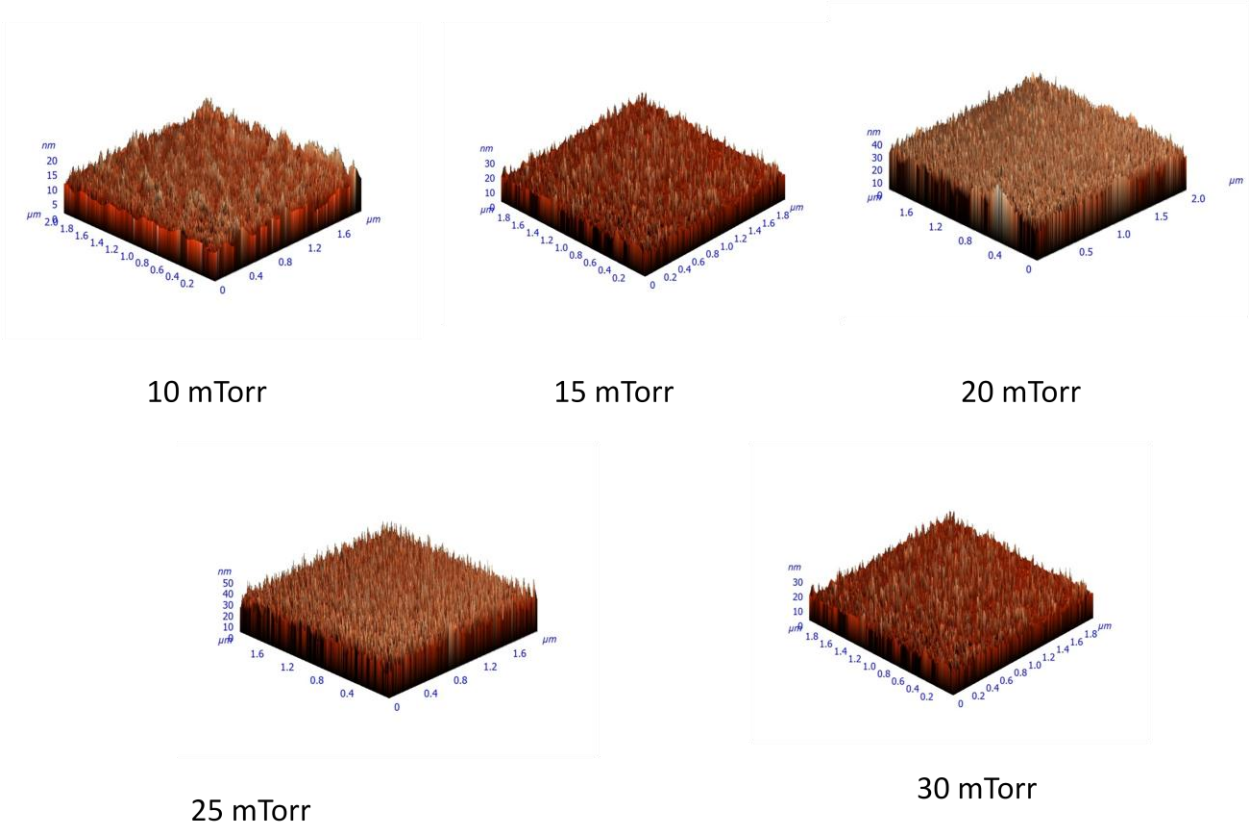

Figure 4.21 *AFM micrographs at different sputtering pressure*

4.4.2.4 Hydrophobicity

Figure 4.21 shows the variation of WCA as a function of sputtering pressure. The WCA increases from 94.03° to 97.23° as the sputtering pressure was increased from 10 mTorr to 20 mTorr and then it starts decreasing beyond 20

mTorr. It is clear from the figure that the WCA bears a linear relationship with roughness thus, justifying the Wenzel model [**188**].

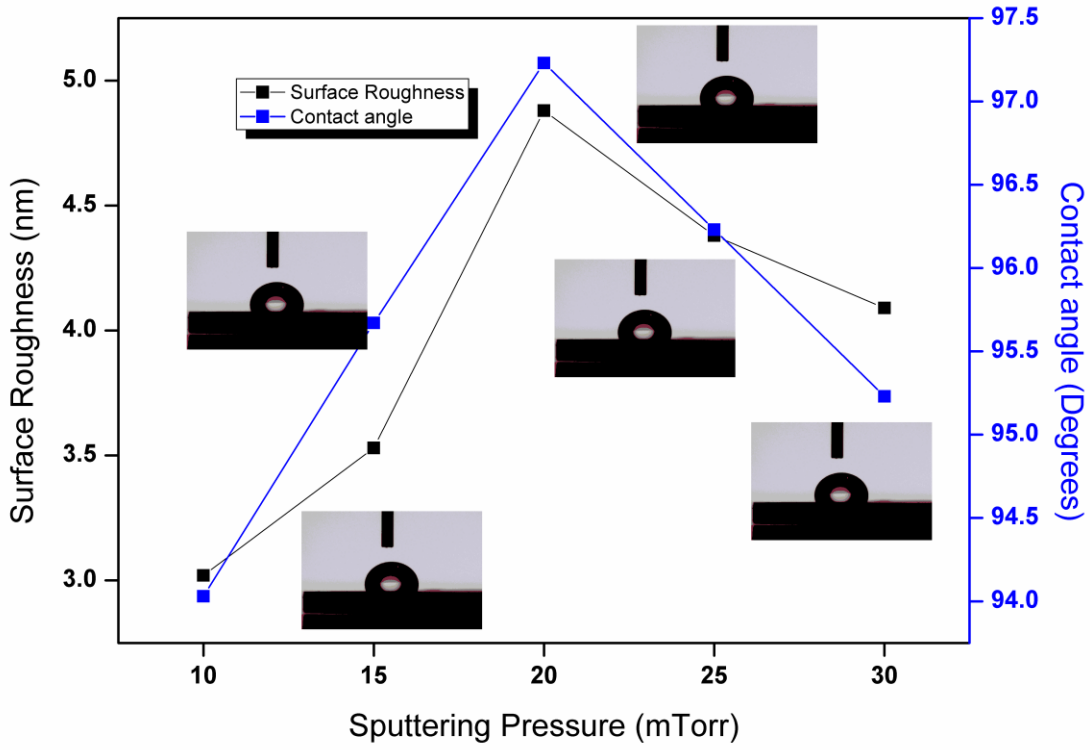

Figure 4.22 *Roughness and water contact angle of deposited film as a function of sputtering pressure*

4.4.2.5 Optical property

The transmission spectra of the deposited films is shown in **figure 4.22**. It exhibits interference-like behaviour. The transparency of the HfO_xN_y films was lower in the ultraviolet spectral range. The refractive index of the film was calculated using manificier method [**121**] at a wavelength of 550 nm and is

shown in Table I. There can be seen a gradual decrease in the refractive index from 2.03 to 1.91 as the pressure is increased from 10 mTorr to 20mTorr. This decrement can be attributed to lower incorporation of nitrogen concentration. Under lower nitrogen incorporation conditions, abundant oxygen vacancies and defects appear which contribute to the decrease of packing density. There is a drastic decrement in the refractive index beyond 20 mTorr pressure. This large drop can be ascribed to the simultaneous working of two factors in the deposited films namely decrement in nitrogen content as well as the thickness [**66**].

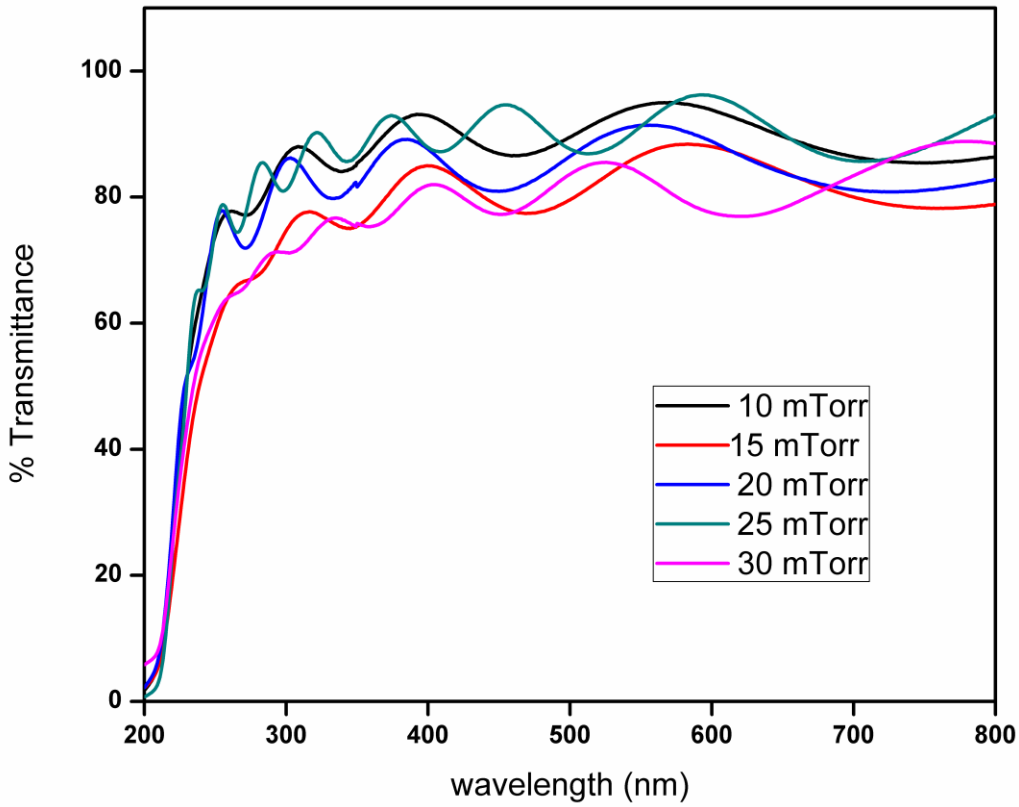

Figure 4.23 *Transmittance spectra of hafnium oxynitride at various pressure*

The optical band gap of the deposited films was calculated using Tauc relation and is shown in **Table 4.9**. The bandgap increasing from 5.04 to 5.35 as sputtering

Table 4.9 *Optical Parameters of hafnium oxynitride film*

Sputtering pressure (mTorr)	Average Transmission (%)	Refractive Index	Band Gap	Extinction Coefficient (λ=350 nm)
10	**90**	**2.03**	**5.04**	**0.026**
15	**89**	**1.95**	**5.06**	**0.031**
20	**88.5**	**1.91**	**5.08**	**0.026**
25	**81**	**1.85**	**5.29**	**0.043**
30	**80**	**1.82**	**5.35**	**0.052**

pressure was enhanced from 10 mTorr to 30 mTorr. This again may be due to increase in the insulating property due to decrement in the nitrogen content.

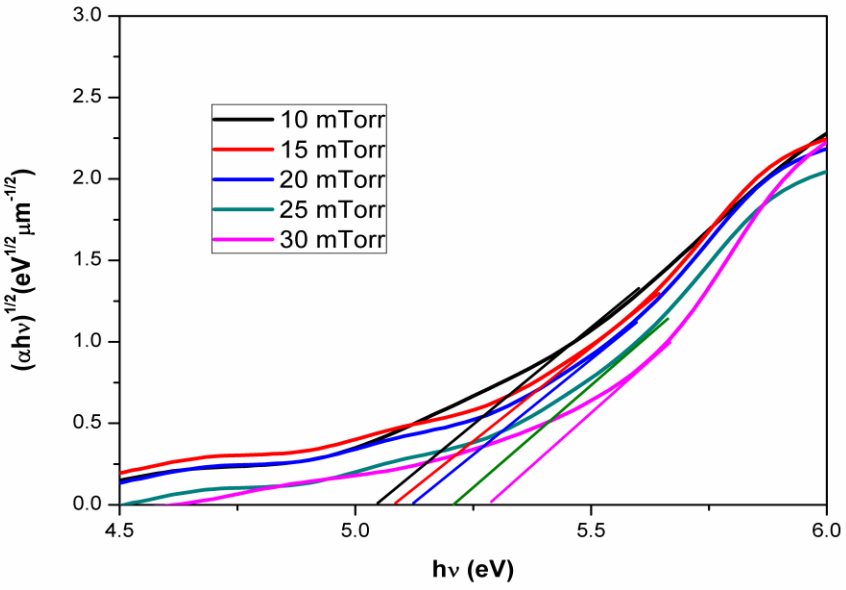

Figure 4.24 *Bandgap Variation with Sputtering Pressure*

4.4.2.6 Electrical property

Figure 4.24 shows the variation of resistivity of deposited HfO_xN_y films with sputtering pressure. The resistivity is of order of 10^5 and in the range of $0.93-1.40 \times 10^5$ Ω cm. The resistivity was following an increasing trend as pressure was increased from 10 mTorr to 30 mTorr. The resistivity of a material is dependent on factors like vacancies, dislocations, lattice strain and distortions which are common in nanocrystalline materials. These imperfections act as hurdle to the motion of charge carries and hence, increases the resistivity. As already stated that with increase in sputtering pressure, defects increases which in turn increases the resistivity.

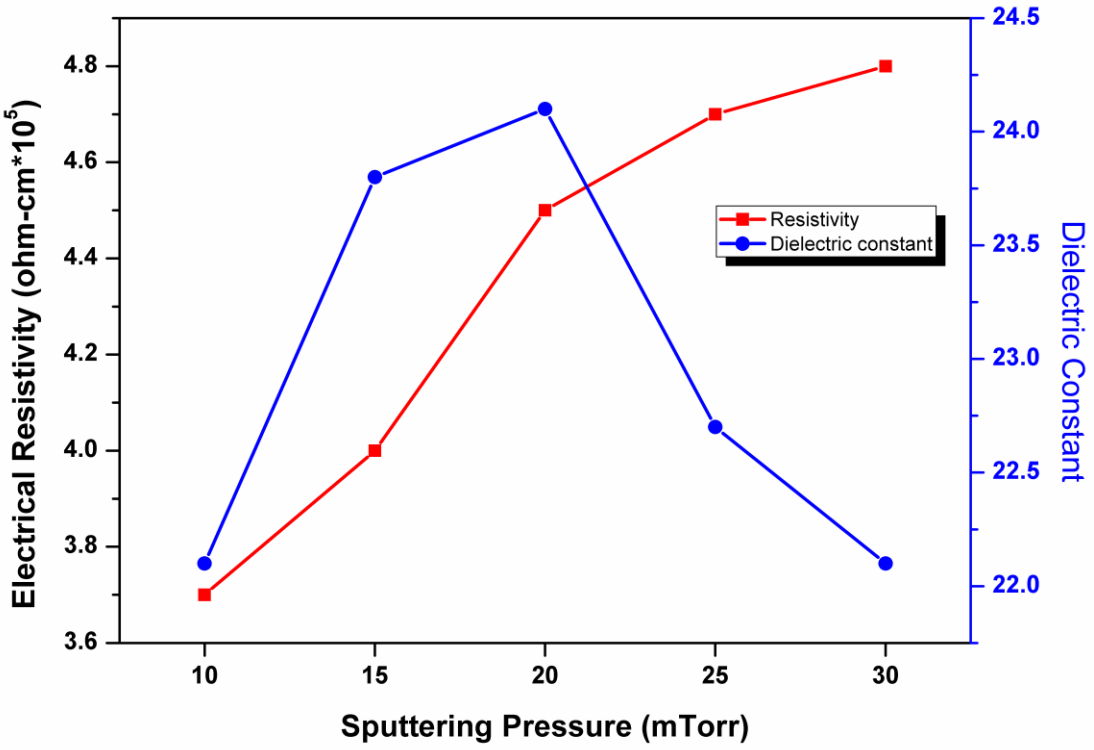

Figure 4.25 *Variation of resistivity and dielectric constant of hafnium oxynitride films as a function of pressure*

The dielectric constant of the deposited films is shown in **figure 4.24** and it is clear that it was maximum for 20 mTorr pressure and further it starts decreasing. This again can be correlated to the thickness of the film.

4.4.3 Conclusions

We have deposited nanocrystalline HfO_xN_y on glass insulators. The optimum pressure was found out to be 20 mTorr where hydrophobicity was maximum and transparency, bandgap and electrical properties were also optimum.

4.5 Effect of sputtering power on structural, hydrophobic, optical and electrical property of nanocrystalline HfO_xN_y thin film.

4.5.1 Experiment

Hafnium oxynitride films were deposited on glass and quartz substrates by DC magnetron sputtering in a custom designed 12 in. diameter chamber (Excel Instruments). The substrates were initially cleaned thoroughly in an ultrasonic bath with a mixture of distilled water and trichloroethylene and were then washed with boiled acetone. Further, the substrates were dried under nitrogen gas and then mounted on the substrate holder of the chamber.
A pure (99.99%) hafnium target of 50 mm diameter and 3 mm thick was mounted on the magnetron cathode of the chamber. The substrate to target distance was fixed to 41mm. High-purity argon (99.99%) was used as a sputtering gas while pure (99.9%) oxygen and nitrogen were used as reactive gases. The flow of the gases was controlled and measured by using mass flow controller

(MKS). A turbo based pumping system was used to achieve a base pressure below $2x10^{-6}$ Torr. The working pressure in the vacuum chamber was kept 20 mTorr and was measured by a compact gauge (Pfeiffer Vacuum). The gas pressure was carefully monitored to keep it constant as the sputtering current is highly sensitive to the sputtering pressure. The deposition was carried out at different sputtering power ranging from 20W to 60W in steps of 10 at room temperature. During each deposition, the target was pre-sputtered for 10 minutes in order to ascertain the same state of the targets in every run. The deposition time was 1 hour for each sample.

4.5.2 Results and Discussion

4.5.2.1 Structural Property

X-ray diffraction analysis was carried out to determine the phase and the preferred orientations of the HfO_xN_y film at different sputtering power. **Figure 4.26** shows the XRD patterns of the deposited films as a function of pressure. The film deposited at 20 W was amorphous in nature while a peak of (-111) orientation was grown at 30 W power. This peak correspond to the monoclinic phase of HfO_2 while HfN peak was absent at 30 W power. Both HfO_2 and HfN peaks were visible at 40 W. Their intensity increases up to 50 W power and becomes constant at 60 W power.

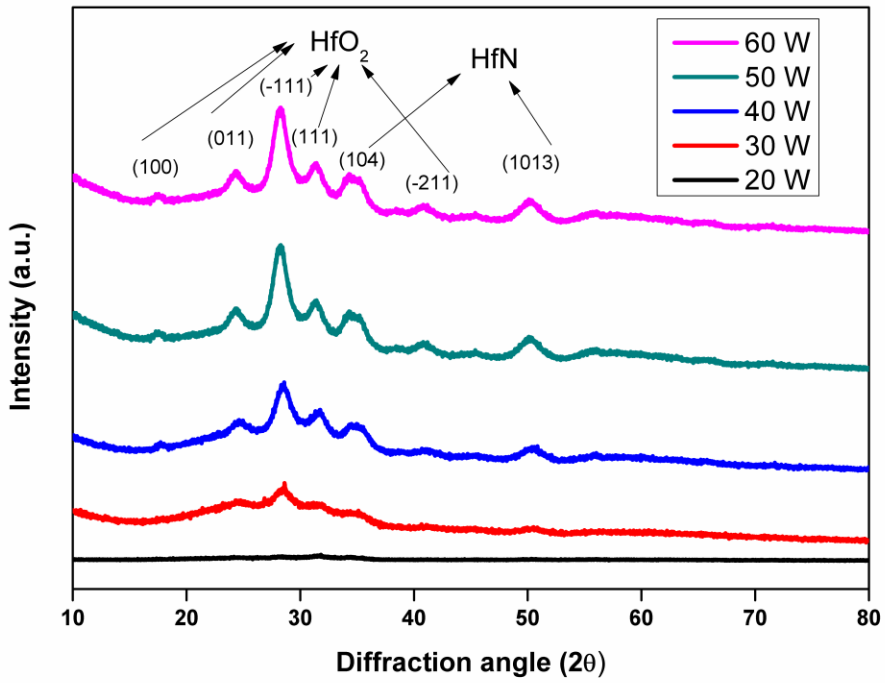

Figure 4.26 *X-ray diffraction pattern of HfOxNy films at different sputtering power*

The average crystallite size of the thin film was calculated using the Debye-Scherrer formula [**30**]. **Table 4.10** shows the variation of crystallite size with sputtering power. The crystallite size lies in the range of 8 - 15 nm. The crystallite size increases with increase in power upto 50 W and then remain constant for 60 W power. The enhancement in the crystallinity and crystal size of hafnium oxide films can be associated with the change of the kinetic energy of the sputtered particles with the DC power. As the sputtering power increases, the kinetic energy of the sputtered particles also increases. Thus, the sputtered particles have sufficient energy to migrate on the substrate and hence results in

the higher growth of the crystallite size. Therefore, the crystallinity is improved. However, the excessive supply of DC power over than 50 W may cause a degradation of the preferred orientation and limits the growth of crystallilty of deposited film. This results into same intensity dominant peak and also same crystallite size. [**29**].

Table 4.10 *Crystallite size of HfOxNy films deposited at different power*

Sputtering Power (Watt)	**Crystallite Size (XRD) (nm)**	**Crystallite size (AFM) (nm)**	**Dislocation Density (10^{15} lines/m^2)**
20	-	-	-
30	8.32	10.32	14.45
40	12.69	14.57	6.21
50	15.65	17.76	4.08
60	15.66	17.76	4.08

4.5.2.2 Surface morphology and chemical composition

The surface morphology of the films was studied using AFM. The three dimensional AFM images obtained for HfO_xN_y films deposited at various DC power at 20 mTorr pressure are shown in **figure 4.27**. The AFM micrographs corresponds to a scan area of 2 μm x 2μm. It can be seen that the HfO_xN_y films have same morphologies. They all are constituted with a large number of nanoscale asperities. **Figure 4.28** lists rms roughness of HfO_2 samples at different sputtering power. It is clear that as sputtering power is increased from

30 to 50 W, roughness value also increases from 2.45 nm to 4.88 nm and then it remain constant to 4.88 nm with further increment of power. This behaviour of roughness may be correlated to the particle size which was earlier calculated through XRD. The increment in power upto 50 W increases the particle size which in turn enhances the roughness.

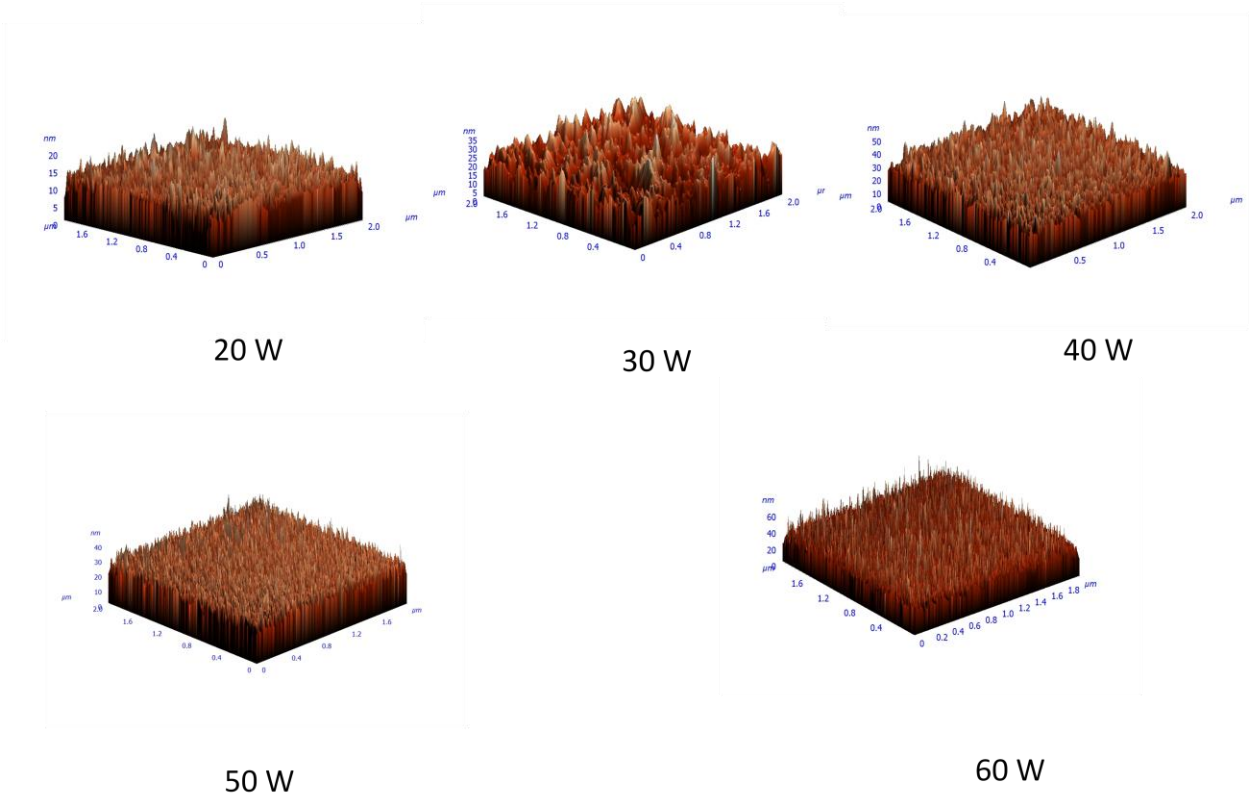

Figure 4.27 *3-D AFM micrographs of hafnium oxynitride films (a)20 W (b)30 W (c) 40 W (d) 50 W (e) 60 W*

The chemical composition analysis was done through EPMA. **Table 4.11** shows the at% of hafnium and oxygen as sputtering power is varied from 20 to

60 W. The oxygen at% is continuously increasing while nitrogen at% is decreasing as the sputtering power is increased from 20 W to 50 W. This can be associated with the fact that the increased kinetic energy due to increment in DC power enhanced the activity of the sputtered particles and thus facilitated the formation of the Hf-O bond. Therefore, the oxidation of Hf atoms is increased and the oxygen vacancy in

the thin films is decreased with increasing DC power.

Table 4.11 *Elemental analysis of HfOxNy films at various power*

Sputtering Power (Watt)	**Elemental Analysis (at.%)**		
	Hf	**O**	**N**
20	**36.67**	**50.82**	**12.51**
30	**35.97**	**53.73**	**10.43**
40	**35.44**	**57.21**	**7.35**
50	**34.81**	**59.63**	**5.56**
60	**34.83**	**59.62**	**5.55**

4.5.2.3 Hydrophobic properties

The wettability of HfO_xN_y coatings were evaluated by measuring the water contact angle using sessile drop method at ambient temperature. The variation of water contact angle and rms roughness of HfO_xN_y films as a function of sputtering power is shown in **figure. 4.28**. All the deposited samples were found to be hydrophobic and the contact angle lies in the range 90.03^o -

97.23^{o}. The contact angle and surface roughness bears a linear relationship, thus satisfying the Wenzel model. The maximum contact angle (97.23^{o}) occurs at a sputtering power of 50 W where roughness is also high (4.88 nm).

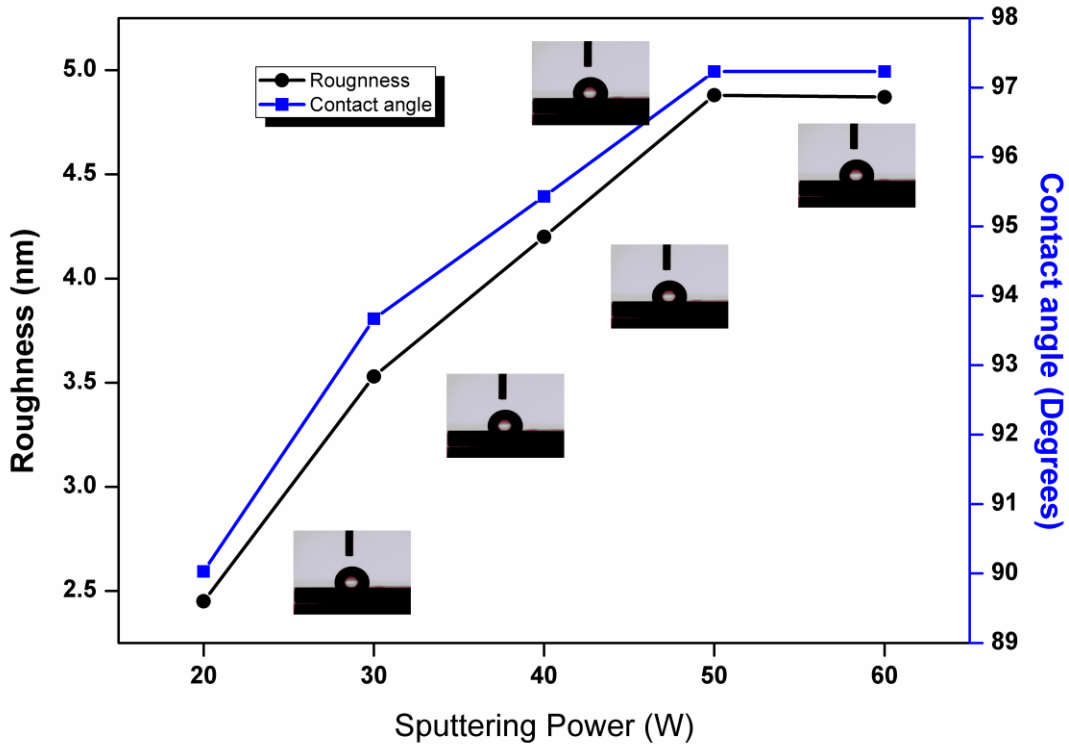

Figure 4.28 *Variation of roughness and contact angle with sputtering power*

4.5.2.4 Optical properties

The sputtering power also influences the optical properties of the deposited films. **Figure 4.29** shows the optical spectra of HfO_{xNy} films deposited at different sputtering power in the wavelength range 200-800 nm. Two important features are evident. Firstly, the transparency decreases as the power increases and secondly, the average transmission for all the samples was found out to be greater than 70% in the visible region. Maximum transparency was observed for film developed at 20 W power. The decrease in transmission as the power is increased was due to enhancement of the surface roughness. Surface roughness and transparency have inverse relationship. Providing surface roughness to the coatings means introducing sources of light scattering which in turn decreases the transparency of the films. The transmission data was used to obtain the refractive index of the film using relation provided by Manifacier [**121**]. The refractive index of the deposited samples calculated at λ=550 nm is shown in **Table 4.12**. The refractive index obtained is consistent with that reported for sputtered HfO_xN_y films [*65-66*]. Also the refractive index values of hafnium oxide films grown under the sputter power of 20, 30 and 40 W are too much lower. However the refractive index for 50 W is very close to that of bulk hafnium oxide [**62**]. Beyond 50 W power, refractive index remain

constant. This can be ascribed to the fact that the sputtered particles at 50 W power have higher kinetic energy which results into high packing density and hence higher refractive index.

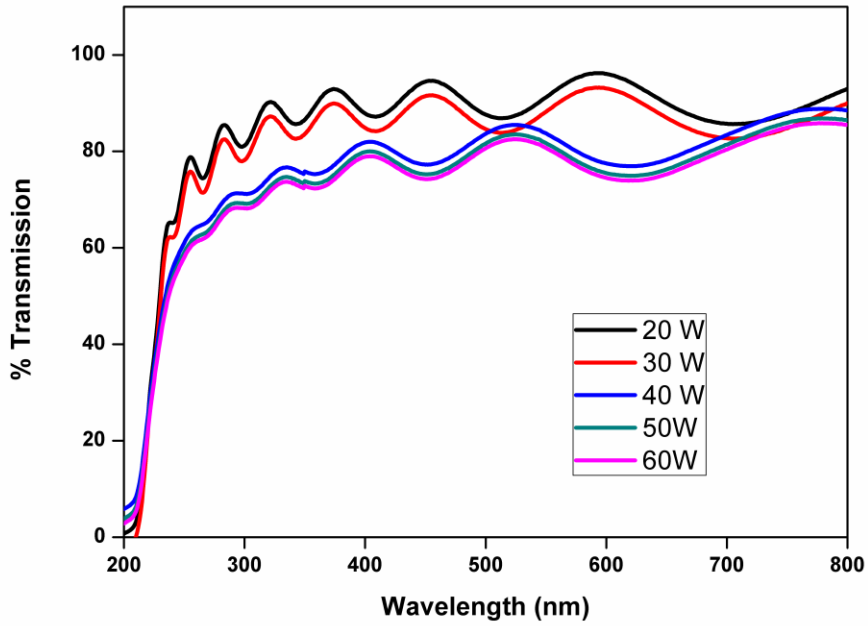

Figure 4.29 *Transmission spectra of hafnium oxynitride films at different power*

Based on the transmission spectra, the measured transmittance T is converted into absorption coefficient (α) and the band gap of the nanocrystalline HfO_xN_y films was estimated from the absorption coefficient (α) using Tauc relation.

Table 4.12 *Optical Parameters as a function of sputtering Power*

Sputtering Power **(**W**)**	**Average Transmission (%)**	**Refractive Index**	**Band Gap**	Thickness (nm)
20	**88**	**1.81**	**5.10**	**650**
30	**87**	**1.83**	**5.12**	**670**
40	**86.5**	**1.85**	**5.20**	**710**
50	**85**	**1.91**	**5.29**	**752**
60	**80**	**1.91**	**5.29**	**750**

The calculated value of band gap at different sputtering power is shown in **table 4.12**. The band gap energy is in the range of 5.10-5.29 eV. The band gap value of all the films is close to the bulk value [**46**] as well as to the theoretically calculated value [**47**] for the poly crystalline HfO_xN_y films. The variation of E_g as a function of sputtering power was found to be linear upto 50 W power. It is also observed that the changes in E_g are insignificant and were linearly increasing with the crystallite size. This reveals that quantum confinement effects are absent and small changes in bandgap may be due to lattice expansion [**48**].

4.5.2.5 *Electrical properties*

Figure 4.30 shows the variation of resistivity of deposited HfO_xN_y films with sputtering power .The resistivity is of order of 10^5 and in the range of 4.5-5.1 x 10^5 Ω-cm. The resistivity was following decreasing trend as DC power is increased from 20 to 60 W. The resistivity of a material is dependent on factors like vacancies, dislocations, lattice strain and distortions which are common in nanocrystalline materials. These imperfections act as hurdle to the motion of charge carries and hence increases the resistivity. Resistivity is also dependent on crystallite size. It is reported to increase with grain size reduction due to the increasing grain boundary volume [**13**]. As a consequence, decreased resistivity is obtained for these samples.

The dielectric constant of the film was calculated by forming a stack of ITO/HfO_2/Ag. The top electrode of Ag was fabricated using shadow mask through sputtering. Figure 4.29 also shows the plot of dielectric constant of HfO_2 film as a function of sputtering power. The dielectric constant shows an increasing trend upto 50 W power. It attains a maximum value of ~24 at 50 W power which is very close to the bulk value [14]. Further increment in power i.e. at 60 W, dielectric constant remain fixed. This behaviour of dielectric constant with increasing power for hafnium oxynitride films can be readily correlated to the thickness of the films. Natori et al. theoretically concluded that

as thickness decreases, dielectric constant also decreases [**132**]. Hwang et al. also showed through experiments that the dielectric properties of high dielectric thin films are critically dependent upon the film thickness [**74**].

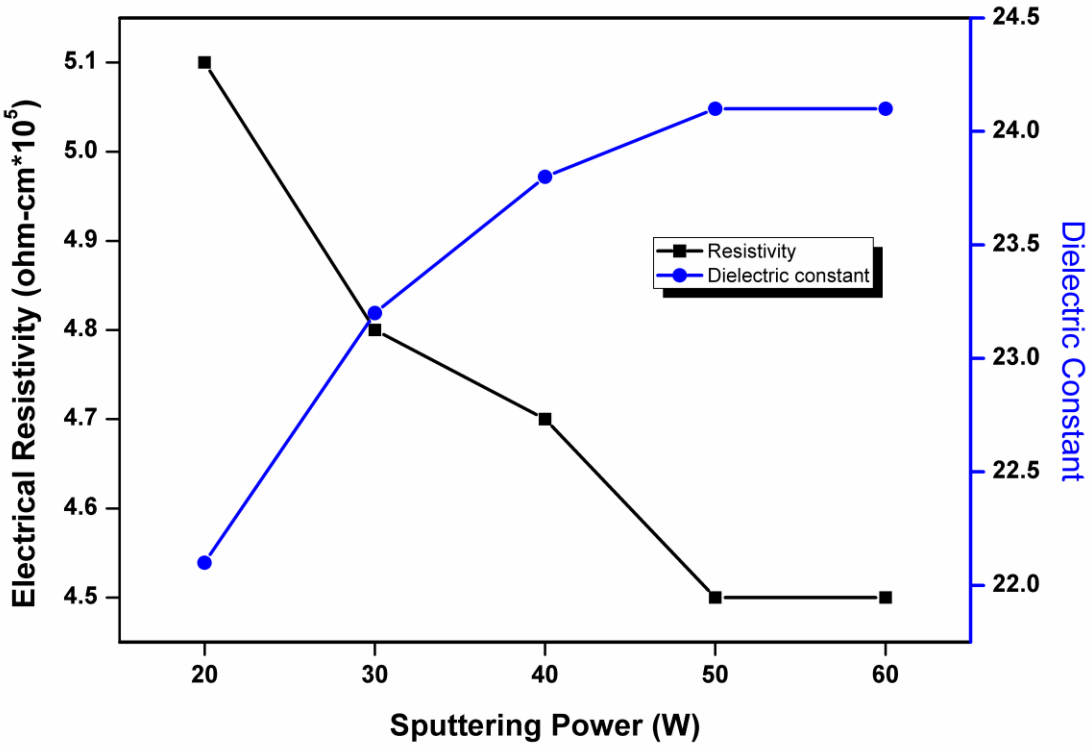

Figure 4.30 *Resistivity and dielectric variation as a function of sputtering po*

4.5.3 Conclusions

The nanostructured hafnium oxynitride films were developed on glass insulator at different DC sputtering power. The microstructural characterization

shows that all the samples (except 20 W) were crystalline in nature with adequate surface roughness to have hydrophobicity and good transparency (> 80%). The contact angle (97.23^{o}), refractive index (1.91), bandgap (5.29 eV), dielectric constant (~24) and deposition rate is maximum for the film deposited at 50 W power. However, the electrical resistivity was found to be less for 50 W power but change in resistivity is very less that it can be neglected for all practical purpose. The high bandgap values ensures that HfO_xN_y in film form still retain the dielectric property. High dielectric constant of the deposited film gives an indication that film can bear high electric field applied to outdoor insulators. Thus, parameters of hydrophobic HfO_xN_y film deposited at 50 W power found to be optimum for the glass insulator.

4.6 Breakdown Test

It is clear from the above analysis that the optimum sputtering parameters for the HfO_xN_y film for outdoor glass insulators are room temperature, 50 W sputtering power and 20 mTorr sputtering pressure. The deposited films at these parameters are hydrophobic, transparent, possess high resistivity and high dielectric constant. Breakdown test was carried out for these optimized HfO_xN_y

deposited glass insulators and the breakdown strength was come out to be 25 kV/mm which is greater than that of uncoated glass (20 kV/mm).

Chapter 5
Synthesis and Characterization of Nanocomposite Hafnium-Titanium Oxide

5.1 Introduction

In a broad sense the word composite means made of two or more different parts. A composite is a combination of two or more different materials that are mixed in an effort to blend the best properties of both. A composite material consists of an assemblage of two materials of different natures completing and allowing us to obtain a material of which the set of performance characteristics is greater than that of the components taken separately. Mostly composite material consists of one or more discontinuous phases of distributed in one continuous phase [**144**]. Hybrid components are that which are with several discontinuous phases of different natures. Discontinuous phase is usually harder and with superior mechanical properties than continuous phase. The continuous phase is called "matrix". The discontinuous phase is called "reinforcement, or reinforcing material [**130-131**].

A nanocomposite is a composite material, in which one of the components has at least one dimension is nanoscopic in size that is around 10^{-9}m. The progress

in nanocomposites is varied and covers many industries. Nanocomposites can be made with a variety of enhanced physical, thermal and other unique properties. They have properties that are superior to conventional microscale composites and can be synthesized using simple and inexpensive techniques. Materials are needed to meet a wide range of energy efficient applications with light weight, high mechanical strength, unique color, electrical properties and high reliability in extreme environments. Applications could be as diverse as biological implant materials, electronic packages, and automotive or aircraft components. Although some of the properties will be common between the applications, others will be quite different. An electronic package polymer composite must be electrically insulating, while an aircraft component may need to be electrically conductive to dissipate charge from lightning strikes.

On the bases of their engineering applications, nanocomposites can be classified either,

(1) Functional materials i.e. based on electrical, magnetic, and/or optical behaviour, example nanolayered semiconductor (semiconductor superlattice) composed of alternating layer of single crystal GaAs and GaAl [**158**].

(2) Structural materials i.e. based on their mechanical properties [**160**].

At present, plasma chemical vapor deposition (CVD) and physical vapor deposition (PVD) methods and their combinations are successfully used to deposit nanocomposite coatings. Plasma CVD [**164**], magnetron sputtering [**7**.96] , pulsed laser deposition [**50**-**51**], cathodic arc evaporation [**56,88**] and dual ion beam assisted deposition are good methods for a basic research but for large scale industrial applications the PVD methods based on sputtering is more convenient as it provides following desirable properties.

(1) Contamination free deposition

(2) Reproducibility

(3) Uniform Deposition

(4) Higher deposition rate

The nanocomposite films are usually sputtered from an alloy target [**98**]. In this case, it is, however, very difficult to change continuously the chemical composition of the sputtered film. This can be achieved, when the two-phase nanocomposite film is sputtered simultaneously from two targets made of different pure elements, i.e. when a dual magnetron is used and co-sputtering is carried out.

Our previous study has clearly depicted that the hafnium oxide possesses hydrophobic property in addition to the high dielectric constant, good mechanical and thermal strength. TiO_2 has a high permittivity of nearly 60 and highly possible of forming solid solutions with HfO_2 [**1**], in which a thin film system serving the purpose can be formed. Methods of obtaining such systems are possible in the form of composite thin films involving direct incorporation of TiO_2 and HfO_2 [**5,7,9,10**].

Hafnium oxide–Titanium oxide nanocomposite films are of interest for a number of fields that require the combinations of properties inherent to the two constituent materials, namely high hardness, high electrical resistance, hydrophobicity, resistance to oxidation and chemical attack as well as thermal stability. A significant increase in dielectric constant has also been observed when promising high-k gate dielectric material HfO_2 has been doped with oxides including Al_2O_3 [19], ZrO_2 [**5**], and TiO_2 [**107**]. Of particular interest is the doping of TiO_2 with HfO_2 to produce a hydrophobic as well as higher dielectric constant coating. However, relatively few attempts to insert TiO_2 into hafnia have been reported to obtain hydrophobic property. More et al has reported the hydrophobic property of TiO_2 using successive ionic layer adsorption and reaction (SILAR) method [**35**].

High-rate deposition of mixed oxide films through sputtering does, however, pose a significant challenge [**1**]. This is due to the poisoning effect of metallic targets in reactive plasmas, in particular titanium, which causes a drastic drop in the rate of film growth. Numerous examples exist in the literature where the effects of target poisoning are either controlled or minimised. In the case of hafnia–titania composites, one such method has been the employment of radio-frequency power supplies with very high pumping speed to ensure a hysteresis-free process. This method enabled controlled growth conditions, using both sputtering from ceramic targets as well as reactive sputtering from metallic targets.

Therefore, the combination of HfO_2 and TiO_2 as complementary materials is a promising approach to enhance the hydrophobicity of the insulators using RF magnetron sputtering technique.

Literature has revealed that the temperature and power dependent nanocomposites give better dielectric, mechanical and hydrophobic properties [**147**]. Hence, substrate temperature and sputtering power will be varied to investigate structural, optical, hydrophobic and electrical property of hafnium-titanium oxide nanocomposite.

5.2 Effect of Substrate Temperature on Structural, Optical, Hydrophobic and electrical properties of DC sputtered Nanocomposite Hafnium-Titanium Oxide thin films

5.2.1 Experimental Detail

Two metallic targets of Hafnium and titanium (99.99% pure, 2 in. diameter and 5-mm thick) were used for depositing nanocomposite transition metal oxide films by reactive magnetron sputtering on glass substrates. The targets were arranged confocally for co-sputtering and substrate to target distance was kept constant at 50 mm during deposition. The substrates were cleaned by rinsing in ultrasonic baths of acetone and methanol. The base pressure was better than 4×10^{-6} torr and the sputtering was carried out in a argon atmosphere along with oxygen as reactive gases. The flow rates of argon and oxygen were 10sccm, 1.3sccm and 40sccm respectively. The deposition time, and gas pressure were kept constant at 60 minutes and 15 mTorr respectively, for all depositions. The power of hafnium target was kept 50 W while that of titanium was kept 150 W. The substrate temperature was varied from 100 °C to 500 °C.

5.2.2 Results and Discussion

5.2.2.1 Structural property

Typical XRD patterns of HfTiO films deposited at different substrate temperature are shown in **figure 5.1**. It can be seen that all the deposited films are crystalline in nature with the pattern of orthorhombic hafnium titanium oxide [**JCPDS 00-014-0103**] and preferred orientation at (111) phase. In addition to the dominant peak (111) existing at diffraction angle of approx. 30^{o}, weak peaks of orientation (103) and (101) were also visible in the XRD pattern. The intensity of the dominant peak was found to be intensified with deposition temperature and was maximum at 500 °C. The reactivity of oxygen atoms arriving at the substrate enhances with the increase of substrate temperature which leads to more crystallization of the films. The coherently diffracting domain size (d_{XRD}) was estimated from the integral width of the diffraction lines using the Scherrer formula.

Table 5.1 shows the variation of crystallite size with substrate temperature. The mean crystallite size was found in the range 10.4-16.43 nm. The average crystallite size increases with increasing deposition temperature due to greater thermal activation and diffusion. Narrowing of XRD peaks width

with increasing temperature agrees well with the above observation of crystallite coarsening at higher deposition temperature.

Table 5.1 *Parameters of HfTiO film*

Temperature (°C)	Crystallite size (nm)	Refractive index	Bandgap (eV)	Thickness (nm)
100	**10.34**	**3.26**	**1.94**	**850**
200	**11.23**	**3.37**	**1.97**	**838**
300	**12.01**	**3.42**	**1.98**	**802**
400	**14.89**	**3.47**	**2.12**	**790**
500	**16.43**	**3.48**	**2.23**	**785**

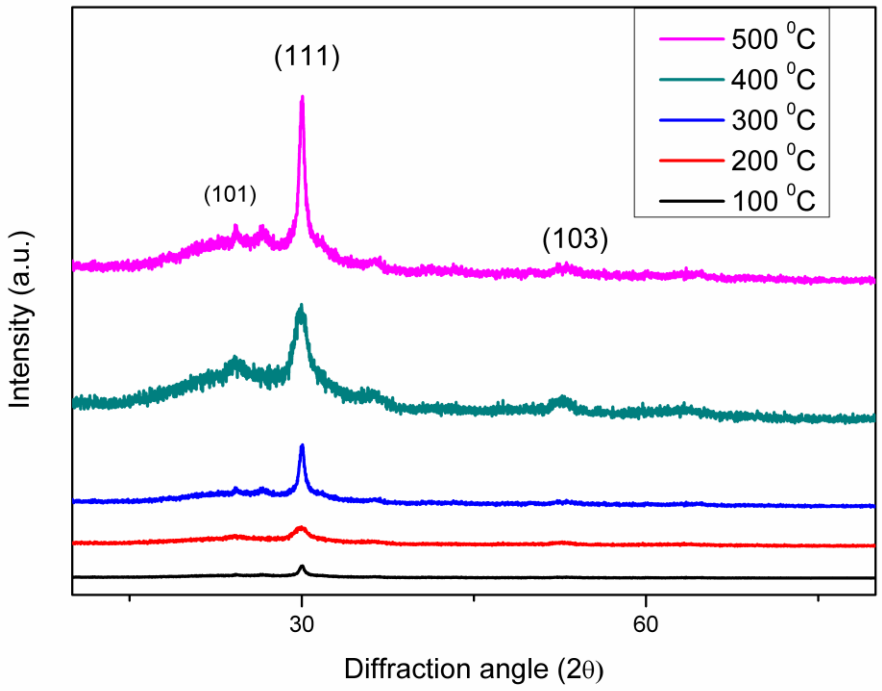

Figure 5.1 *XRD pattern of HfTiO films at different substrate temperature*

5.2.2.2 Composition analysis

The elemental analysis of HfTiO thin film was done through EDS. The variation of the measured composition on the sample is within±0.5 (within EDS error limits). **Table 5.2** lists the at.% of hafnium, oxygen and titanium in the deposited sample at different substrate temperature. It is clear from the table that oxygen at. % almost remain constant while the Ti at. % and Hf at.% changes with the substrate temperature and the theoretical ratio of three element i.e. 1:1:1 was obtained at 500 °C.

Table 5.2 *Elemental analysis of HfTiO films*

Temperature (Degrees)	at.% Hf	at.% Ti	at.% O
100	28.43	38.23	33.34
200	29.54	36.94	33.32
300	30.44	36.28	33.28
400	32.60	34.12	33.28
500	33.34	33.06	33.30

5.2.2.3 Morphological study

The effect of deposition temperature on the microstructure and morphology of the HfTiO was studied by AFM images. **Figure 5.2** shows the 3-D AFM micrographs of HfTiO films deposited at different substrate temperature. It can be observed that the microstructure of all deposited films was characterized by high density columnar structure. Roughness of a thin film plays an important role in describing some of its properties like optical, mechanical and wettability. The root mean square (rms) roughness of the HfTiO film was evaluated and its variation with deposition temperature was portrayed in **Figure 5.3**. The rms roughness bear a linear trend with temperature and lie in the range 7.23- 11.89 nm. The rising trend of surface roughness can be explained through the growth of crystallite size. The crystallize size of the film gradually increases from

10.43 nm to 20.43 nm with the substrate temperature which in turn increases the roughness.

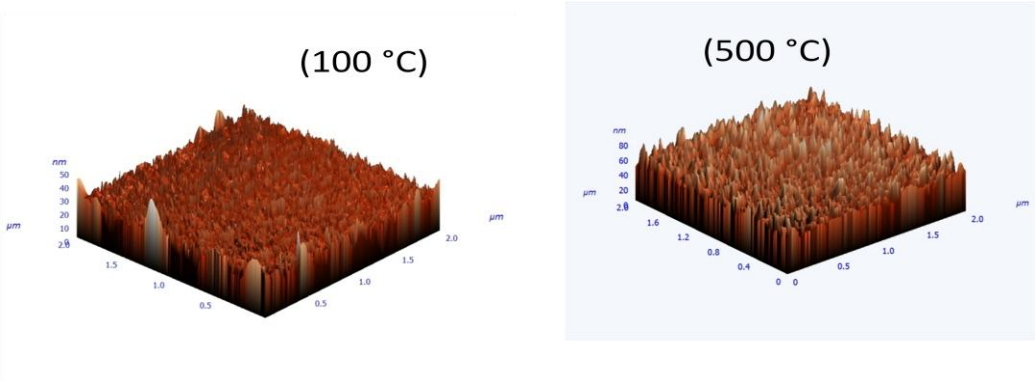

Figure 5.2 *AFM micrographs of HfTiO films at different temperature*

5.2.2.4 Hydrophobicity

The wetting behaviour of HfTiO was characterized by the value of the water contact angle. The water contact angle of a solid is an important parameter in surface science and its measurement provides a simple and reliable technique to interpret the hydrophobic behaviour of surface and its energies. The static water contact angles of HfTiO thin films were measured with water contact goniometry at room temperature by dropping water droplets of 3µl on the respective surfaces using the sessile drop method. A minimum of ten measurements on different spots was recorded for each sample**. Figure 5.3** shows the variation of water contact angle (WCA) with temperature and its

correlation with roughness. All samples were found hydrophobic. Also, the hydrophobicity i.e. WCA bears a linear relationship with surface roughness. The minimum WCA was 103.2 ° for the sample deposited at 100 °C and the maximum contact angle was 107.2° for the sample deposited at 500°C. The maximum (7.23 nm) and the minimum (11.89 nm) surface roughness occurs at the highest and the smallest contact angle. Thus, all samples are satisfying the surface roughness model of the Wenzel.

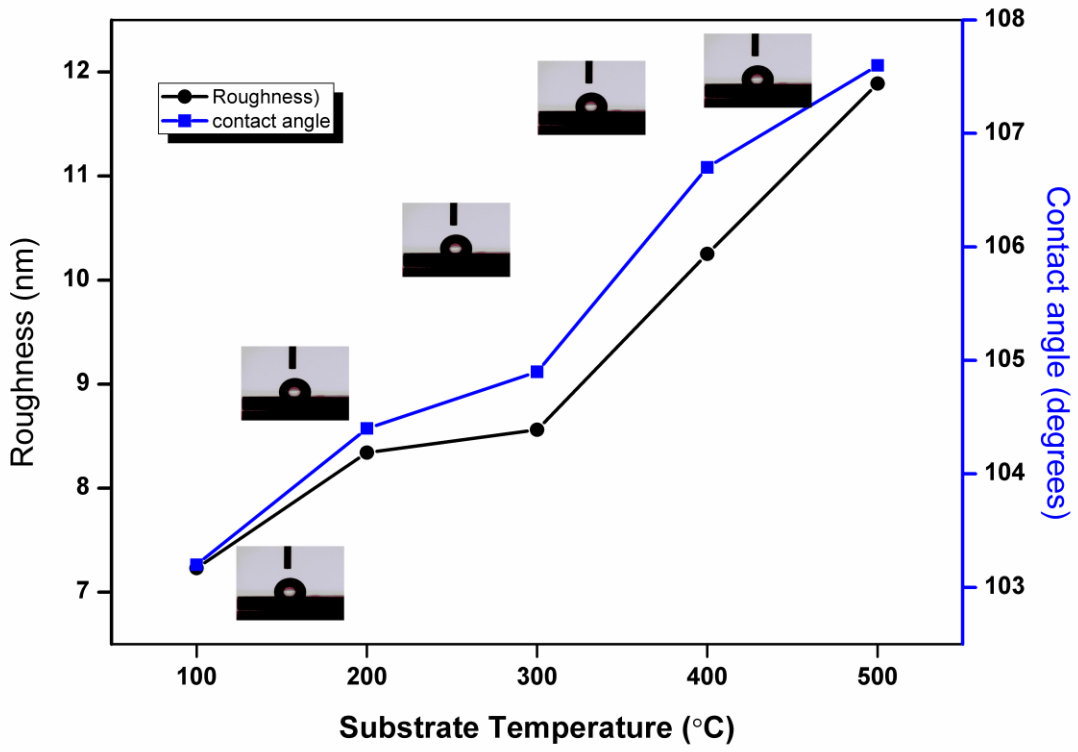

Figure 5.3 *Variation of roughness and Contact angle with substrate temperature*

5.2.2.5 Optical Properties

To investigate the effect of substrate temperature on the optical properties of nanocomposite films, the transmittance spectra of all the samples was measured in the spectral range of 200-800 nm wavelengths. The representative optical transmission spectrum of HfTiO films was shown in **Figure. 5.4**. The oscillations in the spectra were due to the interference effect. The experimental results show that the transparency of the films decreases as the deposition temperature increases. The average transmission was highest for film the film deposited at 100 °C while it was least for the film deposited at 500 °C temperature. The transmission coefficient reduction with temperature can be attributed to changes in the crystallite size and surface roughness of the films. Large crystallite size leads to higher roughness which in turn increases the sources of light scattering and thus, reduces the transmission level. The refractive index of the deposited films was calculated using transmission data using Manifacier model [**122**] and shown in **Table 5.1.** It is clear from the table that the refractive is increasing with temperature. The probable reason may be high packing density with the increasing substrate temperature. The refractive index lies in the range 1.94-2.23 which is close to that of HfO_2 [**105**].The bandgap of the deposited film was calculated using Tauc relation and shown in **Table 5.1**. The bandgap of the nanocomposite film is lower than that of HfO_2

but higher than that of TiO_2 [**107**]. The thickness was also calculated from the transmission data and was found out to be decreasing with temperature.

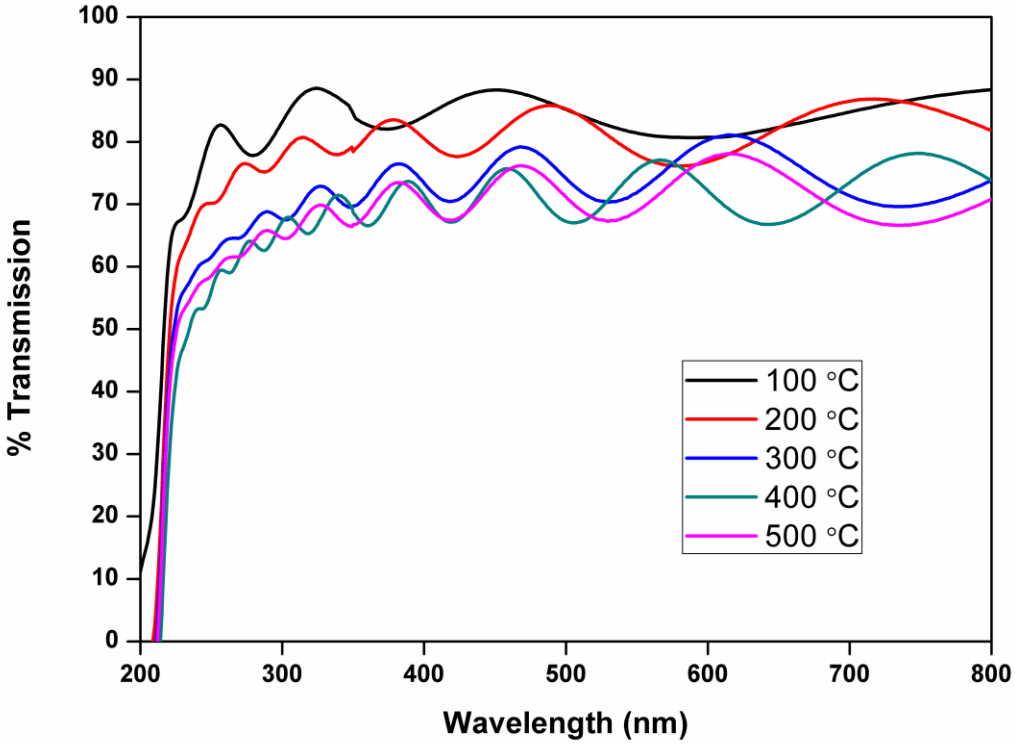

Figure 5.4 *Transmission curve of HfTiO as a function of Temperature*

5.2.2.6 Electrical Property

The variation of electrical resistivity with the substrate temperature is shown in **figure 5.5**. The resistivity is decreasing with the temperature and is of the order

10^4 Ω-cm. The order of resistivity is similar to that of HfO_2. The decrement in the resistivity can be attributed to the grain size as with the decrease in the grain size the grain boundary volume increase which in turn increases the resistivity [**13,175**]. The variation of the dielectric constant is also shown in the **figure 5.5**. The dielectric constant [**173**] was higher at 100 °C in comparison to that of 500 °C but the variation is very small.

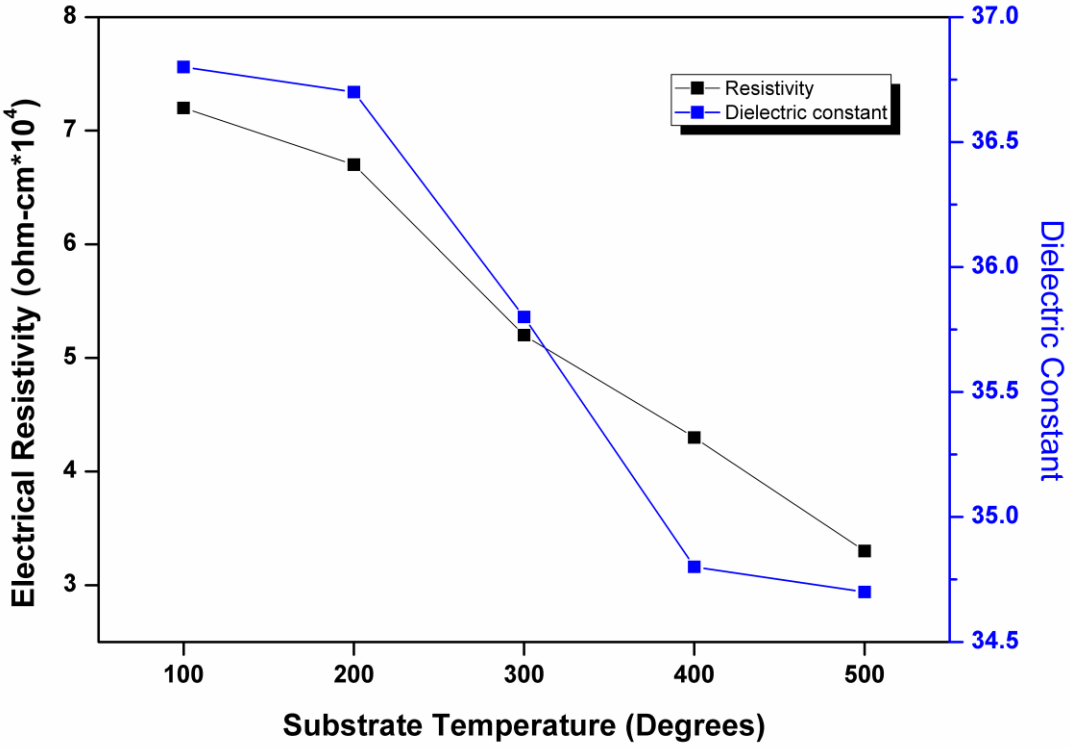

Figure 5.5 *Variation of resistivity and dielectric constant with temperature*

5.2.3 Conclusions

Nanocrystalline HfTiO films were deposited on glass insulators. Higher hydrophobicity was obtained at higher substrate temperature i.e. 500 °C with resistivity of order 10^4 Ω-cm. The dielectric constant was also high (~34) atthis temperature. However, the bandgap was low in comparison (~3 eV) to HfO_2 films. In all, 500 °C can be considered as optimum temperature for hydrophobic HfTiO films.

5.3 Effect of Power on Structural, Optical, Hydrophobic and Electrical properties of Nanocomposite Hafnium-Titanium Oxide Thin films

5.3.1 Experimental Detail

The nanocomposite Hafnium-Titanium oxide films were deposited by RF magnetron sputtering on glass, quartz and ITO glass substrates in a custom designed 12-in. diameter chamber (Excel Instruments, India) at room temperature. A 2-in. diameter and 5-mm thick hafnium and titanium target of 99.99% purity was used for the sputtering. The substrates were thoroughly cleaned by rinsing in an ultrasonic baths of acetone and methanol and dried under nitrogen gas. The chamber was initially evacuated by a turbo molecular pump backed by a rotary pump. During each deposition, the base pressure was better than 2×10^{-6} Torr and the distance between the substrate and the target was kept 50 mm. The sputtering was carried out in an argon (99.999 % pure) atmosphere while oxygen was used as a reactive gas. The flow rate of oxygen and argon in the chamber was 10 sccm and 20 sccm respectively. The gas pressure was kept 15 mTorr for all depositions. The HfTiO coating was fabricated by sputtering parameter namely power. The sputtering power of titanium target was varied from 110 to 150 W in steps of 20 W keeping deposition time 1hr. Before starting the actual experiment, the target was pre-

sputtered for 15 min with a shutter located in between the target and the substrate. This shutter was used to control the deposition time.

5.3.2 Results and Discussion

5.3.2.1 Structural Analysis

X-ray diffraction analysis was carried out to determine the preferred orientations and structural transformation of HfTiO films on glass substrate at different sputtering power. **Figure 5.6** shows the XRD pattern of the nanocrystalline films of hafnium oxide deposited at varying DC power. The XRD curve clearly reveals that all deposited films are crystalline in nature and the dominant peak occurs at $2\theta \approx 30^0$ which corresponds to (111) orientation of orthorhombic phase. The other less dominant peak belongs to (101) and (103) orientation. Moreover, the diffraction peaks in the XRD patterns become more intense and sharper as the RF power of titanium was increased from 110 W to 150W, indicating an enhanced crystallinity for the films deposited at high DC power. The average crystallite size of the thin film was calculated using the Debye-Scherrer formula. **Table 5.3** shows the variation of crystallite size with sputtering power. The crystallite size lies in the range of 10 - 16 nm. The crystallite size increases with increase in power. The enhancement in the crystallinity and crystal size of HfTiO films can be associated with the change

of the kinetic energy of the sputtered particles with the RF power. As the sputtering power of titanium increases, the kinetic energy of the sputtered particles also increases. Thus, the sputtered particles have sufficient energy to migrate on the substrate and hence results in the higher growth of the crystallite size. Therefore, the crystallinity is improved.

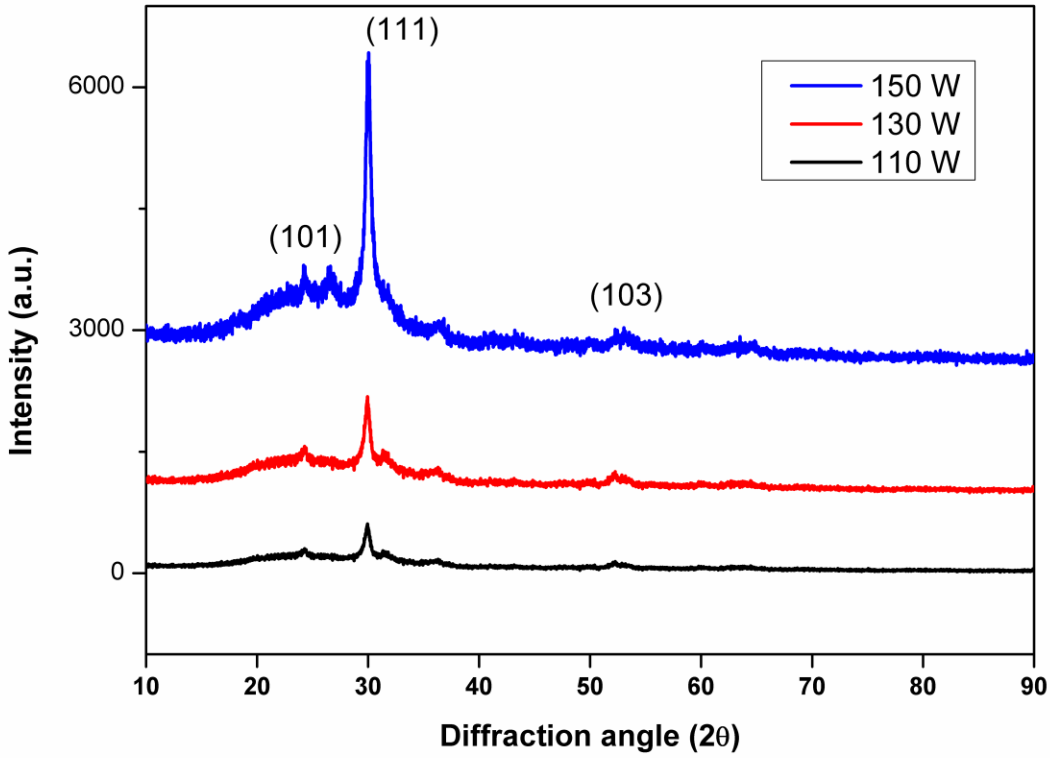

Figure 5.6 *XRD patterns of HfTiO films deposited at different sputtering power*

5.3.2.2 Surface morphology and chemical composition

Table 5.3 *Parameters of HfTiO film at different power*

Sputtering Power (W)	Crystallite size (nm)	Refractive index	Bandgap (eV)	Thickness (nm)
110	**10.45**	**3.34**	**1.97**	**650**
130	**13.34**	**3.42**	**2.10**	**705**
150	**16.43**	**3.48**	**2.23**	**785**

The surface morphology of the HfTiO films was studied using AFM. The three dimensional AFM images obtained for HfTiO films deposited at various RF power at 15mTorr pressure are shown in **figure 5.7**. The AFM micrographs corresponds to a scan area of 2μm x 2μm.It can be seen that the HfTiO films have same morphologies. They all are constituted with a large number of nanoscale asperities. Each asperity consists of surface nanograins that are used to form a surface peak. However the size and roughness of these varies with sputtering power. **Figure 5.8** lists rms roughness of HfTiO samples at different sputtering power. It is clear that as sputtering power is increased from 110 to 150 W, roughness value also increases from 8.23 nm to 11.89 nm This behaviour of roughness may be correlated to the particle size which was earlier

calculated through XRD. The increment in power upto 150 W increases the particle size which in turn enhances the roughness.

Figure 5.7 *AFM micrographs of film deposited at different sputtering power of titanium.*

The chemical composition analysis was done through EDS. **Table 5.4** shows the at% of hafnium and oxygen as sputtering power is varied from 110 to 150 W. The O:Hf:Ti ratio is approximately one for film deposited at 150 titanium power while for all other deposited samples it is different.

Table 5.4 *Elemental analysis of HfTiO films at different power*

Sputtering Power (W)	at.% Hf	at.% Ti	at.% O
110	29.44	37.54	33.02
130	31.55	35.25	33.20
150	33.34	33.06	33.30

5.3.2.3 Hydrophobic property

The wettability of HfTiO coatings were evaluated by measuring the water contact angle using sessile drop method at ambient temperature. The distilled deionised water droplets (about 3 μl) were dropped on the deposited coating surfaces using a microsyringe. The average value of the water contact angle was determined by experimental drop profiles at five different positions for the same sample. The variation of water contact angle and rms roughness of HfO_2 films as a function of sputtering power is shown in **figure 5.8**. All the deposited samples were found to be hydrophobic [**80**] and the contact angle lies in the range 103.3^o-107.6^o. The contact angle and surface roughness bears a linear relationship, thus satisfying the Wenzel model. The maximum contact angle (107.6^o) occurs at a sputtering power of 150 W where roughness is also high (11.89 nm).

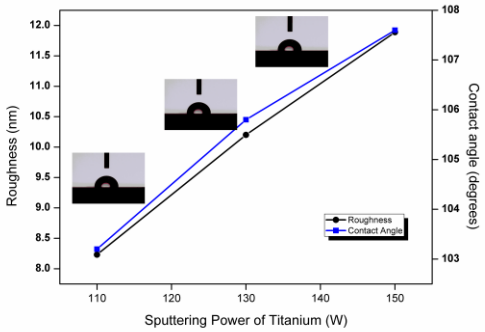

Figure 5.8 *Contact angle and roughness of deposited HfTiO films as a function of power*

5.3.2.4 Optical Property

To investigate the effect of substrate temperature on the optical properties of nanocomposite films, the transmittance spectra of all the samples was measured in the spectral range of 200-800 nm wavelengths. The representative optical transmission spectrum of HfTiO films was shown in **Fig. 5.9**. The oscillations in the spectra were due to the interference effect. The experimental results show that the transparency of the films increases as the power increases. The refractive index of the deposited films was calculated using transmission data using Manifacier model [**121**] and shown in **Table 5.3.** It is clear from the table that the refractive index is increasing with power. The probable reason may be high packing density with the increasing power. The refractive index lies in the range 1.97-2.23 which is close to that of HfO_2.The bandgap of the deposited film was calculated using Tauc relation [**77**] and shown in **Table 5.3**. The bandgap of the nanocomposite film is lower than that of HfO_2 but higher than that of TiO_2. The thickness was also calculated from the transmission data [**167**] and was found out to be increasing with temperature

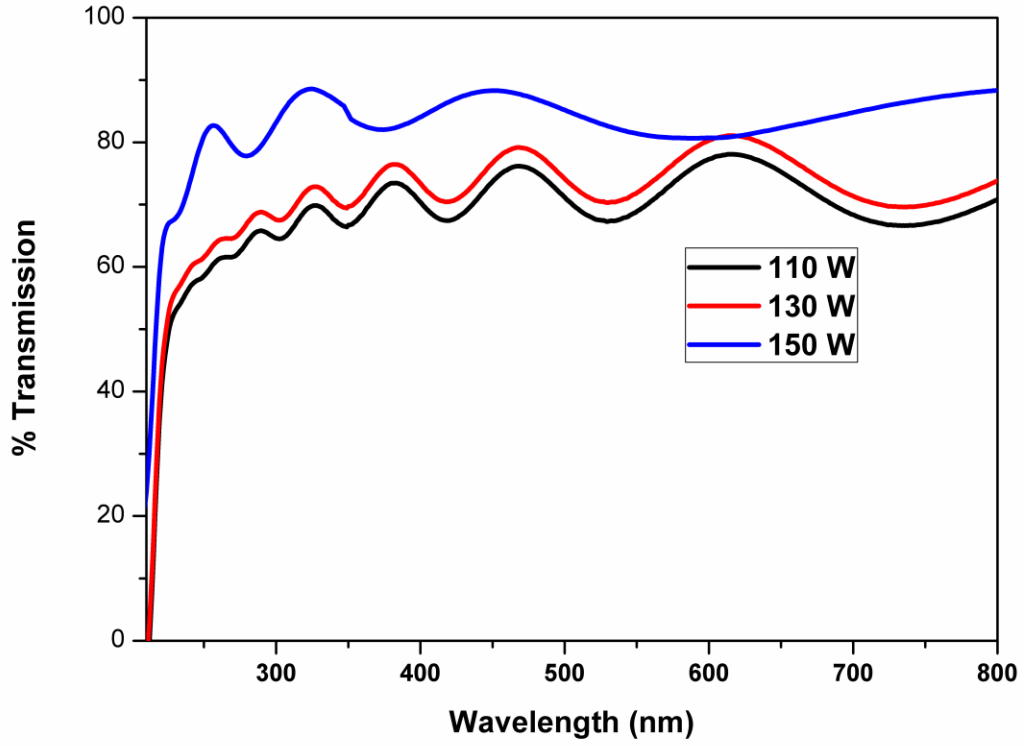

Figure 5.9 Transmission spectrum of HfTiO samples deposited at different power.

5.3.2.5 Electrical Property

The variation of electrical resistivity with the sputtering is shown in **figure 5.10** The resistivity is decreasing with the temperature and is of the order 10^4 Ω-cm. The order of resistivity is similar to that of HfO_2. The decrement in the resistivity can be attributed to the grain size as with the decrease in the grain size the grain boundary volume increase which in turn increases the resistivity. The variation of the dielectric constant measured through impedance analyzer

[**163**] is also shown in the **figure 5.10** The dielectric constant was higher at higher power because of higher thickness [**74**].

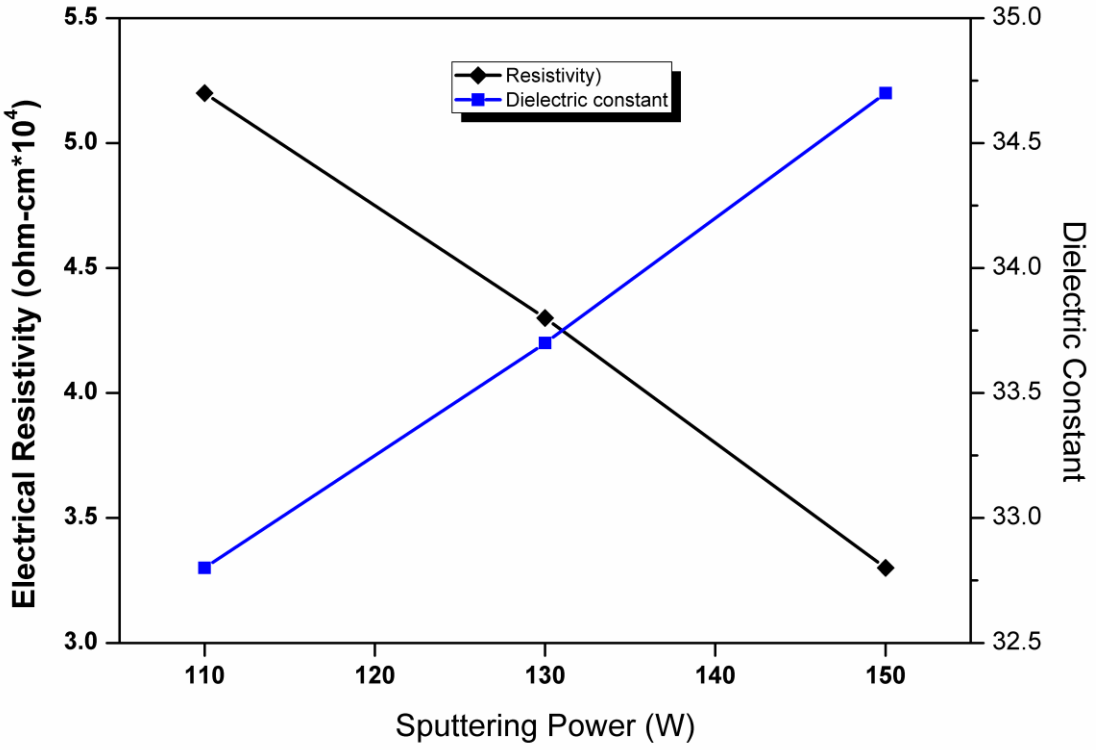

Figure 5.10 *Variation of resistivity and dielectric constant with power*

5.3.3 Conclusions

Nanocrystalline HfTiO films were deposited on glass insulators. Higher hydrophobicity was obtained at higher sputtering power with resistivity of order 10^4 Ω-cm. The dielectric constant was also high (~34) at this power. However, the bandgap was low in comparison (~3 eV) to HfO_2 films. In all,

150 W of sputtering power for titanium target can be considered as optimum power for hydrophobic HfTiO films.

5.4 Breakdown Test

It is clear from the above analysis that the optimum sputtering parameters for the HfTiO film for outdoor glass insulators are 500 °C, 50 W sputtering power for hafnium and 150 W power for titanium target. The deposited films at these parameters are hydrophobic, transparent, possess good resistivity and high dielectric constant. Breakdown test was carried out for these optimized HfTiO films deposited glass insulators and the breakdown strength was come out to be 37 kV/mm which is greater than that of uncoated glass (20 kV/mm).

Chapter 6
Conclusions and Future Scope

The main objective of the present work was to synthesize high quality hydrophobic dielectric coatings for the glass insulators to mitigate contamination problem in high voltage systems .Three type of nanostructured hydrophobic coatings were synthesized namely Hafnium oxide, hafnium oxynitride and hafnium titanium oxide by using DC/Rf sputtering technique. The effect of sputtering parameters on structural, hydrophobic, optical and electrical properties of above mentioned films were also studied. The following is a brief summary and conclusions made based on the results obtained on the aforementioned coatings. The suggestions for the future work are proposed at the end.

6.1 Effect of sputtering parameters on properties of Hafnium oxide films

The hafnium oxide films deposited on glass insulators under different sputtering parameters shows hydrophobic behaviour with polycrystalline nature. The film exhibits resistivity of order 104 Ω-cm and a high dielectric constant. The band gap was also high i.e. > 5 eV and transparency was >80% for most of the films. All these parameters were desirable for the required films. The optimum sputtering parameter for the HfO_2 films were

(i) As deposited in Ar gas

(ii) 15 mTorr sputtering pressure

(iii) 50 W DC power

The water contact angle was 102.3°, resistivity was 1.31×10^4 Ω-cm, dielectric constant was ~22 and the bandgap was 5.32 eV at the above mentioned optimized sputtering parameters. The optimized coated insulator also possess high breakdown strength (23 kV/cm) in comparison to uncoated glass insulator (20 kV/mm).

6.2 Effect of sputtering parameters on properties of Hafnium oxynitride films

The hafnium oxynitride films were also deposited on glass insulators in different sputtering parameter conditions. All deposited films were found out to be hydrophobic and nanocrystalline . However, the hydrophobicity of HfO_xN_y films were less in comparison to the HfO_2 films. The resistivity was of the order 10^5 Ω-cm which was higher in comparison to the HfO_2 films. The dielectric constant was also somewhat higher (~24) in HfO_xN_y in comparison to the HfO_2 films. The optimum sputtering parameters for HfO_xN_y films were

(i) As deposition and Ar as inert gas

(ii) 10 % of O_2 partial pressure

(iii) 20 m Torr sputtering Pressure

(iv) 50 W DC power

The water contact angle was 97.23°, resistivity was 1.31×10^4 Ω-cm, dielectric constant was ~24 and the bandgap was 5.08 eV at the above mentioned optimized sputtering parameters. The optimized coated insulator also possesses high breakdown strength (25 kV/mm) in comparison to uncoated glass insulator.

6.3 Effect of sputtering parameters on properties of nanocomposite hafnium-titanium oxide films

The nanocomposite hafnium-titanium oxide film was also deposited on glass insulators under different sputtering parameter conditions. The optimum sputtering parameter for nanocomposite films were

(i) Hafnium power-50 W, Titanium power-150 W

(ii) Substrate Temperature- 500°C

The nanocomposite films at these optimized parameter were having water contact angle of 107.6°, resistivity $3.3x10^4$ Ω-cm, dielectric constant 34.7 and bandgap 3.48 eV. The breakdown strength of optimized coated glass insulator was very high i.e. 37 kV/mm.

6.4 Comparative study of Deposited coatings

Table 6.1 shows the comparative study of the deposited coatings on glass insulators in respect to four important properties.

Table 6.1 *Comparison between three optimized coatings*

Property	HfO_2	HfO_xN_y	HfTiO
Hydrophobicity (degrees)	102.3	97.23	107.6
Resistivity(Ω-cm)	$\sim10^4$	$\sim10^5$	$\sim10^4$
Dielectric constant	21.4	24	34
Breakdown Strength (kV/mm)	23	25	37

The maximum hydrophobicity (target property) was obtained for nanocomposite HfTiO coating with high dielectric constant and high

breakdown strength. Though the resistivity was less in comparison to HfO_xN_y coating but the other three properties supersede them. Hence, nanocomposite coating HfTiO can be submitted as a best coating for glass insulators to mitigate contamination problem.

6.5 Suggestions for Future Work

Based on the present work carried out on the investigation of thin films such as hafnium oxide, hafnium oxynitride and nanocomposite hafnium-titanium oxide on glass insulators, the following recommendations for the future work are proposed.

1) The investigation of mechanical properties such as hardness, modulus of elasticity and scratch resistance test of hafnium oxide, hafnium oxynitride film and hafiumtitanium oxide thin films can be examined.

2) The nature of bonding and the compositional analysis of these films can be analyzed in detail using XPS technique as it influences various properties of the films.

3) The substrate biasing is one of the important process parameters for films deposited by sputtering, so its effect on the growth of these films and various properties can be investigated.

4) The effect annealing in various gas atmospheres on structural, wettability and optical properties of these films can be examined.

5) The multilayer coatings films can be deposited and its effect on various properties can be studied.

6) The dynamic contact angle measurement for these films can be examined.

7) The dielectric properties of deposited transition metal oxynitride films can be examined by the Ellipsometry technique.

8) The same coating can be tested on porcelain insulators.

9) Zirconium oxide and tantalum oxide can also be studied for this problem in future for comparison purpose.

Bibliography

[1] **Armelao L**., Bertagnolli H., Bleiner D., Groenewolt M., Gross S., Krishnan V., Sada C., Schubert U., Tondello E., Zattin A., "Highly Dispersed Mixed Zirconia and Hafnia Nanoparticles in a Silica Matrix: First Example of a ZrO_2–HfO_2–SiO_2 Ternary Oxide System", Adv. Funct. Mater. 17, 1671-1681 (2007).

[2] **Asahi R**., Morikawa T., Ohwaki T., Aoki K., Taga Y., "Visible-light photocatalysis in nitrogen-doped titanium oxides", Science 293, 269-71 (2001).

[3] **Aygun G.,** Cantas A., Simsek Y., Turan R., "Effects of physical growth conditions on the structural and optical properties of sputtered grown thin HfO_2 films", Thin Solid Films 519, 5820-5825 (2011).

[4] **Aygun G**., Yildiz I., "Interfacial and structural properties of sputtered HfO_2layers", J. Appl. Phys. **106**, 014312 (2009).

[5] **Baker M.A**., Monclus M.A., **Rebholz C.,** Gibson P.N., Leyland A. and Matthews A., "A study of the nanostructure and hardness of electron beam evaporated TiAlBN coatings", Thin Solid Films 518, 4273-4280 (2010).

[6] **Balog M.,** Schieber M., Michman M., Patai S., "Chemical vapour deposition and characterization of HfO_2 films from organo-hafnium compounds", Thin Solid Films 41247-259 (1977).

[7] **Barshilia H.C**., Rajam K.S., Jain A., Gopinadhan K., **Chaudhary S.**, A comparative study on the structure and properties of nanolayered TiN/NbN and

TiAlN/TiN multilayer coatings prepared by reactive direct current magnetron sputtering", Thin Solid Films **503** 158-166 (2006).

[8] **Beloa G.S**., Nakagomib F., Minkoa A., Silva S.W., Moraisb P.C., Buchanana D.A., "Phase transition in sputtered HfO_2 thin films: A qualitative Raman study", Appl. Surf. Sci. 261 727– 729 (2012).

[9] **Bendoraitis J.G**., Salomon R.E., "Optical Energy Gaps in the Monoclinic Oxides of Hafnium and Zirconium and Their Solid Solutions", Journal of Physical chemistry 69 3666 (1965).

[10] **Benkara S**., Zerkout S., Ghamri H., "Synthesis of Sn doped ZnO/TiO2 nanocomposite film and their application to H_2 gas sensing properties", Materials Science in Semiconductor Processing 16 1271–1279 (2013).

[11] **Bharathi K.K.,** Kalidindi N.R., **Ramana C.V**., "Grain size and strain effects on the optical and electrical properties of hafnium oxide nanocrystalline thin films", J. Appl. Phys. 108 083529 (2010).

[12] **Binks B.P**., Clint J.H., "Solid Wettability from Surface Energy Components: Relevance to Pickering Emulsions", Langmuir 18 1270-1273 (2002).

[13] **Brus J.E**., "Electron–electron and electronhole interactions in small semiconductor crystallites: The size dependence of the lowest excited electronic state", J. Chem. Phys. 80 4403-4409 (1984).

[14] **Buchanan D.A**., "Scaling the gate dielectric: Materials, integration, and reliability", IBM J. Res.Dev. 43 245 (1999).

[15] **Carberry R. E.,** Schneider H. M., "Evaluation of RTV coating for station insulators subjected to coastal contamination", IEEE Trans. Power Delivery 4 577-585 (1989).

[16] **Cassie A.B**., Baxter S., "Wettability of porous surfaces", Trans. Faraday Soc. 40 546–551 (1944).

[17] **Chandra R.,** Chawla A.K., Kaur A.K., Ayyub P., "Strucural, optical and electronic properties of nanocrystalline TiN films", Nanotechnology 16, 3053-3056 (2006).

[18] **Chaudhary S.**, Pandya D.K., Kashyap S.C., "Study of the oxygen incorporation and structure in the low pressure sputtered YBCO films", Thin Solid Films **433** 114-118 (2003).

[19] **Chawla A.K**., Singhal S., Gupta H.O., Chandra R., "Influence of nitrogen doping on the sputter-deposited WO_3 films", Thin Solid Films 518 1433 (2009).

[20] **Chawla A.K**., Singhal S., Gupta H.O., Chandra R., "Effect of sputtering gas on structural and optical properties of nanocrystalline tungsten oxide films", Thin Solid Films 517 1042–1046 (2008).

[21] **Chawla A.K**., Singhal S., Gupta H.O.. Chandra R., "Effect of sputtering gas on structural and optical properties of nanocrystalline tungsten oxide films", Thin Solid Films 517 1042–6 (2008).

[22] **Chen L**., Hu J., Lin F., Cadigan C., Cao W., Qi Z., Pozuelo M., Prikhodko S., **Kodambaka S.**, Richards R., "Self-Assembled Single-crystalline ZnO Nanostructures", Cryst Eng Comm. 15, 3780-3784 (2013).

[23] **Chen Y.,** Guo Z., Xu J., Shi L., Li J., Zhang Y., "Inspired superhydrophobi c surfaces by a double-metal-assisted chemical etching route", Mater. Res. Bull. 47 1687–1692 (2012).

[24] **Chio K.J.,** Kim J.H., Yoon S.G., Shin W.C., "Structural and electrical properties of HfO_xN_y and HfO_2 gate dielectrics in TaN gated nMOSCAP and nMOSFET devices", J Vac Sci Technol B 22 1755-58 (2004).

[25] **Chiu S.M.,** Hwang S.J., Chu C.W., Gan D., "The influence of Cr-based coating on the adhesion force between epoxy molding compounds and IC encapsulation mold", Thin Solid Films 515 285-292 (2006).

[26] **Chou W. J.,** Yu G. P., Huang J. H., "Deposition of TiN thin film on Si (100) by HCD ion plating", Surf. Coat. Technol. 140, 206-214 (2001).

[27] **Chow R.,** Falabella S., Loomis G.E., Rainer F., Stolz C.J., Kozlowski M.R., "Silicon dioxide and hafnium dioxide evaporation characteristics from a high-frequency sweep e-beam system", Appl. Opt. 32 5567 (1993).

[28] **Christofsumereder**, "The prospects of nanotechnology in electrical engineering", International conference electricity Distribution,Vienna,2007

[29] **Chrzan K.L**., Vosloo W.L., Holtzhausen J.P., "Leakage Current on Porcelain and Silicone Insulators Under Sea or Light Industrial Pollution", IEEE Trans. Power Del. 26 2051-2052 (2011).

[30] **Cullity B.D**., "Elements of X ray diffraction", 2nd edn Addison-Wesley, London,. 102 (1978)

[31] **D.C.Jolly**, "Contamination flashover Theory and Insulator design", Journal of Franklin Institute, 294 483-500 (1972).

[32] **Deng H**., Hackam R., Cherney E.A., "Influence of thickness, substrate type, amount of silicone fluid and solvent type on the electrical performance of RTV silicone rubber coatings", IEEE Trans. Power Del., 1, 431-443 (1996).

[33] **Dengke C**., Hui Y.J., Xishan W., Lei L., "Research on characterization of RTV silicone rubher/LSlayered silicate electrical insulation nanocomposites". Proceedings of the 2004 IEEE International Conference on Solid Dielectrics", 2 796 – 799 (2004).

[34] **Devendranath D**., Channakeshava, Rajkumar A.D., Leakage current and charge in RTV coated insulators under pollution conditions, IEEE Trans. Dielect Elect Insul. 2, 294-299 (2002).

[35] **Dubourdieu C**., Roussel H., Jimenez C., Audier M., Senateur J. P., Lhostis S., Auvray L., Ducroquet F. , O'Sullivan B.J., Hurley P.K., Rushworth S., Hubert-Pfalzgraf, L., "Pulsed liquid-injection MOCVD of high-K oxides for advanced semiconductor technologies", Mater. Sci. and Eng.Vol. B 118, 105-111 (2005).

[36] **Duncan B.**, Mera R., Leatherdale D., Taylor M., Musgrove R., "Techniques for characterising the wetting, coating and spreading of adhesives on surfaces", NPL Report DEPC MPR **020** 1-42 (2005).

[37] **Edlou S.M**., Smajkiewicz A., Al-Jumaily G.A., "Optical properties and environmental stability of oxide coatings deposited by reactive sputtering", Appl. Opt. 32 5601 (1993).

[38] **Ehsani M**., "Improvement of elelctrical, mechanical and surface properties of silicone Insulators", IEEE conference Proceeding on electrical insulation and dielectric phenomena, 623-626 (2004)

[39] **El Mandouh Z.S**., Selim M.S., "Physical properties of vanadium pentoxide sol gel films", Thin Solid Films 371 259-63 (2002).

[40] **Eldridge K**., Xu J., Yin W., Jeffrey A.M., "Degradation of a Silicone-Based Coating in a Substation Application", IEEE Trans. Power Del. 14 188-193 (1999).

[41] **Esplandiu M.J.,** Avalle L.B., Macagno V.A., Electrochim. Acta 40 (16) 2587-2593 (1995).

[42] **Fang Q.,** Zhang J.Y., Wang Z., Modreanu M., O'Sullivan B.J., Hurley P.K, leedham T.L., Hywel D., Audier M.A., Jimenez C., Senateur J.P., Boyd I.W., Thin Solid Films 453-454 203-207 (2004).

[43] **Feng A.,** McCoy B.J., Munir Z.A., Cagliostro D., "Wettability of transition metal oxide surfaces", Mater. Sci. Eng., A 242 50–56 (1998).

[44] **Fernando M. A. R. M**., Gubanski S**.** NI**.**, Leakage Currents on Non-ceramic Insulators and Materials, IEEE Trans. on Dielectr Electr Insul. 6, 660 (1999)

[45] **Ferrari S.,** Spiga S., Wiemer C., Fanciulli M., Dimoulas A., "Germanium diffusion during HfO_2 growth on Ge by molecular beam epitaxy", Appl. Phys. Lett. 89, 122906 (2006).

[46] **Filipescu M**., Scarisoreanu N., Craciun V., Mitu B., Purice A., Moldovan A., Ion V., Toma O., Dinescu M., "High-k dielectric oxides obtained by PLD as

solution for gates dielectric in MOS devices", Appl. Surf. Sci. 253 (2007) 8184–8191.

[47] **Fua W.E**., Changb C.W., Changa Y.Q., Yaob C.K., Liaob J.D., "Reliability assessment of ultra-thin HfO_2 films deposited on silicon wafer", Appl. Surf. Sci. 258 8974– 8979 (2012).

[48] **Gao P.,** Meng L.J., Dos Santos M.P., Teixeira V., Andritschky M., "Influence of sputtering pressure on the structure and properties of ZrO2 films prepared by rf reactive sputtering", Appl. Surf. Sci. 173 84-90 (2001).

[49] **Gao P.,** Meng L.J., dos Santos M.P., Teixeira V.,.Andritschky M., "Characterisation of ZrO2 films prepared by rf reactive sputtering at different O_2 concentrations in the sputtering gases", Vacuum 56 143 (2000).

[50] **Garg A.,** Barber Z.H., Dawber M., Scott J.F., Snedden A., and Lightfoot P., "Orientation Dependence of Ferroelectric Properties of Pulsed Laser Ablated Bi4-xNdxTi3O12 Films", Applied Physics Letters, 83 (12), 2414-2416 (2003).

[51] **Garg A.,** Snedden A., Lightfoot P., Scott J.F., Hu X., and Barber Z.H., "Investigation of Structural and Ferroelectrics Properties of Pulsed-Laser-Ablated Epitaxial Nd-Doped Bismuth Titanate Films", J. Appl. Phys. 96, 3408-3412 (2004).

[52] **Gencoglu M.T.,** Cebeci M., "The pollution flashover on high voltage insulators", Electric Power Systems Research 78 (2008) 1914–1921.

[53] **Genzer J.** , Efimenko K., "Recent developments in superhydrophobic surfaces and their relevance to marine fouling: a review", Biofouling 22 339 – 360 (2006)

[54] **Gohil S.**, Banerjee R., Bose S., Ayyub P., "Influence of synthesis conditions on the nanostructure of immiscible copper-silver alloy thin films", Scripta Materialia **58** 842- 845 (2008).

[55] **Goodhew P.J.**, Humphreys J., Beanland R., "Electron Microscopy and Analysis", Taylor and Francis London (2001).

[56] **Gopalakrishna D**., Vijayalakshmi K., Ravidhas C., "Effect of annealing on the properties of nanostructured CuO thin films for enhanced ethanol sensitivity". Ceramics International 39 7685–91 (2013).

[57] **Gorur R.S.,** Cherney E., Tourreil C., Dumora D., Harmon R., Hervig H., Kingsbury B., Kise J., Orbeck T., Tanaka K., Tay R., Toskey G., Wiitanen D., "Protective coatings for improving contamination performance of outdoor high voltage ceramic insulators", IEEE Trans. Power Del. 10 (1995) 924-933.

[58] **Gorur R.S**., Chernry E.A., Burnham J.T., "*Outdoor Insulators"*, 1st ed, Gorur Inc, Phoenix, Arizona, USA, 16-245, (1999).

[59] **Grace J. M.,** McDonald D. B., Reiten M. T., Olson J., Kampwirth R. T., Gray K. E., "Effect of oxidant on resputtering of Bi from Bi--Sr--Ca--Cu--O films", J. Vac. Technol. A10 1600 (1992).

[60] **Gubanski S.M**., "Properties of Silicone Rubber Housings and Coatings", IEEE Transactions on Electrical Insulation 27 567-569 (1992).

[61] **Hackam R.,** "Outdoor HV Composite Polymeric Insulators", IEEE Trans. Dielectr. Electr Insul. 6 (5) (1999).

[62] **Hackam R.**,Outdoor High voltage composite polymeric insulators, IEEE Trans Dielectrics 6 557-585 (1999).

[63] **Hall J.,** Orbeck T., "Evaluation of a new protective coating for porcelain insulators", IEEE Trans. Power App. Syst. 101 4689-4696 (1982).

[64] **He G.** , Zhu L.Q., Liu M., Fang Q., Zhang L.D., "Optical and electrical properties of plasma-oxidation derived HfO_2 gate dielectric films", Appl. Surf. Sci. 253 3413-6 (2007).

[65] **He G**., Zhang L.D., Liu M., Zhang J.P., Wang X.J., Zhen C.M., "Thickness-modulated optical dielectric constants and band alignments of HfO_xN_ygate dielectrics", J. Appl. Phys. 105 014109 (2009).

[66] **He G.,** Fanga Q., Li G.H., Zhanga J.P., Zhang L.D., "Structural and optical properties of nitrogen-incorporated Hf_{O2} gate dielectrics deposited by reactive sputtering", Appl. Surf. Sci. 253 8483-8488 (2007).

[67] **He G**., Zhang L.D., Meng G.W., Li G.H., Fang Q., Zhang J.P., "Temperature-dependent structural stability and optical properties of ultrathin Hf–Al–O films grown by facing- target reactive sputtering", J. Appl. Phys. 102 (2007) 094103.

[68] **Hegab N.A**., Bekheet A.E., Afifi M.A., El-Shazly A.A., "Effect of annealing on the optical properties of In2Te3 thin films", Appl. Phys.A 66 235-240 (1998).

[69] **Henry F**., Renaux F., Coppee S., Lazzaroni R., Vandencasteele N., Reniers F., Snyders R., "Synthesis of superhydrophobic PTFE-like thin films by self-nanostructuration in a hybrid plasma process", Surf. Sci. 606 1825–1829 (2012).

[70] **Housa M**., "High K gate Di electric", IPO, Bristal (2004).

[71] **Hu H**., Zhu C.X., Lu Y. F., Yu Y. H., Liew T., Li M. F., Cho B. J., Chio W. K., Yakovlev N., "Physical and electrical characterization of HfO_2 metal–insulator–metal capacitors for Si analog circuit applications", J. Appl. Phys. 94 551 (2003).

[72] **Huang J.H**., Lau K.W., Yu G.P., "Effect of nitrogen flow rate on structure and properties of nanocrystalline TiN thin films produced by unbalanced magnetron sputtering", Surf. Coat. Technol. 191 17– 24 (2005).

[73] **Huanga L.T.** , Changa M.L. , Huanga J.J., Lina H.C., Kuoa C.L. , Leeb M.L., "Improvement in electrical characteristics of HfO_2 gate dielectrics treated byremote NH_3 plasma", Appl Surf Science 266 89– 93 (2013).

[74] **Hwang C.S**., "Thickness-dependent dielectric constants of (Ba,Sr)TiO3 thin films with Pt or conducting oxide electrodes", J. Appl. Phys. 92 432-437 (2002).

[75] **Hwang Y**., Kim H., Umb Y., Park H., "Optical and electronic properties of highly stable and textured hydrogenated ZnO:Al thin films", Mater. Res. Bull. 47 2487–2491 (2012).

[76] **IEEE Working Group**, "A Survey of the Problem of Insulator Contamination in the United States and Canada", IEEE Trans. on Power Apparatus and Systems, 91 l948-1954 (1972**).**

[77] **J Tauc**, "Amorphous and Liquid Semiconductor", Plenium Press, New York, , pp. 159 (1974).

[78] **Jacobson R**., "Inhomogeneous and co-evaporated homogenous thin films for optical applications". Phys Thin films 8 51-55 (1975)

[79] **Janssen G**., "Stress and strain in polycrystalline thin films", Thin Solid Films 515 6654–64 (2007).

[80] **Jeevajothi K**., Crossiya D., Subasri R., "Non-fluorinated, room temperature curable hydrophobic coatings by sol–gel process", Ceramics International 38 (2012) 2971–2976.

[81] **Jerman M.,** Qiao Z., Mergel D., Mergel D., "Refractive index of thin films of SiO2, ZrO2, and HfO2 as a function of the films mass density", Appl. Opt. 44, 3006-3012 (2005).

[82] **Jiao H**., Cheng X., Lu J., Bao G., Liu Y., Ma B., He P., Wang Z., "Effects of substrate temperature on the structure and properties of hafnium dioxide films",Appl. Opt. 50, C312 (2011).

[83] **Jin J.,** Ko K.B., Song H.S., Cuong T.V., **Hong C.H.,** "Zirconium nitride polycrystalline films grown on Si (111) substrates by metal organic chemical vapor deposition", Materials Letters 125 8–11. (2014).

[84] **Jo Y.J**., Lee I.H., Kwak J.S., Zattin A., "In–Ga–Zn–O thin film transistor with HfO_2 gate insulator prepared using various O2/(Ar + O2) gas ratios", Mater. Res. Bull. 47 2919–2922 (2012).

[85] **Jones M.I**., McColl I.R., Grant D. M., "Effect of Substrate Preparation and Deposition Conditions on the Preferred Orientation of TiN Coatings Deposited by RF Reactive Sputtering", Surf. Coat. Technol., 132 143–151 (2000).

[86] **Karady G**., Shah M., Brown R., "Flashover Mechanism of silicone rubber Insulators used for outdoor Insulation", IEEE Trans Power delivery, 101965-1971 (1995)

[87] **Karady G.G**., "Flashover Mechanism of Non-ceramic Insulators", IEEE Trans. Dielectr. Electr. Insul. 6 (1999).

[88] **Kashyap S.C**., Gopinadhan K., Pandya D.K., **Chaudhary S.,** "A study of room-temperature ferromagnetism in transition metal and fluorine-doped spray-pyrolyzed SnO_2 thin films" Journal of Magnetism and Magnetic Materials 321 957–962 (2009).

[89] **Kaufmann E.N**., "Characterization of Materials" John Wiley and Sons Inc. New Jersey (2003).

[90] **Khranovskyy V**., Ekblad T., Yakimova R., Hultman L., 'Surface morphology effects on the light-controlled wettability of ZnO nanostructures", Appl. Surf. Sci. 258 8146– 8152 (2012).

[91] **Khudhayer W.J.,** Sharma R., Karabacak T., "Hydrophobic metallic nanorods with Teflon nanopatches", Nanotechnology 20 275302 (2009)..

[92] **Kim N.G**., Koo Y.S., Won C.J., Hur N., **Jung J.H.**, Yoon J., Jo Y., Jung M.H., "Magnetodielectric effect in $BaTiO_3$-$LaMnO_3$ composites", J. Appl. Phys.102 (1) 014107-014107-4 (2007).

[93] **Kim S.H**. , Cherney E.A., Hackam R., "Hydrophobic Behavior of Insulators Coated with RTV Silicone Rubber", IEEE Trans. Dielectr. Electr. Insul. 27 610-622 (1992).

[94] **Kim J.,** Kim S., Kang H., Choi J., Jeon H., Cho M., Chung K., Back S., Yoo K., Bae C., "Composition, structure, and electrical characteristics of HfO2 gate dielectrics grown using the remote- and direct-plasma atomic layer deposition methods", J. Appl. Phys 98 094504 (2005).

[95] **Kukli K**., Ritala M., Leskela M., Sundqvist J., Oberbeck L., Heitmann J., Schroder U., Aarik J., Aidla A., "Influence of TiO2 incorporation in HfO2 and Al2O3 based capacitor dielectrics", Thin Solid Films 515 6447–6451 (2007).

[96] **Kumar A**., Pandya D.K., **Chaudhary S.** , "Electric field assisted sputtering of Fe_3O_4 thin films and reduction in anti-phase boundaries", J. Appl. Phys., 112(7) 073909 (2012),.

[97] **Kumar A**., Singh P., Kulkarni N., Kaur D., "Structural and Optical studies of nanocrystalline V_2O_5 thin films", Thin Solid films 516 912-918 (2008).

[98] **Kumar A**., **Tandon R.P.,** Awana V.P.S., "Spin dynamics, short-range order and superparamagnetism in superconducting ferromagnet $RuSr_2Gd_{1.4}Ce_{0.6}Cu_2O_{10-\delta}$" Journal of Magnetism and Magnetic Materials 349 224–231 (2014).

[99] **Kumar N.,** Kim N.G., Park Y.A., Hur N., **Jung J.H.,** Han K.J., Yee K.J., "Epitaxial growth of terbium iron garnet thin films with out-of-plane axis of magnetization" Thin Solid Films 516 7753–7757 (2008).

[100] **Kumar V.S**., **Mahendiran R.**, "Effect of impurity doping at the Mn-site on magnetocaloric effect in $Pr_{0.6}Ca_{0.4}Mn_{0.96}B_{0.04}O_3$ (B= Al, Fe, Cr, Ni, Co, and Ru)", J. Appl. Phys.109 (2) 023903-023903-7, (2011).

[101] **Kwak D.J**., Park M.W., Sung Y.M., "Discharge power dependence of structural and electrical properties of Al-doped ZnO conducting film by magnetron sputtering", Vacuum 83 113–118 (2008).

[102]**Lambeth P.J**., Effect of Pollution on High Voltage Insulators, Proc. IEE Reviews, 118 1107-1130 (1971).

[103]**Lee M.**, Lu Z.H., Ng W.T., Landheer D., Wu X., Moisa S., "Interfacial growth in HfOxNy gate dielectrics deposited using $[(C_2H_5)_2N]_4Hf$ with O_2 and NO", Appl. Phys. Lett. 83 2638-2640 (2003).

[104]**Lee T.Y**., **Kodambaka S.**,. Wen J.G, Twesten R., Petrov I., Greene J.E., "Nanostructural evolution of Ti0.8Ce0.2N layers grown on oxidized Si(001) by magnetron sputter deposition as a function of low energy, high flux ion irradiation," Appl. Phys. Lett. 84, 2796 (2004).

[105] **Lehan J**., Mao Y., Bovard B.G., Macleod H.A., "Optical and microstructural properties of hafnium dioxide thin films," Thin Solid Films 203227-250 (1991).

[106] **Lewis T.J**., "Nanometric Dielectrics, IEEE Trans. Dielectric Electr Insul, 1 812-25 (1994).

[107]**Lim Y.V**., Wong T.I., Wang S., "Electronic structure and crystallinity of the HfO_2–TiO_2 thin films", Thin Solid Films 518 e107–e110 (2010).

[108]**Lin S.S**., "The optical properties of Ti-doped TiO_2 nanoceramic films deposited by simultaneous rf and dc magnetron sputtering", Ceramics International 38 3129–3134 (2012).

[109]**Lina S.S**., Liao C.S., "The hydrophobicity and optical properties of the HfO_2-deposited glass", Ceramics International 39: 353–8 (2013).

[110] **Liu M**., Fang Q., He G., Li L., Zhu L. Q., Li G. H., Zhang L. D., **"**Effect of post deposition annealing on the optical properties of HfO_xN_y films", Appl. Phys. Lett. 88 192904 (2006).

[111] **Liu M**., Fang Q., He G., Li L., Zhu L.Q., Li G.H., Zhang L.D., "Effect of post deposition annealing on the optical properties of HfO_xN_y films", Appl Phys Lett 88 192904 (2006).

[112] **Liu M**., Fang Q., He G., Zhu L.Q., Pan S.S., Zhang L.D., "Chemical compositions and optical properties of HfO_xN_y thin films at different substrate temperatures", Mater Sci Semicond Process 9 876-9 (2006).

[113] **Liu M**., Fang Q., He G., Zhu L.Q., Zhang L.D., "Characterization of HfO_xN_y gate dielectrics using a hafnium oxide as target", Appl Surf Sci 252 8673–6 (2006).

[114] **Liu W**., Su X.P., Zhang S.Y., Wang H.B., Liu J.H., Yan L.Q., "Effect of the oxygen fraction on the structure and optical properties of HfOxNy thin films". Vacuum 2008; 82: 1280-4.

[115] **Looms J.S.T**., Insulators for High Voltages, The Institution of Engineering and Technology, London, pp. 2. (1988)

[116] **Lysaught P. S**., P. J. Chen, R. Bergmann, T. Messina, R. W. Murto, H. R. Huff, Journal of Non-Crystalline Solids **303**, 54-63 (2002).

[117] **M.F. Al-Kuhaili**, Optical properties of hafnium oxide thin films and their application in energy-efficient windows, Opt. Mater. 27 (2004) 383-387.

[118] **Mahendiran R.,** Mahesh R., Rayachaudhuri A.K., and Rao C.N., "Room Temperature giant magnetoresistance in $La_{1-x}Pb_xMnO_3$", Journal of Physics D: Applied Physics, 66(2), 233 (1995).

[119] **Mahesh R**., **Mahendiran R.,** Rayachaudhuri A.K., and Rao C.N.R., "Effect of particle size on the giant magnetoresistance of $La_{0.7}Ca_{0.3}MnO_3$", Applied Physics Letters, 68, 2291 (1996).

[120] **Maissel L.I.**, Glang R., Handbook of Thin film Technology, McGraw-Hill, New York. (1970).

[121] **Manifacier C**., Gasiot J., Fillard J.P., "A simple method for the determination of the optical constants *n*, *h* and the thickness of a weakly absorbing thin film", J. Phys. E: Sci. Instrum. 9 1002–1004 (1976).

[122] **Manifacier J.C.,** Gasiot J., Fillard J.P., "A simple method for the determination of the optical constants *n*, *h* and the thickness of a weakly absorbing thin film", J. Phys. E: Sci. Instrum. 9 1002–1004 (1976).

[123] **Martin P.M.**, "Handbook of Depostion Technologies for Films and Coatings: Science, Applications and Technology", Elsevier USA (2010).

[124] **Martınez F.L**., Luque M.T., Gandıa J. J., Arabe J.C., Bohne W., Ohrich J.R., Strub E., Martil I., "Optical properties and structure of HfO2 thin films grown by high pressure reactive Sputtering", J. Phys. D: Appl. Phys. 40 5256–5265 (2007).

[125] **Matovic B**., Bucevac D., Prekajski M., Maksimovic V., Gautam D., Yoshida K., Yano T., "Synthesis and characterization of nanometric yttrium-doped hafnia solid solutions", J Eur Ceram Soc 32 1971–6. (2012)

[126] **Mattox D.M.**, "Handbook of Physical Vapor Deposition (PVD) Processing: Film Formation, Adhesion, Surface Preparation and Contamination Control", Noyes Publications New Jersey (1998).

[127] **Metina H**., Erat S., Durmus S., Arid M., "Annealing effect on CdS/SnO2 films grown by chemical bath deposition", Appl. Surf. Sci. 256 5076–5081 (2010).

[128] **Ming D.**, Eric B., Diebold A.C., "Comparison of methods to determine bandgaps of ultrathin HfO2 films using spectroscopic ellipsometry", J. Vac. Sci. Technol. A 29(4) 041001-9 (2011).

[129] **Moran J.H**., Powell D.G., **"**Resistance graded insulators -the ultimate solution to the contamination problem?", IEEE Trans. Power App. Syst. 91 2453-2548 (1972).

[130] **Murthy Y.,** Rao T.K., Kasiviswanath I.V., and **Singh R., "**Synthesis and Characterization of Nano Silver Ferrite Composites", Journal of Magnetism and Magentic Material 10 1016 (2010).

[131] **Murthy Y.,** Rao T.K., Kasiviswanath I.V., and **Singh R., "**Synthesis and characterization of silver ferrite composite", Journal of Magnetism and Magnetic Materials, 322, 2071-2074, (2010).

[132] **Natori K.,** Otani D., Sano N., "Thickness dependence of the effective dielectric constant in a thin film capacitor", Appl. Phys. Lett. 73 632-634 (1998).

[133] **Neinhuis C**., Barthlott W., "Purity of the sacred lotus, or escape from contamination in biological surfaces", Planta 202 1-8 (1997).

[134] **Neumayer D.A**., Cartier E., "Materials characterization of ZrO2–SiO2 and HfO2–SiO2 binary oxides deposited by chemical solution deposition", J. Appl. Phys. 90 1801 (2001).

[135] **Nosonovsky M**., Bhushan B., "Multiscale dissipative Mechanisms and Hiearchical Surfaces friction: Superhydrophobicity and Biomimetics", Springer, New York, , p.120 (2008).

[136] **Nosonovsky M**. , Bhushan B., "Roughness optimization for biomimetic super hydrophobic surfaces". Microsys Technol 11: 535-49 (2005).

[137] **Noyan I.C.,** Cohen J.B., "Residual Stress: Measurement by Diffraction and Interpretation", Springer-Verlag, New York (1987).

[138] **Oettel H**., Wiedemann R., Preissler S., "Residual stresses in nitride hard coatings prepared by magnetron sputtering and arc evaporation". Surf Coat Technol 273 74-75 (1995).

[139] **Ohring M**., The Materials Science of Thin Films, Academic Press, San Diego, CA (1992).

[140] **Otte K**., Makhova L., Braun A., Konovalov I., "Flexible Cu(In,Ga)Se2 thin-film solar cells for space", Thin Solid Films 511, 613 (2006).

[141] **Owens D.K**., Wendt R.C., "Estimation of the surface energy free energy of polymers", Appl. Polym. Sci. 13 1741-1747 (1969).

[142] **Palacios J.C**., Cruz G.J., Olayo M.G., Carvaya J.A., "Characterization of hydrophobic and hydrophilic polythiophene–silver–copper thin film composites synthesized by DC glow discharges", Surf. Coat. Techno**l.** 203 3032–3036 (2009).

[143] **Palmero A**., Rudolph H., . Habraken F. H. P. M., "One-dimensional analysis of the rate of plasma-assisted sputter deposition", J. Appl. Phys. 101, 083307 (2007).

[144] **Pandeya K.B**., **Singh R.**, Prakash C. & Baijal J.S., "Effect of doping on the spin state of a tris(dithiocarbamato) Iron(III) complex" .Solid State Commun., Vol. 64, No. 5, 801- 804. (1987).

[145] **Park P.K**., Kang S.W.. Enhancement of dielectric constant in HfO_2 thin films by the addition of Al_2O_3. Appl Phys Lett 89: 192905 (2006).

[146] **Pereira L**., Barquinha P., Fortunato E., Martins R., "Influence of the oxygen/argon ratio on the properties of sputtered hafnium oxide", Mater. Sci. Eng. B 118 (2005) 210-213.

[147] **Periasamy C., Prakash R**. and Chakrabarti P., "Effect of Post Annealing on Structural and Optical Properties of ZnO Thin Films Deposited by Vacuum Coating Technique." J Mater Sci: Materials in Electronics, 21 309-315 (2010).

[148] **Pulker H.K**., "Characterization of optical thin films", Appl. Opt 18 12 (1979) 1969-1977

[149] **R. Chandra**, A.K. Chawla, P. Ayyub, J. Nanosci. Nanotechnol. 6 (2006) 1119-1123.

[150] **Ramana C.V**., Vemuri R.S., Fernandez I., Campbell A.L., "Size-effects on the optical properties of zirconium oxide thin films", Applied Physics Letters 95 231905 (2009).

[151] **Ramirez I.**, Cherney E.A., Jarayam S., "Comparison of the Erosion Resistance of Silicone Rubber and EPDM Composites Filled with Micro Silica and ATH", IEEE Trans. Dielectr. Electr. Insul. 19 218-224 (2012).

[152] **Ramos-Gonzaleza R.**, Garcia-Cerdaa L.A., Quevedo-Lopezb M.A., "Study of the surface modification with oleic acid of nanosized HfO_2 synthesized by the polymerized complex derived sol–gel method", Appl. Surf. Science 258 6034– 6039 (2012).

[153] **Rawal S.K.,** Chawla A.K., Jayaganthan R., Chandra R., "Characterization of bi-phased Zr_2ON_2–ZrO_2 coatings deposited by RF magnetron sputtering". Thin Solid Films 520 1589 (2011)

[154] **Reinosa J.J.**, Romero J.J., Jaquotot P., Bengochea M.A., Fernandez J.F., "Copper based hydrophobic ceramic nanocoating". J Eur Ceram Soc 32 277–282 (2012).

[155] **Roy C.K.**, Noor-A-Alam M., Choudhuri A.R., **Ramana C.V.**, "Synthesis and microstructure of Gd_2O_3-doped HfO_2 ceramics", Ceramics International ; 38: 1801–6 (2012).

[156] **S. Kodambaka**, S.V. Khare, W. Święch, K. Ohmori, I. Petrov, and J.E. Greene, Dislocation driven surface dynamics on solids," Nature 429 49 (2004).

[157] **Saarikoski I.**, Korpela F.J., Suvanto M., Pakkanen T.T., "Superhydrophobic elastomer surfaces with nanostructured micronails", Surf. Sci. 606 91–98 (2012).

[158] **Singh A.K**., Singh S.K., Gupta B.K., **Praksh R.** and Rai S.B., "Lanthanide doped dual-mode nanophosphor as spectral converter for promising next generation solar cells." Science of Advanced Materials 13-597-RR (2013).

[159] **Singh P.,** Park Y.A., Sung K.D., Hur N., **Jung J.H.,** Noh W.S., Kim J.Y., J. Yoon, Jo Y., "Magnetic and ferroelectric properties of epitaxial Sr-doped $BiFeO_3$ thin films" , Solid State Communications 150, 431-434 (2010).

[160] **Singh S**., Srivastava V.K., **Prakash R.,** "Mechanical properties and morphological studies of C/C–SiC composites" Materials Science and Engineering A, 534 707– 710 (2012).

[161] **Sinha S.K**., Bhattacharya R., Ray S.K., Manna I., "Influence of deposition temperature on structure and morphology of nanostructured SnO_2 films synthesized by pulsed laser deposition". Materials Letters ; 65: 146–9 (2011)

[162] **Sproul W.D.**, Christie D.J., Carter D.C., "Control of reactive sputtering processes", Thin Solid Films **491** 1-17 (2005).

[163] **Srivastava A**., **Garg A**., Morrison F.D., "Impedance Spectroscopy Studies on Polycrystalline $BiFeO_3$ Thin Films on Pt/Si Substrates", J. Appl. Phys., 105 054103 (2009).

[164] **Stone D.** , Liu J. , Singh D. P. , Muratore C., Voevodin A. A. , Mishra S., **Rebholz C.**, Ge Q., Aouadi S. M., "Layered atomic structures of double oxides for low shear strength at high temperatures", Scripta Mater., 62(10) 735-738 (2010).

[165] **Sulaiman A.E**., Qureshi M.I., "Effect of Contamination on the leakage current of inland desert insulator", IEEE Trans. Dielectr. Electr. Insul. 19 332-339 (1984).

[166] **Sumereder C**., Muhr M., "The Prospect of nanotechnology in Electrical engineering",19th International Conference on Electricity Distribution, Vienna (2007).

[167] **Swanepoel R**., "Determination of the thickness and optical constants of amorphous silicon", Phys. E: Sci. Instrum. 16 1214 (1983).

[168] **Tan R.**, Azuma Y., Kojima I., "Suppression of interfacial diffusion by a predeposited Hf metal layer on SiO 2/Si", Appl. Surf. Sci. 222 346-350 (2004).

[169] **Tan T.,** Liu Z., Li Y., "First-principles calculations of electronic and optical properties of Ti-doped monoclinic HfO2", Journal of Alloys and Compounds 510 78– 82 (2012).

[170] **Tapily K**., Jakes J.E. , Stone D.S. , Shrestha P., Gu D., Baumgart H., Elmustafab A.A.**,** "Nanoindentation Investigation of HfO_2 and Al_2O_3 Films Grown by Atomic Layer Deposition", J. Electrochem. Soc. 155 7 H545-H551 (2008)

[171] **Tauc J.,** Amorphous and Liquid semiconductor, Plenium Press, New York, 1974, pp. 159.

[172] **Tena G.M**.,Corona R.H, Vazquez I.R., "Experiences on pollution level measurement in Mexico", Electric Power Systems Research 76 58–66 (2005).

[173] **Tickoo R**., **Tandon R. P.**, Banzai K. K., Kotru P. N., "Indentation induced testing studies on lanthanum modified lead titanate ceramics", Materials

Science and Engineering B: Solid-State Materials for Advanced Technology 110 (2) 177-184 (2004).

[174] **Tong K.Y.,** Jelenkovic E.V., Liu W., Dai J.Y., "Nitridation of hafnium oxide by reactive sputtering", Microelectron. Eng. 83 293–297 (2006).

[175] **Tripathy M.R**., Joshi R., Mehra N.C., Kumar S., **Tandon R.P.,** "Electrical conduction and gas sensing characteristics of 15Fe2O3–5ZnO–80TeO2", Materials Letters 61, 585–587 (2007).

[176] **Tsotsos C**., Polychronopoulou K., Baker M. A., Hinder S. J., Gibson P. N., Giannakopoulos K., Polycarpou A., Bobel K. and **Rebholz C.,** "Structure and mechanical properties of low temperature magnetron sputtered nanocrystalline Ti(N,C)/amorphous diamond like carbon coatings", Thin Solid Films 519, 24-30 (2010).

[177] **Uthirakumar P**., **Hong C.H.,** "Effect of annealing temperature and pH on morphology and optical property of highly dispersible ZnO nanoparticles" Materials Characterization 60, 1305–1310 (2009).

[178] **Vaz F.,** Carvalho P., Cunha L., Rebouta L., Moura C., Alves E.,. Ramos A.R, Cavaleiro A., Goudeau Ph., Riviere J.P., Thin solid Films 11 469-470 (2004).

[179] **Venkataraj S**., Severin D., Mohamed S.H., Ngaruiya J., Kappertz O., Wuttig M., "Towards understanding the superior properties of transition metal oxynitrides prepared by reactive DC magnetron sputtering", Thin Solid Films 502 228 – 234 (2006).

[180] **W. Lee**, M.K. Jin, W.C. Yoo, and J. K. Lee, Nanostructuring of a polymeric substrate with well-defined nanometer-scale topography and tailored surface wettability. *Langmuir*, 20, 7665-7669 (2004).

[181] **Wang J**., Maier R.L., Schreiber H., Crystal phase transition of HfO_2 films evaporated by plasma ion assisted deposition, Appl. Opt. Suppl. 47 C189-C192 (2008)

[182] **Wang T**., Chang L., Yang S., Jia Y., Wong C., "Hydrophobic properties of biomorphic carbon surfaces prepared by sintering lotus leaves". Ceramics International 39: 8165–72 (2013).

[183] **Wang X.J**., Zhang L.D., Zhang J.P., Liu M., He G., "Effects of nitrogen atom doping on optical properties and dielectric constant of HfO_2 gate oxides", Appl Phys Lett 92: 202906 (2008).

[184] **Wang Y**., Lin Z., Cheng X., Xiao H., Zhang F., Zou S., "Study of HfO_2 thin films prepared by electron beam evaporation", Appl. Surf. Sci. 228 93–99 (2004).

[185] **Wang Y**., Zhang J., Zhang F., Zhang F., Zou S., "Field emission from hafnium oxynitride films prepared by ion beam-assisted deposition", Appl Surf Sci 242: 407-11 (2005).

[186] **Wang Y.Z**., Qiao G.W., Liu X.D., Ding B.Z., Hu Z.Q., "Electrical resistivity of nanocrystalline Fe-Cu-Si-B alloys obtained by crystallization of the amorphous alloy", Mater. Lett. 17 152-154 (1993).

[187] **Washizu E**., Yamamoto A., Abe Y., Kawamura M., K. Sasaki, "Optical and electrochromic properties of RF reactively sputtered WO_3 films", Solid State Ionics 165, 175-180 (2003).

[188] **Wenzel R.N**., "Resistance of solid surfaces to wetting by water", Ind Eng Chem 28: 988–94 (1936).

[189] **Westwood W.D.**, S.M. Rossnagel, J.J. Cuomo,"Reactive Sputter Deposition Handbook of Plasma Processing Technology: Fundamentals, Etching, Deposition and Surface Interactions", eds. Noyes Publications New Jersey (1990).

[190] **Wilk G.D**., Wallace R.M., Anthony J.M., "High-κ gate dielectrics: Current status and materials properties considerations", J.Appl. Phys. 89(2001) 5243.

[191] **Wu K.R**., Wang J.J., liu W.C., Chen Z.S., Wu J.K., "Deposition of graded TiO_2 films featured both hydrophobic and photo-induced hydrophilic properties", Appl. Surf. Sci. 252 5829-5838 (2006).

[192] **Wu L**., Tien-Shou W., Chung-chuang W., "Effects of various substitutions on the DC resistivity of ferrites.", J Phys. D: Appl. Phys. 13 259 (1980).

[193] **Wu M.W**., Liu D.S., Su Y.H., "The densification, microstructure, and electrical properties of aluminum-doped zinc oxide sputtering target for transparent conductive oxide film", J Eur Ceram Soc 32 3265–75 (2012).

[194] **Wu S.,** "Polar and Nonpolar interaction in adhesion", J. Adhesion 5 39-55 (1973).

[195] **X. J. Wang**, L. D. Zhang, J. P. Zhang, M. Liu, and G. He, Effects of nitrogen atom doping on optical properties and dielectric constant of HfO_2 gate oxides, Appl. Phys. Lett. 92 (2008) 202906

[196] **Xiong K**., Robertson J., "Point defects in HfO_2 high K gate oxide", Microelectron. Eng. 80 408-411 (2005).

[197] **Yamamura Y.**, Matasunami, N., Itoh N., "Theoretical studies in the experimental formula for sputtering yields at normal incidence," Radiation Effects **71** 65 (1983).

[198] **Yan L.T**., Rath J. K., Schropp R. E. I., "Electrical properties of vacuum-annealed titanium-doped indium oxide films", Appl. Surf. Sci., 257 9461–9465 (2011).

[199] **Yoffe A.D**., "Low-dimensional systems: quantum size effects and electronic properties of semiconductor microcrystallites (zero-dimensional systems) and some quasi-two-dimensional systems", Adv. Phys. 42, 173-262 (1993).

[200] **Yoshimura N.**, Kumagai S., "Electrical and Environmental Aging of Silicone Rubber Used in Outdoor Insulation", IEEE Transactions on Dielectrics and Electrical Insulation 6, (632)1999.

[201] **Young T.,** "An essay on the cohesion of fluids", Philos Trans R Soc Lond 1805; 95: 65–77.

[202] **Yuan L**., Fang G., Zhou H., Gao Y., Liu C., Zhao X., "Suppression of near-edge optical absorption band in sputter deposited hafnium oxynitride via nitrogen incorporation and annealing", J Phys D Appl Phys 42 145302 (2009).

[203] **Yuzhen L V**, "Synthesis, characterization and anti pollution property of Inorganic coating", IEEE Conference on Properties and Applications of Dielectric Materials ,China, 158-160 (2009).

[204] **Zhu J.,** Liu Z.G., Feng Y., "Thermal stability and electrical properties of pulsed laser-deposited Hf-silicate thin films for high-k gate dielectric applications", J.Phys.D Appl. Phys. 36 3051-3056 (2003).

[205] **Zukic M**., Torr D. G., Spann J. F., Torr M. R., "VUV thin films. Part 2: Vacuum ultraviolet all-dielectric narrowband filters", Applied Optics 29 4284 (1990).